Ph.D Thesis

Dynamics of Confined Laser Induced/Ablative Plasmas and Shock Waves

Nagaraju Guthikonda

हैदराबाद विश्वविद्यालय
University of Hyderabad

प्रतिष्ठित संस्थान
INSTITUTION OF EMINENCE
राष्ट्रीय अपेक्षाएँ, वैश्विक मानक
National Needs, Global Standards

A Thesis entitled

Dynamics of Confined Laser Induced/Ablative Plasmas and Shock Waves

Submitted to

University of Hyderabad

For the award of the degree of

Doctor of Philosophy

in

Physics

by

Nagaraju Guthikonda

(14ACPA01)

Under the Supervision of

Dr. P. Prem Kiran

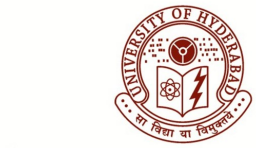

Advanced Centre for Research in High Energy Materials (ACRHEM)
School of Physics
University of Hyderabad
Hyderabad-500046

(November, 2020)

Dedicated to

My Family & Friends

हैदराबाद विश्वविद्यालय
University of Hyderabad

प्रतिष्ठित संस्थान
INSTITUTION OF EMINENCE

Declaration

I, ***Nagaraju Guthikonda*** hereby declare that, the work reported in this thesis entitled, *"Dynamics of Confined Laser Induced/Ablative Plasmas and Shock Waves"*, is original and has been carried out by me under the supervision of *Dr. P. Prem Kiran*, ACRHEM, School of Physics, University of Hyderabad, Telangana, India, as per the Ph.D. ordinances of the University. I also declare that, this work is free from plagiarism and it has not submitted for the award of a research degree at any other University. I hereby agree that my thesis can be deposited in Shodhganga or INFLIBNET.

A report on plagiarism statistics from the university librarian is enclosed.

(NAGARAJU GUTHIKONDA)
Reg. No: 14ACPA01

P. Prem Kiran

(Dr. P. Prem Kiran)
Thesis Supervisor,
ACRHEM, School of Physics,
University of Hyderabad.

Dr. P. Prem Kiran
Associate Professor
School of Physics
University of Hyderabad
Hyderabad-500 046. (TS) INDIA

हैदराबाद विश्वविद्यालय
University of Hyderabad

Certificate

This is to certify that, the thesis entitled *"Dynamics of Confined Laser Induced/Ablative Plasmas and Shock Waves"*, submitted to the University of Hyderabad by *Mr. Nagaraju Guthikonda* bearing *Reg. No. 14ACPA01* in partial fulfilment of the requirements for the award of Doctor of Philosophy in Physics, is a bonafide work carried out by him under my supervision and guidance, which is a plagiarism free thesis. The thesis has not been submitted previously in part or in full to this or any other University or Institution for the award of any degree or diploma.

(Dr. P. Prem Kiran)
Thesis Supervisor,
ACRHEM, School of Physics,
University of Hyderabad.

Dr. P. Prem Kiran
Associate Professor
School of Physics
University of Hyderabad
Hyderabad-500 046. (TS) INDIA

Director,
ACRHEM,
University of Hyderabad.

Dean,
School of physics,
University of Hyderabad.

DEAN
School of Physics
University of Hyderabad
HYDERABAD - 500 046

हैदराबाद विश्वविद्यालय
University of Hyderabad

प्रतिष्ठित संस्थान
INSTITUTION OF EMINENCE
राष्ट्रीय अपेक्षाएँ, वैश्विक मानक
National Needs, Global Standards

Certificate of Course Work

This is to certify that the thesis entitled *"Dynamics of Confined Laser Induced/Ablative Plasmas and Shock Waves"*, submitted to the University of Hyderabad by *Mr. Nagaraju Guthikonda* bearing *Reg. No. 14ACPA01*, in partial fulfilment of the requirements for the award of Doctor of Philosophy in Physics at ACRHEM, School of Physics, University of Hyderabad, is a bonafide work carried out by him under my supervision and guidance. This thesis is free from the plagiarism and has not been submitted previously in part or in full to this or any other University or Institution for the award of any degree or diploma.
Further, the student has the following publications before submission of the thesis for adjudication:

- **Nagaraju Guthikonda**, E. Manikanta, Ch. Leela, S. Sai Shiva, S. Sree Harsha, V. R. Ikkurthi and P. Prem Kiran, *Interaction of two counter-propagating laser induced plasmas and shock waves in air*, Physics of Plasmas 27, 023107 (2020). (**Chapter 3**)

- **Nagaraju Guthikonda**, Ch. Leela and P. Prem Kiran, *Interaction of Two Counter-Propagating Laser Induced Shock Waves in air*, Bulletin of Indian Laser Association: Kiran, vol. 26, No.1 (2017). (**Chapter 3**)

Manuscripts under preparation/review:

- **Nagaraju Guthikonda**, S. Sai Shiva, D. P. S. L. Kameswari, P. Prem Kiran, C. D. Sijoy and V. R. Ikkurthi, *Effect of Focusing Plane on Laser Blow-off Shock Waves from Confined Aluminum and Copper Foils*, Journal of Physics D (2020). (**Chapter 4**)

- **Nagaraju Guthikonda**, D. P. S. L Kameswari, E. Manikanta, S. Sai Shiva, S. Sree Harsha and P. Prem Kiran, *Dynamics of confined laser induced air plasma inside a hollow tube*, Optic Letters (2020). (**Chapter 5**)

- **Nagaraju Guthikonda**, E. Manikanta, G. Muthukumaran and P. Prem Kiran, *Shadowgraphy Imaging of Laser Induced Shock waves in Transparent Media* (2020).

(**Chapter 6**)

Also, made presentations in the following conferences:

- **Nagaraju Guthikonda**, Ch. Leela and P. Prem Kiran, *Interaction of Two Counter-Propagating Laser Induced Shock Waves in air*, 25^{th} DAE-BRNS National Laser symposium (NLS-25), KIIT University, Bhubaneswar, India, $20 - 23^{th}$ December (2016). (**Best Poster award**)

- **Nagaraju Guthikonda**, Ganesh Muthukumaran B and P Prem Kiran, *Shadowgraphy Imaging of Laser Blow-off of metal and polymer films*, 5^{th} National Symposium on Shock Waves, TBRL, Chandigarh, India, $26 - 28^{th}$ February (2018). (**Best Oral Presentation award**)

The following courses have taken as part of the course work:

Course No.	Course offered at	Title of the Course	Credits	Pass/Fail
PY804	School of Physics	Advanced EM Theory	4	Pass
AC807	ACRHEM	Research Methodology	4	Pass
AC808	ACREHM	Non-linear Optics	4	Pass
AC810	ACRHEM	Introduction to HEMs	4	Pass

P. Prem Kiran

(Dr. P. Prem Kiran)
Thesis Supervisor,
ACRHEM, School of Physics,
University of Hyderabad.

Dr. P. Prem Kiran
Associate Professor
School of Physics
University of Hyderabad
Hyderabad-500 046. (TS) INDIA

V. Venkatesan

Director,
ACRHEM,
University of Hyderabad.

Director
ACRHEM

Dean,
School of physics,
University of Hyderabad.

DEAN
School of Physics
University of Hyderabad
HYDERABAD - 500 046.

Acknowledgments

श्रीराम राम रामेति रमे रामे मनोरमे ।
सहस्रनाम तत्तुल्यं राम नाम वरानने ॥ २७ ॥

"...may the LORD RAMA bless us all... "

Immeasurable appreciation and deepest gratitude for the help and support are extended to the following persons who in one way or another have contributed in making this research possible.

Firstly, I am grateful to my supervisor *Dr. P. Prem Kiran* whose expertise, understanding, continuous support, generous guidance and consistent encouragement made it possible for me to work on the topic of interest of me. Sharing his knowledge, helping in analysis of data, writing manuscripts and improving in my presentation skills has put me on a different level. I could not have imagined having a better advisor and mentor for my Ph.D. study both academically and personally. Personally he is a noble and inherent with high human values and has helped me in difficult times to get through those situations. I extend my sincere thanks to past and present *Director, ACRHEM*; *Dean, School of Physics* for their unconditional academic support. I would like to thank my doctoral committee members *Dr. Ashok Vudayagiri* and *Dr. G. Manoj Kumar*, University of Hyderabad for showing their straightforward approach/understanding to the problems which i had faced during the analysis of my experimental data, art of imparting knowledge and skills that have been instructive and inspirational to me to learn/understand new approaches to the problems. I also like to thank *Prof. S. Venugopal Rao* and *Prof. A. K. Chaudhary* for their teachings in the course work. I would like to thank DRDO, Govt of India through ACRHEM for their financial support and office staff (ACRHEM and School of Physics)for their administrative support.

I have to mention my best thanks to *Dr. Sree Harsha* and *Dr. Rakesh Kumar* for their consistent help in suggesting the systematic learning and presentation approaches through their WH questions ?? (they are really like puzzles to me!!), throughout my research and writings of thesis. It has been a very pleasant experience to work in the warm and friendly atmosphere with my senior lab-mates: *Dr. Ch. Leela*, who gave initial training on Lasers and experiments (it's like training at Dehradun!!); *Dr. S. Sai Shiva*, who taught me theory behind experiments and theoretical correlation with experimental results (it's like a technical detective thriller!!) ; *Dr. E. Manikanta*, who shared the lab experiences (technical failures) which led me to the understand each and every aspects of the instruments we have used in the lab (it's like Mani's Autography-sweet memories!!); *Dr. P. Venkateshwarulu, Dr. L. Vinoth Kumar and Juniors' Phani Sree, Samuel Anurag*

and J. Yellaiah. I also thank all my energetic friends *Dr. B. Chandu, M. Mahendar, J. Rajendhar, D. Ganesh (Gani), Dr Kalam, Dr. Ravi Kiran, M.S.S. Bharathi, Linga, KK, Arun, Dr. Konda, Dr Simha* and my super seniors in ACRHEM for the enthusiastic discussions in subject will be remembered. I would like to thank all my ACRHEM and School of Physics friends for helping and supporting me unconditionally on this long and sometimes difficult journey.

Especially, I convey my heartfelt thanks and love to my wife *HARINI*, for her understanding of research life and continued to encourage/support me for fulfilling my dream. I would like to give my lovely heartfelt wishes and blessings to my younger brothers: *Nagendra and Venky (and their families)*, for taking care responsibilities at home in my absence and a special thanks to friends in my village for giving an invaluable memories from my childhood. I will utilize this opportunity to specially thank my parents:*Mr.&Mrs. Ilamma Rajamallu garu* (infinitely; the word is not enough), for their continuous blessings from my childhood for giving me full freedom and having faith in me to achieve my dreams. I am grateful to my best buddies (*Dr. Ramya Uday, Mahee, Rama, Kanda, Geetha, Radhi, Sathi, Venu, Bheem, Banda,Akhi, Joo, Ajay*) for being with me whenever I needed. The memories and stories from time we spent together would fill a book thicker than this one. I thank my family uncles and cousins for understanding me throughout research work that I could not spare time with them. I will never forget the teachers (from school to college days) who inspired and encouraged me throughout my career for laying necessary foundations to achieve my big dream.

A big $\mathcal{THANK\ YOU}$ to my parents, my family and friends for their unconditional love and support!!!.

JAI HIND!!!

-Nagaraju Guthikonda

Abstract

This thesis discusses the dynamics of the confined laser induced/ablative plasmas and shock waves visualized through shadowgraphy technique to understand and develop a nano-second laser based milli-meter (mm) sized shock tube. The downscaling of the shock wave effects such as pressure, velocity attenuation during propagation, laminar and turbulence flow from macroscopic to mm or micro range, requires a proper extensive study to balance the interplay between the down scaling of the shock waves to mm size and maintaining the shock wave properties. This can be achieved by studying the enhancement of the plasma and shock wave properties in different confined geometries. Based on the experimental geometry used for plasma confinement, the confinement methods can be divided into two categories, (a) Axial confinement (b) Lateral or spatial confinement. In axial confinement, the plasma source is confined by a fluid (liquid/plasma/gas) or solid (glass) confining layer along laser propagation axis. The collision dynamics of the two counter propagating laser induced plasmas (S1 and S2) and shock waves in ambient air revealed the effect of the separation distance (d) between the confining plasma and confining medium (another plasma as fluid confinement). Here, the plasma source S2 is used as the temporally expanding fluid confining medium, which confines the plasma source S1 generated with 25 mJ laser energy. This study also helps to understand the effect of the relative impedance of the confining plasma and fluid confining medium with different impedances ($Z = \rho U_{sw}$) along with the effect of separation distance between two plasma sources (S1 and S2). The results showed that, when the two laser pulses are focused with d $<$ 2 mm separation distance, both the plasma sources were merged into a single colliding plasma source which lead to the increment in plasma and shock wave properties. For d $\geq$ 2 mm, we have observed the plasma jetlet formation in the source S1 due to the impedance mismatch between S1 and S2 plasma sources, along with a stagnation layer at the interaction zone.

The evolution dynamics of the laser induced blow off shock waves (LIBO SWs) in ambient air from metal films (Al, Cu, Ti) and polymer films (PVA, Au doped PVA) confined with glass (BK-7) substrate, revealed that the efficient blow off the shock waves can be achieved for optimal laser input energy by varying focusing conditions. This has resulted in the efficient coupling of the laser energy to the target material. In this study, we have shown that the efficient laser energy coupling to the target material can be achieved by precisely shifting the laser focal plane around the interface. This study also useful in understanding the effect of the relative impedance between target and confining metal layer on the blow

off shock wave properties. The results showed that the PVA and AuPVA polymers gave higher LIBO SWs than Al (20 μm), Cu (20 μm) foils by shifting the focal plane to F2 (2 mm) focusing condition with an optimal 50 mJ laser input energy. The study of the spatial confinement of the air plasma inside mm size tubes (with 4.7 to 13 mm tube diameters) revealed the inter-dependency and interaction of the plasma and shock waves, which highly depend on the input laser energy and tube aspect ratio (L/D). In spatial confinement of air plasma, the reflected radial/transverse shock waves compression increased the plasma properties such as plasma length, plasma life time, plasma number density and plasma temperature. The squeezing of the air plasma forced out the plasma mass density which increased the axial shock wave position i.e., its velocity. This study also helped us to understand the air plasma generated shock wave propagation inside mm sized tubes and the effect of spatial confinement on axial shock wave propagation.
Finally, this work also investigated the shock wave propagation inside transparent solid material, which will be helpful to understand the Laser Shock Peening (LSP) process. The dynamics of the temporal evolution of the laser induced/ablative shock waves inside a transparent dielectric material, BK-7 glass slab is used to understand the effects of both the axial confinement and spatial confinement on the shock wave propagating inside a transparent solid material. The axial confinement of shock waves is achieved using an overlay of 20 μm Al/Cu foils, while the dimensions of BK-7 glass have provided the spatial confinement to shock waves launched and propagated inside BK-7 glass slab. The results showed that, the shifting of the laser beam focal plane from F0 to F2 (6 mm) focusing condition enhanced (around 0.6 - 2.2 km/s) the shock wave velocities inside the BK-7 glass due to the 20 μm Al foil confinement of the BK-7 glass, but it has not affected for the 20 μm Cu foil confinement of the BK-7 glass. The energy dependence study on the shock wave propagation inside BK-7 glass revealed that, the enhancement of the shock wave inside BK-7 glass greatly depends on the relative acoustic impedance of the confining layer (20 μm Al and Cu thin foils) and BK-7 glass as well as on the laser energy density in the focal volume at the interface. Future roadmap for the development of nano-second laser based micro shock tubes with optimal input laser energies, better laser focusing conditions, selection of confining layer material and aspect ratio (L/D) of the tube based on the thesis is proposed.

Table of Contents

Page

Abstract **i**

List of Figures **vii**

List of Tables **xv**

1 Introduction **1**

1.1 Temporal evolution of the plasma in background gas 5

1.2 Temporal evolution of the shock waves 6

1.3 Motivation 7

1.4 Role of confinement on the laser induced plasma and shock waves 8

1.5 Organization of the Thesis 10

2 Experimental Details **23**

2.1 Introduction 23

2.2 Shadowgraphy Imaging 24

2.3 Details of the laser systems 24

2.3.1 SpitLight 1200 laser system 24

2.3.2 TITAN-5 laser system 24

2.3.3 Probe beam 28

2.3.4 Imaging diagnostics 29

2.4 Experimental configurations 31

2.4.1 Double pulse configuration 31

2.4.2 Single pulse configuration 32

2.5 Summary 35

3 Interaction of two counter propagating plasmas and shock waves in air **37**

3.1 Introduction . . . 38
3.2 Experimental Details . . . 42
3.3 Time integrated imaging of the two counter propagating plasma plumes collision . . . 44
3.4 Fast imaging of the collision of two counter propagating plasma plumes with different energy ratios . . . 44
3.5 Shadowgraphy imaging of the two counter propagating plasma plumes collision . . . 47
3.6 Collision dynamics of two counter propagating plasma sources with separation distance (d) < 2 mm . . . 49
3.7 Collision dynamics of two counter propagating plasma sources with equal energy ratio and d ≥ 2 mm . . . 52
3.7.1 Plasma Outer Region (POR)/ Contact Front (CF) Evolution . . . 54
3.7.2 Shock Front (SF) evolution . . . 57
3.8 Collision dynamics of two counter propagating plasma plumes with unequal energy ratio and d ≥ 2 mm . . . 59
3.8.1 POR/CF Evolution of two counter propagating plasma plumes with unequal energy ratio and d ≥ 2 mm collision . . . 61
3.8.2 Sources of energy ratio 1:1.7 . . . 61
3.8.3 Sources of energy ratio 1:3.7 . . . 64
3.8.4 Shock Front (SF) evolution of two counter propagating plasma sources with unequal energy collision and d ≥ 2 mm . . . 66
3.8.5 Sources of energy ratio 1:1.7 . . . 66
3.8.6 Sources of energy ratio 1:3.7 . . . 67
3.9 Plasma Jetlet Evolution in the two counter propagating plasma plumes of unequal energy collision . . . 69
3.10 Summary . . . 73

4 Dynamics of Laser induced Blow-off plasma and shock waves in air 79
4.1 Introduction . . . 79
4.2 Experimental Details . . . 84
4.3 Shadowgraphy imaging of the Laser Blow-off plasma from metal foils . . . 85
4.3.1 Effect of F0 focusing condition . . . 87
4.3.2 Effect of F2 focusing condition . . . 88
4.3.3 Effect of the input laser energy on blow off shock waves in F0 and F2 focusing conditions . . . 90
4.3.4 Morphology of the blow off region from the foils . . . 92
4.4 Shadowgraphy imaging of Laser Blow-off plasma from metal thin films . . . 93
4.5 Shadowgraphy imaging of laser Blow-off plasma from polymer films . . . 97

4.6 Conclusions . . . 101

5 Dynamics of spatially confined ns laser induced air plasma and shock waves 107

5.1 Introduction . . . 107
5.2 Spatial confinement of the laser induced plasma and shock waves . . . 108
5.2.1 Effect of spatial confinement of plasma . . . 109
5.3 Experimental Details . . . 110
5.4 Dynamics of spatially confined air plasma in rectangular geometry . . . 111
5.4.1 Visualization of Spatial confinement of air plasma inside rectangular hollow glass tube of L/D=1.5 . . . 112
5.4.2 Energy dependence on the spatial confinement of air plasma and shock waves inside rectangular cavity . . . 114
5.4.3 Energy dependence on the temporal evolution of plasma length . . 114
5.4.4 Energy dependence on the temporal evolution of axial shock waves 116
5.4.5 Energy dependence on the temporal evolution of radial shock waves 117
5.4.6 Energy dependence on the temporal evolution of secondary shock wave . . . 119
5.4.7 Self emission study of air plasma inside a rectangular glass cavity with L/D=1.5 . . . 121
5.4.8 Aspect ratio (L/D) dependence on the plasma and shock waves inside the rectangular glass cavity . . . 124
5.4.9 Aspect ratio (L/D) dependence on the temporal evolution of plasma length . . . 125
5.4.10 Aspect ratio (L/D) dependence on the temporal evolution of shock waves . . . 126
5.4.11 Summary of the spatially confined air plasma inside rectangular cavity 127
5.5 Dynamics of spatially confined air plasma inside cylindrical cavity . . . 127
5.5.1 Visualization of spatial confinement of air plasma inside cylindrical hollow copper tube . . . 128
5.5.2 Energy dependence on the temporal evolution of the shock waves from spatially confined air plasma inside a cylindrical copper tube with L/D=1.5 . . . 129
5.5.3 Aspect ratio (L/D) dependence on the temporal evolution of shock wave from spatially confined air plasma inside cylindrical copper tube 131
5.5.4 Role of the cavity/tube diameter in terms of aspect ratio (L/D) on air plasma confinement in cylindrical geometry . . . 131
5.5.5 Glass cylindrical tube . . . 132
5.5.6 Plastic (PVA) cylindrical tube . . . 133

5.5.7 Stainless steel (SS) cylindrical tube . . . 135
5.5.8 Summary of the spatially confined air plasma in cylindrical geometry 137
5.6 Conclusions . . . 137

6 Dynamics of laser ablative shock waves inside transparent dielectric media 143
6.1 Introduction . . . 144
6.2 Experimental Details . . . 145
6.3 Shadowgraphy imaging of Laser induced breakdown of BK-7 glass: initial study . . . 147
6.4 Effect of the laser focusing conditions on direct and confined ablation of the BK-7 glass . . . 150
6.4.1 Direct ablation of the BK-7 glass . . . 151
6.4.2 Confined ablation of the BK-7 glass . . . 152
6.4.3 Effect of Acoustic impedance of materials . . . 156
6.5 Conclusions . . . 159

7 Conclusions 165
7.1 Summary and Conclusions . . . 165
7.2 Future Work . . . 172

List of Publications 175

List of Figures

1.1 Schematic of nano second laser ablation of solid material (Ref.[2]) 2
1.2 Snapshot of the different confinement geometries used in the thesis study. . 10

2.1 Internal layout of the TITAN-5 high power Nd:YAG laser system. 25
2.2 Q-switching principle of TITAN-5 laser cavity. 26
2.3 Internal synchronization timing diagram of TITAN-5 laser cavity. 26
2.4 Characterization of TITAN-5 laser beam (a) beam diameter (b) laser beam snapshot using Vision software (c-d) spatial and temporal distribution of laser pulse of 2 J laser output energy. 27
2.5 Laser energy variation w.r.t. HWP angle representing malus law; ■ represents p-polarised light and ▲ represents s-polarised light. 28
2.6 He-Ne probe beam imaged using (a) CCD camera (b,c) ICCD camera along with graph sheet 29
2.7 Experimental schematic used for the interaction of two counter propagating laser induced plasma and shock waves in air (double pulse configuration). . 32
2.8 Experimental schematic used for single laser pulse ablation configuration in Chapters 4, 5 and 6. 33

3.1 Time integrated CCD images of two counter-propagating colliding plumes with varying separation distance 'd' and for energy ratio (a) S1:S2=1:1 (b) S1:S2=1:1.7 (c) S1:S2=1:3.7 43
3.2 Temporal evolution of 2D emissions from (a) a single source at 25 mJ compared to two counter-propagating laser induced plasma sources of separation distance (d=4 mm) with different energy ratios (b) S1:S2=1:1 (c) S1:S2=1:1.7 (d) S1:S2=1:3.7 respectively. 45
3.3 Temporal evolution of single plasma source with varying energy (a) 25 mJ (b) 41 mJ (c) 92 mJ 47

3.4 Shadowgrams of the temporal evolution of the (a) single plasma S1 evolution; colliding plasma sources of (b) equal and (c-d) unequal energy ratios with d= 1 mm 49
3.5 The temporal evolution of the POR of the two counter-propagating colliding plumes with varying separation distance 'd' compared to the individual plasma sources (S1/S2) (a-d) S1:S2=1:1 (e-f) S1:S2 = 1:1.7 (g-h) S1:S2 = 1:3.7 50
3.6 Temporal evolution of interaction of two counter propagating colliding plasma sources of equal input energy (a) for d= 2 mm, (b) for d=4 mm and (c) for d=6 mm at t=2, 6, 10, 20, 30 μs 53
3.7 Temporal evolution of the interaction dynamics of shock waves and the plasma in the counter-propagating configuration with sources of equal input energy (a-h) for d=2 mm (closely separated sources) (i-p) for d=6 mm (far separated sources) 54
3.8 Time evolution of Contact Fronts (PORs) of S1 and S2 of colliding plasmas (a-d) S1= 25 mJ and (e-h) S2=25 mJ (energy ratio 1:1) with d = 2, 4, 6 mm compared with respective single source along ±Z, ±Y directions (circled portion shows the discontinuity in S1 as well as in S2 caused by interaction of two equal energy sources). 55
3.9 Time evolution of Shock Fronts (SFs) of colliding plasma sources (a-d) S1= 25 mJ and (e-h) S2=25 mJ (energy ratio 1:1) with d= 2, 4, 6 mm compared with respective single source along ±Z, ±Y directions 58
3.10 Shadowgrams of the temporal evolution of the interaction of the two counter propagating plasma sources of unequal input energy ratio (a-c) S1:S2=1:1.7 (d-f) S1:S2=1:3.7 for d= 2, 4, 6 mm at t=2, 6, 10, 20, 30 μs 59
3.11 Temporal evolution of the interaction dynamics of plasma and shock waves in the counter-propagating configuration with sources of unequal input energy ratio S1:S2=1:1.7 (a-h) for d=2 mm (closely separated sources) (i-p) for d=6 mm (far separated sources) 61
3.12 Time evolution of Contact Fronts (PORs) of S1 and S2 colliding plasmas (a-d) S1= 25 mJ and (e-h) S2=41 mJ (energy ratio 1:1.7) with d= 2, 4, 6 mm compared with respective single source along ±Z, ± Y directions (circled portion shows discontinuity in S1 caused by interaction of two unequal energy sources) 62
3.13 Time evolution of Contact Fronts (PORs) of S1 and S2 of colliding plasma (a-d) S1= 25 mJ and (e-h) S2=92 mJ (energy ratio 1:3.7) with d= 2, 4, 6 mm compared with respective single source along ±Z, ±Y directions. Circled portion shows discontinuity in S1 caused by interaction of two unequal energy sources 65

3.14 Time evolution of Shock Fronts (SFs) of colliding plasmas (a-d) S1= 25 mJ and (e-h) S2=42 mJ for energy ratio 1:1.7 with d= 2, 4, 6 mm compared with respective single source along ±Z, ±Y directions 67
3.15 Time evolution of Shock Fronts (SFs) of colliding plasmas (a-d) S1= 25 mJ and (e-h) S2=92 mJ for energy ratio 1:3.7 with d= 2, 4, 6 mm compared with respective single source along ±Z, ±Y directions 68
3.16 Temporal evolution of Contact front radius of S1 alone and the S1 of colliding plasma in the presence of shock front of S2 in the colliding plasma configuration and S2 alone for the input laser energies of S1 = 25 mJ and (a-c) S2= 41 mJ (1:1.7) (d-f) S2= 92 mJ (1:3.7) with d= 2, 4, 6 mm respectively 70
3.17 Temporal evolution of plasma jetlet diameter from POR of S1= 25 mJ due to (a) S2= 41 mJ (1:1.7) (b) S2= 92 mJ (1:3.7) at separation distance d= 2, 4, 6 mm 71

4.1 Schematic diagram for (a) laser ablated plasma (LAP) process (b) direct LIBO process and (c) confined LIBO process 81
4.2 Schematic of laser blow-off from thin foil confined with glass substrate for focusing conditions at (a) exactly on the glass-foil interface (F0) and (b) 1 and 2 mm deep (F1 and F2) from the glass-foil interface. 85
4.3 Shadowgrams of the laser induced blow-off plasma from the rear side of (a) ≈ 10-11 μm Al foil (b) 20 μm Al foil targets at 500 mJ laser energy for F0 focusing condition. 86
4.4 Shadowgrams of the laser induced blow-off plasma from the rear side of 20 μm (a-b) Al and (c-d) Cu foil targets at 25 mJ laser energy for F0 and F2 focusing conditions 87
4.5 Temporal evolution of laser blow-off shock wave from rear side of 20 μm Al and Cu foils (a) in F0 (b) in F2 focusing conditions at 25 mJ laser energy. 88
4.6 Temporal evolution of laser blow-off shock waves from rear side of 20 μm (a) Al and (b) Cu foils in F0 and F2 focusing conditions at 25 mJ laser energy. 89
4.7 Shadowgrams of laser blow-off plasma and shock waves from rear side of (a,c) Al and (b,d) Cu foils for F2 focusing condition at 50 mJ and 200 mJ respectively 90
4.8 Temporal evolution of the laser blow-off shock waves from 20 μm (a) Al and (b) Cu thin foils in F0 and F2 focusing conditions at 25, 50 and 200 mJ energies respectively. 91
4.9 Variation of average blow off diameter of 20 μm Al and Cu foils for different energies at F0 and F2 focusing conditions 92

4.10 Shadowgrams of the laser blow-off plasma and shock waves from rear side of 1.1μm Cu thin film in F0, F1 and F2 focusing condition at 25 mJ laser energy. . . . 94
4.11 Temporal evolution of the laser blow-off shock waves from 1.1μm Cu thin film (a) in F0, F1 and F2 focusing condition at 25 mJ and 50 mJ laser energy (b) compared to the 20 μm Cu foil blow off shock velocity at 25 mJ. 95
4.12 Shadowgrams of the laser blow-off plasma and shock waves from rear side of 200 nm thin film in F0, F1 and F2 focusing condition at 25 mJ laser energy. . . . 95
4.13 Temporal evolution of the laser blow-off shock waves from 200 nm Ti film (a) compared to 1.1 μ Cu film at 25 mJ energy (b) at 50 mJ in F0, F1 and F2 focusing conditions. . . . 96
4.14 (a) FESEM image of the electro spun PVA nano fibres (b) thickness of the PVA nano fibre film measured using profilometer; the image (a) is used with permission [55] . . . 98
4.15 (a) UV-Visible absorption spectra of gold (Au) nano particles (b) TEM image of the colloidal gold (Au) nano particles (c) FESEM image of the Au nano particle doped PVA nano fibres (d) thickness of the Au doped PVA nano fibre film; the images (a-c) are used with permission [55, 56] . . . 99
4.16 Shadowgrams of the temporal evolution of the laser blow-off shock wave from (a,c) 60 μm PVA and (b,d) 35 μm AuPVA films at 25 mJ and 50 mJ laser energy in F2 focusing condition . . . 99
4.17 Temporal evolution of the laser blow-off shock wave velocities from 20 μ Al, Cu foils, 60 μm PVA and 35 μm AuPVA polymer films at (a-b) 25 mJ and (c-d) 50 mJ laser energy in F0 and F2 focusing conditions respectively. 100

5.1 (a) rectangular and (b) cylindrical geometry hollow tubes used for spatial confinement of air plasma . . . 111
5.2 Shadowgrams of temporal evolution of air plasma and shock waves in spatial confinement inside a rectangular glass cavity with L/D=1.5 with different laser input energies (a) 50 mJ (b) 200 mJ (c) 400 mJ . . . 113
5.3 Energy dependence on temporal evolution of plasma contact front position along $\pm$Z in spatial confinement of air plasma inside a rectangular hollow glass tube of L/D=1.5 . . . 114
5.4 Energy dependence on the temporal evolution of shock waves along $\pm$Z (axial) direction in spatial confinement of air plasma inside a rectangular hollow glass tube with L/D=1.5 . . . 116
5.5 Formation of the shock and mass density vortices along cavity edges in spatial confinement of air plasma inside a rectangular cavity with L/D=1.5 117

5.6 Temporal evolution of (a) shadowgrams of plasma and shock waves (b) transverse shock waves along +Y direction; the plasma self emission images of (c) spatial confinement of air plasma of 200 mJ energy inside a rectangular hollow glass tube with L/D=1.5 (d) freely expanding air plasma with 92 mJ energy; the -ve sign along Y axis (shock front position) is used represent the reflected transverse shock wave propagation from one end of the tube to other end through plasma centre 118
5.7 Energy dependence on temporal evolution of secondary shock wave along ±Z direction in spatial confinement of air plasma inside a rectangular glass cavity with L/D=1.5 120
5.8 Temporal evolution of self emission study from spatial confinement of air plasma created with 200 mJ input laser energy inside a rectangular glass cavity with L/D=1.5 122
5.9 Contour plots of Line profile of (a) air plasma of 200 mJ energy along ± Z direction in spatial confinement inside a rectangular glass cavity with L/D=1.5; free expansion of air plasma at 92 mJ energy (b) along ± Z direction (c) along ± Y direction. 123
5.10 Shadowgrams of temporal evolution of 50 mJ air plasma and shock waves in spatial confinement inside a rectangular glass cavity with different L/D ratios 124
5.11 Aspect ratio (L/D) dependence on temporal evolution of plasma length along ±Z in spatial confinement of air plasma inside a rectangular glass cavity 125
5.12 Aspect ratio (L/D) dependence on temporal evolution of the shock waves along ±Z in spatially confined air plasma inside a rectangular glass cavity . 126
5.13 Shadowgrams of the temporal evolution of 200 mJ air plasma and shock waves inside a cylindrical hollow copper tube with different L/D ratios . . 128
5.14 Energy dependence on the temporal evolution of axial shock waves along ± Z direction in spatially confined air plasma inside a cylindrical copper tube with L/D=1.5 130
5.15 Aspect ratio(L/D) dependence on the temporal evolution of axial shock waves along ± Z direction in spatially confined air plasma inside a cylindrical copper tube 131
5.16 Shadowgrams of the temporal evolution of spatially confined air plasma inside a cylindrical glass tube 132
5.17 Temporal evolution of the shock waves along ±Z direction exited from the spatial confinement of air plasma inside a cylindrical glass tube 133
5.18 Shadowgrams of the temporal evolution of spatially confined air plasma and shock waves along ±Z direction inside a cylindrical plastic tube 134

5.19 Temporal evolution of the shock waves along ± Z direction exited from the spatial confinement of air plasma inside a cylindrical plastic tube 134
5.20 Shadowgrams of the temporal evolution of spatially confined air plasma inside a cylindrical SS tube 135
5.21 Temporal evolution of the shock waves along ± Z direction exited from the spatial confinement of air plasma inside a cylindrical SS tube 136

6.1 Schematic of laser induced breakdown of BK-7 glass in (a-b) direct ablation mode and (c-d) Confined (Al/Cu + BK-7) ablation mode for different focusing conditions 146
6.2 The focal spot diameter at the target surface measured using burn patterns (a) at F0 focusing condition (b) at F2 focusing condition 147
6.3 Shadowgrams of laser induced breakdown of BK-7 glass in direct ablation mode at (a-c) 2 J (d) 0.5 J laser input energies 148
6.4 Energy dependence on (a) temporal evolution of shock waves propagation (b) optical breakdown length and width inside BK-7 glass 150
6.5 Shadowgrams of the laser ablative shock waves in ambient air as well as inside BK-7 glass from direct ablation of BK-7 glass at 0.5 J in (a) F0 (b) F2 focusing geometries 151
6.6 Temporal evolution of laser induced shock waves inside BK-7 glass from direct ablation of BK-7 glass at 0.5 -2 J laser energy for F0 and F2 focusing geometries 152
6.7 Shadowgrams of the laser induced shock waves from (a-b) Al confined to BK-7 glass (Al+BK-7) (c-d) Cu confined to BK-7 glass (Cu+BK-7) at 0.5 J laser energy for F0 and F2 focusing conditions 153
6.8 Energy dependence on the temporal evolution of transmitted shock waves inside BK-7 glass due to the ablation of BK-7 glass (direct ablation) and Al, Cu thin foils confined to BK-7 glass (confined ablation) in F0 focusing condition 154
6.9 Energy dependence on the temporal evolution of the transmitted shock waves inside BK-7 glass from the ablation of BK-7 glass (direct ablation) and the Al, Cu thin foils confined to BK-7 glass (confined ablation) in F2 focusing condition 156
6.10 Energy dependent temporal evolution of laser induced shock waves inside BK-7 glass from the confined ablation of the 20 μm Al and Cu thin foils confined to the BK-7 glass at F0 and F2 focusing conditions 157
6.11 Energy dependent temporal evolution of laser induced shock waves inside BK-7 glass from the confined ablation of the 20 μm Al and Cu thin foils confined to the BK-7 glass at F0 and F2 focusing conditions 159

7.1 Flow chart of the different confinement geometries used in the thesis study 166
7.2 Schematic used for the confined laser ablative shock waves inside the BK-7 glass. 172
7.3 (a) Schematic used for the LIBO SWs propagation inside the mm sized tubes (b) experimental visualization of ns laser shock tube using rectangular tube geometry 173

List of Tables

2.1 Specifications of Nd:YAG laser systems used in the study 25
2.2 Technical specifications of diagnostic tools used in the study 30
2.3 Specifications of different lasers used in the study 34
2.4 Technical details of diagnostic tools used in the study 34

3.1 Experimental and Numerical work on laser produced colliding plasma plumes 40
3.2 Plasma dimensions of S1 and S2 for different input energy ratios from 2D emission images captured using ICCD at a delay 1 μs. 46
3.3 Maximum increment of plasma and shock wave properties in counter propagating colliding plumes along laser axis (the corresponding time scales are given in bracket) 51
3.4 Plasma Jetlet evolution for different input energy ratios 72

4.1 Effect of F0 and F2 focusing condition on the blow-off shock velocities from Al and Cu thin foils at 1.45 μs delay time with varying energy 91
4.2 The LIBO shock wave velocity of Ti (200 nm) and Cu (1.1 μm) thin films were compared to the Al, Cu foils (20 μm) at 1.05 μs 97
4.3 Effect of focusing conditions on LIBO shock wave velocity from 60 μm PVA and 35 μm AuPVA films compared to the 20 μm Al and Cu foils at 1.05 μs. 101

5.1 Dimensions of the hollow tubes used for spatial confinement of air plasma in rectangular geometry 112
5.2 Exit time scales of shock waves along $\pm$Z direction w.r.to the variation of input laser energy in spatial confinement of air plasma inside a rectangular cavity with L/D=1.5 117
5.3 Reflection time scales of transverse shock wave along $\pm$Y direction w.r.to the variation of input laser energy and aspect ratio (L/D) in spatial confinement of air plasma inside a rectangular glass cavity 119

5.4 Exit time scales of shock waves along ±Z direction w.r.to the variation of input laser energy and aspect ratio (L/D)in spatial confinement of air plasma inside a rectangular glass cavity 126
5.5 Dimensions of the different cylindrical hollow tubes used in spatial confinement of air plasma in cylindrical geometry 128
5.6 Exit time scales of the axial shock waves along ±Z direction w.r.t. the variation of input laser energy and aspect ratio (L/D) in spatially confined air plasma inside a cylindrical copper tube 130
5.7 Dimensions of the different cylindrical tubes used to study the effect of tube diameter on the spatially confined air plasma in cylindrical geometry 132

6.1 Averaged Dimensions of the permanent damage tracks inside the BK-7 glass with varying laser input energy 149
6.2 Mechanical properties of Al, Cu and BK-7 glass 154
6.3 The velocity of shock waves inside the BK-7 glass in direct and confined ablation geometry at 1.4 μs 155

Chapter 1

Introduction

When a target material is irradiated by a ns laser pulse with an intensity greater than the break down threshold ($\sim$ GW/cm^2 for many metals), the laser radiation is absorbed by the material results in heating, melting and vaporization, thus creating the material plasma. This process occurs at very fast rate than the adiabatic expansion of the ablated material due to laser pulse (ns) interaction. The properties of the plasma generated depends on (a) laser parameters such as wavelength, polarization, pulse width, pulse duration, pulse shape, focusing spot size & shape and intensity etc. (b) target material properties such as composition, density, geometry, atomic weight, surface reflectivity, conductivity, elasticity and compressibility etc. (c) an efficient coupling of laser energy to the target material and (d) influence of the external environment [1, 2, 3, 4, 5, 6, 7, 8, 9, 10, 11, 12, 13]. The plasma formation due to the laser ablation of the target material can be divided into three stages [13, 14]:

- **Laser-matter interaction:** when leading edge of laser pulse incident on target material, a fraction of laser pulse is reflected from the material surface (following Fresnel laws) and remaining fraction of pulse penetrates the surface within the skin depth. The absorbed pulse energy is converted into material internal energy (inside material) and hot vapour cloud (consisting of ions, electrons and neutrals of the composition) of material is formed (outside material). The internal energy of the material partially converts into the kinetic energy of the ablated material particles. The distance over which a laser pulse penetrates into the target material is known as skin depth (δ) of the material and it it expressed as [10, 14, 15]:

$$\delta = \left(\frac{2}{\omega\mu\sigma}\right)^{\frac{1}{2}} \tag{1.1}$$

  where ω is the angular frequency of laser, μ is the magnetic permeability of free-

space and σ is the conductivity of the material. For a nano second laser of 1064 nm wavelength, the skin depth is about $\sim$ 10 nm in the case of Al target. Within the skin depth, laser radiation is absorbed by free electrons of material through different processes like: photo-absorption, single photon photo-ionization and multi-photon ionization. The energy absorbed by the free electrons transfer their energy into the bulk material through heat transfer mechanism that depends on the heat penetration depth (L_{th}) is given by [10, 14, 15]:

$$L_{th} \approx (2D\tau_L)^{\frac{1}{2}} \tag{1.2}$$

Where D is the heat diffusion coefficient; $D = \frac{\kappa}{\rho C}$, κ is the thermal conductivity, ρ is the mass density, C is the specific heat capacity and τ_L is the laser pulse duration. For nanosecond (ns) laser pulse the heat penetration depth is $\sim$ 1 μm which is much greater than the skin depth (δ). Hence, for short (ns) laser pulse the incident pulse energy is thermally transferred from the surface of the material at skin depth into the bulk material. As a result, the material phase changes from initial solid state to liquid and vapour states. Due to this heat conduction, the thermal stress is induced into the bulk material leading to micro cracks and heat-affected zone (HAZ) (as shown in Figure 1.1) [2]. In case of ultra short (pico second (ps) and femto second (fs)) laser pulses, the material undergoes solid phase to vapour state directly due the high intensity and heat penetration depth is almost equal to the skin depth of the material. Hence, the thermal conduction into the material is almost zero or negligible for ultra short laser pulses (ps, fs) [2].

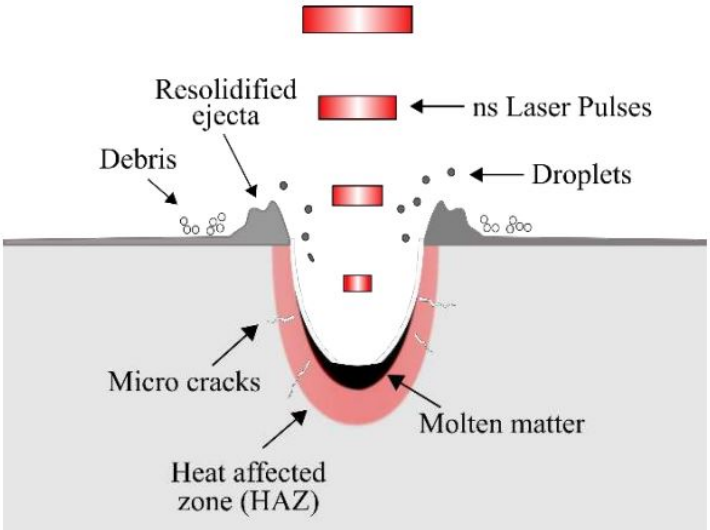

Figure. 1.1 Schematic of nano second laser ablation of solid material (Ref.[2])

In short pulse laser ablation, the material removal rate exceeds one-tenth of a single layer per pulse (typically) which alters the surface composition at the surface. If

material particles (in the form of ions, electrons and neutrals) are ejected from the surface but there is no detectable change in the surface composition, it is known as laser-induced desorption. During short pulse ablation, in the process of phase change of solid material, vaporization stage requires much more energy than the melting stage. The evaporation of the material occurs when the energy stored in the bulk material (up to L_{th}) per unit volume exceeds the latent heat of evaporation per unit volume. The ablation depth ($D_{ablation}$), of the evaporated material approximately calculated using [14, 15]

$$D_{ablation} \approx \frac{A_s(F_L - F_{th})}{\rho L_v} \tag{1.3}$$

Where A_s is the surface absorption coefficient of material, F_L is the laser fluence, F_{th} is the break-down threshold fluence of material and L_v is the latent heat of the material. The threshold fluence required to ablate the material to a depth L_{th} (heat penetration depth) is given by [15]:

$$F_{th} \approx \frac{\rho C \Delta T_m L_{th}}{A_s} \tag{1.4}$$

where ΔT_m is the difference between melting temperature and initial temperature of the material. The threshold fluence mainly depends on the square root of the laser pulse width ($F_{th} \propto {\tau_L}^{1/2}$) which in turns can be converted to breakdown intensity I_{th} (W/cm^2) of the material. The typical breakdown threshold intensity values for most of solids is in the range of $10^8 - 10^{10} W/cm^2$ which is less than the ambient air breakdown threshold range $10^{10} - 10^{11} W/cm^2$ [10]. For pure aluminium target, the breakdown threshold is $\sim 1.75 \times 10^8 W/cm^2$ [14, 16].

- **Laser-plasma interaction:** After the formation of the plasma on the target surface due to the leading edge, the remaining part of the laser pulse will interact with the plasma leading to more absorption of energy and further excitations of the atoms and ions occurs. At the same time, rapid expansion of the plasma also takes place. In laser-plasma interactions, the main absorption processes are: photo-ionization and inverse Bremsstrahlung.
  In photo-ionization (PI), the absorbed photons will excite and liberate a bound electron within an atom and has an absorption coefficient α_{PI} given by [13, 14, 15]:

$$\alpha_{PI}(cm^{-1}) = \sigma_{PI} n_N \approx \sum_N 2.9 \times 10^{-17} \frac{(\varepsilon_N)^{\frac{5}{2}}}{(h\nu)^3} n_N \tag{1.5}$$

where σ_{PI} is photo-ionization cross section (in the order of $\approx 10^{-17}$ cm^2), $h\nu$ is the photon energy (eV), ε_N is the ionization energy (in eV) and n_N number density (cm^{-3}) of excited species in state N and the summation is over all bound states N that satisfies the condition $h\nu > \varepsilon_N$. In inverse Bremsstrahlung (IB), the

absorption of incident photons takes place by free electrons in the vicinity of an ion. As photo-ionization increases the electron density inside plasma; the free electrons are further excited by the inverse Bremsstrahlung absorption process. The inverse Bremsstrahlung (IB) absorption coefficient (α_{IB}) is given by [14, 15]:

$$\alpha_{IB} = \sigma_{IB} n_e = \frac{4}{3}\left(\frac{2\pi}{3k_B T_e}\right)^{1/2} \frac{Z^2 e^6}{hcm_e^{3/2}\nu^3} n_i n_e g_{ff}\left(1 - exp\left(-\frac{c\nu}{k_B T_e}\right)\right) \tag{1.6}$$

Where σ_{IB} is the inverse Bremsstrahlung cross section, n_i and n_e are the ion and electron densities (cm^{-3}), e and m_e are electron charge and mass respectively, Z is the ion charge, k_B is the Boltzmann's constant, and T_e is the electron kinetic temperature (K). g_{ff} is known as the Gaunt factor for exact theory of the absorption coefficient, and is usually assumed to be 1 by Kramer's rule [14, 15]. The energy absorbed by the free electrons due to the inverse bremsstrahlung, further excite the plasma species through collisional process such as electron impact ionization which leads to the critical plasma density (n_c). The critical plasma density is given by:

$$n_c(cm^{-3}) = \frac{\varepsilon_0 m_e \omega^2}{e^2} \approx \frac{10^{21}}{\lambda^2} \tag{1.7}$$

If the plasma density reaches the critical density, the incident radiation will be reflected from the critical density layer as the plasma becomes opaque to the laser light. During this time, the plasma expands into ambient medium thus lowering the electron number density of the plasma. Once the plasma density becomes lower than the critical density, the laser pulse penetrates again through the plasma leading to the absorption of incident laser energy and the plasma density increases further. This process of laser absorption and plasma plume expansion occurs during the pulse duration. The plasma expansion is isothermal in nature during the laser pulse, because the volume of the plasma increases during expansion at constant temperature (the expansion time $\gg$ heating time).

- **Plasma expansion:** During the phase of continuous ablation and heating (laser-plasma interaction), a high thermal pressure builds within the plasma plume volume. Due to the high thermal pressure and temperature, the plasma plume will begin to expand rapidly into the surrounding medium. The surrounding medium can either be vacuum or any background gas medium (such as air, N_2 and Ar gas) with different ambient pressures. The plasma expansion is different in various surrounding media [13, 14, 15, 16, 17, 18].

  Vacuum: In vacuum, while expansion of the plasma, it losses energy via electro magnetic (EM) emissions (such as visible emissions as in LIBS) and Radio Frequency (RF) emissions. During the plasma expansion, the thermal energy of the plasma is converted into the kinetic energy of the plasma species (electrons, ions and neutrals). The plasma expansion in vacuum can be explained by adiabatic

expansion model [13]. This model treats plasma plume as an ideal gas with high pressure and temperature which expands rapidly into vacuum. This model depends on the masses of the plasma species, so the electrons (as $m_e \ll m_i$ or m_n) expansion rate is higher than the ions, hence the electrons move towards the outer regions of the plasma leading to charge separation [17] thus creating ambipolar field. The initial plasma dimension is more at the surface of material (depends on spot size i.e., in few 100 μm) and small along parallel to the surface (due to isothermal expansion i.e., in few μm). So, the plasma expansion is more towards normal to the material surface leading to an anisotropic expansion of the plasma. Thus the plasma shape will be elongated along the normal direction of the target material during the laser pulse. After termination of the pulse, the plasma expansion is adiabatic and the EM radiation becomes the dominant mechanism of energy loss.

Air or various background gas mediums: The plasma expansion into a background gas has three stages [18]: (i) formation of shock front and its propagating into the gas medium as well as into the material, (ii) spatial confinement of the plasma due to the interaction of plasma and background gas, and (iii) an increase in the plasma emissions due to enhanced collisions between the plasma expansion front and background gas along with the inter plasma collisions. During the cyclic process of continuous ablation and heating, the high thermal pressures build inside the plasma which is suddenly released into the background gas leading to the generation of hemi-spherical shock wave front or blast wave [2] in the background gas as well as into the target material (due to momentum conservation). The strength of the shock wave depends on different variables of laser matter interaction and surrounding gas medium.

1.1 Temporal evolution of the plasma in background gas

At early stages, the laser produced plasma is smaller in size than the distance upto which plasma plume is observed. In vacuum, the plasma expands freely as an adiabatic expansion. But when the plasma expands into the background gas, the plasma contact front velocity is decelerated and density of the plasma is increased due to the pressure exerted by surrounding gaseous medium, which acts as a confinement. The deceleration and eventual stopping of plasma expansion, due to the plasma front collision with background gas can be explained by shock wave or point strong explosion model at initial time scales ($<$ 500 ns) at short distances and Drag model at later time scales (>500 ns) at longer distances. The drag model states that [18]:

$$R = R_0 \left(1 - exp(-\beta t)\right) \tag{1.8}$$

Where R_0, is the plasma plume stopping distance, and β is the slowing coefficient such that $R_0\beta = V_0$, where V_0 is initial velocity of the plasma plume. During the plasma expansion into the background gas medium, the enhancement in emissions from the different atomic species due to the plasma collision with the ambient gas molecules increases the electron density via ionization [18].

1.2 Temporal evolution of the shock waves

The rapid expansion of plasma plume into the background gas leads to the generation of shock wave, which is a discontinuity between the plasma plume and background gas. As the shock wave expands into the background medium, the temperature behind the shock wave front decreases rapidly, and reaches to a lower values (<10,000 K). The detachment of shock wave from the plasma plume occurs around 0.5 μs. Before this time, the plasma plume contact front (CF) and shock wave front (SF) has equal expansion velocity. The temporal evolution of laser induced shock waves and its geometry mostly depends on laser energy; temperature, pressure and shape of the plasma. If the laser energy focused into a small area or spot size the plasma is in spherical shape, the shock waves will be spherical (in air medium) or hemi-spherical (in solid medium) [19]. If the plasma is elongated (i.e., in liquid medium), the shock waves are in cylindrical shape [19]. According to Sedov-Taylor theory, the temporal evolution of shock wave in ambient air is expressed as [1, 20, 21, 22, 23, 24]:

$$R_{SW} = \Phi_0 \left(\frac{E_s t^2}{\rho_0}\right)^{\frac{1}{n+2}} \tag{1.9}$$

where E_s is the energy associated with shock wave, t is the time elapsed since the plasma generation to generate the shock wave, ρ_0 is the density of the ambient medium (for air ρ_0=1.184 Kg/m^3), 'n' corresponds to dimensionality of the shock wave nature: if n=1 $\rightarrow$ planar, n=2 $\rightarrow$ cylindrical and n=3 $\rightarrow$ spherical and Φ_0 is a constant dependent upon the specific heat ratio, γ of the ambient medium (γ=1.4 for air). The shock wave velocity and pressures in ambient air is expressed as [1, 22, 23, 24]:

$$V_{SW} = \frac{2}{5}\Phi_0^{5/2}\left(\frac{E_s}{\rho_0}\right)^{\frac{1}{2}} R_{SW}^{-3/2} \tag{1.10}$$

$$P_{SW} = \frac{2}{\gamma+1}\rho_0 V_{SW}^2 \tag{1.11}$$

The shock wave pressures inside the any material is derived from the conservation equations of mass, momentum and energy across the discontinuity which have led to the well-known "Rankine-Hugoniot jump (R-H) equations" [1, 20, 21, 22, 23, 24]. They are

$$\rho_0 U_s = \rho_1 (U_s - U_p) \tag{1.12}$$

$$P_1 - P_0 = \rho_0 U_s U_p \tag{1.13}$$

$$E_1 - E_0 = \frac{1}{2}(P_1 + P_0)(V_0 - V_1) \tag{1.14}$$

The simplified Hugoniot relations for shock velocity and pressures are :

$$U_s = C_0 + sU_p \tag{1.15}$$

$$P_0 = \rho_0 U_s U_p \tag{1.16}$$

Where C_0 is the bulk sound speed of the material and s is dimensionless quantity which depends on the material and U_s, U_p are shock and particle velocities respectively. Shock waves generated from laser induced optical breakdown of materials have found many applications like laser spark ignition for fuel-air mixtures, internal combustion engines, pulse detonations engines [25], laser shock peening [26], surface cleaning [27], laser propulsion [28], biological applications like shock wave lithotripsy [29], orthopedics [30] etc and to mimic micro-explosions in atmosphere [31, 32, 33].

1.3 Motivation

Over the decades, the study of the dynamic states of matter under extreme conditions has gained great interest. Conventional methods like detonations, pinch plasmas, diamond anvil cell and shock tubes were used to generate shock waves and its propagation through the materials [1, 34, 35]. A conventional shock tube is a long ($\sim$ few meters) tube of cylindrical or rectangular cross section ($\sim$ few centi-meters) with two regions separated by a thin diaphragm. The first region consists of a high pressure gas known as driver section and other region consists of a low pressure gas. When the diaphragm is suddenly burst open, the sudden expansion of gas into low pressure region creates a plane shock wave, which propagates through the tube and interacts with material under study. The main drawback of the conventional methods are: low pressure values ($<$ GPa), long time scales ($\sim$ ms) [34, 35, 36] and huge operational/maintenance costs. With the invention of lasers, the high shock pressures $>$ GPa at short times scales (fs to μs) can be achieved by focusing the single or multiple laser pulses over a small volume onto a target material, creates material plasma and then shock wave occurs and propagates into the material and surrounding medium simultaneously [2, 3, 4, 5, 33, 37]. This study finds applications in high energy density physics (HEDP) [6, 33, 35, 37], equation of state (EOS) of materials [38], inertial confinement fusion (ICF) [39] and astrophysics [40] etc. In recent years, with the availability of high power lasers, the ablation pressures $>$ TPa can be achieved at the material surface [4, 5, 6, 41]. For high intensity lasers (10^{16}-10^{19} W/cm^2), the light pressure (ponderomotive pressure) itself generate the shock waves in MPa-GPa range.
As the laser ablative shock waves behaves analogous to the mechanically generated shock waves (i.e., shock wave from a shock tube), the recent studies on laser induced shock waves propagating in small channels and in tubes with milli-meter to micro meter sized

diameter which acts as *miniaturized laser shock tubes* have attracted much interest among researchers [42, 43, 44]. But scaling down of the shock wave effects such as pressure, velocity attenuation during propagation, laminar and turbulence flow from macroscopic to mm or micro range requires a proper extensive study. Although several theoretical and very few experimental investigations are available in this field [42, 43, 44, 45, 46], there is a strong need for experimental visualization of the laser induced shock wave propagation inside mm or micro sized channels. The miniaturization of laser shock tube requires the generation of the laser induced metal plasma at the entrance of the mm or micro tube as driver, the high pressured metal plasma launches the shock wave into the mm or micro sized tube and propagates through it [47]. This work mostly deals with the shock wave propagation in confined geometry and depends greatly on laser properties and tube properties and the confinement geometry. So, motivated by the literature reports [42, 43, 44, 45, 46, 47], in this thesis work, we have visualized the temporal evolution of laser induced plasma and shock waves in different confining geometries and addressed few problems for better confinement to achieve more enhanced plasma and shock wave properties.

1.4 Role of confinement on the laser induced plasma and shock waves

Over the last two decades, a lot of researchers have investigated different methods to improve the enhancement of optical and mechanical emissions from laser induced plasma using confinement. The enhancement of optical emissions from plasma is desirable for higher sensitivity and efficient detection of the LIBS signal. The high accuracy and precision in LIBS signal compared to other conventional analytical techniques, makes LIBS technique highly desirable for application in many areas such as: identification of materials [48, 49, 50, 51, 52], biomedical identification [38, 51, 52, 53], environmental monitoring [48, 51, 52, 54], agriculture [55, 56], space exploration [57, 58], industrial analysis [59, 60] and many more. The enhancement of mechanical emissions i.e., shock waves from plasma find applications in laser shock peening [26, 61, 62], laser propulsion [58, 63], laser spark ignition of fuel-air mixtures, pulse detonation engines etc [25]. To enhance the optical and mechanical emission from plasma, different experimental methods such as dual-pulse excitation [48, 64, 65, 66, 67, 68, 69, 70], spatial confinement, magnetic confinement, spark discharge, adding of transparent overlays (tamping layer) or absorbing polymer as confining medium [26, 71, 72] or any combination of these confinement processes [19, 58, 59, 60, 61, 62, 63, 64, 65, 66, 67] have been used. Based on the experimental geometry used for plasma confinement, the confinement methods can be divided into two categories:

(a) Axial Confinement: If the confinement is applied along laser propagation axis, it is known as axial confinement. Double pulse configuration and adding a transparent

overlay to the substrate, comes into this category. These are commonly employed in LIBS and laser shock peening (LSP) applications. Double pulse configuration is most widely used and is an effective approach to improve or enhance the plasma emissions. In the double pulse configuration, two different lasers or two laser beams from a single laser is used for experiments. Though usage of two separate lasers provides more flexibility in configuration, such as different pulse widths and inter-pulse delay, it is very challenging to synchronize and align both the laser pulses. Hence, it is preferred to use single laser based double pulse configuration which offers great spatial and temporal synchronization with accurate inter-pulse delays. Based on the geometry of the double pulse configuration, it is further divided as: collinear, cross beam, counter-propagating and orthogonal geometries [48, 64, 65, 66, 67, 68, 69, 70]. Most of the research work on double pulse configuration has been done in vacuum for optical emission enhancement. The effect of mechanical emissions i.e., shock waves and acoustic waves in ambient air/background gas from a double pulse configuration is not understood fully. The Chapter 3 of the thesis provides a detailed understanding of effect of fluid confinement of the plasma, on the mechanical emissions in the counter-propagating geometry [65].
Another way of axial confinement is to add either a transparent overlay or a laser absorbing polymer/metal film to the target surface as a confining medium. The laser beam is focused at the interface of the confining medium and the target surface. During the plasma expansion, the confining medium confines the expansion of the plasma plume opposite to the laser propagation direction, resulting in the enhancement of the recoiling momentum along the laser direction and into the target. The confining media can be water, quartz, glass, perspex or silicone rubber. The choice of confining medium mainly depends on the substrate/target material, its density and the acoustic impedance of both the target and the confining material [26, 71, 72]. A detailed discussion on the role of acoustic impedance of target (Al, Cu foils) and the transparent confinement medium (BK-7 glass) is presented in Chapter 4 of the thesis. This Chapter 4 presents the spatio temporal evolution of the laser induced blow-off shock waves (LIBO SWs) from confined Al, Cu foils (glass confinement) expanding into ambient air. The effect of shifting of focal plane on LIBO SWs, which resulted in enhanced shock/flyer velocities is also discussed.

(b) Lateral/Radial Confinement: If the confinement is applied along the radial direction of the laser propagation, it is known as lateral/radial confinement. This is also known as spatial confinement of plasma. It is flexible and cost effective method to enhance the optical as well as mechanical emissions, where the plasma is confined to a small size by cavities of different geometries. In lateral confinement, the size/aspect ratio (length (L)/diameter (D)), shape, geometry and material of the cavity plays an important role in determining the enhancement of plasma properties. Although several authors have attributed the enhancement of plasma properties to the shock wave reflection and com-

pression of the plasma [48, 73, 74, 75, 76, 77, 78, 79, 80, 81, 82, 83], a clear visualization and understanding of the whole process is sparsely available. In Chapter 5 of the thesis, we have studied the spatial confinement of air plasma inside macro (mm size) hollow tubes to get an insight into how the reflected radial shock wave affects the plasma properties, such as plasma length, size, plasma number density, plasma temperature and the life time of the plasma. The effect of laser energy, cavity geometry, cavity aspect ratio (L/D) on spatial confinement of the air plasma as well as shock waves are presented in detail.
A combination of both the axial and radial confinement of shock waves is described in Chapter 6. A transparent dielectric material BK-7 glass is used as a target to study the effect of confinement inside the target material. The propagation of shock wave inside the BK-7 glass slab and the reflection of the shock wave due to the impedance mismatch at interfaces is presented.
The experimental work carried out on different confinement methods in this thesis is summarized in Figure 1.2.

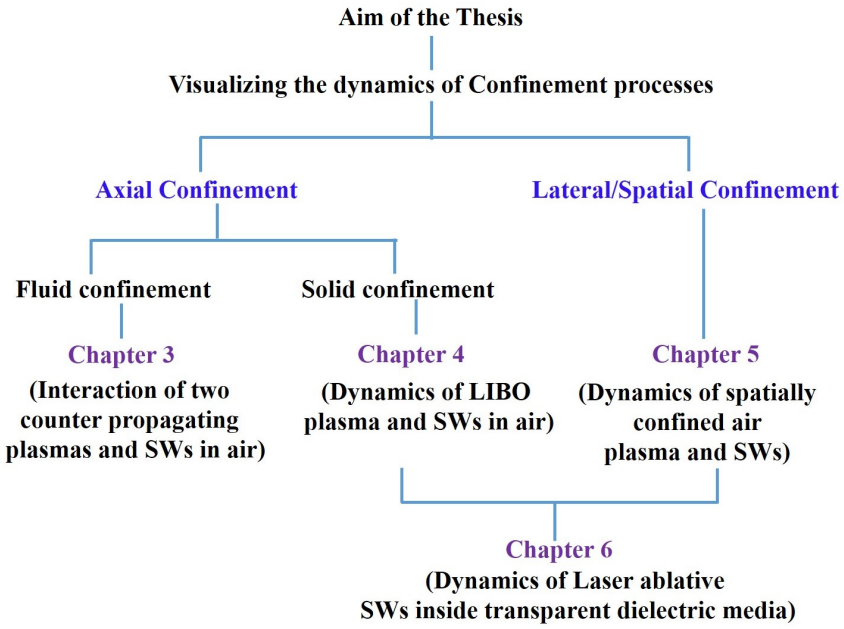

Figure. 1.2 Snapshot of the different confinement geometries used in the thesis study.

1.5 Organization of the Thesis

The thesis presents a clear visualization of different processes involved in the enhancement of nano-second laser induced plasma and the shock waves properties in confined geometry in ambient air as well as within the target material. The visualization is done by using high resolution photography and shadowgraphy [22, 65, 84]. The thesis work is organized into seven chapters which includes introduction, experimental details, four chapters with experimental results and a conclusion chapter. The brief description of the each chapters is given below.

Chapter 1

This chapter gives the general introduction of laser ablation process and evolution of the plasma in different background conditions with relevant applications. This is followed by the characterization of temporal evolution of the shock waves from conservation laws to obtain/calculate the shock wave properties (such as velocity, pressure and density), brief discussion of the plasma confinement methods, with relevant applications. Finally, the organization of the various thesis chapters with brief description is presented.

Chapter 2

This chapter describes the laser systems, diagnostic instruments (ICCD, CCD cameras), Imaging methods such as shadowgraphy [84], experimental schematics used for the different confinement methods and the details of the target materials used in the thesis. We have used the second harmonic of an Nd:YAG laser for laser induced breakdown of air/target material. The spatio-temporal evolution of the plasma and shock waves (in the form of shadowgrams) were captured using a fast (ns) gating ICCD camera. The plasma emissions were captured using a CCD and/or an ICCD camera.

Chapter 3

In this chapter, the interaction of two counter propagating laser induced plasmas and the shock waves in air is presented. This chapter gives an insight into the axial confinement of the plasma source with another expanding plasma as a confinement medium. Although a lot of work has been published on colliding plasma plumes in vacuum, studies of colliding plasma plumes in ambient atmosphere are sparse [85, 86]. Hence, we have studied the interaction of two counter propagating Nd:YAG (7 ns, 532 nm) laser produced colliding plasma plumes in ambient air using high resolution photography. Collisionality parameter (ζ) [87] plays a crucial role in the interaction of colliding plasmas, So the effect of collisionality parameter on interaction of colliding plasma plumes in terms of (i) varying the separation distance (d) between the two plasma sources and (ii) by increasing the laser energy used to create the plasma in one of the sources (termed as S2 in the thesis) which in turn increases the number density is studied in counter-propagation geometry. These energy ratios of two plasma sources mimic the collision of fluids with varying impedances $Z_{S1} \approx Z_{S2}$, $Z_{S1} < Z_{S2}$. The energy of the plasma source S1 is kept constant by fixing the laser pulse energy at 25 $\pm$ 0.5 mJ in all cases (through out the study). While the energy of the plasma source S2 is varied by changing the laser pulse energy as 25 $\pm$ 0.4 mJ, 41 $\pm$1.2 mJ and 92 $\pm$ 1.5 mJ. When two laser pulses are focused at the same position i.e., d=0 mm or with separation of 1 mm (d=1 mm) between the two plasma sources, a single colliding plasma source was observed. For the interaction of two plasma sources with separation distance (d) $\geq$ 2 mm, two kinds of stagnation layers are observed at the interaction zone (d=0 mm). In this chapter, we present the experimental results on the effect of the separation distance (d) on the plasma and shock wave properties of the sources

S1/S2 in interaction of the two plasma sources with different energy ratios and compared with the freely expanding individual plasma sources (S1/S2). Due to the compression one plasma by the axial shock waves of other plasma lead to the discontinuity, known as *plasma jetlet*, which showed an interesting behaviour with the separation distant (d) between the two plasma sources and their energy ratio.
The highlights of the work are published in, N. Guthikonda et. al., *Interaction of two counter-propagating laser induced plasmas and shock waves in air*, Physics of Plasmas 27, 023107 (2020) [65].

Chapter 4
In this chapter the experimental results on the evolution dynamics of laser induced blow-off shock waves (LIBO SWs) in ambient air from the metal films or foils (Al, Cu, Ti) and polymer films (PVA, Au doped PVA) confined with glass (BK-7) substrate is presented. This chapter gives an insight into the evolution of LIBO SWs in ambient air due to the effect of axial confinement of plasma by the BK-7 glass substrate. The role of shifting focal plane on LIBO plasma and the shock wave properties, aimed at achieving the optimal blow-off shock waves is presented. Although a lot of study has been done on confined LIBO, the efficient coupling of laser energy to the target material, which is crucial for LIBO plasma and shock wave properties, is still inadequate [28, 63, 88]. Hence, we have studied the effect of focusing conditions on LIBO plasma and shock waves from the rear side of target foils to optimize the laser energy for efficient blow off shock pressures. This study also gave the chance to understand the effect of relative acoustic impedance of the confining layer and target material on the LIBO shock waves in ambient air. The initial studies were done with 20 μm Al and Cu foils adhered to the glass substrate at different focusing conditions (F0, F1 and F2) and upon optimizing the laser energy to 50 mJ, the LIBO studies were further extended to the 1.1 μm Cu, 200 nm metal thin films and polymer films of 60 μm PVA and 35 μm Au nano rods doped PVA films.
The highlights of the experimental LIBO work on 20 μm Al, Cu foils along with numerical validation were summarized in, N. Guthikonda et. al., *Effect of Focusing Plane on Laser Blow-off Shock Waves from Confined Aluminum and Copper Foils*, (Manuscript under preparation) (2020) [89].

Chapter 5
In this chapter, the dynamics of spatially confined laser induced air plasma and shock waves were presented. The spatial confinement of the air plasma is achieved using rectangular and cylindrical hollow tubes. The dimensions of tubes are varied over 4.7 mm to 18 mm. For the confinement geometries, the aspect ratio (tube length to inner diameter ratio) is varied over 1 to 2.5. The role of laser energy on spatial confinement for a given aspect ratio and vice-versa were presented. Although many research groups [48, 73, 74, 75, 76, 77, 78, 79, 80, 81, 82, 83] reported the enhancement of plasma emission

through semi confinement (confinement of laser ablative plasma from solids i.e, only one end of the cavity is open and plasma entered the cavity from other end), clear visualization of [74, 77, 83] the processes (radial shock wave reflections, plasma compression and squeezing) resulting in plasma emission enhancement are sparse. Hence, we have studied the spatially confined air plasma in detail to get an insight of the physical processes such as radial shock wave reflection, compression and squeezing of the plasma due to reflected shock waves leading to enhanced plasma emissions. The evolution of spatially confined air plasma and shock waves were captured using shadowgraphy and self-emission imaging for different laser input energy and different cavity aspect ratios. For a clear visualization of the physical processes a hollow rectangular glass tube of constant inner diameter (8 mm) with varying lengths (8-16 mm) giving the aspect ratios of L/D=1, 1.5 and 2 were used. The evolution of the confined plasma and the shock waves is compared to the unconfined/free expansion of air plasma under similar experimental conditions to quantify the confining effects. To get an insight into the enhancement of plasma properties (number density, temperature) due to reflected radial shock wave compression of air plasma inside a rectangular glass tube, we have performed the 2-D numerical simulations using modified FLASH-2D hydrodynamic codes [90]. The simulated plasma and shock wave properties show good agreement with the experimental results. The numerical simulation results are not included in this thesis, as they form thesis of my colleague D.P.S.L. Kameswari.
After the visualization of plasma and shock wave dynamics in a transparent rectangular glass tube, the studies were extended to cylindrical geometry. A cylindrical hollow copper tube with an inner diameter of 4.7 mm and of different lengths 4.7, 7.05 and 9.14 mm leading aspect ratios of 1,1.5 and 2 respectively, are used for spatial confinement. Since the cylindrical tube is opaque, only the evolution of the shock waves exiting along the Z direction can be seen along with the plasma mass density. The effect of laser energy and cavity aspect ratio on axial shock wave exit times and its evolution is studied in this chapter. The spatial confinement studies were further extended to understand the effect of tube diameter on the plasma mass density and axial shock wave evolution by confining the air plasma with 200 mJ of laser energy inside hollow cylindrical tubes of different diameter with same length. Three different materials such as: glass (L=15 mm, D=10.5, 12.5 mm), plastic (L=17.8 mm, D=13, 16 mm) and SS (L=12.72 mm, D=5.4, 6.47 mm) were used for this study. Based on the experimental results, this study was used to optimize the tube diameter for efficient enhancement of the plasma and shock wave properties in the spatial confinement of the air plasma.
The highlights of the spatial confinement of air plasma inside rectangular glass tube with validated simulation results were summarized in, N. Guthikonda et. al., *Dynamics of confined laser induced air plasma inside a hollow tube*, (Manuscript under preparation)(2020) [90].

Chapter 6

The effects of axial confinement presented in Chapter 4 and spatial confinement studied in Chapter 5 are combined to understand the evolution of laser induced/ablative shock waves inside a transparent dielectric material, BK-7 glass slab. The axial confinement of shock waves is achieved using an overlay of Al/Cu foils, while the dimensions of BK-7 glass have provided the spatial confinement boundary to shock waves launched and propagated inside BK-7 glass slab. In this chapter, the dynamics of laser induced shock waves inside BK-7 glass under the following conditions are presented: (a) effect of acoustic impedance of confining overlays by using Al, Cu foils of same thickness (20 μm) $Z_{Cu}(3.93) > Z_{Al}(1.45) > Z_{BK-7}(1.27)$ (in $10^6 g/cm^2 - s$) (where $Z = \rho U_{sw}$) (b) effect of laser focal plane position w.r.t. the glass-foil interface and (c) effect of input laser pulse energy. Though most of the studies on the confinement of laser ablative plasma confirmed the enhancement of the plasma and shock wave properties, all these studies were either based on plasma emission signal intensities (in surrounding medium) [73, 74, 75, 76, 77, 78, 79, 80, 81, 82, 83] or the amount of compression that the material undergone, which is studied via residual stress measurement [26, 71, 72]. The studies on the visualization of shock wave propagation inside the solid material are sparsely available due to the opaqueness of solids to visible radiation as it needs sophisticated instruments such as X-ray sources, detectors and VISAR with streak camera to monitor the shock wave inside solid material [91, 92]. If the material is transparent to visible radiation, one can visualize the evolution shock waves inside the material and quantify the shock wave characteristics in terms of radius/velocity. Hence, we have used BK-7 glass slab of 50 mm×50 mm×15 mm (l×b× h) which is transparent to the probe beam (633 nm). The temporal evolution of laser ablative shock waves inside BK-7 due to ablation of the confining layer and direct ablation geometries is studied. The Al (20 μm), Cu (20 μm) foils are used as overlay in the confinement geometry.

In direct ablation geometry, the effect of the laser energy on the laser induced breakdown of BK-7 glass slab and the evolution of the shock waves inside the BK-7 glass as well in the ambient air were studied. The effect of the shifting of focal plane (F0- laser focuses on the BK-7 surface and F2- laser focuses 6 mm deep inside BK-7) on the shock wave evolution inside BK-7 glass slab is also investigated to visualize the enhancement of the shock wave properties inside BK-7 glass. To understand the effect of axial confinement, Al and Cu foils of 20μm were adhered to the BK-7 glass surface. Due to the ablation of Al and Cu thin foils, the laser ablative shock wave propagating inside the Al and Cu foil transmitted into the BK-7 similar to the propagation of shock waves from one medium (Z1) to other medium (Z2) [1, 24, 93]. The effect of the laser energy and the shifting of focusing plane (F0 and F2) on the transmitted ablative shock wave inside the BK-7 glass is studied in confinement geometry. This study gave a chance to understand the

effect of relative acoustic impedance (Z) of the confining layer and target material on the transmitted laser ablative shock wave propagation inside the solid target material.

Chapter 7

This chapter summarizes the work presented and gives the future scope in terms of few applications. A roadmap on utilizing the work presented to design laser based macro shock tubes (few mm diameter) [42, 43, 44, 45, 46, 47] for characterization of materials using laser plasma produced shock waves is discussed. As the laser ablative shock waves behave analogous to that of a mechanically generated shock waves (that involve huge operational cost), the laser plasma based mm-sized shock tubes may be the future [42, 44, 47]. Optimization of laser coupling via different confining materials and overlays is essential for industrial processes such as laser shock peening [26]. The shock wave propagation in micro-channels (for example, veins) [94, 95] using fs laser generated shock waves can pave the way to create surgical tool to remove the clots by fine tuning of laser shock lithotripsy. Moreover, the lab scale laser based shock tube experiments can help in designing the efficient systems like gas/oil/mining ducts that involve extreme pressure and temperature conditions [96, 97].

References

[1] Y. B. Zel'dovich and Y. P. Raizer, *Physics of Shock Waves and High-Temperature Hydrodynamic Phenomena*, Dover Publications/Academic Press Inc., New York (2012).

[2] K. Chaudhary, S. Z. H. Rizvi and J. Ali, *Laser-Induced Plasma and its Applications*, Intech-open publishers (2016).

[3] F. F. Chen, A. Rubenchik, S. Witkowski, *Physics of Laser Plasmas*, Edition 3, North Holland, Amsterdam (1991).

[4] A. Dwivedi, *Recent advances in pulsed laser ablated plasma plumes:A review*, Surface Review And Letters, 14(1):57-69 (2007).

[5] C. Phipps, *Laser Ablation and its Applications*, Springer Series in Optical Sciences, Vol. 129 (2007).

[6] D. Batani, A. Balducci, D. Beretta, A. Bernardinello, T. Lower, M. Koeing, A. Benuzzi, B. Faral and T. Hall, *Equation of state data for gold in the pressure range $<$ 10 TPa*, Phys.Rev. B 61, 14, 9287-9294 (2000).

[7] P. Mulser, R. Sigel, and S. Witkowski, *Plasma production by laser*, Physics Reports 6, 187-239 (1973).

[8] A. Vogel, V. Venugopalan, *Mechanisms of pulsed laser ablation of biological tissues*, Chem. Rev. 103, 577–644 (2003).

[9] J. P. Singh and S.N. Thakur, *Laser-Induced Breakdown Spectroscopy*, Elsevier Science (2007).

[10] D. A. Cremers, L. J. Radziemski, *Handbook of Laser-Induced Breakdown Spectroscopy*, Second Edition, John Wiley & Sons (2013).

[11] C. Pasquini, J. Cortez, L. M. C. Silva and F. B. Gonzaga, *Laser Induced Breakdown Spectroscopy: Review*, J. Braz. Chem. Soc.,Vol. 18, No. 3, 463-512(2007).

[12] S. I. Anisimov, B. S. Lukyanchuk, and A. Luches, *An analytical model for three-dimensional laser plume expansion into vacuum in hydrodynamic regime*, Appl.Surf. Sci. 96, 24 (1996).

[13] R. K. Singh and J. Narayan., *Pulsed-laser evaporation technique for deposition of thin films:*

Physics and theoretical model, Phys. Rev. B 41, 8843 (1990).

[14] J. Stephen Davitt, *Colliding Plasmas in Air*, Ph. D. thesis, Dublin City University, Ireland (2018).

[15] S. Amoruso, R. Bruzzese, N. Spinelli, R. Velotta, *Characterization of laser-ablation plasmas*, J. Phys. B,32(14) (1999).

[16] L. M. Cabalin and J. J. Laserna, *Experimental determination of laser induced breakdown thresholds of metals under nanosecond Q-switched laser operation*, Spectrochimica Acta Part B 53, 723-730 (1998).

[17] P. Hough, C. McLoughin, T. J. Kelly, P. Hayden, S. S. Harilal, J. P. Mosnier, *Electron and ion stagnation at the collision front between two laser produced plasmas*, J. Phys. D Appl. Phys., 42(5) (2009).

[18] S. S. Harilal, C. V. Bindhu, M. S. Tillack, F. Najmabadi, A. C. Gaeris, *Internal structure and expansion dynamics of laser ablation plumes into ambient gases*, J. Appl. Phys., 93(5), 2380–8 (2003).

[19] B. Campanella, S. Legnaioli, S. Pagnotta, F. Poggialini and V. Palleschi, *Review:Shock Waves in Laser-Induced Plasmas*, Atoms 7, 57 (2019).

[20] Y. P. Raizer, V. I. Kisin, and J. E. Allen, *Gas Discharge Physics*, Springer, Berlin, Heidelberg (2011).

[21] P. L. Sachdev, *Shock waves and Explosions*,Chapman & Hall/CRC monographs and surveys in pure and applied mathematics 132, CRC press (2004).

[22] Ch. Leela, *Spatio-temporal imaging of laser induced shock waves and plasma plume from ambient air, metals, periodic structured surfaces and sub-micron sized compacted powders*, Ph. D. thesis, University of Hyderabad, India (2014).

[23] S. Sai Siva, *Numerical Investigations of ns Laser Induced Shock Waves from Aluminum and Air*, Ph. D. thesis, University of Hyderabad, India, 2016.

[24] C. E. Needham, *Blast Waves: Shock Wave and High Pressure Phenomena*, Springer-Verlag Berlin Heidelberg (2010).

[25] E. Schwarz, S. Gross, B. Fischer, I. Muri, J. Tauer and E. Wintner, *Laser-induced optical breakdown applied for laser spark ignition*, Laser and Particle Beams 28, 109-119 (2010).

[26] K. Ding and L. Ye, *Laser Shock Peening Performance and simulation*, Woodhead publishing Limited (2006).

[27] B. Luk'yanchuk, *Laser surface cleaning*, World Scientific Publishing Co. Pte, Ltd (2002).

[28] C. R. Phipps, J. P. Reilly and J. W. Campbell, *Optimum parameters for laser launching objects into low Earth orbit*, Laser and Particle Beams 18, 661-695 (2000).

[29] M. Kawahara, N. Ioritani, K. Kambe, S. Orikasa and K. Takayama, *Anti-miss-shot control device for selective stone disintegration in extracorporeal shock wave lithotripsy*, Shock Waves

1, 145-148 (1991).

[30] M. Delius, *Medical applications and bio-effects of extracorporeal shock waves*, Shock Waves 4, 55-72 (1994).

[31] B. Wang, K. Komurasaki, T. Yamaguchi, K. Shimamura and Y. Arakawa, *Energy conversion on a glass-laser-induced blast wave in air*, Journal of Applied Physics 108, 124911 (1-6) (2010).

[32] S. H. Jeong, R. Greif, R. E. Russo, *Propagation of the shock wave generated from excimer laser heating of aluminum targets in comparison with ideal blast wave theory*, Applied Surface Science, 127-129, 1029-1034 (1998).

[33] D. Batani, H. Stabile, A. Ravasio, G. Lucchini, F. Strati, T. Desai, J. Ullschmied, E. Krousky, J. Skala, L. Juha, B. Kralikova, M. Pfeifer, C. Kadlec, T. Mocek, A. Präg, H. Nishimura and Y. Ochi, *Ablation pressure scaling at short laser wavelength*, Physical Review E 68, 067403 (2003).

[34] N. K. Bourne, J. C. F. Millet and G. T. Gray, *On the shock compression of polycrystalline metals*, J Mater. Sci. 44, 3319-3343 (2009).

[35] N. K. Bourne, *Akrology: materials: physics in extremes*, AIP Conf. Proc. 1426, 1331-1334 (2012).

[36] H. J. Davies and H. D. Curchack, *Shock Tube techniques and Instrumentation*, Technical report-1429, US army command, Harry Diamond Laboratory (1969).

[37] A. Benuzzi-Mounaix et al., *Laser-driven shock waves for the study of extreme matter states*, Plasma Phys. Control. Fusion 48, B347 (2006).

[38] V. E. Fortov and I. V. Lomonosov,*Shock waves and equations of state of matter*, Shock Waves 20, 53–71 (2010).

[39] J. Lindl, *Development of the indirect-drive approach to inertial confinement fusion and the target physics basis for ignition and gain*, Phys. Plasmas 2, 3933–4024 (1995).

[40] D. S. Spicer, R. W. Clark and S. P. Maran, *A model of the pre-Sedov expansion phase of supernova remnant-ambient plasma coupling and X-ray emission from SN 1987A*, Astrophys. J. 356, 549 (1990).

[41] B. P. Fairand and A. H. Clauer, *Laser generation of high-amplitude stress waves in materials*, Journal of Applied Physics 50, 1497–502 (1978).

[42] U. Teubner, Y. Kai, T. Schlegel, D. E. Zeitoun and W. Garen, *Laser-plasma induced shock waves in micro shock tubes*, New J. Phys. 19, 103016 (2017).

[43] M. Brouillette, *Shock waves at micro scales*, Shock Waves 13, 3–12 (2003).

[44] G. Mirshekari, *Micro scale shock tube*, Ph.D. Thesis, University of Sherbrooke, Canada (2008).

[45] D. E. Zeitoun, *Correlations of shock mach number attenuation in small size diameter tubes*, Phys. Fluids 27, 011701 (2015).

[46] D. E. Zeitoun and Y. Burtschell, *Navier-stokes computations in micro shock tubes*, Shock Waves

15, 241–6 (2006).

[47] Y. Kai, W. Garen and U. Teubner, *A novel shock tube with a laser-plasma driver*, Laser Particle Beams (2017).

[48] Y. Li, D. Tian, Y. Ding, G. Yang, K. Liu, C. Wang and X. Han, *A review of laser-induced breakdown spectroscopy signal enhancement*, Applied Spectroscopy Reviews, Vol. 53, No.1, 1-35 (2018).

[49] A. K. Myakalwar, S. Sreedhar, I. Barman, N. C. Dingari, S. Venugopal Rao, P. Prem Kiran, S. P. Tewari and G. Manoj Kumar, *Laser-induced breakdown spectroscopy-based investigation and classification of pharmaceutical tablets using multivariate chemometric analysis*, Talanta 87, 53-59 (2011).

[50] C. Gautier, P. Fichet, D. Menut and J. Dubessy, *Applications of the double-pulse laser-induced breakdown spectroscopy (LIBS) in the collinear beam geometry to the elemental analysis of different materials*, Spectrochim. Acta Part B At. Spectrosc. 61 (2), 210–219 (2006).

[51] D. W. Hahn and N. Omenetto, *Laser-Induced Breakdown Spectroscopy (LIBS), Part I: Review of Basic Diagnostics and Plasma–Particle Interactions: Still-Challenging Issues Within the Analytical Plasma Community*, Appl. Spectrosc. 64, 335A-366A (2010) .

[52] D. W. Hahn and N. Omenetto, *Laser-Induced Breakdown Spectroscopy (LIBS), Part II: Review of Instrumental and Methodological Approaches to Material Analysis and Applications to Different Fields*, Appl. Spectrosc. 66, 347-419 (2012).

[53] A. E. Hussein, A. K. Kassem, H. Ismail and M. A. Harith, *Exploiting LIBS as a spectrochemical analytical technique in diagnosis of some types of human malignancies*, Talanta 82 (2), 495–501 (2010)

[54] S. Pandhija, N. K. Rai, A. K. Rai and S. N. Thakur, *Contaminant concentration in environmental samples using LIBS and CF-LIBS*, Appl. Phys. B 98 (1), 231–241 (2010).

[55] T. Hussain and M. A. Gondal, *Monitoring and assessment of toxic metals in Gulf War oil spill contaminated soil using laser-induced breakdown spectroscopy*, Environ. Monit. Assess.136 (1–3), 391–399 (2008).

[56] L. C. Nunes, G. A. Silva, L. C. Trevizan, D. S. Junior, R. J. Poppi and F.J. Krug, *Simultaneous optimization by neuro-genetic approach for analysis of plant materials by laser induced breakdown spectroscopy*, Spectrochim. Acta Part B At. Spectrosc. 64 (6), 565–572 (2009).

[57] N. Melikechi et.al., *Correcting for variable laser-target distances of laser-induced breakdown spectroscopy measurements with ChemCam using emission lines of Martian dust spectra*, Spectrochim. Acta Part B At. Spectrosc. 96 (6), 51–60 (2014).

[58] L. Balika, C. Focsa, S. Gurlui, S. Pellerin, N. Pellerin, D. Pagnon and M. Dudeck, *Laser-induced breakdown spectroscopy in a running Hall Effect Thruster for space propulsion*, Spectrochim. Acta Part B At. Spectrosc. 74–75 (8), 184–189 (2012).

[59] R. Kumar, A. K. Rai, D. Alamelu and S. K. Aggarwal, *Monitoring of toxic elements present in sludge of industrial waste using CF-LIBS*, Environ. Monit. Assess. 185 (1), 171–180 (2013).

[60] A. Mansoori, B. Roshanzadeh, M. Khalaji and S. H. Tavassoli, *Quantitative analysis of cement powder by laser induced breakdown spectroscopy*, Opt. Lasers Eng. 49 (3), 318–323 (2011).

[61] A. Kruusing, *Underwater and water-assisted laser processing: part 1-general features, steam cleaning and shock processing*, Opt. Lasers Eng. 41, 307-327 (2004).

[62] A. Kruusing, *Underwater and water-assisted laser processing: part 2-etching, cutting and rarely used methods*, Opt. Lasers Eng. 41, 329-352 (2004).

[63] C. Phipps, M. Birkan, W. Bohn, H. A. Eckel, H. Horisawa, T. Lippert, M. Michaelis, Y. Rezunkov, A. Sasoh, W. Schall, S. Scharring and J. Sinko, *Review-Laser Ablation Propulsion*, Journal of Propulsion and Power 26 (4), 609-637 (2010).

[64] S. L. Gupta, P. K. Pandey and R. K. Thareja, *Dynamics of laser ablated colliding plumes*, Phys. Plasmas 20, 013511 (2013).

[65] N. Guthikonda, E. Manikanta, Ch. Leela, S. Sai Shiva, S. Sree Harsha, V. R. Ikkurthi and P. Prem Kiran, *Interaction of two counter-propagating laser induced plasmas and shock waves in air*, Physics of Plasmas 27, 023107 (2020).

[66] R. Sangines and H. Sobral, *Time resolved study of the emission enhancement mechanisms in orthogonal double-pulse laser-induced breakdown spectroscopy*, Spectrochim. Acta Part B At. Spectrosc. 88 (10), 150–155 (2013).

[67] W. Bleakney and A. H. Taub, *Interaction of Shock Waves*, Reviews of modern physics, 21, 584 (1949).

[68] S. S. Harilal, C. V. Bindhu and H. J. Kunze, *Time evolution of colliding laser produced magnesium plasmas investigated using a pinhole camera*, J. Appl. Phys.89, 4737 (2001).

[69] B. Kumar, R. K. Singh, S. Sengupta, P. K. Kaw and A. Kumar, *Investigation of shock-shock interaction and Mach reflection in laterally colliding laser-blow-off plasmas* , Phys. Plasmas 22, 063505 (2015).

[70] K. F. Al-Shboul, S. M. Hassan and S. S. Harilal, *Molecular formation in the stagnation region of colliding laser-produced plasmas*, Plasma Sources Sci Technol. 25 (6) (2016).

[71] X. Hong, S. Wang, D. Guo, H. Wu, J. Wang, Y. Dai, X. Xia and Y. Xie, *Confning Medium and Absorptive Overlay: Their Effects on a Laser-induced Shock Wave*, Optics and Lasers in Engineering 29, 447-455 (1998).

[72] A. K. Gujba and M. Medraj, *Laser Peening Process and Its Impact on Materials Properties in Comparison with Shot Peening and Ultrasonic Impact Peening*, Materials 7, 7925-7974 (2014).

[73] A. M. Popov, F. Colao and R. Fantoni, *Enhancement of LIBS signal by spatially confining the laser-induced plasma*, J. Anal. At. Spectrom. 24 (5), 602–604 (2009).

[74] P. Yeates and E. T. Kennedy, *Spectroscopic, imaging, and probe diagnostics of laser plasma plumes expanding between confining surfaces*, J. Appl. Phys. 108 (9)(2010).

[75] X. K. Shen, J. Sun, H. Ling and Y.F. Lu, *Spatial confinement effects in laser-induced breakdown*

spectroscopy, Appl. Phys. Lett. 91 (8) (2007).

[76] S. S. Harilal, M. S. Tillack, B. O'Shay, C. V. Bindhu and F. Najmabadi, *Confinement and dynamics of laser-produced plasma expanding across a transverse magnetic field*, Phys. Rev.E 69 (2)(2004).

[77] X. Li, Z. Wang, X. Mao and R. E. Russo, *Spatially and temporally resolved spectral emission of laser-induced plasmas confined by cylindrical cavities*, J. Anal. At. Spectrom. 29 (11), 2127–2135 (2014).

[78] D. S. Meng, N. J. Zhao, M. J. Ma, Y. Wang, L. Hu, Y. Yu, L. Fang and W. Q. Liu, *Heavy metal detection in soils by laser induced breakdown spectroscopy using hemispherical spatial confinement*, Plasma Sci. Technol. 17 (8), 632–637 (2015).

[79] S. S. Mao, X. Zeng, X. Mao and R. E. Russo, *Laser-induced breakdown spectroscopy:Flat surface vs. cavity structures*, J. Anal. At. Spectrom. 19 (4), 495–498(2003).

[80] X. Zeng, X. Mao, S. S. Mao, S. B. Wen, R. Greif and R.E. Russo, *Laser-induced shock wave propagation from ablation in a cavity*, Appl. Phys. Lett. 88 (6)(2006).

[81] L. B. Guo, W. Hu, B. Y. Zhang, X. N. He, C. M. Li, Y. S. Zhou, Z. X. Cai, X. Y. Zeng and Y. F. Lu, *Enhancement of optical emission from laser-induced plasmas by combined spatial and magnetic confinement*, Opt. Express 19 (15), 14067–14075 (2011).

[82] Q. Wang, A. Chen, D. Zhang, Y. Wang, L. Sui, S. Li, Y. Jiang and M. Jin, *The role of cavity shape on spatially confined laser-induced breakdown spectroscopy*, Physics of Plasmas 25, 073301 (2018).

[83] Y. Fu, Z. Hou and Z. Wang, *Physical insights of cavity confinement enhancing effect in laser breakdown spectroscopy*, Optics express Vol. 24 No.3, 3055 (2016).

[84] G. S. Settles, *Schlieren and Shadowgraph Techniques: Visualizing Phenomena in Transparent Media*, Springer Berlin Heidelberg (2001).

[85] H. Zhang, J. Lu and X. Ni, *Optical interferometric analysis of colliding laser produced air plasmas* , J. Appl. Phys. 106, 063308 (2009).

[86] Z. Yang, W. Wei, J. Han, J. Wu, X. Li and S. Jia et al., *Experimental study of the behaviour of two laser produced plasmas in air*, Phys.Plasmas 22, 073511 (2015).

[87] P. T. Rumsby, J. W. M. Paul, and M. M. Masoud, *Interactions between two colliding laser produced plasmas*, Plasma Phys.16, 969 (1974).

[88] R. Fabbro, J. Fournier, P. Ballard, D. Devaux and J. Virmont, *Physical study of laser-produced plasma in confined geometry*, Journal of Applied Physics 68, 775 (1990).

[89] N. Guthikonda, S. Sai Shiva, D. P. S. L. Kameswari, P. Prem Kiran, C. D. Sijoy and V. R. Ikkurthi, *Effect of Focusing Plane on Laser Blow-off Shock Waves from Confined Aluminum and Copper Foils*, (Manuscript under preparation) (2020).

[90] N. Guthikonda, D. P. S. L. Kameswari, E. Manikanta, S. Sai Shiva, S. Sree Harsha and P. Prem

Kiran, *Dynamics of confined laser induced air plasma inside a hollow tube*, (Manuscript under preparation)(2020).

[91] P. A. Naik, V. Arora, S. Bagchi, Y. B. S. R. Prasad, S. Barnwal and P. D. Gupta, *Laser induced shock studies at RRCAT, Indore* , J. Phys.: Conf. Ser. 377, 012052 (2012).

[92] Y. Prasad, S. Barnwal, P. A. Naik, Y. Yadav, R. Patidar, M. P. Kamath, *Shock wave propagation in soda lime glass using optical shadowgraphy*, Pramana 87 (1), 9 (2016).

[93] P. W. Cooper, *Explosives engineering*, Wiley-VCH (1996).

[94] T. M. Squires and S. R. Quake, *Microfluidics: fluid physics at the nano-liter scale*, Rev. Mod. Phys. 77, 977 (2005).

[95] W. Sparreboom, A. Van Den Berg and J. C. T. Eijkel, *Transport in nano-fluidic systems: a review of theory and applications*, New J. Phys. 12, 015004 (2010).

[96] H. P. Schildberg, *Gas-Phase Detonations in Pipes: the 8 Possible Different Pressure Scenarios and their Static Equivalent Pressures Determined by the Pipe Wall Deformation Method (part 1)*, Chemical Engineering Transactions, 48, 241-246 (2016).

[97] G. Ben-Dor, O. Igra and T. Elperin, *Handbook of Shock Waves: Volume 2, Shock wave Interactions and Propagation*, Academic Press (2001).

Chapter 2

Experimental Details

To understand the spatio temporal evolution of confined laser induced/ablative plasma and shock waves into ambient air or into the transparent material, we have used different laser systems, diagnostic instruments (ICCD, CCD cameras), optical imaging methods such as shadowgraphy and self emission imaging and different target samples. This chapter gives brief description of the laser systems, synchronization of ICCD/CCD camera with laser system, optical imaging methods(shadowgraphy), experimental schematics for different confinement methods and details of the target materials. In this thesis, shadowgraphy imaging with fast gated (ns) ICCD camera and plasma self emission study using CCD and/or ICCD camera are the main diagnostics used to study the evolution of the plasma plume and shock waves in different confinement geometries.

2.1 Introduction

The enhancement of optical (radiation) and mechanical (shock wave) emissions from the plasma is very essential to different fields such as laser induced breakdown spectroscopy, laser shock peening, laser propulsion and plasma diagnostics in tokamaks etc [1, 2, 3, 4]. The plasma and shock wave properties are enhanced by different confinement methods such as dual-pulse excitation, spatial confinement, magnetic confinement and adding of transparent overlays or absorbing metal/polymer as confining medium. Although many reports are available on plasma and shock wave enhancement, a clear visualization of the confinement process leading to enhancement of plasma and shock wave properties are sparse. In this work, spatial and temporal evolution of the confined plasma and shock waves and role of shock waves on enhancement of plasma properties were clearly visualized with the help of optical diagnostic methods such as, shadowgraphy and self emission imaging. A detailed description of Laser systems used for plasma generation and probing of plasma, instruments used for optical diagnostics and experimental schematics used for different confining methods were given below.

2.2 Shadowgraphy Imaging

Shadowgraphy technique works on the principle of refraction. When the probe beam passes through the plasma, it gets refracted due to the gradient in the refractive index of a phase object, leading to variations of intensity causing bright zones and shadows. Variations in the intensity of a shadowgram depend up on the second derivative of refractive index of the medium. Different shadowgraphy techniques such as direct, focused, defocused and Z-type shadowgraphy techniques [5] are available. Focused shadowgraphy gives the information mostly about the evolution of plasma volume and shock front position w.r.t. the time delay from the laser pulse. This technique gives the knowledge of ionization of a material, the dynamics of the ejected mass (in the present study, it is plasma plume) and shock wave front propagation through the ambient medium. In our work we have used defocused (Chapter 3) and focused (Chapters 4, 5, 6) shadowgraphy by placing the ICCD camera slightly off after the focal plane of the collecting lens (L5) placed in front of the camera [6].

To study the information about the finer density details (with variable magnification) and to study the inner and outer fringes surrounding the plasma core revealing spatial density gradients more clearly, the defocusing shadowgraphy is more useful. In defocused shadowgraphy, the ICCD camera is placed before the focal plane of collecting lens (L5).

2.3 Details of the laser systems

In this thesis work, we have used two Nd:YAG laser systems with different pulse durations to create plasma in ambient air or inside the target material. The brief description of laser working and technical details are given below.

2.3.1 SpitLight 1200 laser system

A Q-switched INNOLAS spitlight-1200 Nd:YAG laser system was used to create the air plasma sources in axial confinement of air plasma in double pulse (DP) configuration (Chapter 3). Spitlight-1200 laser could be operated at 1064 nm, 532 nm, 355 nm, 266 nm producing maximum pulse energies of 1300 mJ, 700 mJ, 320 mJ and 130 mJ respectively [6]. In this thesis, linearly polarised laser pulses having second harmonic wavelength (532 nm) and 7$\pm$ 1 ns Full Width at Half Maximum (FWHM) with Gaussian beam profile were used. The detailed description of laser working is provided elsewhere [6, 7]. The important characteristics of the laser have been summarized in Table 2.1.

2.3.2 TITAN-5 laser system

TITAN-5 from Amplitude Technologies, is a high power Nd:YAG laser system that can deliver higher pulse energies upto 7 J at 1064 nm and 5 J at 532 nm respectively with short pulse (10 ns) duration and quasi-Top-Hot beam profile. It can be operated at either 5 Hz or single shot mode. This laser system is used to create plasma in axial confinement (single pulse configuration) and radial confinement of plasma studies (Chapters 4,5,6).

Table 2.1 Specifications of Nd:YAG laser systems used in the study

	SpitLight-1200	**TITAN-5**
Wavelength	1064,532,355&266 nm	1064,532 nm
Pulse width(FWHM)	7± 1 ns	10±1 ns
Beam profile	Gaussian	quasi Top-Hat
Beam diameter	8 mm	22 mm
Repetition rate	0.5-10 Hz	5 Hz or Single Shot
Energy/pulse (Max.)	1300,700,320&130 mJ	7000,5000 mJ
Beam divergence	<0.5 mrad	<0.5 mrad
Time jitter	<1 ns rms	<0.5 ns rms

The important specifications of the laser have been summarized in Table 2.1[8]. The internal layout of TITAN-5 high power Nd:YAG laser system with 10 ns pulse width (FWHM) is shown in Figure 2.1. The TITAN-5 laser is composed with three major parts: the laser head, the power supplies and the cooling unit. The laser head consists of an oscillator, two power amplifiers (i.e., two stage amplification) and, a second harmonic generation and harmonic filter setup. The TITAN-5 laser oscillator consists of 12.7 mm diameter Nd:YAG rod pumped by two Krypton flash lamps, generates IR (1064 nm) laser pulses with p-polarization. The laser cavity of the Nd:YAG oscillator is an unstable Q-switched resonator with Gaussian type mirror (reflectivity is higher at the center than on the edge). The cavity is optimized for efficient energy extraction of a large diameter Nd:YAG rod in a single transverse spatial mode (TEM_{00}). The designed cavity then has multiple resonance frequencies (spectrally multi-mode).

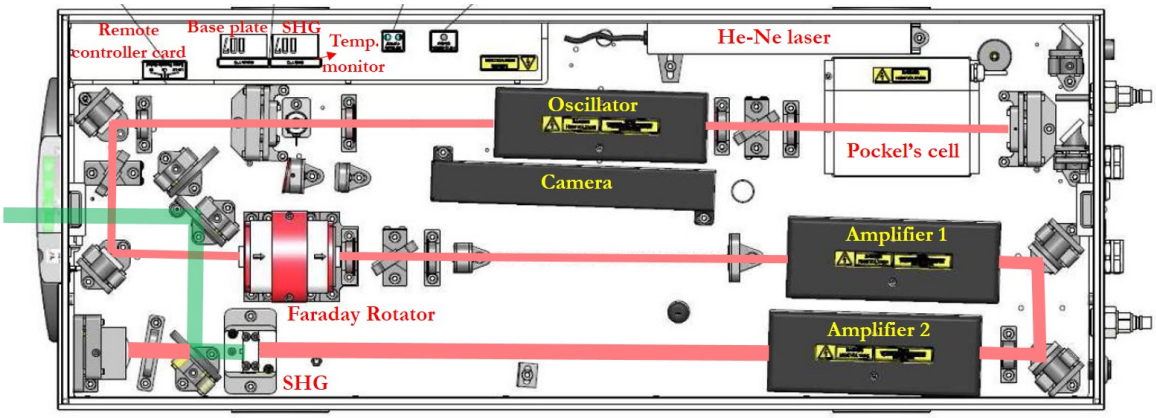

Figure. 2.1 Internal layout of the TITAN-5 high power Nd:YAG laser system.

When the Pockels cell(PC) is inactive, the p-polarized beam is transmitted through the dielectric polarizer (p-type) and is converted into circularly polarized beam by the quarter wave plate; the Pockels cell does not affect it. On its way back, the beam has its

polarization transformed from circular to s-polarization (linear vertical) by the quarter wave plate and is extracted out of the cavity by the dielectric polarizer (p-type) (Figure 2.2). This configuration inhibits laser oscillation and no laser beam is extracted through the output coupler. When the Pockels cell is activated (a 4 kV voltage is applied to the electrodes), the circularly polarized beam is transmitted by the quarter wave plate and is converted into s-polarized beam by the Pockels cell. On its way back, the beam polarization is converted into p-polarization by the Pockels cell (still activated) and the quarter wave plate. The beam is then totally transmitted through the dielectric polarizer and laser oscillation is enabled within the cavity (Figure 2.2).

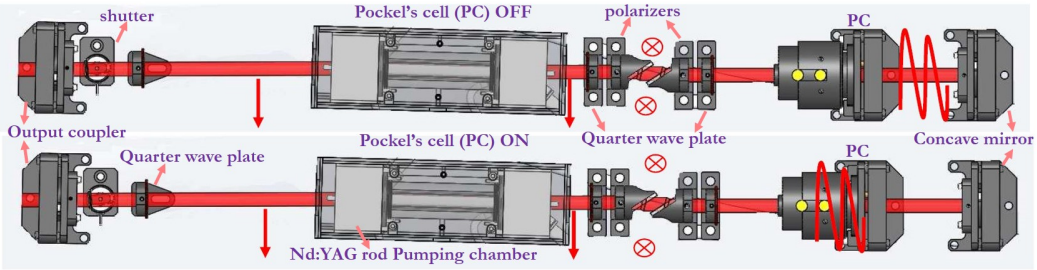

Figure. 2.2 Q-switching principle of TITAN-5 laser cavity.

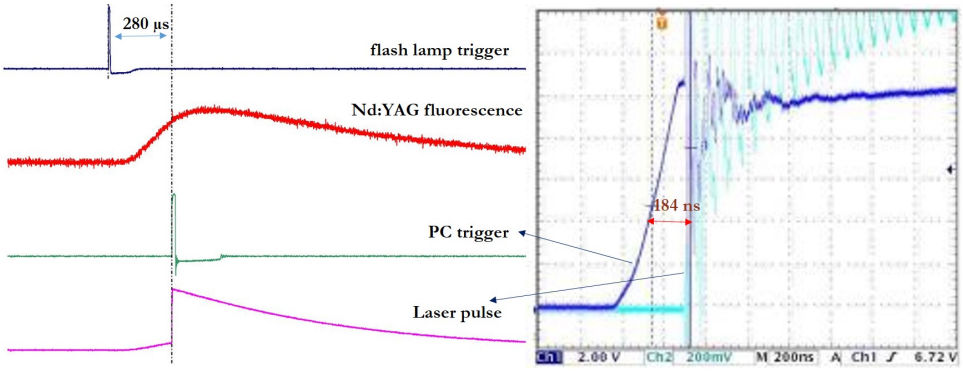

Figure. 2.3 Internal synchronization timing diagram of TITAN-5 laser cavity.

Figure 2.3 shows the internal synchronization timing diagram of TITAN-5 laser cavity. When the flash lamps are triggered, the Nd:YAG rod emits the fluorescence and after reaching to saturation, the fluorescent energy is extracted from the cavity by triggering the Pockels cell. The delay between the flash lamp trigger and the Pockels cell trigger is in the order of 280 μs, known as the fluorescence delay. After the Pockels cell trigger, the laser pulse is emitted from the laser cavity. The delay between the Pockels cell trigger and laser pulse emission is in the order of 184 ns. After the laser pulse emission from cavity, it is propagated through a first stage amplifier (Amplifier 1) having 16.5 mm diameter Nd:YAG rod (single pass) leading to $\sim$ 3 times amplification in pulse energy and 1.3 times increase laser beam diameter (Figure 2.4). The laser pulse is further propagated through

second stage amplifier (Amplifier 2) having 21 mm diameter Nd:YAG rod (single pass) to increase the pulse energy by ∼ 3 times, with 1.3 times increase laser beam diameter (Figure 2.4 (a)). The advantage of this laser system is that, we can monitor the laser cavity output beam profile of laser pulse and the laser energy distribution within the pulse in real time mode. The *Vision*® software along with BASLER *ACE*® camera is used for the real time monitoring of pulse profile and pulse energy distribution [9]. Figure 2.4 (b) shows the laser beam snapshot from oscillator is captured using *Vision*® software at 2 J (532 nm) output energy. It clearly shows that the pulse energy distribution within beam diameter is like quasi-TOP-HAT while it has a Gaussian type temporal profile as shown in Figure 2.4 (c,d).

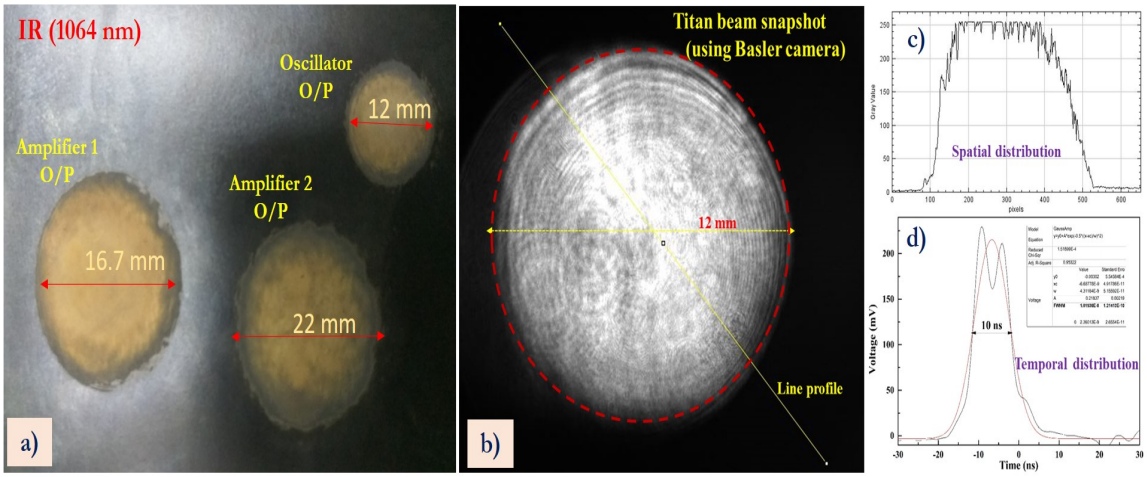

Figure. 2.4 Characterization of TITAN-5 laser beam (a) beam diameter (b) laser beam snapshot using Vision software (c-d) spatial and temporal distribution of laser pulse of 2 J laser output energy.

The final output of IR beam (after amplification) has ∼6 times pulse energy than the pulse energy from cavity with 22 mm laser beam diameter. For second harmonic generation (SHG), a 25 mm diameter LBO (Lithium Borate) Type-I crystal with appropriate harmonic filters (Dichroic mirrors) is used. The LBO crystal has different coatings 1064 nm, 532 nm on each face with an arrow showing laser propagation direction. The input and output faces are wedged around 2.5° to avoid the input face reflection back into the ceramic on the side of the pumping chamber. For efficient SHG, we can tune the phase-matching angle by regulating the crystal temperature at 40° C (thermally stable). This LBO Type-I crystal has around 70 % energy conversion efficiency. The second harmonic laser pulses are passed through harmonic filters (dichroic mirrors) to eliminate residual 1064 nm wavelength and exited through laser head manual exit aperture. The power supplies and cooling unit (internal chiller) are combined into a single laser cabinet [8].

Since the TITAN-5 is a high power laser system (5 J max. @ 532 nm), it is optimised (oscillator voltage at 1450 V and amplifier voltages at 1350 V) for delivering ∼ 3 J energy

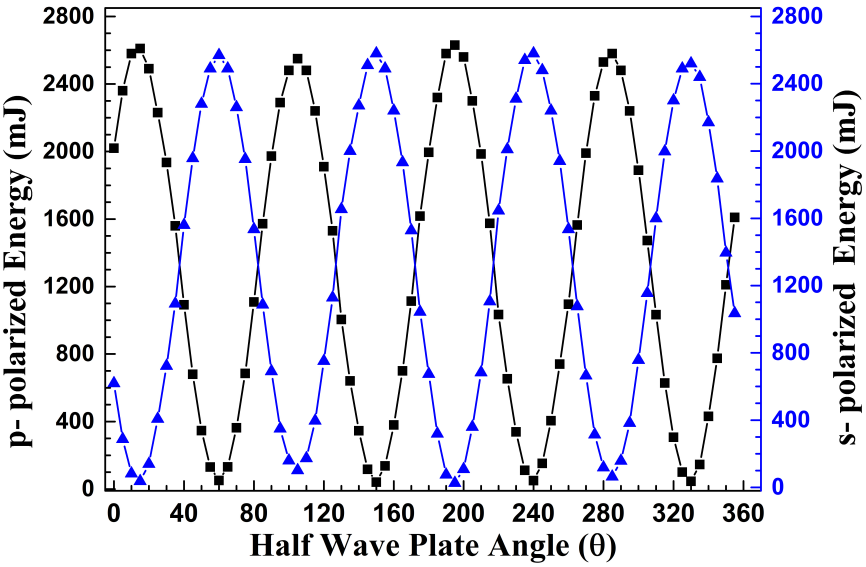

Figure. 2.5 Laser energy variation w.r.t. HWP angle representing malus law; ■ represents p-polarised light and ▲ represents s-polarised light.

with 532 nm wavelength for this thesis work. It is to note that, for different laser energy requirements (for lower energies), continuous changing of the oscillator and amplifiers voltages is not advised, because it can cause serious damage to the Nd:YAG rods. So, the output of TITAN-5 laser is fed into an attenuator, which consist of a half wave plate (HWP) and a Brewster polariser. The attenuator splits the beam into s-polarisation and p-polarisation laser beam with different energies based on HWP angle (according to malus law $I = I_0 Cos^2\theta$). The Figure 2.5 shows the energy variation of laser beam w.r.t. the HWP angle. For all the work performed with TITAN laser, we have used s-polarised laser beam.

2.3.3 Probe beam

A continuous He-Ne laser from M/s Melles–Griot (model: 25-LHP-828–230) with 25 mW output power and 632.8 nm wavelength was used as a probe beam to capture the dynamics of plasma plume and shock waves from Air and different target materials. The initial probe beam diameter ($\sim$ 1.5 mm) was expanded to $\sim$ 4.5 mm and collimated by using a beam expander (BR3X, Thor Labs). Later, this probe beam (4.5 mm) was further expanded (20X) and collimated by using a telescopic lens system which consists of two plano-convex lenses with focal lengths 50 mm (L3) and 1000 mm (L4) separated by sum of the focal length distances (f3+f4), respectively. The final output probe beam has 33 mm diameter. A spatial filter (aperture) was placed at the focal plane of the first lens (L3) to filter out the higher spatial frequency components in order to get the smoother

beam profile. The collimated probe beam of 33 mm traverses through the plasma region of the irradiated sample with the help of 50 mm diameter He-Ne mirrors and loosely focused on to the ICCD camera using 50 mm diameter palno-convex lens (L5) with 200 mm focal length. As the He-Ne laser probe beam propagates through the plasma, it can either be refracted by a region with high density gradients or absorbed by dense plasma plume particulates, thus leads to bright and dark regions in the shadowgraphy images. A band pass filter transparent to 632.8 nm and a notch filter of 532 nm placed in front of the ICCD camera to prevent the background illumination. This probe beam (33 mm) is used for the experiments using spitlight 1200 laser system i.e., 7 ns laser pulses.

The shadowgraphy set up was upgraded for experiments with TITAN high power laser

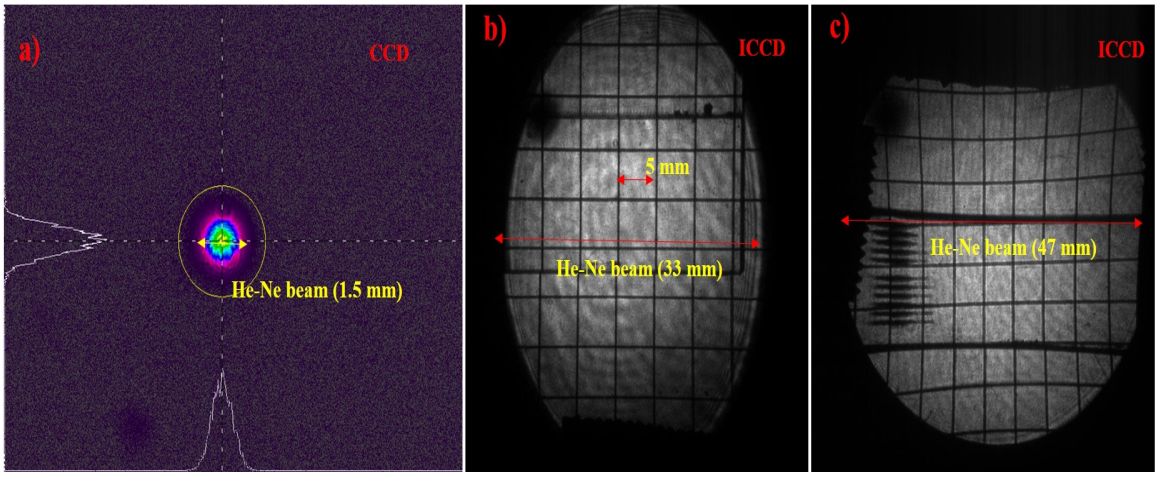

Figure. 2.6 He-Ne probe beam imaged using (a) CCD camera (b,c) ICCD camera along with graph sheet

system i.e., 10 ns laser pulses. The initial probe beam diameter ($\sim$ 1.5 mm) was expanded to $\sim$ 47 mm (limited by lens diameters (50 mm)) and collimated by using a beam expander (BR3X, Thor Labs) and telescopic lens system (13X) which consists of two plano-convex lenses with focal lengths 50 mm (L3) and 650 mm (L4). The collimated probe beam of 47 mm traverses through the plasma region of the irradiated sample with the help of 150 mm diameter He-Ne mirrors and loosely focused on to the ICCD camera using 150 mm diameter palno-convex lens (L5) with 200 mm focal length. Figure 2.6 (a) shows the image of initial He-Ne probe beam captured using CCD camera, Figure 2.6 (b-c) shows the calibrated image of He-Ne probe beam captured by ICCD camera which is further used for shadowgram analysis.

2.3.4 Imaging diagnostics

CCD: Normal imaging of the plasma provides a qualitative information about the plasma size (length and diameter of the plasma). An Ophir-spiricon camera (SP 620U) with 200-1300 nm spectral range, 4.4 μm $\times$ 4.4 μm spatial resolution and $\sim$ms (integrated)

temporal resolution along with CCTV zoom lens (50X) is used to image the plasma self emission. The camera is also fast triggerable with laser pulse. The detailed description of CCD working is provided elsewhere [10]. The technical specifications of the CCD camera have been summarized in Table 2.2.

ICCD: ICCD cameras with ns and ps gating are extensively used for the studies of the laser produced plasma, for studying temporal evolution, spectral distribution and instability studies. The ICCD consists of a CCD camera behind an image intensifier, which enhances the low light photons for short duration of time. The amplification of light is done by photo cathode and multi channel plate (MCP). The presence of photo cathode in ICCD makes the ICCD a camera having an extremely fast shutter. The gating of photo cathode can be electrically controlled by the amplitude of the voltage, width and delay time. The ICCD is controlled and synchronised with laser by using a external delay generator (SRS 645 DDG). We have used an Andor ICCD (Andor iStar DH-734U) camera [11] with ns gating for spatial and temporal evolution of plasma and shock waves. We performed fast imaging of laser produced plasma plume using an ICCD with a Nikon 85 mm f/1.4D infinity corrected zoom lens. The technical specifications of the ICCD camera have been summarized in Table 2.2.

Table 2.2 Technical specifications of diagnostic tools used in the study

	ICCD	**CCD**
Model	Andor iStar DH-734U	Ophir-Spiricon: SP-620U
Type	Gated, fast triggered	Non-Gated, triggerable
Spectral Range	200-900 nm	200-1300 nm
Temporal resolution (min.)	1.5 ns	Integrated ($\sim$ ms)
Pixel size	15 μm $\times$ 15 μm (calibrated)	4.4 μm $\times$ 4.4 μm (calibrated)
Active area	15.4 mm $\times$ 15.4 mm (calibrated)	7 mm $\times$ 6 mm
Frame rate	0.8 Hz	10 Hz

Calibration of ICCD: The important requirement for imaging diagnostics is in-situ calibration of camera and probe beam. The calibration of ICCD is required to provide quantitative information about the size, position and geometry of the plasma plume and shock waves. A standard graph paper with 5 mm lines is used for mapping of spatial position of the plasma plume and shock wave position to the camera pixels so that the plasma plume and shock wave front positions can be accurately determined. Figure 2.6

(c,d) shows the image acquired using ICCD camera by placing a graph sheet perpendicular to the probe beam at the location of plasma formation. The calibration is performed again if any of the components i.e., mirrors, lens system is modified/aligned. The calibrated ICCD shadowgraphy images are further analysed using self-written *Matlab*® program to obtain the position of shock wave front and plasma contact front.

2.4 Experimental configurations

This section gives the experimental details such as experimental schematics, technical values used for imaging detectors and sample targets used in the thesis work.

2.4.1 Double pulse configuration

The double pulse configuration has divided into four geometric configuration depending on direction and sequence of laser beams [1]. They are: (a) collinear geometry, in which both the laser pulses (pre pulse, main pulse) are propagates along same optical path and interacts with sample (b) orthogonal geometry, in which one laser pulse creates sample plasma and another laser pulse is parallel to sample surface which reheats the plasma (c) cross beam geometry or a quasi-collinear geometrical configuration, in which two laser pulses irradiates the sample surface at an angle (d) counter propagating geometry, in which both pulses propagate collinear and interacts with sample at 180^o. Since the studies of two plasma interaction in counter propagating geometry in ambient air are very rare due to difficulty in experimental set up, we have studied the temporal and spatial dynamics of interaction of two counter propagating laser induced plasmas and shock waves using double pulse configuration as shown in Figure 2.7. This study revealed the role of separation distance and energy ratios between two plasma sources on the interaction along with the effect of the propagation of shock waves through interaction zone.

The second harmonic beam (532nm) of Nd: YAG Laser (INNOLAS SPITLIGHT 1200, 7 ns, 10 Hz repetition rate) of 8 mm diameter is propagated through an attenuator, which consists of half wave plate (HWP) and Brewster polariser (BP) (Figure 2.7). The p-polarised laser beam is propagated through beam splitters (BS), which divides the input laser beam into two coherent beams with equal or different energies. The two beams are focused using plano-convex lenses of equal focal length (L1 = L2 $\approx$ 75 mm) in f/#9 geometry to get two collinear, counter-propagating plasma sources around the respective focal planes with $140 \pm 10\mu$m in ambient air. The optical path between two laser beams are adjusted with the help of harmonic mirrors (M1, M2.... M9) to achieve zero delay between two laser pulses. The He-Ne probe beam is expanded and collimated to 33 mm diameter using a beam expander (3X) along with a lens system (L3 =50 mm, L4=1000 mm). The probe beam passes through the plasma perpendicularly, the beam will be refracted by a region with high density gradients or absorbed by dense plasma plume particulates, leading to the shadowgraphy images and can be visualized by loosely

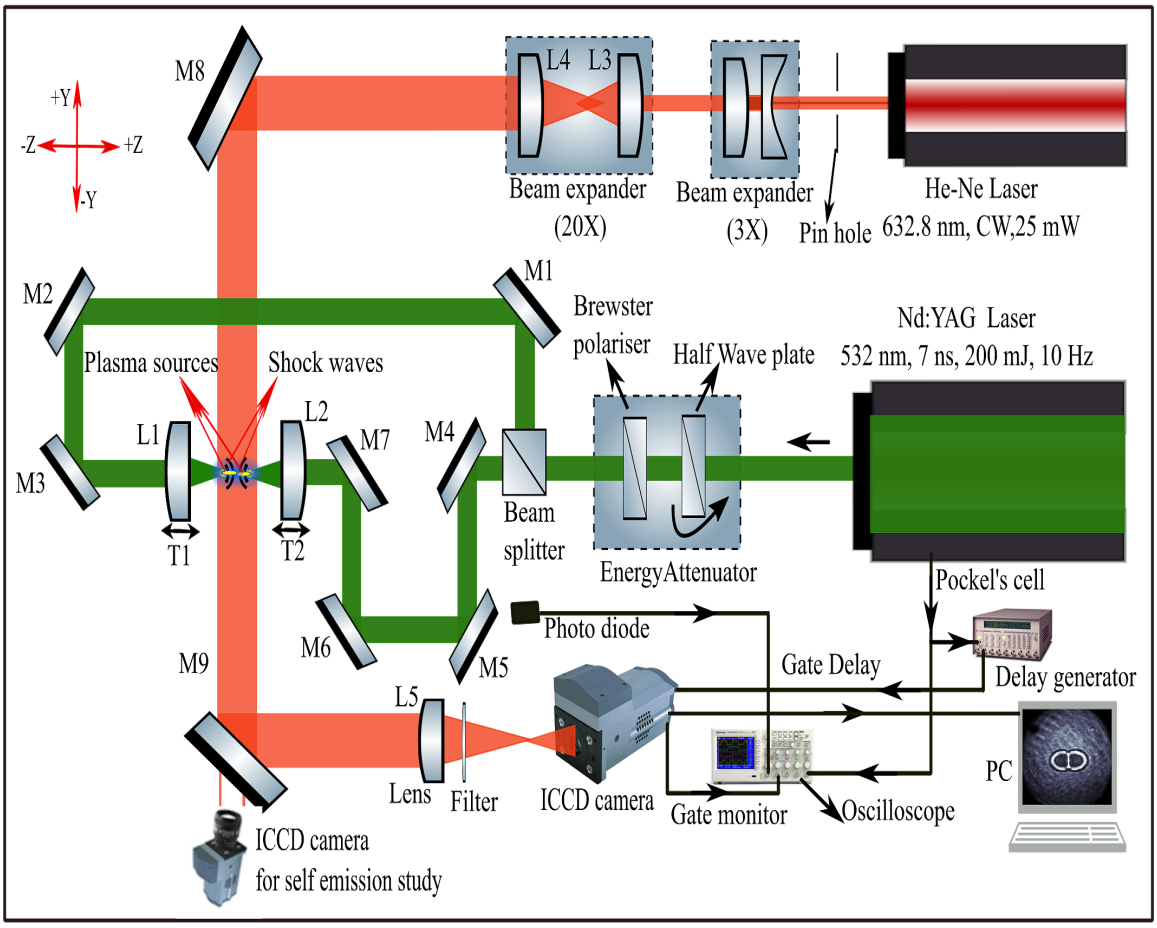

Figure. 2.7 Experimental schematic used for the interaction of two counter propagating laser induced plasma and shock waves in air (double pulse configuration).

focusing the probe beam on to ICCD detector using 200 mm lens (L5). The energy of the plasma source S1 is kept constant at 25±0.5 mJ in all cases, while the energy of the source S2 is varied as 25 ± 0.4 mJ, 41±1.2 mJ and 92±1.5 mJ using the beam splitters with R:T = 50:50, 40:60 and 20:80 respectively. The ICCD camera is synchronized with the pockel cell (PC) of the Nd:YAG laser with the help of a external delay generator (SRS DDG 645). For 2D emission images, the camera (CCD/ICCD) is placed perpendicular to the both plasma sources or in the probe beam path (in the absence of the probe beam) as shown in experimental schematic. The CCD camera will give the time integrated radiation emissions from both the plasma sources. The ICCD camera along with a Nikon 85 mm f/1.4D infinity corrected zoom lens is used for capturing the temporal evolution of the radiative emissions from both the plasma sources. The captured 2D emission images using ICCD and CCD camera are given in Chapter 3.

2.4.2 Single pulse configuration

The spatio temporal evolution of laser induced blow off (LIBO) studies of metals and polymer thin films (Chapter 4), spatial confinement of laser induced air plasma (Chapter

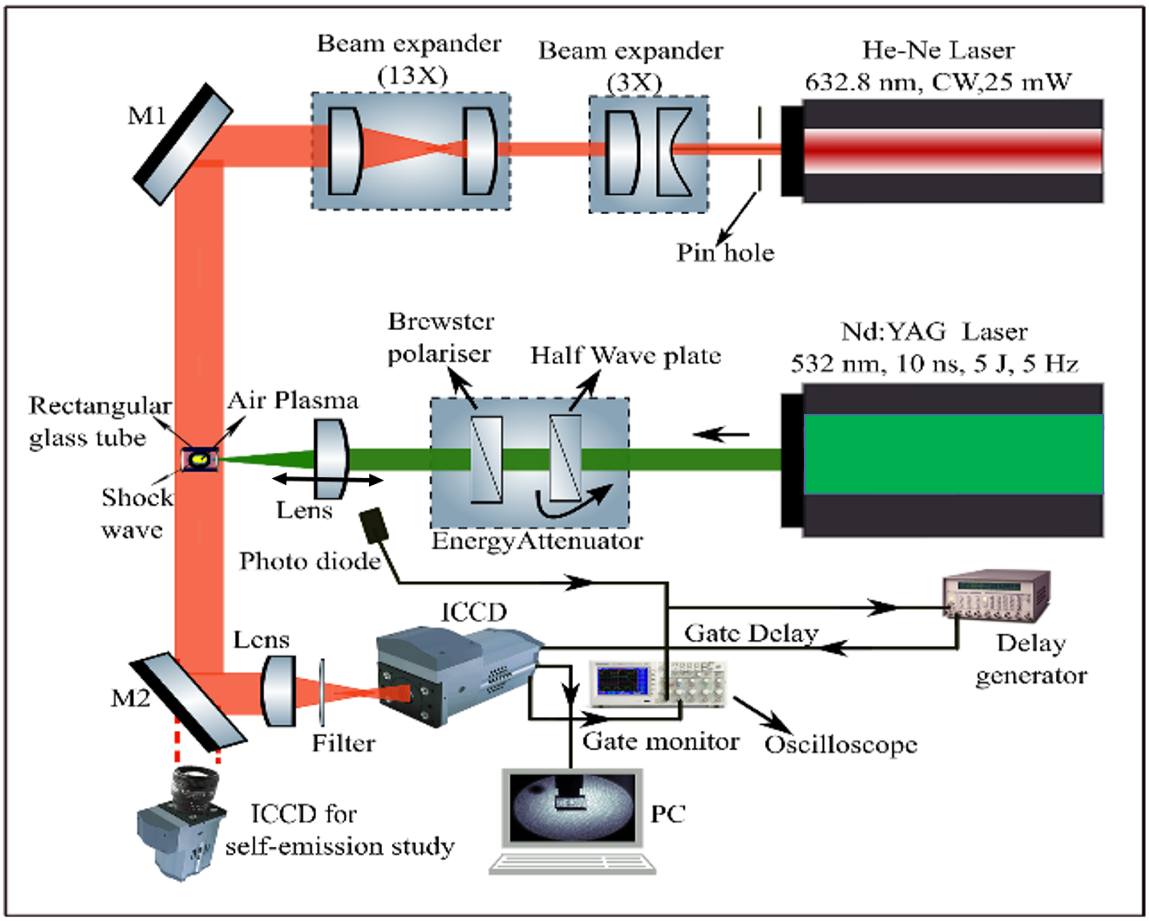

Figure. 2.8 Experimental schematic used for single laser pulse ablation configuration in Chapters 4, 5 and 6.

5) and laser ablation of BK-7 glass (Chapter 6) is studied using the single pulse configuration. Figure 2.8 shows the experimental schematic used in the single pulse configuration for Chapters 4, 5 and 6, which consists of a high power Nd:YAG laser system (TITAN-5, 532 nm, 10 ns, 5 J, 5 Hz) used for the ablation of the target sample. The second harmonic pulses of 10 ns pulse width are propagated through an attenuator (consists of HWP and BP), from which laser pulses with s-polarisation are focused using a 150 mm plano-convex lens in f/#7 geometry with $500\pm50\mu$m focal spot size. The systematic shifting of the laser focal plane from F0 to F2 (upto 6 mm) is achieved using a manually controlled translation stage. The He-Ne probe beam is expanded and collimated to 47 mm diameter with the help of a beam expander (3X) and lens system (L2=50 mm, L3= 650 mm), which passes through the plasma focused on to the ICCD camera using a 200 mm lens (L4). The ICCD camera was triggered using a photo diode (DET 10 A, 1 ns rise time, Thor Labs) signal with the help of an SRS delay generator. The ICCD camera along with a Nikon 85 mm f/1.4D infinity corrected zoom lens is used for capturing the temporal evolution of the 2D plasma emissions from spatially confined air plasma as given in Chapter 5. The technical

details of the lasers, diagnostic instrument (camera) settings utilized in the experiments are summarized in Tables 2.3, 2.4.

Table 2.3 Specifications of different lasers used in the study

	Pump laser		**Probe laser**
	Nd:YAG	Nd:YAG	He-Ne
Model	SpitLight 1200[7]	TITAN-5[8]	25-LHP-828-230
Wavelength	532 nm	532 nm	632.8 nm
Pulse width(FWHM)	7± 1 ns	10±1 ns	CW
Beam profile	Gaussian	quasi Top-Hat	Gaussian
Beam diameter	10 mm	22 mm	33 mm, 47 mm
Polarization	p-polarized	s-polarised	p-polarized
Rep. rate (Hz)	0.8	1	-
Energy/Power	25-92 mJ	25-2000 mJ	25 mW
Intensity	23-85 GW/cm^2	1.2-100 GW/cm^2	-
Focusing geometry	f/9	f/7	-
Focal spot size	140 ±10 μm	500± 50μm	-

Table 2.4 Technical details of diagnostic tools used in the study

	ICCD	**CCD**
Model	Andor iStar DH-734U	Ophir-Spiricon: SP-620U
Temporal resolution	2 ns (shadowgraphy)	Integrated ($\sim$ ms)
	50 ns -15 μs (self-emission)	-
Gate delay	400 ns - 30 μs from t=0	-
Pixel size	15 μm × 15 μm (calibrated)	4.4 μm × 4.4 μm (calibrated)
Active area	15.4 mm × 15.4 mm (calibrated)	7 mm × 6 mm
Frame rate	0.8 Hz	10 Hz
Spatial calibration	20.19 ± 0.4 μm/pixel (defocused shadowgraphy)	14.6 ± 0.1 μm/pixel
	52.8 ± 0.4 μm/pixel (focused shadowgraphy)	
	89.55 ± 10 μm/pixel (self-emission study)	

2.5 Summary

In this chapter, the details of the laser sources, technical specifications of ICCD and CCD cameras, He-Ne probe beam and experimental schematics of shadowgraphy method developed to study the dynamics of plasma and shock wave in single pulse and double pulse configurations were presented. For the imaging processing technique, *Matlab*® software was used to obtain the position of expanding plasma and shock wave fronts.

References

[1] Y. Li, D. Tian, Y. Ding, G. Yang, K. Liu, C. Wang and X. Han, *A review of laser-induced breakdown spectroscopy signal enhancement*, Applied Spectroscopy Reviews, Vol. 53, No.1, 1-35 (2018).

[2] K. Ding and L. Ye, *Laser Shock Peening Performance and simulation*, Woodhead publishing Limited (2006).

[3] C. Phipps, M. Birkan, W. Bohn, H. A. Eckel, H. Horisawa, T. Lippert, M. Michaelis, Y. Rezunkov, A. Sasoh, W. Schall, S. Scharring and J. Sinko, *Review-Laser Ablation Propulsion*, Journal of Propulsion and Power 26 (4), 609-637 (2010).

[4] J. Thomas, Ph. D. thesis, Nirma University, India, 2020.

[5] G.S. Settles, *Schlieren and Shadowgraph Techniques: Visualizing Phenomena in Transparent Media*, Springer Berlin Heidelberg (2001).

[6] Ch. Leela, Ph. D. thesis, University of Hyderabad, India, 2014.

[7] SpitLight 1200 Nd:YAG laser, User's Manual, Innolas laser technologies (www.innolas-photonics.com).

[8] TITAN-5 high power Nd:YAG laser, User's Manual, Amplitude technologies (www.amplitude-laser.com/produit/titan).

[9] Basler camera software for vision monitoring, User's Manual (www.baslerweb.com/en/products/cameras)

[10] Ophir-Spiricon CCD camera, User's Manual, MKS-ophir technologies (www.ophiropt.com).

[11] Andor ICCD's, User's Manual, Andor Technology (www.andor.oxinst.com).

Chapter 3

Interaction of two counter propagating plasmas and shock waves in air

When two laser produced plasma sources interacted, the outcome results are: (i) the interpenetration of plasmas and/or, (ii) formation of stagnation layer at the collision front. The degree of interpenetration (or stagnation) is determined by collisionality parameter which is the ratio of the separation distance between individual single (seed) plasmas to the ion-ion mean-free path. Previous work on colliding plasmas in vacuum has shown that when stagnation layer is formed, they exhibit an enhancement in plasma emission with uniform spatial distribution of electron density, electron temperature along the stagnation layer. These characteristics of stagnation layer is of much interest to the laser research community, however the research has been done in vacuum only. Not only the study of interaction of colliding plasmas in ambient air are limited but the counter propagating interaction geometry is also very limited in the research field. In this chapter we present the interaction of two counter propagating laser induced colliding plasma plumes in ambient air produced by second harmonic of Nd:YAG laser pulses of 7 ns (FWHM) pulse width with the help of shadowgraphy imaging technique. The effect of separation distance (d) between the two plasma sources and their energy ratio on the interaction of two counter propagating plasma and shock waves is presented. The interaction dynamics of the two counter-propagating colliding plasma plumes and shock waves (SW) are compared with that of respective dynamics of single (seed) plasma source and shock waves to explicitly bring out the energy exchange between two plasma sources, the effect of the shock wave compression on the plasma Jet and plasma Jetlet evolution during the interaction.

3.1 Introduction

The study of two colliding plasma plumes interaction has attracted several researchers for past few decades from mid-1970's, covering both fundamental physics and some potential applications. The physical interactions and collisions between two or more plasma plumes can be useful to understand the design of indirect inertial confinement fusion (Hohlrums), X-ray laser research [1, 2, 3, 4], higher ionic temperature and charged particle acceleration using Thomson scattering in conjunction with proton radiography etc [5, 6]. These laser produced plasma plume interaction dynamics has also been used in understanding the Super novae remnants (SNR), the super novae (SNe) [7] to model and understand various astrophysical processes [8, 9]. On the other hand, low density colliding plasma plumes are useful in the minimization of re-condensation of ablated material to increase the efficiency of the pulsed laser deposition (PLD) process [10], the formation of molecules [11, 12, 13] and the formation of nano particles [14]. To understand the collision of two plasma plumes in vacuum different target combinations were utilized. The popular geometries are collinear, crossed and orthogonal configurations [15, 16, 17, 18, 19, 20] with different shaped samples (flat targets or wedge-shaped targets) to create collinear or counter-propagating plasma plumes.

The initial research on colliding plumes were performed by Rumsby et. al. [15] in 1974, where they investigated the two carbon plasma plumes generated next to each other on flat surface colliding in lateral direction. Photon scattering techniques and time integrated photographs were used to study the expansion dynamics and plasma parameters from the interaction region for different plume separations. The 1D multi-fluid hydrodynamics model developed by Rambo and Denavit [16] standardized a single parameter to study the transition regime between stagnation and interpenetration of colliding plumes. The parameter is known as *collisionality parameter (ζ)* and was expressed by [15, 16, 17]:

$$\zeta = \frac{D}{\lambda_{ii}} \tag{3.1}$$

Where D is distance between two seed plasmas, λ_{ii} is the ion-ion mean-free path (mfp) which is defined as [16]:

$$\lambda_{ii}(1 \rightarrow 2) = \frac{m_i^2 v_{12}^4}{4\pi q^4 Z^4 n_i ln\Lambda_{1\rightarrow 2}} \tag{3.2}$$

Where m_i is the ion mass, v_{12} is the relative plasma velocity between two seed plasmas, q is the elementary charge, Z is the average ionisation state of the plasma, n_i is the plasma density at the collision plane (all in SI units) and $\ln\Lambda_{1\rightarrow 2}$ is the Coulomb logarithm, which is unit-less and generally between 5 and 10 for laser produced plasmas (LPP) [17].

Coulomb logarithm depends on :

$$ln\Lambda = ln(\frac{\lambda_D}{l_{min}}) \tag{3.3}$$

Where λ_D is the Debye length of the plasma and is defined as:

$$\lambda_D = \sqrt{\frac{\epsilon_0 k_B T}{n_e e^2}} \tag{3.4}$$

Where ϵ_0 is the permittivity of free space, k_B is Boltzmann's constant, T is the plasma temperature and e is the electron charge. l_{min} is the minimum impact parameter, defined as the classical distance of closest approach between an electron and an ion. The parameter l_{min} is defined as $l_{min} = k_B T_e / Ze^2$, where T_e is the electron temperature of the plasma. The interaction of two expanding plasma plumes may be either collision dominated or collision-less type. In collision-less plasmas, the collective interactions play an extremely important role in the plasma [15, 18, 19, 20]. For example, the excitation of collective electron motions can explain the damping of shock waves in a collision-less plasma. In collision dominated plasmas case, when two expanding plasmas are colliding two extreme cases may occur: stagnation or interpenetration.

The interaction of colliding plasma plumes at the interaction zone will depend on the collisionality parameter (ζ), which in turn depends on the relative velocity between two seed plasma sources and the ion-ion mean free path (mfp) (Eq.3.1) [15, 16, 17]. If the ion-ion mean free path is longer than the separation distance between two plasmas, in other words, if the two seed plasmas have a large relative velocity and low density at the interaction zone the plasma plumes will try to interpenetrates. It is known as **soft stagnation layer** and the binary coulomb collision between plasma constituents (ions) in each seed plasma, drives the heating processes to occur. If the ion-ion mean free path is smaller than the separation distance between two plasmas, in other words, if the relative velocities between the plasmas is small, the plasma interpenetration is relatively small and plasma constituents will tend to decelerate abruptly at the interaction zone and the interaction is dominated by collisions between ionic species from each of the opposing seed plasmas resulting in a build-up of plasma mass density. As time progresses this plasma mass density material will be compressed by other plasma mass density giving rise to a region of increased temperature and density, called as **Hard stagnation layer**. The stagnation layer formed in colliding plasma plumes in vacuum has an increase in the duration of optical emissions compared to the case of a single plasma plume; uniform spatial distribution of ions and atoms; and an enhanced line emission intensity. The properties of a stagnation layer depend on the collisionality parameter, which in turn is dependent on the target geometry and the seed plasma properties. By controlling the properties of the seed plasmas the stagnation layer can effectively be tuned for shape, ionization balance, electron temperature and electron density. The Table 3.1 summarizes the brief history of

Table 3.1 Experimental and Numerical work on laser produced colliding plasma plumes

Author	**Experimental/ Theoretical details**	**Diagnostics**
Rumsby [15]	Nd:glass laser, 45 ns, 4.5 J	Photon scattering & integrated photography
Rambo [16]	1D-Mutli fluid simulations	Collision parameter (ζ) defined defined
Rambo [21]	MC-PIC simulations	Multi-fluid collisional coupling coefficients defined
Rancu [22]	Nd:glass laser, 0.53 μm, 600 ps, ∼20 J	X-ray spectrography
Harilal [23]	Ruby laser, 0.69 μm, 15 ns, 6 J	XUV pinhole photography & spectroscopy
Zhang [24]	Nd:YAG, 1.06 μm,7 ns, 160 mJ	Interferometry
Dardis [25]	Nd:YAG, 1.06 μm, 170± 20 ps, 200 mJ	Optical Emission Spectrography (OES) & fast imaging
Hough [19]	Nd:YAG, 1.06 μm, 6 ns, 600 mJ	OES and fast imaging
Harilal [26]	Nd:YAG, 1.06 μm, 6 ns, 140 mJ	OES and fast imaging
Ross [27]	OMEGA laser, 0.35 μm, 1 ns, 500 J	Thomson scattering
Sanchez-Ake [28]	Nd:YAG, 1.06 μm, 8 ns, 50 mJ, KrF, 0.24 μm, 30 ns, 150 mJ	OES and fast imaging
Gambino [29]	Nd:YAG, 1.06 μm, 6 ns, 800 mJ	OES, fast Imaging and langmuir probe
Gupta [14]	Nd:YAG, 1.06 μm, 8 ns, ∼ 50 mJ	OES and fast Imaging
Cummins [30]	Nd:YAG, 1.06 μm, 7 ns, 650 mJ	OES and time integrated Imaging
Yang [31]	Nd:YAG, 1.06 μm, 15 ns, 15 mJ	Shadowgraphy, Schlieren and Interferometry
Bupesh [32]	Nd:YAG, 1.06 μm, 10 ns, ∼ 30 mJ	OES and fast Imaging
Zastrau [33]	MEC laser @ SLAC, 0.52 μm, 5 ns, ∼ 6 ±1 J	X-ray scattering and MULTI 2D simulations
Alamgir [34]	ND:YAG, 1.06 μm,8 ns, ∼ 100 mJ	OES and fast Imaging

previous experimental and Numerical work on colliding plasma plumes in vacuum and air with different target geometries. The interaction of colliding plumes have been studied by spectroscopic, fast photography (imaging) [15, 35] and laser interferometry methods [19]. Rumsby et. al. [15] proposed models to explain the interaction of colliding plasmas based on the classical ion-ion collision interactions in high density plasma (at initial time scales) and electron-electron or electron-ion collision interactions for low density plasma (at latter time scales). Experimentally they measured density and temperatures of initial and latter plasmas using photon scattering. Rambo et. al. [16] investigated the two colliding plasma plumes using single fluid and multi fluid models and studied double foil configuration experimentally to improve X-ray laser performance. Dardis et. al. [25] characterized the stagnation layer in terms of collisional geometry and elemental composition using optical emission spectroscopy. Harilal et. al., [26] investigated experimentally the jet formation in laterally colliding plasma plumes and concluded that the plasma life time and spatial expansion of plasma is enhanced in colliding plasma than single plasma. Theoretically, Sizyuk et al. [12] confirmed the jet formation due to colliding plasma. Most of the researchers studied the interaction of laterally (radially) expanding plasma plumes [11, 12, 13, 14, 15, 16, 17, 18, 19, 20, 21, 22] while the laser beams were propagating along Z-axis. Lim et al. [36] reported the instability and reconnection leading to fundamental changes in the topology of flows and their variation with Reynolds number in the head on collision of two vortex fluid rings. Gupta et. al. [14] reported the interaction of collinearly expanding ZnO plumes and compared the spectroscopic properties of colliding plumes with that of from a single plume. A one to one correlation between spectroscopic signal and fast imaging was demonstrated concluding that though the temporal evolution of electron density is similar in both the cases the temperature is high for colliding plumes than that of from a single source. Bupesh Kumar et. al. [32], investigated the shock-shock interaction in laterally colliding laser blow off plumes. But all of these studies are done in vacuum with different target geometries and different seed plasma properties.

The temporal expansion dynamics of a laser-produced plasma in ambient gas is very different to that of a plasma expanding in vacuum. The laser Ablation into a gas results in shock waves and expansion fronts as well as plume splitting, plasma rolling and sharpening effects that are not seen in vacuum. Very little work has been done on the expansion on the interaction of colliding plasmas in ambient air. Two studies can be highlighted: Zhang et. al. [24] reported the colliding plasma plumes in air, where the seed plasmas are formed by tilting the laser focusing lens to create spherical aberration. Due to the interaction of two laterally colliding shock waves, background gas stagnation layer was formed which enhanced the gas density as well as the electron density also. Yang et. al. [31] also reported the background gas stagnation due to the shock waves interaction. After the interaction, both the shock waves are reflected from the interaction zone and

propagated along opposite to laser direction. Due to transfer of energy from seed plasmas to the shock waves at initial time scales, causing them (both plasma sources) not to have enough kinetic energy and thermal motion. However other work by Sánchez-Aké [28] is also worth noting that, they reported the electric signal based on the external electric field perturbation for different geometries and separation between plasmas. In view of the availability of limited studies on the interaction of plasma plumes in ambient air, the interaction of two counter propagating laser induced plasma plumes and the shock waves in air created by a second harmonic of Nd:YAG laser pulses of 7 ns pulse width is presented in this chapter. Since the interaction of colliding plumes at the interaction zone will depend on the collisionality parameter (ζ), the collisionality parameter can be changed experimentally by two important ways: (i) changing the separation between the seed plasmas, (ii) changing the particle number density in the seed plasmas by varying the laser energy. So, the effect of (i) separation distance 'd' between two plasma sources and (ii) the input laser pulse energies that created the seed plasmas, on the interaction dynamics of two counter propagating plasma plumes is presented. The separation distance 'd' is varied from 0 – 6 mm and the input laser energies are varied in the ratio of 1:1, 1:1.7, 1:3.7. This mimic the collision of fluids with varying impedances $Z_{S1} \approx Z_{S2}$, $Z_{S1} < Z_{S2}$ where $Z = \rho u$ is the impedance due to the plasma sources with 'ρ' being the plasma density and 'u' the velocity of the plasma in the medium.

3.2 Experimental Details

The detailed experimental schematic for the interaction of two counter-propagating plasma plumes in air is described in chapter 2. The second harmonic (532 nm) of *Nd: YAG* Laser beam of 7 ns (FWHM) pulse width and 8 mm diameter is divided into two beams of different energies using beam splitters of different Reflection and Transmission *(R:T)* ratios. The two beams are focused using Plano-convex lenses of equal focal length (L1 = L2 ≈ 75 mm) to get two collinear counter-propagating plasma sources of different energies deposited around their respective focal planes in ambient air. The two seed plasma sources are represented by S1, S2 and their corresponding shock fronts by SF1, SF2 and plasma outer regions (or contact fronts) by POR1, POR2 respectively. Since the interaction zone will depend on the collisionality parameter (ζ), we have changed collisionality parameter by (i) changing the separation between the seed plasmas, (ii) changing the particle number density in the seed plasmas by varying the laser energy. The energy of the laser pulse creating the plasma source S1 is kept constant at 25 ± 0.5 mJ in all cases, while the energy of the laser pulse creating the source S2 is varied as 25 ± 0.4 mJ, 41 ±1.2 mJ and 92 ± 1.5 mJ with corresponding intensities ∼ 2.3 - 8.5 × 10^{10} W/cm^2 using the beam splitters with R:T::50:50, R:T::40:60 and R:T::20:80 respectively. The energy of the two laser pulses measured before the focusing lenses (L1 & L2) having energy ratios 1:1, 1:1.7 and 1:3.7 creates two plasma sources which resembles two media with

different impedances i.e., $Z = \rho u$; where $'\rho'$ is the density of the plasma and $'u'$ is the shock velocity. The optical path lengths travelled by the counter-propagating beams is made equal before focusing to ensure that both the pulses arrive at same time at their respective focal planes to generate breakdown of atmospheric air creating the expanding plasmas. The separation distance 'd' between two plasma plumes is varied systematically by using translational stages (T1 & T2), which moves the focusing lenses (L1 & L2) in equal distance from the focal plane of both the lenses. The two plasma sources overlapped spatially at d=0 mm (i.e., the point where the focal plane of two lenses coincide) as shown in Figure 3.1(a-c). At d=0 mm, though two plasma sources are present, it looks almost similar to that of a single source. The interaction dynamics of the colliding plasmas is imaged through the defocused shadowgraphy technique [27, 28, 29] by using an *ICCD* camera with *1.5 ns* temporal resolution.

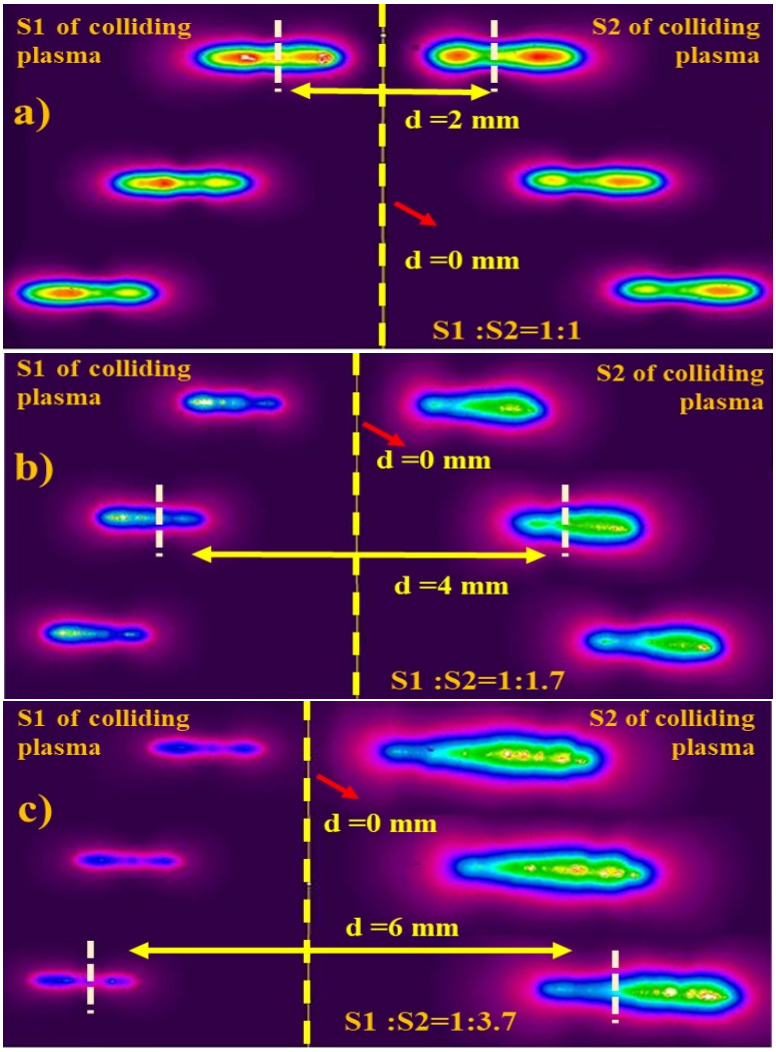

Figure. 3.1 Time integrated CCD images of two counter-propagating colliding plumes with varying separation distance 'd' and for energy ratio (a) S1:S2=1:1 (b) S1:S2=1:1.7 (c) S1:S2=1:3.7

3.3 Time integrated imaging of the two counter propagating plasma plumes collision

The time integrated images captured using CCD (Ophir Spiricon SP 620U) camera are shown in Figure 3.1 for different impedance ratios with varying separation distance (d). From the CCD images, we can visualize the spatial evolution of the plasma systematically, with the variation of separation distance (d) from the d=0 mm line. Although S1 is kept at constant energy, the intensity profile of S1 is observed to change from image to image (Figure 3.1 (a-c)) as more optical density filters were used to avoid saturation of CCD due to high energy of S2. The two bright spots appearing around S1 and S2 are due to the asymmetric laser energy deposition at the focal volume. The breakdown of the air medium happens during the leading edge of the laser pulse and the trailing edge interacts with the air plasma (since sufficient free electrons are available at this point). As a result, the plasma front moves continuously towards the lens until the termination of the laser pulse, leading to an asymmetric energy deposition [37, 38]. The plasma temperature, pressure and mass densities in these regions (in two spots) forms localized hot spots in the plasma region, which lead to the hydrodynamic instabilities [39, 40, 41].

3.4 Fast imaging of the collision of two counter propagating plasma plumes with different energy ratios

The interaction of the two colliding plasma plumes with different energy ratios with separation distance d= 4 mm is visualized using the self emission study using ICCD fast imaging. Figure 3.2 (a-d) shows the temporal evolution of the plasma self emission (2D emission) from from a single source at 25 mJ (first column) compared to two counter-propagating laser induced plasma sources of separation distance (d=4 mm) with energy ratios S1:S2=1:1 in the second column, S1:S2=1:1.7 in the third column and S1:S2=1:3.7 in the fourth column at t=2, 6, 10, 14, 18, 22, 26, 30, and 50 μs, respectively. The vertical lines in the second, third and the fourth columns represent d=0. For self emission study the Andor ICCD camera along with Nikon 85 mm f/1.4D infinity corrected zoom lens is used to image the collision of the two plasma plumes for delays 400 ns to 50 μs with a step size of 400 ns. The gate width (2 ns to 15 μs) and gain (100 to 250) of the ICCD camera is adjusted such that we get a proper image of the colliding plasma plumes.

From the Figure 3.2 (a), it is evident that the single plasma source (S1=25 mJ) evolution morphology is an oblate at initial time scales < 3 μs and it is becomes spherical around $\sim$ 10 μs and becomes prolate at later time scales > 10 μs. The same behaviour is observed in the case of the colliding plasma plumes until the discontinuity or jetlet evolution observed as shown in Figure 3.2 (b-d). In the case of equal energy, we have not observed plasma

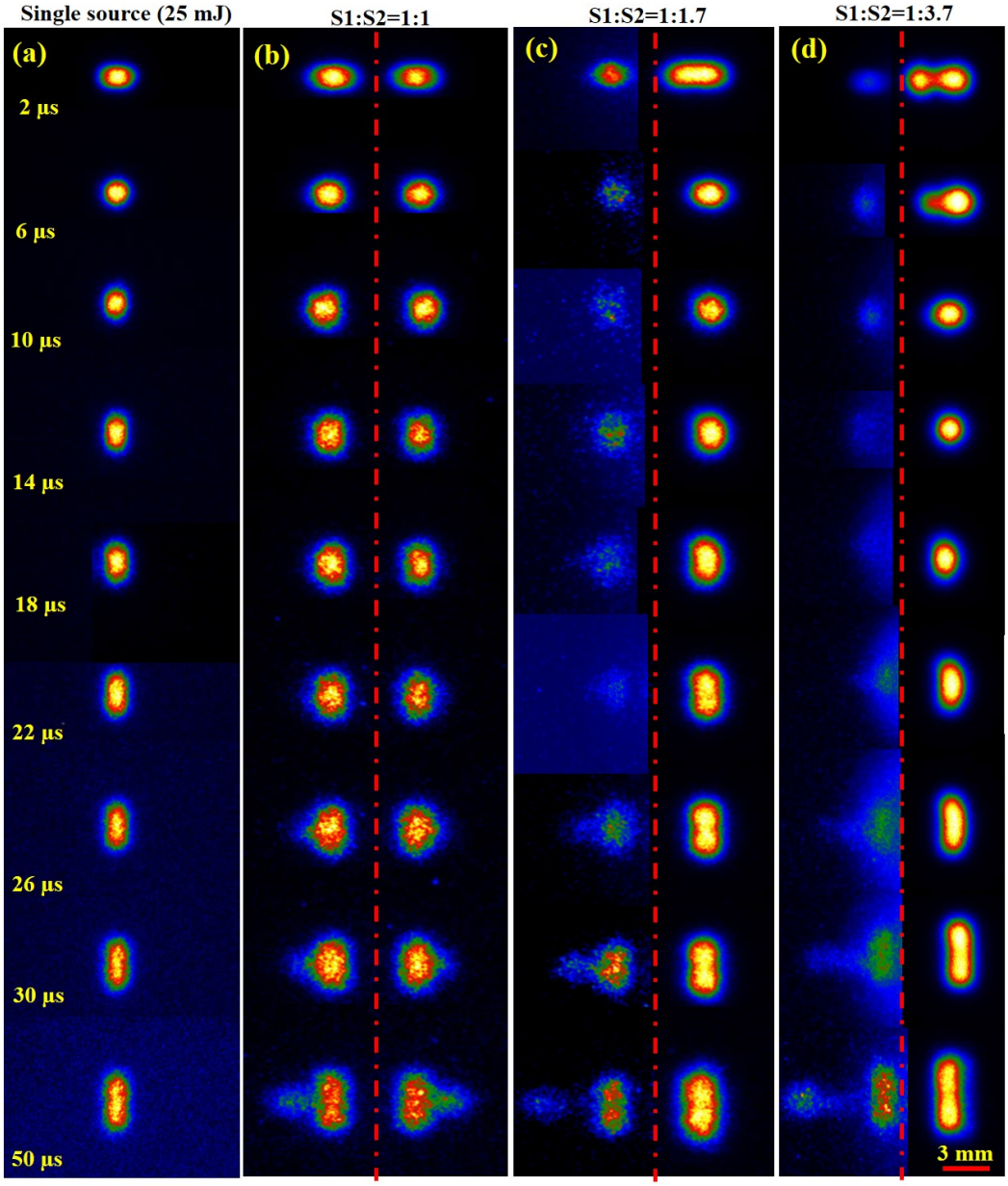

Figure. 3.2 Temporal evolution of 2D emissions from (a) a single source at 25 mJ compared to two counter-propagating laser induced plasma sources of separation distance (d=4 mm) with different energy ratios (b) S1:S2=1:1 (c) S1:S2=1:1.7 (d) S1:S2=1:3.7 respectively.

jetlet formation until the time scales used in this chapter i.e., 30 μs but beyond 30 μs we have observed the jetlet formation from both the sources as shown in Figure 3.2(b). This is due to collision of plasma plumes in the counter propagating direction and the resultant line of force acts along 180^o to the collision plane of the both sources [42]. In the case of the unequal energy ratio sources collision, due to the higher energy of the plasma source S2, the self emission from the S1 plasma sources is fainted In the case

of the S1:S2=1:3.7 energy ratio, it is more evident. To overcome this problem, we have done image processing of the captured images to enhance the self emission intensity as shown in Figure 3.2 (c-d). The images towards left of the vertically dotted line shows the processed images using Andor ICCD camera software (*Solis*®). From the Figure 3.2 (c-d), the plasma jetlet evolution is observed due to discontinuity created by the collision of the two unequal energy ratio plasma sources (S1:S2=1:1.7, 1:3.7). The plasma jetlet evolution is observed more prominent after 10 μs only and it is higher for S1:S2=1:3.7 energy ratio than S1:S2=1:1.7 case. At longer time scales, we can observe the plasma jetlet in the shape of a bubble. This study confirms the plasma jetlet formation from the low energy plasma source (S1) due effect of the other plasma source S2. The reason behind the plasma jetlet formation and its evolution is revealed by the shadowgraphy imaging of the collision two counter propagating plasma sources, which is discussed in the next section (Section 3.5). From the captured self emission images of the individual plasma sources as well as the collinearly interacting two counter-propagating plasma sources, we have calculated plasma properties like diameter, length of individual S1 and S2 for all input laser energy ratios. The FWHM of the line profiles of the plasma sources (from ICCD images) along the laser axis and the radial direction at 1 μs are taken as the plasma length and plasma diameter, respectively. Table 3.2 summarizes the plasma dimensions for each input laser energy ratio used in the study. The values are the average of plasma dimensions at each separation distance (d). No significant variation in the plasma length and diameter were observed with the separation distance 'd'.

Table 3.2 Plasma dimensions of S1 and S2 for different input energy ratios from 2D emission images captured using ICCD at a delay 1 μs.

Input Energy (mJ)	**Absorbed Energy** (mJ) (in %)	**Input Energy Ratio**	**Absorbed Energy Ratio**	**Plasma Length** (mm)	**Plasma Diameter** (mm)
25±0.4	12±1 (∼48)	1:1	1:1	1.46±0.2	1.09±0.05
41±1.2	22.5±1 (∼55)	1:1.7	1:1.9	2.26±0.2	1.16±0.05
92±1.5	59±1 (∼64)	1:3.7	1:4.9	3.41±0.2	1.23±0.05

From Table 3.2, the plasma length, diameter of S1 and S2 were observed to vary between 1.46 – 3.41 mm and 1.09 - 1.23 mm, respectively, with increasing the energy. Based on the minimum length of each plasma source, the interaction dynamics are further divided into interaction of closely separated sources (d $\leq$ 2 mm), interaction of well separated sources (d=4 mm) and interaction of far separated sources (d$\geq$ 6 mm). The evolution dynamics of the individual sources are labelled as: "*S1 single*" and "*S2 single*", while counter-propagating colliding plumes are labelled as: "*S1 of colliding plasma*" and "*S2 of colliding plasma*", respectively. The interaction of colliding plumes in counter-propagation

geometry is studied and compared along ± Z, ± Y directions to understand the effect of varying impedance ratio and the separation distance (d) between two plasma sources on the collision geometry.

3.5 Shadowgraphy imaging of the two counter propagating plasma plumes collision

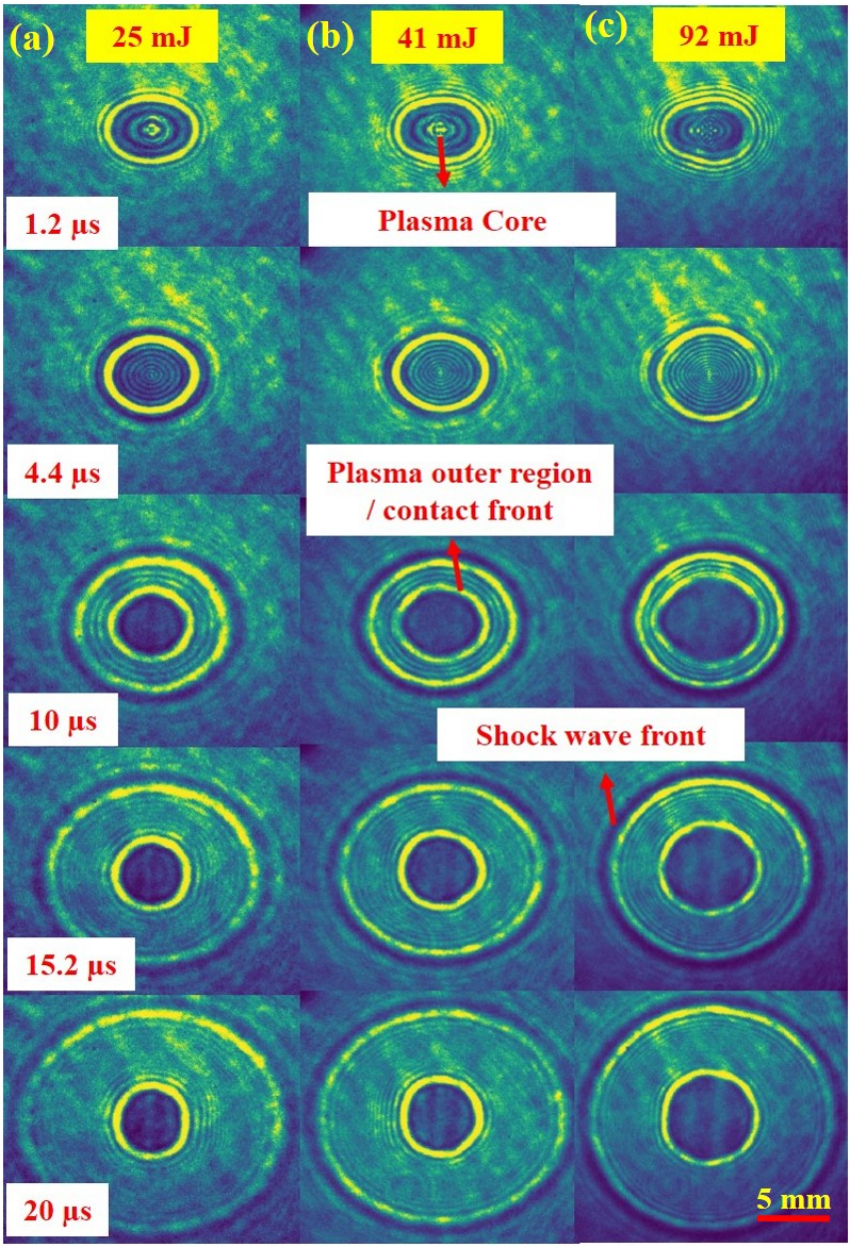

Figure. 3.3 Temporal evolution of single plasma source with varying energy (a) 25 mJ (b) 41 mJ (c) 92 mJ

The interaction dynamics are divided into two parts: the interaction of equal energy plasma sources (S1:S2 ≈ 1:1) and unequal energy sources (S1:S2 ≈ 1:1.7, 1:3.7). For both

the cases, the interaction dynamics are studied as a function of separation between the seed plasma sources. The properties of these two colliding plasma sources are compared with single plasma sources generated individually with their corresponding laser energy. The evolution of plasma and the associated shock wave of the individual single plasma (S1) are captured by blocking the other source (S2) and vice-versa. The shadowgraphy images of single source for different laser energies are shown in Figure 3.3. The evolution dynamics of Plasma Core (PC), Plasma Outer Region (POR) or Contact Front (CF) and Shock Wave Fronts (SF) from single source are explained by our earlier work [39, 40, 41, 43].

The seed plasma sources have the average temperature of $\sim$ 15000 K, where the ionized air will have both neutral N and O atoms and their respective singly ionized species of N^+ and O^+. The ratio of neutral atoms to the singly ionized species in the air composition is $\sim$2.93 and 4.77, respectively [38]. Hence the electron-ion (e-i) and electron-neutral (e-n) interactions will play a crucial role in the plasma dynamics. The plasma front mass density (ρ) and its speed (U_{plasma}) during the early times (100 - 500 ns) have been estimated from 2D-radiation hydrodynamic simulations considering the inverse Bremsstrahlung (IB) coefficient due to e-i and e-n interactions for the laser absorption in the focal volume while arriving at the temporal behaviour of the electron temperature and density [40, 41]. For the laser input energies 25, 41 and 92 mJ, the values are found to be varying between $\sim$ 4.3 – 3.0 kg/m^3 and 8.2 – 2.8 km/s, 9.1 – 3.0 km/s, and 11 – 3.3 km/s, respectively. The impedance $Z = \rho U_{plasma}$, during these time scales (100-500 ns) were found to be between 2.6 – 1.1 $\times 10^4$, 2.7 – 1.2 $\times 10^4$ and 3.3 – 1.4 $\times 10^4$ kg/$m^2 s$, respectively for 25, 41 and 92 mJ. This clearly shows that the plasma impedance increases with increasing input laser energy. Hence, the two plasmas formed in the energy ratios 1:1.7 and 1:3.7 will have different impedances when they interact with each other. In our study the plasma interaction happens on the time scales > 2 μs. At this time scale the shock wave starts to detach from the plasma. This leads to the oscillatory behaviour of plasma, analogous to that of cavitation bubble following Rayleigh-Plasset equation with the pressure gradient between the plasma and the ambient atmospheric air as the source term [39]. In the interaction of two colliding plumes, the electron mean free path (*mfp*) plays an important role at early time scales for formation of stagnation layer. The *mfp* in ambient air is given by the relation, $l(cm) = (kT)^2/(ne^4 ln\Lambda)$, which depends on plasma temperature, number density, and Coulomb logarithm. As the temperature increases, the number of free electrons increases and the *mfp* is predominantly controlled by the temperature of the plasma. The decrease in the *mfp* length signifies the increase in number of collisions [38]. The *mfp* for electrons in ambient air is $\sim$ 6 microns, which is well within the focal volume of the laser beam. According to the recombination model [44], the loss of plasma by recombination is proportional to the product of electron and ion number densities. After the plasma density becomes lower than its initial value, it decays reciprocally with time.

At the input laser intensities used in our work, the number of charged species and their velocities in the under dense plasma are relatively lower and making the collision of charge particle-neutral dominant. In the atmospheric plasmas, the oscillating charged species, colliding with neutrals of mass almost closer to that of the ions, result in emissions of RF frequencies over MHz range, that are closer to the ion plasma frequencies [45]. These collisions depend on the initial plasma parameters like temperature and density, and in turn vary the pressure gradient between the plasma leading to the onset of cavitation bubble-like dynamics that sustain up to 30 μs. The plasma core of the laser induced breakdown (LIB) plasma in ambient atmosphere is observed to sustain up to 4-5 μs and once the shock wave detaches from the plasma, it is observed to oscillate up to 200 μs for ns LIB [39, 46]. Though the plasma decays very quickly, the energy transferred to the ambient air leads to a hotter zone (contact front) that oscillates up to 30 μs.

3.6 Collision dynamics of two counter propagating plasma sources with separation distance (d) < 2 mm

When two laser pulses are focused at the same position i.e., d=0 mm or with separation of 1 mm (d=1 mm) between the two plasma sources, we have observed a merged colliding plasma source. Figure 3.4 (a-d) shows the shadowgrams of the temporal evolution of the two counter propagating plasma source interaction with separation distance (d)=1 mm for equal and unequal energy source ratios compared to the single plasma source (S1).

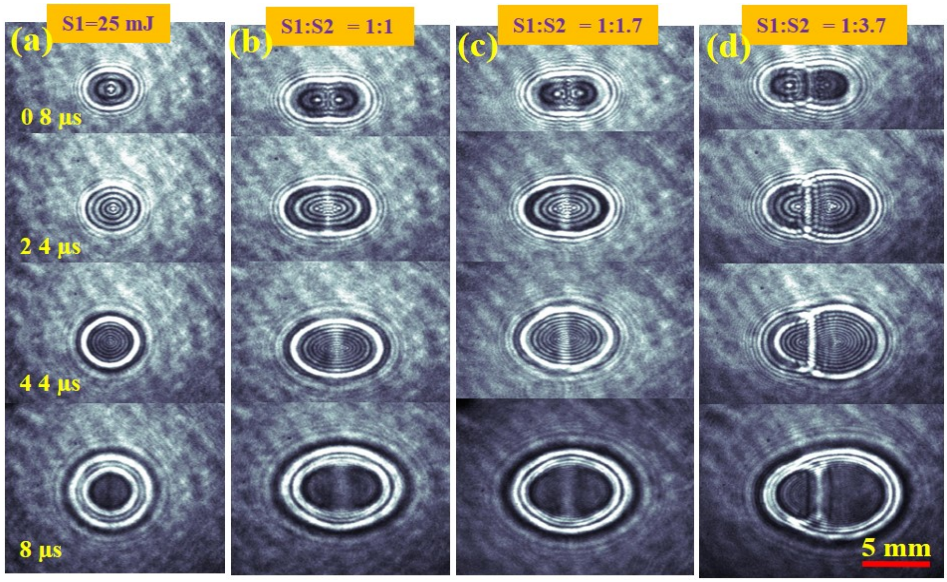

Figure. 3.4 Shadowgrams of the temporal evolution of the (a) single plasma S1 evolution; colliding plasma sources of (b) equal and (c-d) unequal energy ratios with d= 1 mm

From the Figure 3.4 it is evident that, we have not observed any stagnation layer because of complete overlap/merger of two plasma sources into one. The merged plasma source and its shock wave evolution is similar to the single plasma source evolution (S1/S2) except that the plasma morphology is elliptical in the case of colliding plasma plumes rather than spherical as in the case of single source (S1/S2). Figure 3.5 (a-h) shows the temporal evolution of the plasma contact front/PORs radius in the case of colliding plasma plumes with d=0, 1 mm for equal and unequal energy source ratios compared to the single plasma source S1 and S2 PORs radius.

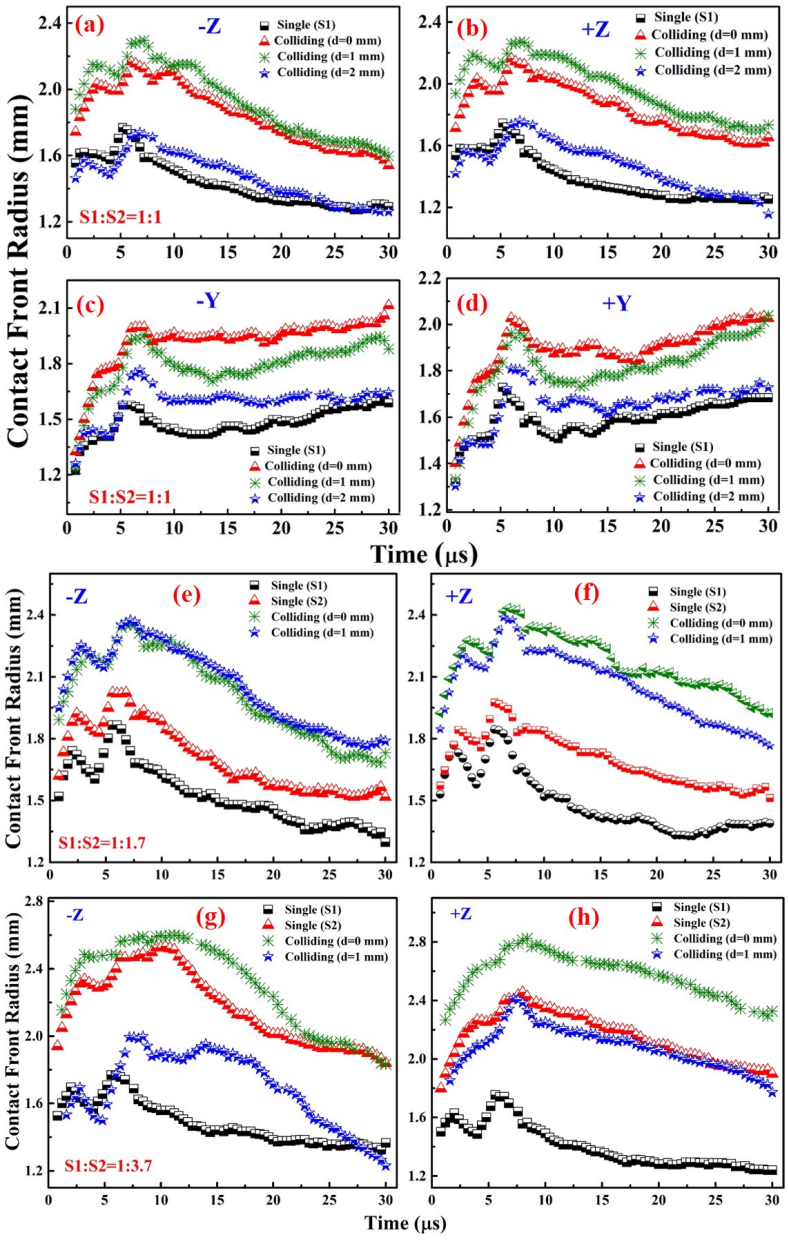

Figure. 3.5 The temporal evolution of the POR of the two counter-propagating colliding plumes with varying separation distance 'd' compared to the individual plasma sources (S1/S2) (a-d) S1:S2=1:1 (e-f) S1:S2 = 1:1.7 (g-h) S1:S2 = 1:3.7

Figure 3.5 (a-d) shows the temporal evolution of the plasma contact front (CF) radius value for d= 0, 1, 2 mm compared to the single plasma source S1 in the case of the equal energy ratio (S1:S2=1:1). From the observed data, it is evident that the CF/POR radius values are increased in all directions (± Z, ±Y) in the colliding plasma sources than single plasma source S1/S2, because of the laser deposited energy at the focal volume is doubled in the colliding sources that lead to the increment. The increment in the PORs radius value follows the trend: d=1 mm > d=0 mm > d=2 mm along ± Z direction while it follows d=0 mm > d=1 mm > d=2 mm along ± Y direction. So the plasma morphology is elliptical for collision of plasma plumes with d > 0 mm. Figure 3.5 (e-f) shows the temporal evolution of the plasma contact front radius for d= 0, 1 mm compared to the single plasma source S1 and S2 in the case of the unequal energy ratio 1:1.7 (S1:S2=1:1.7) along laser propagation direction (± Z). In this case, the POR radius of the colliding plasma plumes with d= 0, 1 mm are higher than the single plasma source S1 and S2 values. The increment in the PORs radius is almost similar for d=0,1 mm along -Z direction, but it is higher for d=0 mm than d= 1 mm along +Z direction when compared to S1 and S2 single sources.

Table 3.3 Maximum increment of plasma and shock wave properties in counter propagating colliding plumes along laser axis (the corresponding time scales are given in bracket)

S1:S2	***d***	**CF Radius (mm)**		**SF Velocity (km/s)**	
		-Z	*+Z*	*-Z*	*+Z*
1:1	0 mm	0.59 [10 μs]	0.61 [11.6 μs]	0.48 [0.8 μs]	0.49 [0.8 μs]
(comp. to S1)	1 mm	0.7 [7.2 μs]	0.76 [11.6 μs]	0.63 [0.8 μs]	0.77 [0.8 μs]
1:1.7	0 mm	0.68 [12 μs]	0.85 [14 μs]	0.59 [0.8 μs]	0.59 [0.8 μs]
(comp. to S1)	1 mm	0.68 [7.6 μs)	0.73 [14 μs]	0.56 [0.8 μs]	0.49 [0.8 μs]
1:1.7	0 mm	0.45 [12 μs]	0.59 [7.6 μs]	0.41 [0.8 μs]	0.41 [0.8 μs]
(comp. to S2)	1 mm	0.5 [16.4 μs]	0.5 [7.6 μs]	0.38 [0.8 μs]	0.31 [0.8 μs]
1:3.7	0 mm	1.09 [14 μs]	1.34 [17.2 μs]	0.3 [2μs]	0.4 [2 μs]
(comp.to S1)	1 mm	0.5 [14 μs]	0.83 [17.2 μs]	-	0.15 [2 μs]
1:3.7	0 mm	0.27 [16 μs]	0.48 [17.2 μs]	0.1 [1.2 μs]	0.2 [1.2 μs]
(comp. to S2)	1 mm	-	-	-	-

Figure 3.5 (g-h) shows the temporal evolution of the plasma contact front radius for d=

0,1 mm compared to the single plasma source S1 and S2 in the case of the unequal energy ratio 1:3.7 (S1:S2=1:3.7) along laser propagation direction (± Z). When compared to S1 source, the POR values of the colliding plasma plumes are increased for d=0 mm for all time scales, but for d=1 mm the increment is observed between 6 to 27 μs time scales along -Z direction, while the POR values of the colliding plasma plumes increased for both d=0, 1 mm along +Z direction for energy ratio 1:3.7. When compared to S2 source, the POR values of the colliding plasma plumes are increased for d=0 mm but they decreased for d=1 mm along ± Z direction. The corresponding shock wave analysis also revealed that, the increment in the shock front (SF) velocity is observed only at the initial time scales. The maximum increment in CF radius and SF velocity for both cases is summarized in Table 3.3.

3.7 Collision dynamics of two counter propagating plasma sources with equal energy ratio and d ≥ 2 mm

In this case the laser input energy of both the sources S1 and S2 is kept at 25 mJ per pulse and the dynamics of POR and SWs are studied by varying 'd' over 2 mm, 4 mm and 6 mm. The experimentally obtained shadowgraphy images of the two counter propagating plasma plumes of equal energy ratio for d = 2, 4, 6 mm at different time scales are shown in Figure 3.6 (a-c).

The two plasma sources with separation of 'd' between them, expands into ambient air at initial time scales (up to 2-6 μs) and interacts at the interaction zone (d=0). Due to the collision of two plasma sources, a hard stagnation layer [10] is formed and the electron density builds up at the interaction zone as shown in Figure 3.6 (b). According to Dardis et. al. [25], if ion-ion mean free path is smaller compared to the separation distance between the two seed plasmas a hard stagnation layer is formed, where two plasmas decelerate with little or no penetration. In the equal energy ratio (S1:S2 = 1:1) case, a similar hard stagnation layer is observed (Figure 3.6 (a-c)), where the interaction of two PORs is dominated by collisions between internal species of plasmas. Although the PORs stagnate at the interaction zone, the corresponding shock waves SF1 & SF2 penetrate through each other plasma/shock wave. Due to the propagation of SF1 through S2 and SF2 through S1, bright spots moving towards each other PORs of S1 and S2 from the stagnation layer are observed, which we call as **Plasma Jet** (Figure 3.6 (b)).

The shock wave from one plasma plume propagating through another plasma plume compresses the particles in that plasma plume, creating the plasma instabilities along its propagation direction. Due to these instabilities the local temperature is increased, changing the interaction dynamics at the interaction zone leading to the plasma Jet. The energy

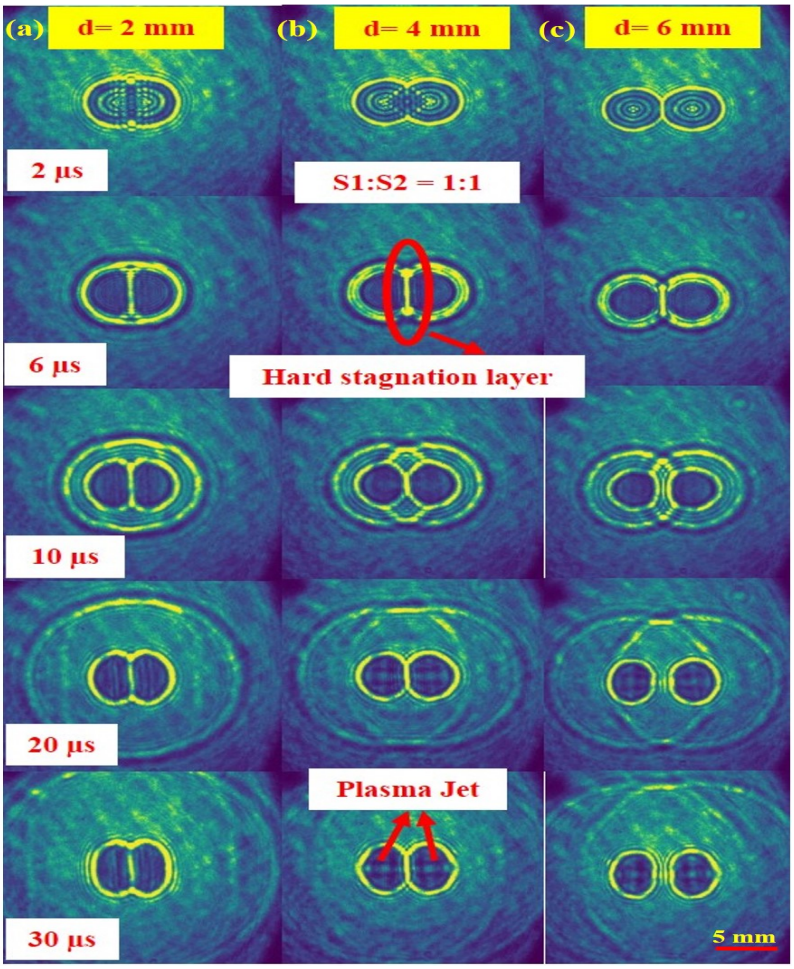

Figure. 3.6 Temporal evolution of interaction of two counter propagating colliding plasma sources of equal input energy (a) for d= 2 mm, (b) for d=4 mm and (c) for d=6 mm at t=2, 6, 10, 20, 30 μs

transfer from the ions to the electrons and the equilibration of their temperatures takes place, post propagation of the shock wave through the plasma (S1 and S2) over comparatively longer time scales [24, 38]. During the interaction of counter propagating plasmas or shock waves, due to momentum conservation, the plasma jet dynamically shifts and we can observe the plasma jet on both sides of the stagnation layer [26]. As both the shock waves are interacting in the counter-propagating direction, which is also the laser propagation direction, the line of force is also observed along the laser propagation direction (+Z and – Z) [42]. Hence, we can observe the plasma jet on both sides of the stagnation layer. The evolution of the plasma jet is observed to depend on the impedance of the two sources. If both the plasma sources have equal impedance, the plasma jet is visible in both PORs along their corresponding laser propagation direction [42]. Since both plasma sources have equal energy, we have observed the initiation of discontinuity in both POR of S1 (along -Z direction) & S2 (along +Z direction) for d=4, 6 mm separation distance

as shown in Figure 3.6 (a,f) at longer time scales (> 10 μs) but it is not resulted into the jetlet evolution within the observed time scales in the study i.e., 30 μs. But the fast imaging of plasma emissions from the colliding plasma with equal energy at d= 4 mm, showed (or confirmed) the plasma jetlet evolution from both the plasma sources S1 and S2 for time scales > 30 μs as shown in the Figure 3.2 (b).

3.7.1 Plasma Outer Region (POR)/ Contact Front (CF) Evolution

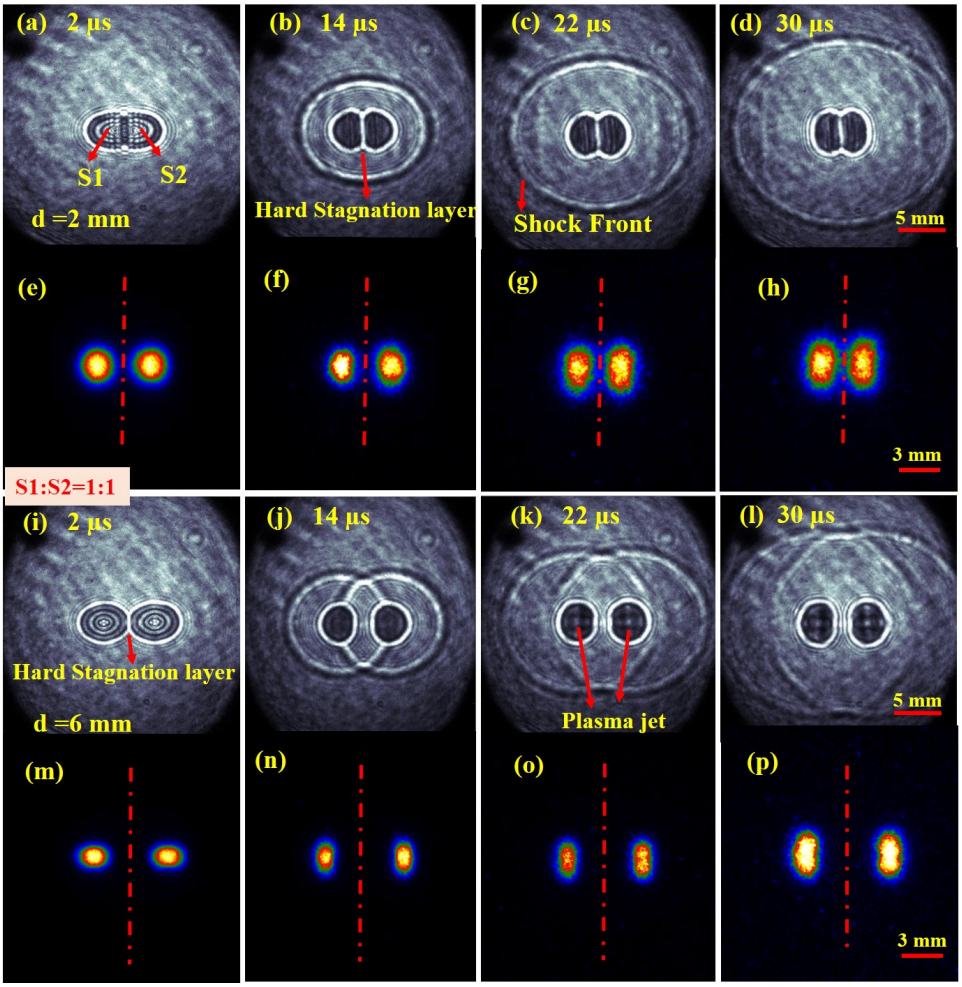

Figure. 3.7 Temporal evolution of the interaction dynamics of shock waves and the plasma in the counter-propagating configuration with sources of equal input energy (a-h) for d=2 mm (closely separated sources) (i-p) for d=6 mm (far separated sources)

Figure 3.7 (a-d) shows the shadowrams of the temporal evolution of the colliding plasma sources at d=2 mm separation distance and Figure 3.7 (e-h) shows the corresponding 2D emission images for t=2, 14, 22 and 30 μs time scales. For the case of d = 2 mm, the outer regions of the plasmas start interacting at earlier time scales of 2 μs and the stagnation layer remains intact for quite longer time scales up to 30 μs despite the shock waves due to S1 and S2 propagating through each other's plasma plume. When a shock

wave passes through the plasma, it heats only the ions, while the electrons remain cold. The energy transfer from ions to electrons and equilibration of their temperatures takes place down streaming of a shock wave over comparatively longer time scales [37, 41] which is observed as plasma jet as indicated in Figure 3.7 (k). For d=2 mm there is no formation of plasma jetlet/discontinuity in both PORs along -Z direction of S1 and +Z direction of S2 because the total length of both plasmas (Table 3.2) is more than the separation distance (d) between them, as there is not enough time for both plasmas to fully expand and interact with each other upto the observed time scales. Figure 3.8

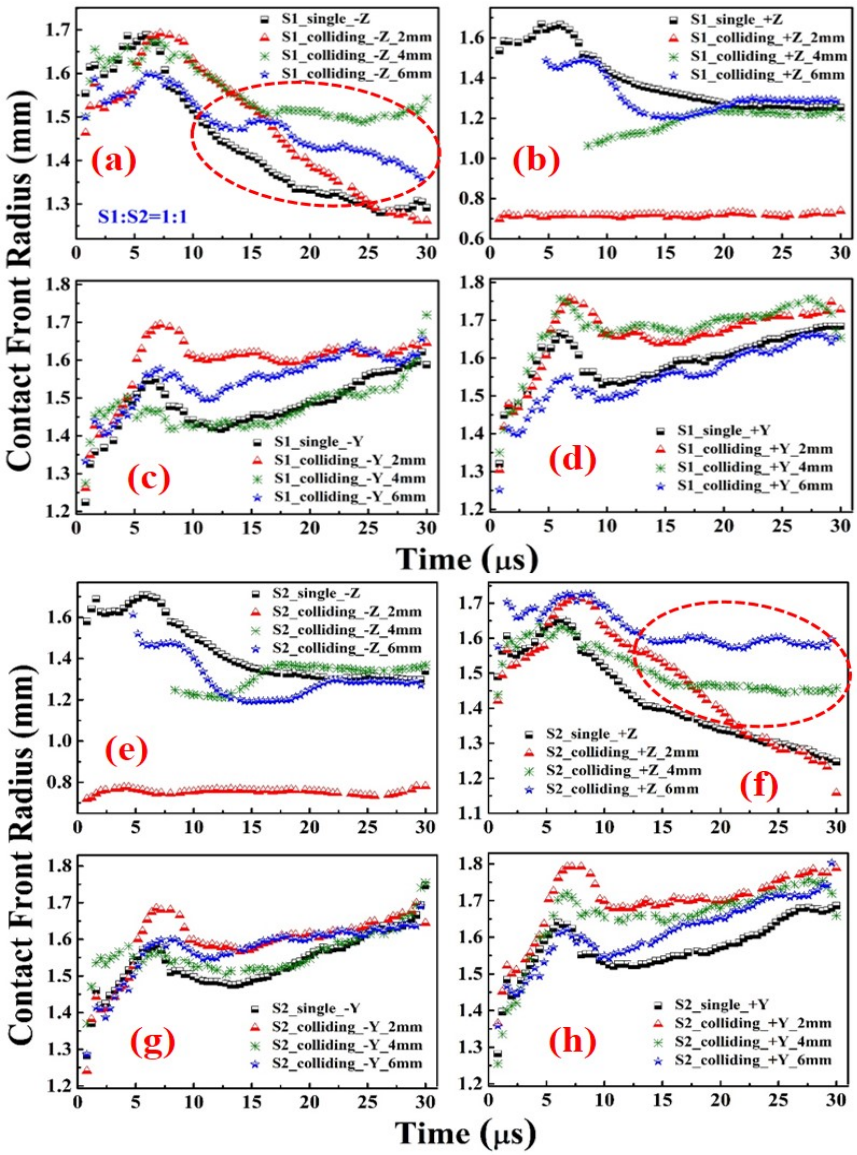

Figure. 3.8 Time evolution of Contact Fronts (PORs) of S1 and S2 of colliding plasmas (a-d) S1= 25 mJ and (e-h) S2=25 mJ (energy ratio 1:1) with d = 2, 4, 6 mm compared with respective single source along ±Z, ±Y directions (circled portion shows the discontinuity in S1 as well as in S2 caused by interaction of two equal energy sources).

(a-h) shows the temporal evolution of POR of S2 (25 mJ) of colliding plasma with its respective single source (25 mJ) (S2) along ±Z, ±Y directions. At initial time scales (up to 4-6 μs), the POR of S1 & S2 expands with high velocity into ambient air due to the predominant collisions between their internal species. At later time scales (> 6 μs), the collision between internal species of S1 & S2 and ambient air are predominant which decreases the POR velocity of S1 & S2 as seen in Figure 3.8. The two expanding PORs of S1 & S2 interact and try to interpenetrates each other. Due to the equal energy ratio of S1 and S2, the interacting plasma plumes forms a hard stagnation layer at the interaction zone (+Z direction of S1 and -Z direction of S2) up to 30 μs. Figure 3.8 (b & e) confirmed the formation of stagnation layer at the interaction zone. The POR radii of colliding plasmas S1 & S2 is more when compared to their respective single source POR in all directions except at the interaction zone over 10 – 30 μs time scales. At the interaction zone, due to the hard stagnation layer the POR radii is almost constant and the resultant momentum is conserved by increasing the POR radii of S1&S2 as shown in Figure 3.8 (a-h), with more POR radii along ± Y direction than ± Z directions. This indicates that the plasma energy expands more along the transverse direction at the interaction zone leading to the decrease in the POR radii of both sources at the interaction zone compared to single source radii. The difference in the POR radii of single source and colliding plasma (-Z direction of S1 and +Z direction of S2) along their respective directions gives an insight into the formation and evolution of small discontinuity in POR of source(s) called as **Plasma Jetlet**.

For d=4 mm, at the interaction zone an oscillating hard stagnation layer is observed. Due to the momentum conservation, the POR radii of both sources increase along all directions except at the interaction zone. In this case, we have observed the initiation of discontinuity in both POR of S1 (along -Z direction) & S2 (along +Z direction) around ∼ 16 to 17 μs because of the equal energy of the plasma sources as shown in Figure 3.8 (a, f). Although we observed the increase in the POR radii, the POR radii is either decreasing or constant with time which confirms the initiation of plasma jetlet but it is not evolved upto the observed time scale i.e., 30 μs. In this case, the maximum observed difference of POR with respect to that of a single source is around 0.25 mm (in POR of S1) to 0.2 mm (in POR of S2).

Figure 3.7 (i-l) shows the shadowrams of the temporal evolution of the colliding plasma sources at d=6 mm separation distance and Figure 3.7 (m-p) shows the corresponding 2D emission images for t=2, 14, 22 and 30 μs time scales. In the case of d = 6 mm, the PORs are not physically in contact with each other and the shock waves of both the sources pass through each other's POR as shown in Figure 3.7 (i-p). Around the interaction zone, the expansion of the POR is restricted almost up to 20 μs forming a non-contact stagnation layer. By 30 μs, the PORs show a small bump indicating that the

plasma and the shock wave are trying to inter-penetrate into each other. For d=6 mm, the hard stagnation layer is observed at 7.6 μs after which the two sources are apart and act like individual sources. The evolution of less enhanced plasma jet is due to the higher separation distance between the two sources leading to a very small momentum/energy transfer between both PORs. Due to momentum conservation, we observed an increase in PORs radii of both sources along all directions except at the interaction zone. The sharp rise in the POR radii leading to the plasma jeltlet along -Z direction of S1 and +Z direction of S2 is observed around $\sim$ 10 to 11 μs as shown in Figure 3.8 (a, f). But it is not resulted in the jetlet evolution within the time scales used in the experimental study. In this case, the maximum observed difference of the POR with respect to that of a single source is around 0.15 mm (in POR of S1) to 0.3 mm (in POR of S2).
Overall, in the case of equal energy sources, for d= 2 mm, the POR radii of both sources is increased along all directions except at the interaction zone. For d=4, 6 mm, we have observed the opposite behaviour of the POR radii of S1 & S2 along $\pm$ Z directions and similar behaviour along $\pm$ Y directions. In the interaction zone, the POR radii of S1&S2 are smaller than their respective single source radii for all separation distances, but after $\sim$ 20 μs they are similar for d=4, 6 mm except in the d=2 mm case (Figure 3.8 (b,e)). This clearly indicates the interaction of counter propagating shock waves and the dynamic energy exchange between them evolving with time and separation of the two sources. We have observed a maximum increase of $\sim$ 0.3 mm in the POR radii of both plasmas (S1&S2) along all directions due to the plasma jet enhancement from stagnation layer over the time. Although we observed the increment in the POR of S1 and S2 at longer time scales, it is not resulted in to the jetlet evolution over the observed experimental time scales.

3.7.2 Shock Front (SF) evolution

The creation of two plasma sources S1 and S2 has led to the interaction of two counter propagating, collinear shock waves along the laser propagation axis. In our experiment we have observed that these two counter propagating shock waves (SF1/SF2) influence the evolution of the other plasma source depending on the energy and separation between the sources due to which the plasma jet/jetlet is formed. In this section we present the effect of stagnation layer formation and variation of separation distance on the shock waves in the case of equal energy sources.

Figure 3.9 (a-h) shows the temporal evolution of shock front (SF) due to S1 (25 mJ) and S2 (25 mJ) of colliding plasmas with their respective single source SF radius along $\pm$Z, $\pm$Y directions. For all the other directions, the SF radii of S1 and S2 colliding plasma looks almost similar to their respective single source SF radii in case of equal energy ratio sources over observed time scale (30 μs). For all separation distances d= 2, 4, 6 mm, at the interaction zone (i.e., +Z direction of S1 and -Z direction of S2), the SF radii of

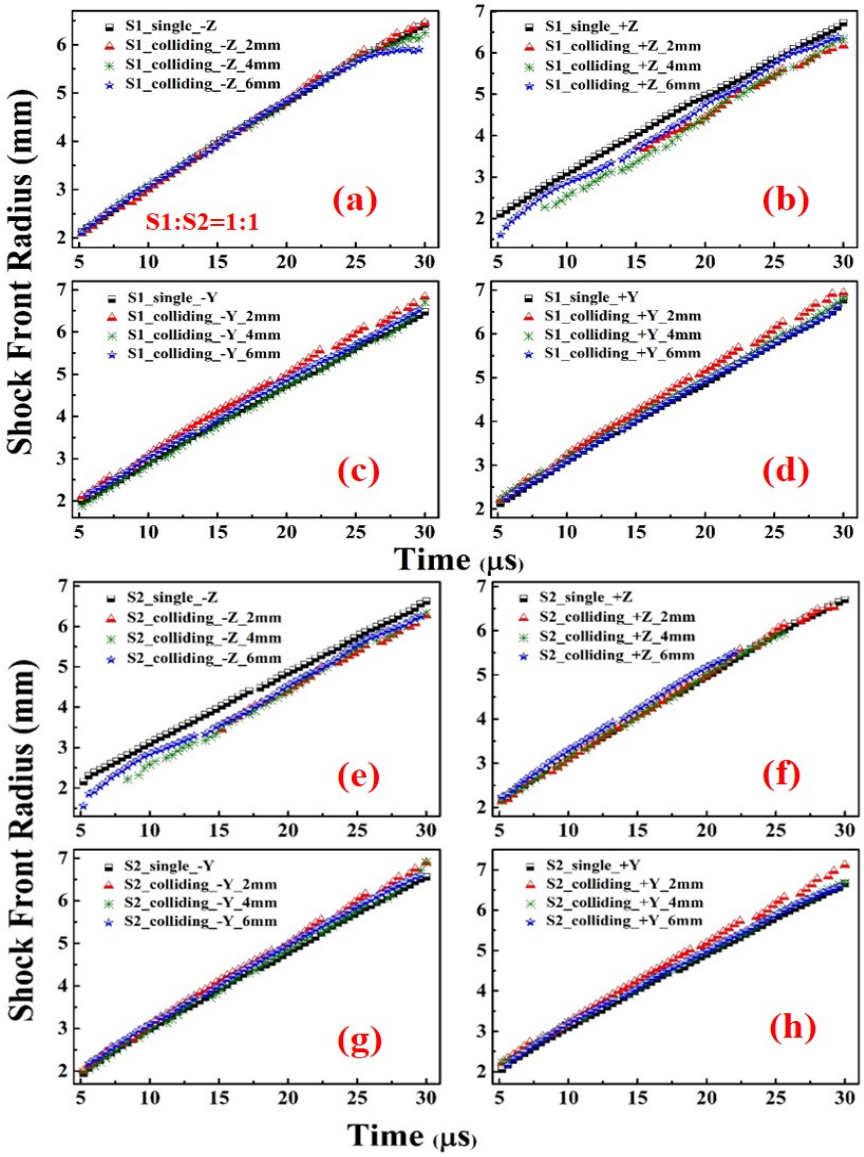

Figure. 3.9 Time evolution of Shock Fronts (SFs) of colliding plasma sources (a-d) S1= 25 mJ and (e-h) S2=25 mJ (energy ratio 1:1) with d= 2, 4, 6 mm compared with respective single source along ±Z, ±Y directions

colliding plasma is less than the SF radius of single source due to presence of other plasma source (S2 or S1). This indicates that the shock wave of S1 or S2 travels through the plasma generated by source S2 or S1 leading to reduced shock expansion (Figure 3.9 (a, b)). This is indicated by the formation of hard stagnation layer as shown in Figure 3.8 (a). The SF radii of S1&S2 decreased along –Z direction of S1 and +Z direction of S2. The SF evolution is observed to change slightly along ±Z directions while it is increased along -Y direction of S1 & S2. The SF radii of S1 is increased along +Y direction while SF radii of S2 is decreased.

3.8 Collision dynamics of two counter propagating plasma plumes with unequal energy ratio and d $\geq$ 2 mm

In the case of unequal energy ratio, the laser input energy of the sources S1 is kept at 25 mJ per pulse and the energy of S2 was varied (41, 92 mJ). Figure 3.10 (a-c) shows the shadowgraphy images of the colliding plasma source interaction for input source energy ratio of 1:1.7, while Figure 3.10 (d-f) shows the shadowgraphy images of the colliding plasma sources with energy ratio of 1:3.7 for a separation distance of d = 2, 4, 6 mm at t=2, 6, 10, 20, 30 μs. Due to these unequal energy ratio of S1 and S2 (1:1.7, 1:3.7), the interacting plasma plumes forms a soft stagnation layer at the interaction zone (+Z direction of S1 and -Z direction of S2) up to 30 μs leading to interpenetration of the plasma plumes as shown in Figure 3.10 (b,e). Due to the propagation of SF1 through S2 and SF2 through S1, bright spots moving towards each other PORs of S1 and S2 from the stagnation layer are observed. The shock wave from one plasma plume propagating through another plasma plume compresses the particles in that plume, creating the plasma instabilities along its propagation direction. Due to these instabilities the local temperature is increased, changing the interaction dynamics at the interaction zone leading to the plasma jet as shown in Figure 3.10 (b,e).

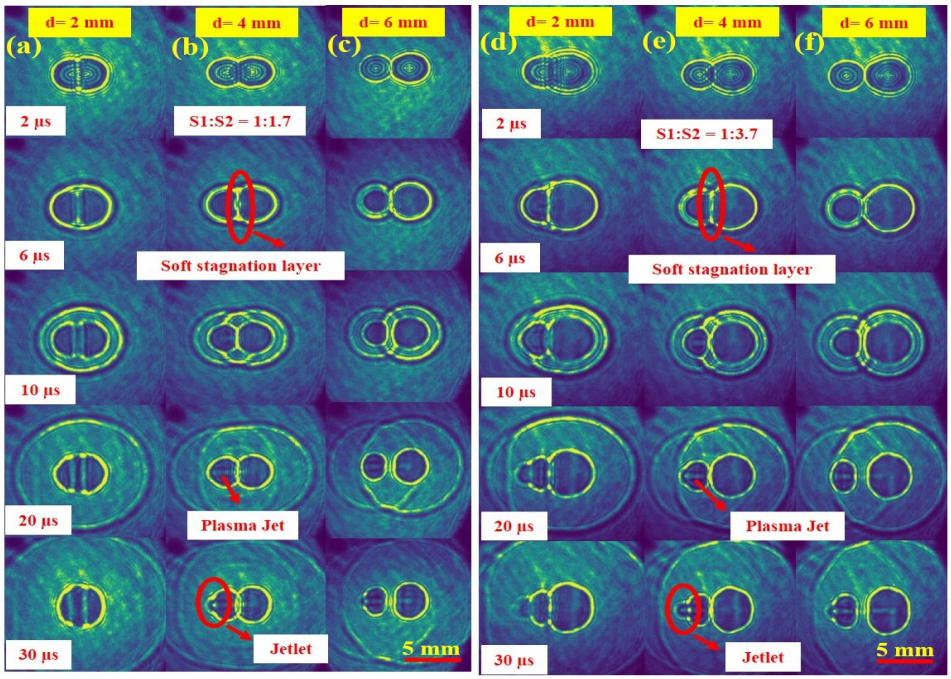

Figure. 3.10 Shadowgrams of the temporal evolution of the interaction of the two counter propagating plasma sources of unequal input energy ratio (a-c) S1:S2=1:1.7 (d-f) S1:S2=1:3.7 for d= 2, 4, 6 mm at t=2, 6, 10, 20, 30 μs

The energy transfer from the ions to the electrons and the equilibration of their temperatures takes place, post propagation of the shock wave through the plasma (S1 and S2) over comparatively longer time scales [24, 38]. Because of the unequal energy of S1 & S2, the enhanced plasma jet is only observed in low density/energy source (S1). Since the area of POR of S1 is small compared to POR of S2, the enhanced plasma jet penetrates into POR of S1 along -Z direction and creates more discontinuity than in the equal input energy sources case.The evolution of the plasma jet depends on the impedance of the two sources (Figure 3.10 (b,e)). In the case of plasma sources of unequal impedance, plasma jet is clearly visible in low impedance source only [42]. When this plasma jet interacts with other end of POR of S1, it creates a discontinuity in the POR of S1 leading to a well-known **plasma jetlet** formation as shown in Figure 3.10 (b,e). The number of charge species and their velocities in the under-dense plasma are relatively lower and hence the charge particle-neutral atom collisions are dominant. The under-dense plasma formed in our case, while expanding gives rise to the charge separation between the electrons and ions/neutrals, that drift with different velocities [47]. The velocity of electrons higher than the ions/neutrals leading to the macroscopic charge fluctuations in the plasma. In this case, the relaxation time for the kinetic energy of the electrons is longer than that of the average velocity that is governed by a factor of m_n/m_e, where m_n and m_e are the masses of neutrals and electrons respectively [44, 48, 49]. Thus the charge particle-neutral atom collisions under the influence of the shock wave from the high energy source S2 lead to the formation of plasma jetlet at the time scales > 6 μs which becomes significant at later times. Compared to the case of equal energy sources, considerable variation in the evolution of stagnation layer is observed with increase in separation distance.

Kodama et. al., [50] observed a similar jet formation up to few mm in laterally colliding plasma plumes. Farley et. al., [51], described this jet like formation at the interaction zone similar to astrophysical jets with high Mach number. But, both experiments were performed at laser power density $> 10^{15} W/cm^2$. Harilal et. al., [23] also observed a similar jet like formation with 1 mm length and 75 μm width using the laser power density $\sim 10^{11} W/cm^2$. But all these jet-like formations were observed in laterally colliding plasma plumes with equal energy ratio under vacuum conditions. In our experiment, the jet like formation in counter propagating plasma plumes in ambient air is observed to be predominant in the case of unequal energy ratio, with laser power densities $\sim 10^{11} W/cm^2$. The laser power densities used are similar to those used in pulsed laser deposition [51]. All the previous works reported [24, 29, 50, 51] the jet like structures which are conical in shape (in vacuum), but in our case the jetlet is observed to be in the form of a bubble/circle. As the jetlet formation takes place at times > 5 μs, the SF from S2 propagates through S1 and attains a spherical shape with self-similar expansion. Hence, the SF imparts equal pressure on the plasma source of S1, which at later times leads to the jetlet appearing

as bubble/circle shape. The spatio-temporal evolution of this bubble-like jetlet in case of unequal energy ratio sources with varying separation distance and varying energy ratio is presented in Section 3.9.

3.8.1 POR/CF Evolution of two counter propagating plasma plumes with unequal energy ratio and d $\geq$ 2 mm collision

3.8.2 Sources of energy ratio 1:1.7

Figure 3.10 (a-c) shows the shadowgraphy images of the colliding plasma source interaction with energy ratio of 1:1.7, for a separation distance of d = 2, 4, 6 mm. Appearance of a soft stagnation layer allowing the exchange of energy across the interaction zone, can be seen clearly for all the three separation distances. Figure 3.11 (a-d) shows the shadowrams

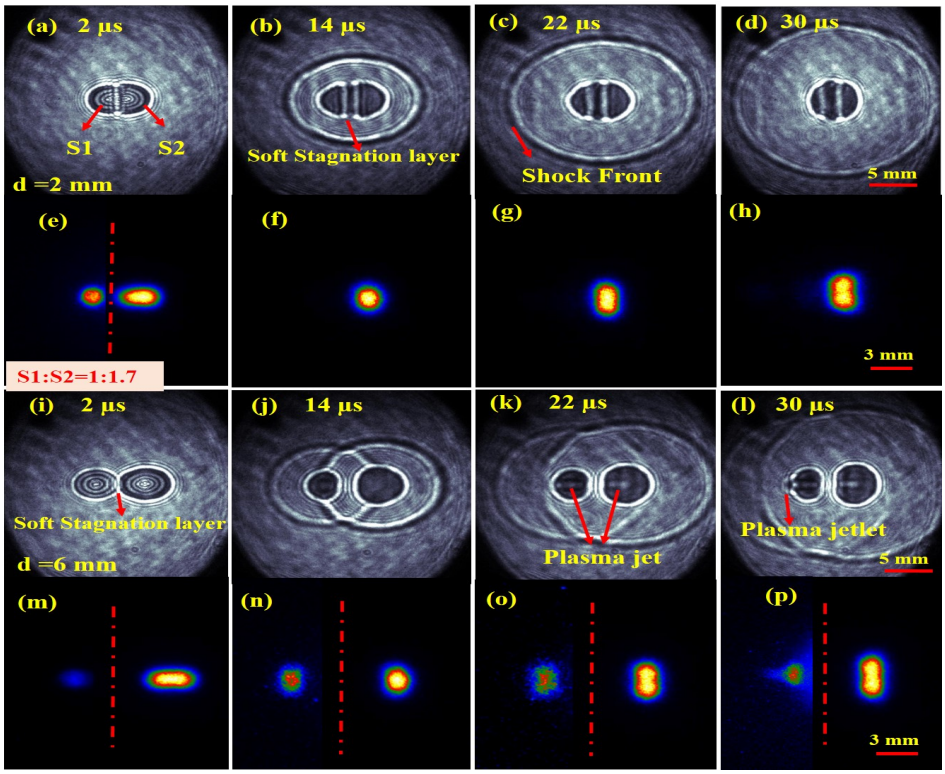

Figure. 3.11 Temporal evolution of the interaction dynamics of plasma and shock waves in the counter-propagating configuration with sources of unequal input energy ratio S1:S2=1:1.7 (a-h) for d=2 mm (closely separated sources) (i-p) for d=6 mm (far separated sources)

of the temporal evolution of the colliding plasma sources at d=2 mm separation distance and Figure 3.11 (e-h) shows the corresponding 2D emission images for t=2, 14, 22 and 30 μs time scales. For the d= 2 mm case, a clearly separated plasma sources is observed at the initial time scales 2 to 20 μs as shown in the Figure 3.11 (a), which later on merge into a single one by 30 μs as shown in Figure 3.11 (b-d). The corresponding 2D emission images also shows the same (Figure 3.11 (e-h)). The shock wave evolution is also observed

to be similar to that of a single source with a higher energy. Although the POR radius of plasma source S1 is increased due to the merging, the plasma jetlet formation was not observed in this case. The 2D emission study also confirms it (Figure 3.11 (b-d). This clearly indicates the exchange of the energy without resulting in the plasma jetlet. For the case of d= 4 mm and 6 mm, due to the reasonable separation, the plasma jet is observed around 10 μs and 16 μs, respectively, leading to the formation of plasma jetlet. The jetlet was observed not to detach from the POR of S1 within the time of observation up to 30μs.

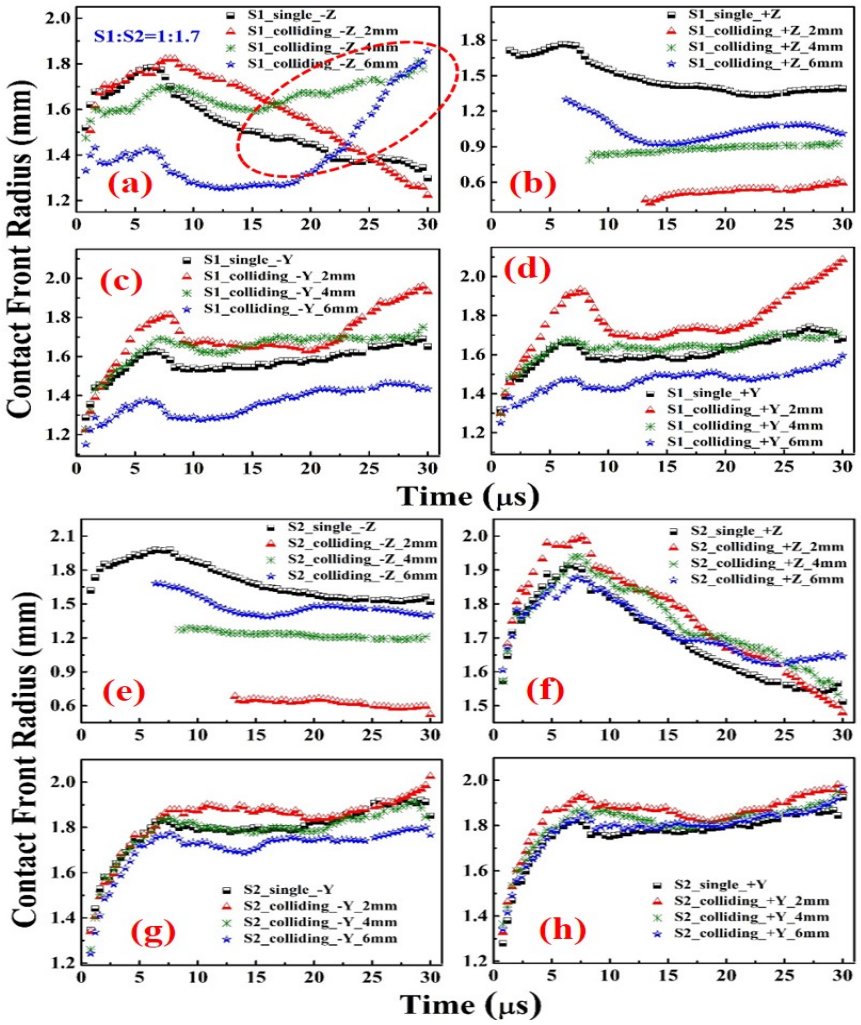

Figure. 3.12 Time evolution of Contact Fronts (PORs) of S1 and S2 colliding plasmas (a-d) S1= 25 mJ and (e-h) S2=41 mJ (energy ratio 1:1.7) with d= 2, 4, 6 mm compared with respective single source along ±Z, ± Y directions (circled portion shows discontinuity in S1 caused by interaction of two unequal energy sources)

Figure 3.12 (a-d) shows the temporal evolution of POR of S1 (25 mJ) of colliding plasma with its respective single source (25 mJ) (S1) along ±Z, ± Y directions. Figure 3.12 (e-h) shows the temporal evolution of POR of S2 (41 mJ) of colliding plasma with its respective

single source (41 mJ) (S2) along ± Z, ± Y directions. Due to the unequal energy ratio of S1 and S2 (1:1.7), the interacting plasma plumes forms a soft stagnation layer at the interaction zone (+Z direction of S1 and –Z direction of S2) up to 30 μs leading to interpenetration of the plasma plumes. Figure 3.12 (b,e) confirms the formation of stagnation layer that remains intact during the observation period. The POR evolution of S1 (along +Z) and S2 (along -Z) is almost constant over the observation time for d = 2, 4 mm. However, the variation of stagnation layer for d = 6 mm is more due to the interaction of less velocity PORs of S1&S2 as shown in Figure 3.12 (b,e). Due to higher energy of S2 than S1, the plasma jet from the stagnation layer with more momentum/energy reaches POR of S1 quickly and creates plasma jetlet in S1 as shown in Figure 3.12 (a). In the interaction zone, the POR radii of S1&S2 are very smaller than their respective single source radii (Figure 3.12 (b,e)).

For d=2 mm the stagnation layer is observed up to 4 μs after which, the stagnation layer is split into two lines with small separation at the interaction zone at 14 μs as shown in Figure 3.11 (b-d)). The two interacting plasma sources look like mirrored 'D' shape across the focal plane around 6 to 14 μs as shown in Figure 3.10 (a), 3.11 (b), before merging in to a single one. Though the sources have different energies with small separation distance between them, both sources merged into a single source at later time scales of 30 μs. Although the POR radius of S1 is increased between 7 to 25 μs, we have not observed the jetlet formation because of the small separation distance and the merging of both sources. Due to the soft stagnation layer, the radius of POR in interaction zone is almost constant and less than the single source POR radius. But, the resultant momentum is conserved by increasing the PORs radii of S1&S2 (Figure 3.12 (a-h)) along all directions except at the interaction zone. We have also observed the sharp rise in POR radii of S1 from 20 μs along ± Y direction as shown in Figure 3.12 (c, d). For d=4 mm, the stagnation layer is almost constant over the observed time of 10-30 μs as shown in Figure 3.12 (b,e) and POR radii of S1&S2 in the interaction zone is smaller than their respective single source POR radius. The soft stagnation caused the sharp rise in the POR radius of S1 around 17 μs (Figure 3.12 (a)) along –Z direction, which represents the jetlet formation. Due to high energy ratio between the two sources, the plasma jet evolution is seen in low density/energy source (S1) only. We have observed minimal increase in the PORs of both sources along all directions except at the interaction zone. Figure 3.11 (i-l) shows the shadowgrams of the temporal evolution of the colliding plasma sources at d=6 mm separation distance and Figure 3.11 (m-p) shows the corresponding 2D emission images for t=2, 14, 22 and 30 μs time scales. For d= 6 mm, the stagnation layer is formed up to 8 μs, after that they behave like two independent spherical sources attached to each other as shown in Figure 3.10 (c), 3.11 (j-l). Figure 3.12(b,e) shows the oscillation of the stagnation layer formed with POR radii of S1&S2 that are smaller than their individual

single source POR radii. Though the POR radius of S1 is decreased along all directions for d= 6 mm, we observed the formation of jetlet around 22 μs as shown in Figure 3.12 (a), 3.11 (l,p) in POR of S1 due to the unequal input energy ratio and the soft stagnation layer. Due to the effect of soft stagnation, the POR radius of S2 is decreased along -Z, -Y directions and increased along +Z direction at later times scales $>$ 15 μs.
Overall, in this energy ratio 1:1.7 case the PORs radii of both sources is increased along $\pm$Z, $\pm$ Y directions except at interaction zone for d=2, 4 mm. But for d= 6 mm, the POR radii is either decreased or almost constant along $\pm$Z, $\pm$Y directions of S1&S2. Due to the long separation distance d= 6 mm, we have observed the plasma jetlet at later time scales $>$ 20 μs (Figure 3.10 (c), 3.11 (l,p)). The POR radii of both sources decreased with increase in the separation distance along all directions while opposite behaviour is observed at the interaction zone.

3.8.3 Sources of energy ratio 1:3.7

Figure 3.10 (d-f) shows the shadowgraphy images of the colliding plasma source interaction for input source energy ratio of 1: 3.7 for a separation distance of d = 2, 4, 6 mm. Due to the higher energy ratio of S1 and S2 (1:3.7), the interacting plasma plumes forms a soft stagnation layer at the interaction zone (+Z direction of S1 and –Z direction of S2) and it oscillates within the time of observation up to 30 μs. Appearance of a soft stagnation layer allowing the exchange of energy across the interaction zone can be seen clearly for all the three separation distances. The POR evolution of S1 (along +Z) and S2 (along -Z) is varying more with increasing the separation distance. Due to higher energy of S2 than S1, the plasma jet from the stagnation layer with more momentum reaches POR of S1 quickly and creates the plasma jetlet in S1 around $\sim$ 6.4 μs. Figure 3.13 (a-d) shows the temporal evolution of POR of S1 (25 mJ) of colliding plasma with its respective single source (25 mJ) (S1) along $\pm$Z, $\pm$Y directions. Figure 3.13 (e-h) shows the temporal evolution of POR of S2 (92 mJ) of colliding plasma with its respective single source (92 mJ) (S2) along $\pm$Z, $\pm$Y directions. In the interaction zone the POR radii of S1&S2 are smaller than their respective single source radii as shown in Figure 3.13 (b,e). Figure 3.13 (b,e) confirms the formation of stagnation layer and the sharp rise in POR radius of S1 for d=2, 4, 6 mm from 6.4 μs indicates the formation of plasma jetlet as shown in Figure 3.13 (a). However, in the case of the energy ratio 1:3.7, the penetration is more dominant than for the energy ratio 1:1.7 (Figure 3.12 (a), 3.13 (a)).

For d= 2 mm, the stagnation layer is visible up to 6 μs, after that we have clearly observed the interpenetration of two sources S1&S2 from 6 μs to 16.8 μs, later POR of S2 only appeared due to high density/energy over observed time 30 μs. In this case, the plasma jetlet evolution started early around $\sim$ 6.4 μs as shown in Figure 3.10 (d), 3.13 (a) due to the very high energy of S2. Due to the colliding plasma interaction, the POR radii of S1 increased more along -Z, -Y directions than respective single source (S1) POR radius,

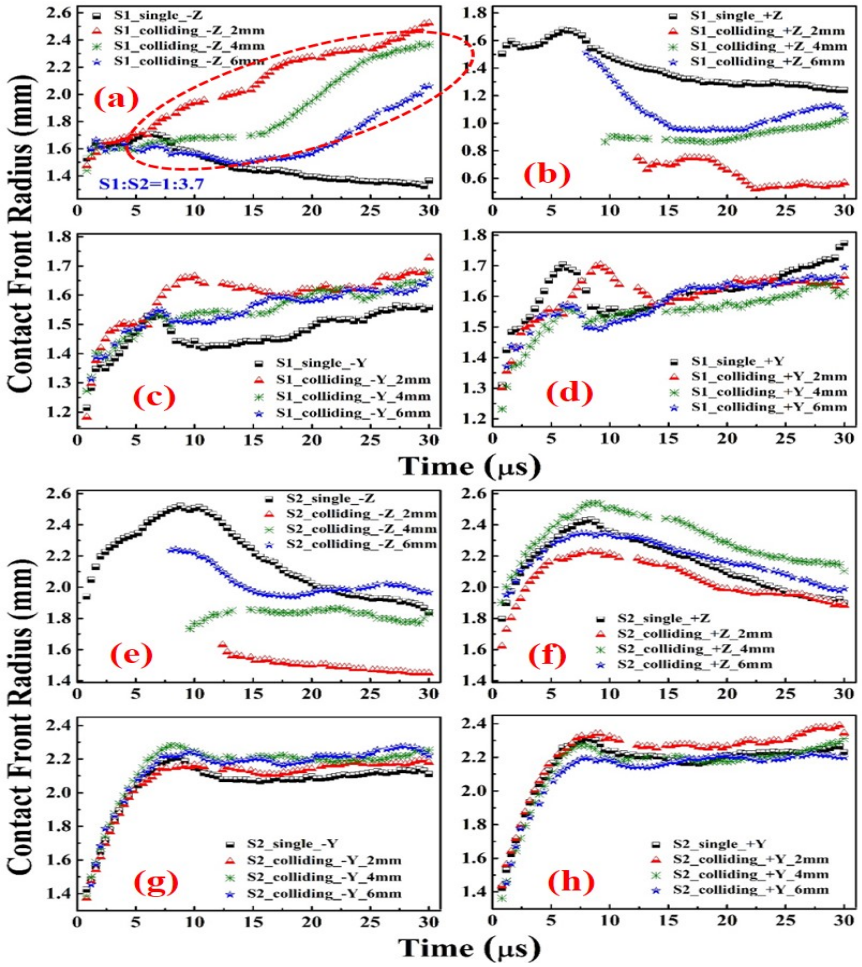

Figure. 3.13 Time evolution of Contact Fronts (PORs) of S1 and S2 of colliding plasma (a-d) S1= 25 mJ and (e-h) S2=92 mJ (energy ratio 1:3.7) with d= 2, 4, 6 mm compared with respective single source along ±Z, ±Y directions. Circled portion shows discontinuity in S1 caused by interaction of two unequal energy sources

while it remains almost constant along +Y direction. The POR radii of S2 decreased along +Z direction while it increased along ± Y direction.

For d=4 mm, the soft stagnation layer is formed but most of the energy of S2 is utilized to increase the plasma jet in POR of S1. So the interpenetration of two sources is not observed. The plasma jetlet appears around ∼ 8 μs as shown in Figure 3.10 (e), 3.13 (a) and increases continuously up to 30 μs. The POR radii of S1 increased along -Z direction and -Y direction but decreased along +Y direction. The POR radii of S2 increased slightly along +Z, +Y directions due to the conservation of energy, while it is almost constant along -Y direction.

For d= 6 mm, the stagnation layer is formed and visible up to 9.2 μs, after that both the sources behave like two independent spherical sources attached to each other. Though

both the sources have larger separation distance, due to the higher energy of S2 the plasma jetlet is observed around 9.6 μs as shown in Figure 3.10 (f), 3.13(a), compared to the case of S1:S2 = 1:1.7. The POR radii of S1 increased sharply along -Z, -Y directions and is almost constant along +Y direction. The POR radii of S2 is slightly increased along +Z, -Y directions and is almost constant along +Y direction. At the interaction zone, the POR radii of both sources decreased for all separation distances.
Overall, in this case as the separation distance increases the POR radii of S1 decreased along -Z, -Y directions and shown mixed behaviour along +Z, -Y direction of S2, i.e., it followed the trend: d= 2 mm < d= 6 mm < d= 4 mm. At the interaction zone the POR radii of both sources increased with the increase in separation distance, but they are less than their respective single source POR radius. A slight asymmetry of contact front radius of S1 w.r.t. Y-axis as shown Figure 3.10 (d), 3.13 (c-d), is observed for the case of unequal energy sources for d = 2 mm around $\sim 4 - 10$ μs only. While for the other two separation distances no significant asymmetry w.r.t. Y-axis is observed. This may be attributed to oscillations of the POR of S2 during the shock detachment that modifies the ellipticity of S1 at the interaction zone [39].

3.8.4 Shock Front (SF) evolution of two counter propagating plasma sources with unequal energy collision and d $\geq$ 2 mm

The two counter propagating shock waves SF1 and SF2 influence on the evolution of the other plasma source, and that depends on the energy and separation between the plasma sources due to which the plasma jet and plasma jetlet is formed. Here, we present the effect of the stagnation layer formation and variation of separation distance between two plasma sources on the evolution of the shock waves in the case of unequal energy sources. In case of unequal energy sources, the effect of separation distance on shock front expansion is clearly visible in both sources along all the directions.

3.8.5 Sources of energy ratio 1:1.7

In this case, the sources S1 and S2 are created by using energy of 25 mJ per pulse and 42 mJ per pulse respectively. Figure 3.14 (a-d) compares the temporal evolution of SFs due to S1 (25 mJ) of colliding plasma with its respective single source of same energy (25 mJ) along $\pm$ Z, $\pm$Y directions. With increasing the separation distance 'd' a considerable change of SF radii that is more explicit at later time scales is observed. For all separation distances studied, the SF radius of S1 & S2 of colliding plasma is observed to be less than their respective individual sources along $\pm$Z directions as shown in Figure 3.14(b). The SF radius of lower energy source S1 has slightly increased along $\pm$Y direction from $\sim$ 5 μs onwards for d= 2, 4 mm, which is eventually similar to the SF of single source. While for d = 6 mm the SF radius has reduced as shown in Figure 3.14 (c,d). This demonstrates the transfer of energy during the interaction of higher energy source (S2) with lower energy

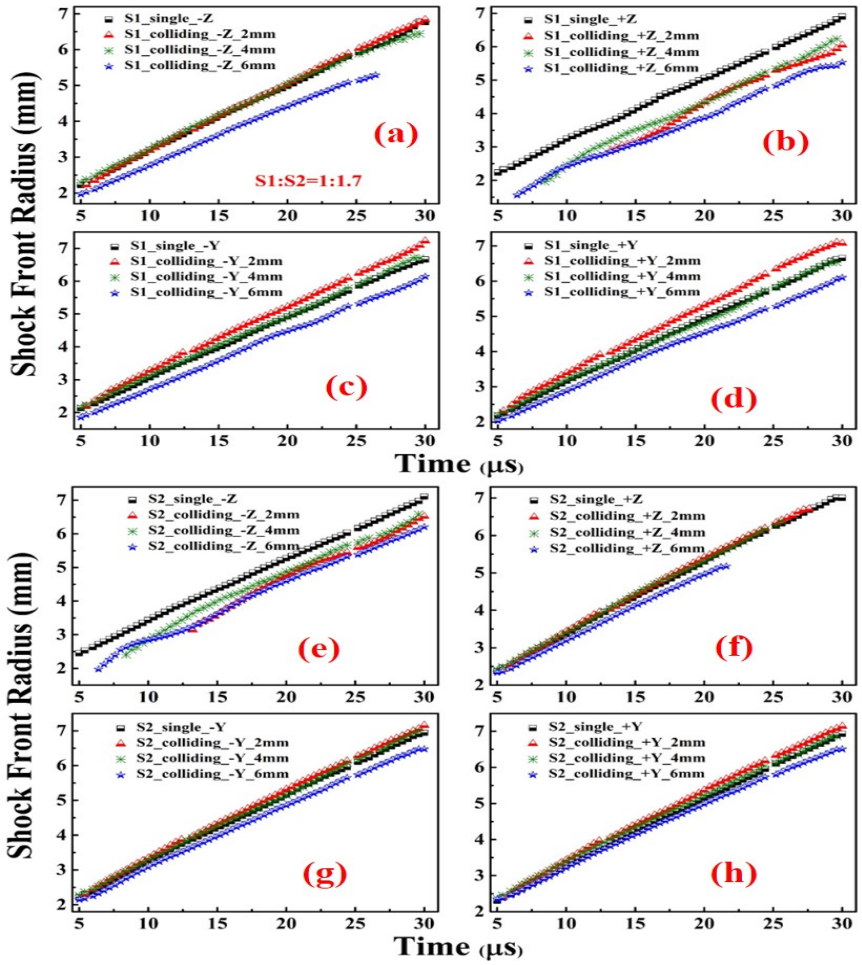

Figure. 3.14 Time evolution of Shock Fronts (SFs) of colliding plasmas (a-d) S1= 25 mJ and (e-h) S2=42 mJ for energy ratio 1:1.7 with d= 2, 4, 6 mm compared with respective single source along ±Z, ±Y directions

source (S1) (Figure 3.14(c,d)). No corresponding change is observed in the higher energy source (S2) SF radius. The transfer of energy along ± Z direction of lower energy source is more than that observed for ±Y directions. This clearly corroborate the directionality of laser induced shock waves. Of the three separation distances of 2, 4, 6 mm, for d= 2 mm, there is a considerable increase of SF radius along ±Y directions.

3.8.6 Sources of energy ratio 1:3.7

In this case, laser pulse energy used to create the sources S1 and S2 is 25 mJ and 92 mJ respectively. Figure 3.15 (a-d) compares the temporal evolution of SF of S1 (25 mJ) of colliding plasma with its respective single source of same energy (S1) along ±Z, ±Y directions. While Figure 3.15 (e-h) compares the temporal evolution of SF of S2 (92 mJ) of colliding plasma with its respective single source (92 mJ) along ±Z, ±Y directions. The SF radius of both plasma source S1 & S2 decreased at the interaction zone (+Z direction of S1 & -Z direction of S2). This clearly confirms the energy transfer dynamics

of the SFs at the interaction zone. While the SF radius of S1 along -Z direction has not varied much as shown in Figure 3.15 (a), while SF radius of S2 along +Z, ±Y direction has either reduced slightly or remained almost similar as shown in Figure 3.15 (e-h). The lower energy source S1 has expanded slightly along ±Y directions for all the three

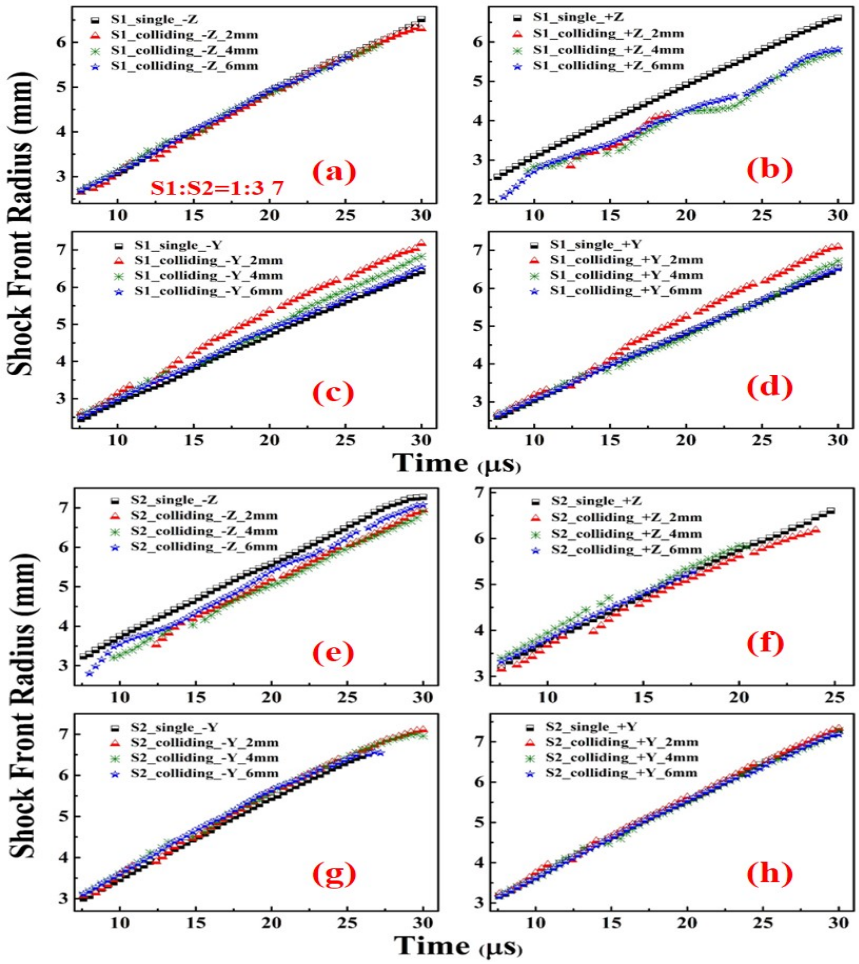

Figure. 3.15 Time evolution of Shock Fronts (SFs) of colliding plasmas (a-d) S1= 25 mJ and (e-h) S2=92 mJ for energy ratio 1:3.7 with d= 2, 4, 6 mm compared with respective single source along ±Z, ±Y directions

separation distances from ∼ 10 μs onwards. The increase is higher for d= 2 mm that eventually reduced for d= 4, 6 mm. While no corresponding change in the evolution of SF of S2 along ±Y direction is observed with in the duration of observation. Due to the interaction of very high energy source (S2) with lower energy source, the evolution of SF of S2 has not changed at all. This clearly confirms the effect of high energy source is dominant in S1:S2=1:3.7 case, while S1 has minimal or no effect on S2 plasma source. As the separation distance increases, the SF radius of S1 and S2 of colliding plasma is either equal or less than the SF radius of the individual single source with an exception for S1 along ±Y directions for d= 2 mm. This is attributed to the high energy transfer from S2

to S1 at d = 2 mm, where the plasma sources are closer to each other compared to d = 4, 6 mm.

3.9 Plasma Jetlet Evolution in the two counter propagating plasma plumes of unequal energy collision

The dominant mechanism for the evolution of the plasma jet and the plasma jetlet is observed to be the propagation of high energy shock wave of S2 through the low energy plasma source of S1. To explicitly show the energy transfer mechanism leading to the formation of plasma jet and jetlet, the temporal evolution of contact front (POR) radius of S1 in the colliding plasma configuration is compared to that of S1 single plume, in the presence of both shock front (SF) of S2 in the colliding plasma configuration and S2 single plasma plume as shown in Figure 3.16. For all the three separation distances studied, the evolution of POR and SF for input laser energy ratios of 1:1.7 and 1:3.7 are shown in Figure 3.16 (a-c), 3.16 (d-f), respectively. For both the cases of unequal energy sources, the POR radius of S1 in the colliding plasma configuration has clearly shown a different evolution in the presence of S2. In the case of S1:S2 = 1:1.7, for d =2 mm, the POR radius of S1 has started decreasing continuously from $\sim$ 7.5 μs. While for d = 4 mm and 6 mm, the POR radius of S1 decreases initially and increases again at later time scales. During the same time scales the plasma jetlet diameter appears and starts to follow a similar evolution as the shock wave in Figure 3.17 (a). While for the case of S1:S2 = 1:3.7, the POR radius of S1 in colliding plasma configuration, has clearly shown a continuous increase in the presence of SF of S2. Figure 3.17 (b) shows the similar evolution of plasma jetlet diameter around the same time scales. This confirms that the evolution of jetlet is controlled by the evolution of S2 plasma source due to the energy transfer during the propagation of shock front of S2 plasma source through the S1 plasma [38]. Due to the momentum energy transfer from stagnation layer, bright spots are appeared towards both the sources along the laser propagation axis, which is shown as plasma jet (in Figure 3.6, 3.10). This is observed after the shock front has propagated through the S1 plasma source. In the case of equal energy sources, the plasma jet can be seen on both sides of hard stagnation layer (Figure 3.6). In the case of unequal energy sources, plasma jet is visible clearly in low energy plasma but partially visible in high energy source (Figure 3.10 (a-f)). As the plasma length and impedance of S1 is lower than that of S2, the plasma jet in S1 comes out of POR of S1, forming a plasma jetlet (Figure 3.10 (a-f)). This is also due to the fact that along the laser propagation axis the initial plasma temperature and density is much higher. The shock front of S2 while going through the plasma of S1 will modify the temperature or density leading to a plasma jetlet in the plasma source S1. The velocity of the shock front of S2 while going through

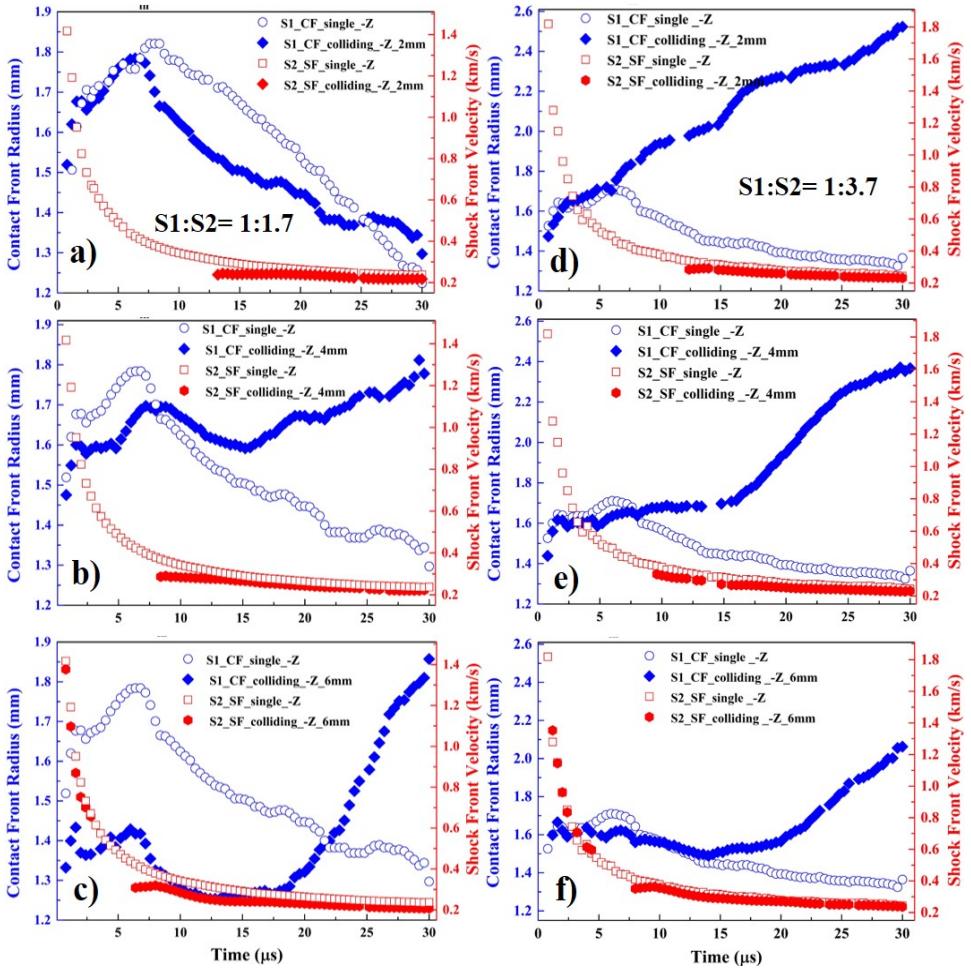

Figure. 3.16 Temporal evolution of Contact front radius of S1 alone and the S1 of colliding plasma in the presence of shock front of S2 in the colliding plasma configuration and S2 alone for the input laser energies of S1 = 25 mJ and (a-c) S2= 41 mJ (1:1.7) (d-f) S2= 92 mJ (1:3.7) with d= 2, 4, 6 mm respectively

the plasma of S1 will vary from 1.8 km/s to less than 0.33 km/s during 0.4 μs to 7-12 μs depending on the energy ratio and separation distance between the two plasma sources. The effect of propagation of rapidly decaying shock front through the other plasma source is manifested as plasma jet [38]. In the case of equal impedances both sources will be having the same energy, temperature, velocity and pressure gradient. As a result both plasma sources imparts equal momentum on each other which leads to the accumulation of mass density, increase in the pressure and temperature resulting in the hard stagnation layer. Due to the rise in the temperature, the number of free electrons in the stagnation layer increases. Similarly, in the case of unequal impedance of two sources, due to the interpenetration of plasma source S2 into plasma source S1 (that lead to the plasma jetlet formation) the accumulation of mass density is small at the interaction zone leading to formation of a soft stagnation layer. Hence, the rise in the temperature and electron

number density is small compared to that of the hard stagnation layer. The temporal

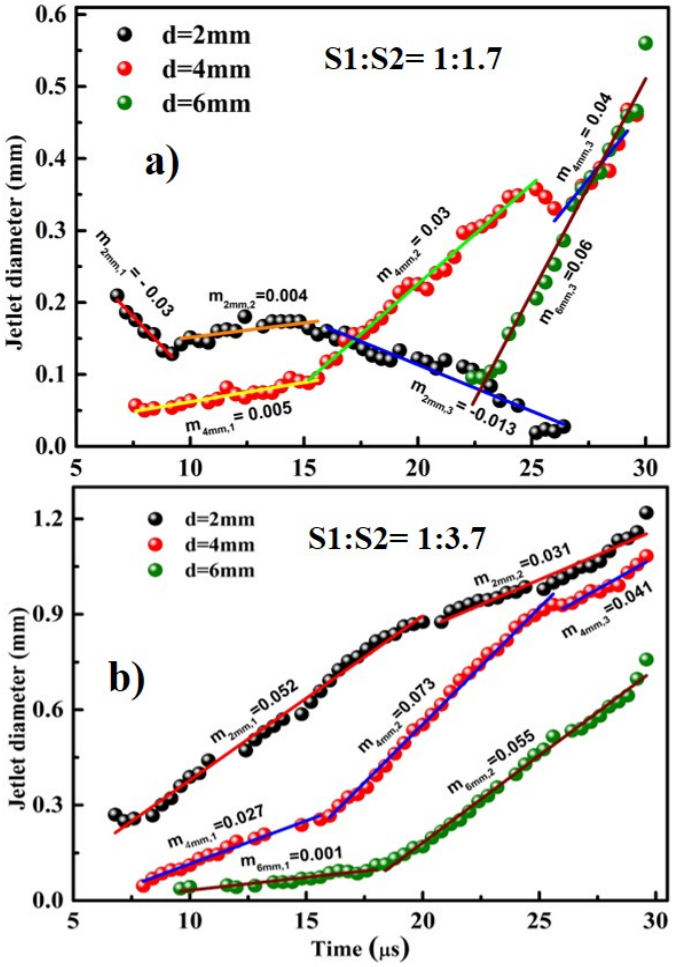

Figure. 3.17 Temporal evolution of plasma jetlet diameter from POR of S1= 25 mJ due to (a) S2= 41 mJ (1:1.7) (b) S2= 92 mJ (1:3.7) at separation distance d= 2, 4, 6 mm

evolution of plasma jetlet diameter with separation distance 'd' between the two plasma sources is shown in Figure 3.17 (a,b). With increase in the energy of plasma source S2 with respect to S1, the plasma jetlet diameter also increases drastically as shown in Figure 3.17 (b). The time of appearance of plasma jetlet also increased with separation distance (d) because the time taken for the enhanced plasma jet to reach other end of POR of S1 from stagnation layer increases. The graphs are fitted with linear function with either increasing or decreasing slope to describe the plasma jetlet evolution with time. The evolution of jetlet diameter with time is tabulated in Table 3.4.

For the case of energy ratios of 1: 1.7; for d = 2 mm, the plasma jetlet has shown a gradual reduction of the jetlet diameter. While for d = 4 mm the diameter starts increasing from its appearance with a fluctuation at $\sim$ 23 μs as shown in Figure 3.17 (a). For d = 6 mm the plasma jetlet appears around 22 μs and increases continuously. In the case of energy ratio 1:1.7, for d= 2 mm the POR of S1 decays linearly from 3.6 μs - 9.2 μs with 0.03 slope

Table 3.4 Plasma Jetlet evolution for different input energy ratios

Energy ratio (S1:S2)	Seperation distance (d)	Jetlet Evolution (km/s)		
		m_1	m_2	m_3
1:1.7	2 mm	-0.03	0.004	-0.013
	4 mm	0.005	0.03	0.04
	6 mm	×	×	0.06
1:3.7	2 mm	0.052	0.031	×
	4 mm	0.027	0.073	0.041
	6 mm	0.001	0.055	×

and tries to gain energy till 16 μs with a slope of 0.004, beyond which it decays from 16.4 μs- 26.4 μs with slope of 0.013 as shown in Figure 3.17 (a). This clearly confirms that the jetlet is not formed. For d= 4 mm, we observed the jetlet diameter increases linearly from 7.6 μs – 15.6 μs with a slope of 0.005, beyond which it rises from 16 μs- 25.4 μs with 0.03 slope and further increases from 26 μs - 29.2 μs linearly with 0.04 slope. This shows that the plasma jetlet expansion is more rapid at initial time scales but gradually slows down at later time scales. The sharp rise indicates that most of the energy transferred from stagnation layer is utilized to increase the plasma jetlet diameter. For d=6 mm the plasma jetlet diameter increases sharply from 22.4 μs to 30 μs with a slope of 0.06. This shows that the plasma jetlet grows rapidly than that at d= 4 mm at long time scales. For d= 4, 6 mm the maximum plasma jetlet diameter is measured to be 0.46, 0.56 mm at t=29.2, 30 μs respectively. From the evolution of plasma jetlet, it is clear that the interaction of plasma plumes plays a crucial role in the jetlet dynamics. The increase in jetlet diameter for d= 4, 6 mm confirms that the jetlet is more dependent on the interaction of POR of individual sources and their energies.

In the case of energy ratios of 1: 3.7; for d = 2 mm the plasma jetlet diameter continuously increases up to 18 μs before slightly slowing down. While for the other two separation distances of 4, 6 mm; the plasma jetlet diameter increases monotonously for d = 4 mm having higher rate of increase. For both d = 4, 6 mm the plasma jetlet diameter increases with two different slopes indicating the change in the interaction dynamics. In all the three separation distances studied, around 15 μs, the plasma jetlet evolution has slowed down for d = 2 mm while for d = 4 mm and 6 mm the plasma jetlet evolution started accelerating.

In the case of energy ratio 1:3.7, the temporal evolution of plasma jetlet is observed early due to the higher energy of S2 than S1 as shown in Figure 3.17 (b). For d= 2 mm the plasma jetlet increases linearly from 6.4 μs to 19.2 μs with a slope of 0.052 and from 19.6

μs onwards with a 0.031 slope. For d= 4 mm, we observed the plasma jetlet diameter increases linearly over 8 μs to 15.6 μs with 0.027 slope and from 16 μs to 25.6 μs increases rapidly with 0.073 slope before slowing down from 26 μs with 0.041 slope. For d=6 mm, the plasma jetlet diameter increases linearly over 9.6 μs to 17.2 μs with 0.001 slope before accelerating rapidly from 17.6 μs with 0.055 slope. For smaller separation distance i.e., d=2 mm the plasma jetlet will have more energy, thus it increases rapidly and at longer time scales $>$ 15 μs the plasma jetlet slows down. For d= 4, 6 mm jetlet diameter increases slowly at initial time scales and it increases continuously at longer time scales. The maximum jetlet diameter is observed to be 1.21, 1.08 and 0.75 mm for d=2, 4, 6 mm respectively. From Figure 3.17 (a-b), we observe that the plasma jetlet diameter decreases with increasing the separation distance.

3.10 Summary

The colliding dynamics of two counter-propagating plasma plumes and shock waves in air from ns laser induced plasma with varying energy ratio and varying the separation distance between them is studied qualitatively to understand the effect of collisionality parameter. The results of these counter propagating colliding plasma sources and shock waves was compared to the shock waves generated by a single source of same energy. The results bring out the role of shock wave from a high energy plasma source on that of a low energy source. The interaction of plasma plumes is investigated at three different energy ratios of the two sources: 1:1. 1:1.7 and 1:3.7 with varying separation distances of d = 2, 4 and 6 mm between them. From the observed results, we conclude that the two plasma plumes/sources interacting in counter propagating direction form a stagnation layer, whose brightness increases with increasing energy and decrease with increasing separation distance 'd'. We have observed plasma jet formation in the form of bright spots along the laser propagation direction on either side of d=0 mm. In the case of equal energy sources, the plasma jet is visible in both the plasma sources while in case of unequal energy sources it is visible only in low energy source. This plasma jet upon reaching the other side of POR of low energy source (S1), it is observed to cause discontinuity in POR of S1, known as plasma jetlet. This plasma jetlet shows an interesting behaviour with increasing energy ratio, as well as with the separation distance between the two plasma sources. In the case of equal energy sources, we have not found any observable discontinuity until the observed time scales. As the energy of S2 increases with respect to S1 (as in the case of unequal energy ratio sources of 1:1.7 and 1:3.7), the plasma jetlet diameter also increases. The propagation of shock front of the high energy source (S2) through the plasma of the low energy source (S1) is observed to be determining the evolution of the plasma jetlet. Though the shock front of S1 and S2 are observed to pass through each other without any considerable affect as reported earlier [34], we observed that the propagation of shock wave of S2 through the plasma of S1 in the colliding plasma configuration has led to the

evolution of plasma jet and plasma jetlet. The properties of the shock waves of lower energy source (S1) is observed to vary with interaction of two plasma sources while higher energy source properties are almost unaffected. The shock front radius of the S1 and S2 are observed to slightly decrease compared to their respective single sources around the interaction zone. Consequently, due to the formation of stagnation layer, the SF radius of lower energy source (S1) is increased along ±Y directions. The deposited energy is conserved by increasing plasma jetlet evolution as well as increasing SF radius of lower energy source (S1). From our observation, in the interaction of two unequal energy sources most of the energy stagnated at the interaction zone, is utilized to create plasma jetlet in lower energy source (S1) and remaining energy is utilized to increase its SF radius.

References

[1] T. R. Dittrich, S. W. Haan and M. M. Marinak et al, *Review of indirect-drive ignition design options for the National Ignition Facility*, Phys. Plasmas 6, 2164 (1999).

[2] C. Baranger, A. Burbeau-Augoula, P. Seytor, P. Hoch, O. Larroche, J. Metral, and B. ebourcet, *Numerical modeling of a self-colliding plasma*, Int. J. Numer. Methods Fluids 65, 1451 (2011).

[3] H. J. Kunze, K. N. Koshelev, C. Steden, D. Uskov, and H. T. Wieschebrink, *Lasing mechanism in a capillary discharge*, Phys. Lett. A 193, 183 (1994).

[4] S. H. Glenzer, C. A. Back, L. J. Suter, M. A. Blain, O. L. Landen, J. D. Lindl, B. J. MacGowan, G. F. Stone, R. E. Turner, and B. H. Wilde, *Thomson Scattering from Inertial-Confinement-Fusion Hohlraum Plasmas*, Phys. Rev. Lett. 79, 1277 (1997).

[5] V. Malka, J. Faure, C. Rechatin, A. Ben-Ismail, J. K. Lim, X. Davoine, and E. Lefebvre, *Laser-driven accelerators by colliding pulses injection: A review of simulation and experimental results*, Phys. Plasmas 16, 056703 (2009).

[6] M. J. Rosenberg, J. S. Ross, C. K. Li, R. P. J. Town, F. H. Seguin, J. A. Frenje, D. H. Froula, and D. Petrasso, *Characterization of single and colliding laser-produced plasma bubbles using Thomson scattering and proton radiography*, Phys. Rev. E 86, 056407 (2012).

[7] D. S. Spicer, R. W. Clark, and S. P. Maran, *A model of the pre-sedov expansion phase of supernova remnant-ambient plasma coupling and X-ray emission from SN 1987A*, Astrophys. J. 356, 549 (1990).

[8] D. Mascali, S. Tudisco, A. Bonanno, N. Gambino, S. Ivanovski, A. Anz-alone, S. Gammino, R. Miracoli, and F. Musumeci, *Colliding laser-produced plasmas: a new tool for nuclear astrophysics studies*, Radiat. Eff. Defects Solids 165, 730 (2010).

[9] S. L. Ivanovski, A. Bonanno, S. Tudisco, N. Gambino, and D. Mascali, *Plasma astrophysics and laser experiments: hydrodynamical simulation of colliding plasmas*, Radiat. Eff. Defects Solids 165, 457 (2010).

[10] A. Tselev, A. Gorbunov, and W. Pompe, *Cross-beam pulsed laser deposition: General characteristic*, Rev. Sci. Instrum. 72, 2665 (2001).

[11] K. F. Al-Shboul, S. M. Hassan, S. S. Harilal, *Molecular formation in the stagnation region of colliding laser-produced plasmas*, Plasma Sources Sci. Technol. 25 (6) (2016).

[12] T. Sizyuk, J. Oliver, P. K. Diwakar, *Mechanisms of carbon dimer formation in colliding laser-produced carbon plasmas*, J Appl Phys. 122 (2) (2017).

[13] K. F. Al-Shboul, S. S. Harilal, S. M. Hassan, A. Hassanein, J. T. Costello, T. Yabuuchi et al., *Interpenetration and stagnation in colliding laser plasmas*, Phys. Plasmas. 21 (1) (2014).

[14] S. L. Gupta and R. K. Thareja, *Photo-luminescence of nanoparticles in vapor phase of colliding plasma*, J Appl Phys. 113 (14) (2013).

[15] P. T. Rumsby, J. W. M. Paul, and M. M. Masoud, *Interactions between two colliding laser produced plasmas*, Plasma Phys. 16, 969 (1974).

[16] P. W. Rambo and J. Denavit, *Interpenetration and ion separation in colliding plasmas*, Phys. Plasmas 1, 4050 (1994).

[17] C. Chenais Popovics, P. Renaudin, O. Rancu et. al., *Kinetic to thermal energy transfer and interpenetration in the collision of laser-produced plasmas*, Phys.Plasmas 4 (1), 190-208 (1997).

[18] E. K. Zavoiskii, *Collective interactions and the production of a high temperature plasma*, Translated from Atomnaya. Energfya., Voh. 14, No. 1, pp. 57-65 (1963).

[19] P. Hough, C. McLoughlin, S. S. Harilal, J. P. Mosnier, and J. T. Costello,*Emission characteristics and dynamics of the stagnation layer in colliding laser produced plasmas*, J. Appl. Phys. 107, 024904 (2010).

[20] H. Luna, K. D. Kavanagh, and J. T. Costello, *Study of a colliding laser-produced plasma by analysis of time- and space-resolved image spectra*, J. Appl. Phys.101, 033302 (2007).

[21] P. W. Rambo and R. J. Procassini, *A comparison of kinetic and multifluid simulations of laser-produced colliding plasmas*, Phys.Plasmas 2, 3130 (1995).

[22] O. Rancu, P. Renaudin, C. Chenais-Popovics, H. Kawagashi, J. C. Gauthier, M. Dirksmoller et. al., *Experimental evidence of interpenetration and high ion temperature in colliding plasmas*, Phys. Rev. Lett. 75, 3854 (1995).

[23] S. S. Harilal, C. V. Bindhu and H. J. Kunze, *Time evolution of colliding laser produced magnesium plasmas investigated using a pinhole camera*, J. Appl. Phys. 89, 4737 (2001).

[24] H. Zhang, J. Lu and X. Ni, *Optical interferometric analysis of colliding laser produced air plasmas*, J. Appl. Phys. 106, 063308 (2009).

[25] J. Dardis and J. T. Costello, *Stagnation layers at the collision front between two laser-induced plasmas: A study using time-resolved imaging and spectroscopy*, Spectrochim. Acta, Part B 65, 627 (2010).

[26] S. S. Harilal, M. P. Polek, and A. Hassanein, *Jetlike Emission From Colliding Laser-Produced Plasma*, IEEE transactions on plasma science, 39 (11) (2011).

[27] J. S. Ross, H. S. Park, R. Berger et. al., *Collisionless Coupling of Ion and Electron Temperatures*

in Counter-streaming Plasma Flows, Phys. Rev. Lett. 110 (14) (2013).

[28] C. Sanchez-Ake, F. Bredice and M. Villagran-Muniz, *Electric field-perturbation measurement of the interaction between two laser-induced plasmas*, Rev. Sci. Instrum. 83 (2) (2012).

[29] N. Gambino, P. Hayden, D. Mascali, J. Costello, C. Fallon, P. Hough, P. Yeates, A. Anzalone, F. Musumeci, S. Tudisco, *Dynamics of colliding aluminium plasmas produced by laser ablation*, Applied Surface Science 272, 69-75 (2013).

[30] T. Cummins, C. O'Gorman, P. Dunne, E. Sokell, G. O'Sullivan and P. Hayden, *Colliding laser-produced plasmas as targets for laser-generated extreme ultraviolet sources*, Appl. Phys. Lett. 105 (4), 1-5 (2014).

[31] Z. Yang, W. Wei, J. Han, J. Wu, X. Li and S. Jia et. al., *Experimental study of the behavior of two laser produced plasmas in air*, Phys.Plasmas 22, 073511 (2015).

[32] B. Kumar, R. K. Singh, S. Sengupta, P. K. Kaw, and A. Kumar, *Investigation of shock-shock interaction and Mach reflection in laterally colliding laser-blow-off plasmas*, Phys. Plasmas 22, 063505 (2015).

[33] U. Zastrau, E. J. Gamboa, D. Kraus and J. F. Benage et.al., *Tracking the density evolution in counter-propagating shock waves using imaging X-ray scattering*, Applied Physics Letters 109, 031108 (2016).

[34] A. Mondal, B. Kumar, R. K. Singh, H. C. Joshi and A. Kumar, *Spectroscopic investigation of stagnation region in laterally colliding plasmas: Dependence of ablating target material and plasma plume separation*, Phys. Plasmas 26, 022102 (2019).

[35] E. Irissou, F. Vidal, T. Johnston, M. Chaker, D. Guay, and A. N. Ryabinin, *Influence of an inert background gas on bimetallic cross-beam pulsed laser deposition*, J. Appl. Phys. 99, 034904 (2006).

[36] T. T. Lim and T. B. Nickels, *Instability and reconnection in the head-on collision of two vortex rings*, Nature 357, 225-227 (1992).

[37] Y. P. Raizer, V. I. Kisin, and J. E. Allen, *Gas Discharge Physics*, Springer, Berlin, Heidelberg (2011).

[38] Y. B. Zel'dovich and Y. P. Raizer, *Physics of Shock Waves and High-Temperature Hydrodynamic Phenomena*, Dover Publications, Academic Press Inc., New York (2012).

[39] Ch. Leela, S. Bagchi, V. Rakesh Kumar, S. P. Tiwari and P. Prem Kiran, *Dynamics of laser induced micro-shock waves and hot core plasma in quiescent air*, Laser Particle Beams 31 (02), 263–272 (2013).

[40] S. Sai Shiva, Ch. Leela, P. Prem Kiran, C. D. Sijoy, V. R. Ikkurthi, S. Chaturvedi, *Numerical investigation of nanosecond laser induced plasma and shock wave dynamics from air using 2D hydrodynamic code*, Phys. Plasmas 24, 083110 (2017).

[41] S. Sai Shiva, Ch. Leela, P. Prem Kiran, C. D. Sijoy, V. R. Ikkurthi, S. Chaturvedi, *Role of laser absorption and equation-of-state models on ns laser induced ablative plasma and shockwave*

dynamics in ambient air: Numerical and experimental investigations, Phys. Plasmas 26, 072108 (2019).

[42] Walker Bleakney and A. H. Taub, *Interaction of Shock Waves*, Reviews of modern physics 21, 584 (1949).

[43] B. Sitalakshmi, A. Vudayagiri, S. Sreedhar, and N. K. Viswanathan, *On-axis time-resolved spatial characterization of shock-induced refractive fringes in liquid water*, J. Opt. Soc. Am. B 30(8), 2206 (2013).

[44] F. F. Chen, *Introduction to Plasma Physics and Controlled Fusion Vol 1: Plasma Physics*, 2nd ed., Plenum Press (1984).

[45] L. Vinoth Kumar, E. Manikanta, Ch. Leela, and P. Prem Kiran, *Effect of laser intensity on radio frequency emissions from laser induced breakdown of atmospheric air*, Journal of Applied Physics 119, 214904 (2016).

[46] S. S. Harilal, B. E. Brumfield, and M. C. Phillips, *Lifecycle of laser-produced air sparks*, Phys. Plasmas 22, 063303 (2015).

[47] H. Nakajima, Y. Shimada, T. Somekawa, M. Fujita, and K. A. Tanaka, *Non-destructive sensor using microwaves from laser plasma by subnanosecond laser pulses*, IEEE Geosci. Remote Sens. Lett. 6, 718 (2009).

[48] J. S. Pearlman and G. H. Dahlbacka, *Emission of rf radiation from laser-produced plasmas*, J. Appl. Phys. 49, 457 (1978).

[49] J. A. Bittencourt, *Fundamentals of Plasma Physics*, 3rd ed. Springer (2004).

[50] R. Kodama, K. A. Tanaka, Y. Sentoku, T. Matushita, K. Takahashi, H.Fujita, Y. Kitagawa, Y. Kato, T. Yamanaka, and K. Mima, *Long-Scale Jet Formation with Specularly Reflected Light in Ultraintense Laser-Plasma Interactions*, Phys. Rev. Lett. 84, 674 (2000).

[51] D. R. Farley, K. G. Estabrook, S. G. Glendinning, S. H. Glenzer, B. A. Remington, K. Shigemori, J. M. Stone, R. J. Wallace, G. B. Zimmerman and J. A. Harte, *Radiative Jet Experiments of Astrophysical Interest Using Intense Lasers*, Phys. Rev. Lett. 83, 1982 (1999).

Chapter 4

Dynamics of Laser induced Blow-off plasma and shock waves in air

The formation and dynamics of the laser induced blow-off (LIBO) plasma is different from that of the laser ablative plasma (LAP). The confined LIBO studies were useful in understanding the shock wave processing of materials such as laser shock peening (LSP), where the transparent overlays such as glass, rubber and thin metal foil were used to confine the material plasma to enhance the shock wave pressure inside the material. But the shock wave enhancement inside material mainly depends on laser properties, confining material properties and the relative acoustic impedance of the confining layer and target material. Along with these properties, an efficient laser energy coupling to the material also plays a crucial role. Hence, a detailed understanding of the spatial and temporal behaviour of the laser induced blow-off (LIBO) plasma and shock waves (SW) is essential for applied research. Hence, in this chapter, the spatio temporal evolution of LIBO plasma and shock waves in ambient air from metal foils (Al, Cu and Ti) and polymer foils (PVA, Au doped PVA) confined with glass (BK-7) substrate is presented. This chapter gives an insight into the axial confinement of the plasma confined by the BK-7 glass substrate. The role of shifting of the laser beam focal plane on LIBO plasma and shock waves properties, aimed at achieving the optimal LIBO shock waves is also presented.

4.1 Introduction

When a nanosecond (ns) laser pulse with sufficient energy interacts with a solid surface, the plasma is produced by ablating the material. Laser ablation of solids with ns pulses of high intensity leads to complicated interactions of the laser beam with both the solid and the ablated material. There exist a number of processing parameters, which determine the dynamics of ablation and properties of the generated plasma [1, 2, 3]. The laser ablation is

of two types: Laser ablated Plasma (LAP) and Laser induced Blow-off (LIBO) plasma. In laser ablative plasma, a high power laser focused into a solid material, known as 'target', leads to the rapid ionisation and the generated plasma propagates in the opposite direction to the laser beam, i.e. normal to the target surface. Laser ablated/produced plasmas (LAP/LPP) were more interested in different fields because of its substantial applications to areas like inertial confinement fusion (ICF), X-ray lasers, material processing, plasma diagnostics, lithography, space applications and pulsed laser deposition etc [4, 5, 6, 7, 8, 9, 10, 11, 12, 13].

The more detailed explanation of laser ablated plasma (LAP) is given in the chapters 1 & 6. In contrast to LAP, the formation and dynamics of laser induced Blow-off plasma (LIBO) is different. The Figure 4.1 gives the schematic diagram to differentiate laser ablative plasma process and LIBO processes based on target geometry and thickness of the target. The Laser Induced Blow-off (LIBO) Plasma can be generated in two types: free blow-off mode and Confined blow-off mode [14, 15, 16, 17]. In free blow-off mode; the laser pulse directly interacts with the thin film/foil target and the produced plasma plume and shock waves propagates in the forward direction i.e., along the laser propagation direction. This process is also known as laser induced spallation technique [14, 15, 18, 19]. In confined blow-off mode, also known as laser induced forward transfer (LIFT) technique, the laser interacts with a substrate first, which is transparent to the laser wavelength before interacting with the thin film target which absorbs the laser beam. The thin film/foil may be coated or glued/adhered to the substrate. It can be either single layer or multi layer of several thousand Angstroms (A^o) thickness [16, 17, 20, 21, 22]. As the laser pulse is irradiated through the transparent substrate onto the thin film/foil, the pulse will be absorbed by thin film/foil and an expanding plasma cloud is formed. The interaction of sufficiently high intensity pulsed laser with thin film or thin foil targets confined with glass induces the material blow-off (plasma) or ejection of flyer from its rear side. The main mechanism involved in the laser induced blow-off (LIBO) technique is the mechanical confinement of thin films with other transparent materials like glass, black tape, water etc. [20, 23] which allows the confinement of the ablated plasma formed at the front surface of the target. As a result, the evolution of the plasma towards the laser propagation direction is obstructed by the confined material which resulted in the significant enhancement of the hydrodynamic efficiency. Due to this, very high pressures, temperature and density are generated along the laser affected region whose perimeter depends on the focused beam diameter [16, 17, 18, 21, 22, 23, 24]. Within short course of time, high stress waves are generated in this region that are launched onto the target front surface. When the magnitude of these stress waves exceed the shear strength of the material, then the unvaporized part ahead of the affected region ruptures, which eventually leads to the ejection of high velocity blow-off plasma and flyers in the laser propagation

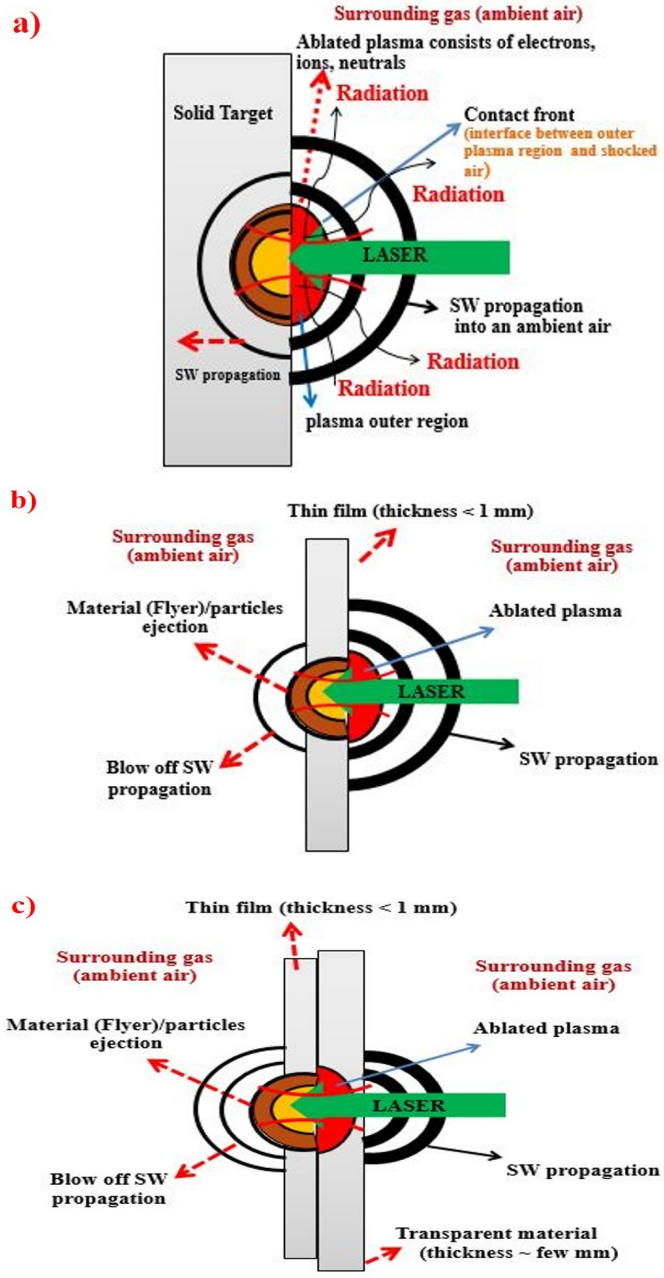

Figure. 4.1 Schematic diagram for (a) laser ablated plasma (LAP) process (b) direct LIBO process and (c) confined LIBO process

direction [25, 26, 27, 28]. According to Fabbro et. al. [16, 17], the confinement process will be described in three steps:

- **Heating Phase:** During the laser pulse duration, the absorbed laser energy is used to increase the internal energy of the plasma inside the interface (confining layer and target material interface) and the pressure generated by the plasma induces a shock wave which propagates into the target and the confining material. Thus, the generated pressure is higher for the same laser pulse properties in confining

geometry than direct ablation geometry.

- **Adiabatic Cooling:** When the laser is switched off, the plasma still maintains the high pressure which decreases during its adiabatic cooling. In confining geometry, the pressure is applied over a period much longer than the laser pulse duration. This will increase the impulse momentum delivered to the shock wave.

- **Macroscopic motion of finite targets:** Finally, for longer times, after the complete recombination of the plasma, the "canon-ball-like" expansion of the heated plasma inside the interface adds more momentum to the target. Since the target and the confining medium have finite thickness, they will experience a macroscopic "canon-ball" acceleration whose consequence will give the target an additional momentum.

If the target used was thick enough ($\sim$ few mm) in order to allow the propagation of the generated shock wave inside it. The confinement is explained using above three steps. If the target is very thin ($\sim$ few tens of nm to μm), in such a way that the transit time of the shock wave through it is smaller than the laser-pulse duration, the process of target acceleration is different. In thin foil target confinement, during the laser pulse the target is accelerated in a first step by the "canon-ball" expansion of the plasma, which is heated. After the laser pulse, the target is further accelerated by the adiabatic expansion of the plasma, as in the previous case. Thus, we will have acceleration of very thin foils known as *target/material flyers* having an area equal to or greater than the laser spot size for every laser shot, in the confinement of thin foil plasmas [29]. This technique has been investigated for years due to its important applications in many disciplines. From these studies it was well established both theoretically and experimentally that the hydrodynamic efficiency of the ablated and blow-off plasma at the front and rear side of the target depends on various parameters such as, target material used and its thickness, input laser intensity (energy), wavelength, pulse duration, beam size, focal length, confined substrate, surrounding ambient gas pressure conditions [22, 23, 24, 26, 30, 31, 32] and relative acoustic impedances of the film and confined materials [16, 17, 20, 29]. The conversion efficiency of the input laser energy to the film target also depends on other factors such as, roughness, adhesion etc. Although a lot of study has been done on the confined LIBO plasma and shock waves, the efficient coupling of the laser energy to the target material, which is crucial for enhancement of the LIBO shock wave properties is still inadequate. Zhao et al. [33] have used the fiber-coupled laser for the effective coupling of the input laser energy to the target film. The coupling of the laser energy depends on many factors. For example, Fabbro et. al. [16] have proposed an analytical expression of how the pressure scales up in the plasma region at the interface based on the conversation of energy which shows that the pressure depends on the absorbed intensity, wavelength

and pulse duration and impedances of the film and confined materials used. In confined ablation, the induced shock pressure inside the material depends on [16]:

$$P(GPa) = 0.01\sqrt{\frac{\alpha}{2\alpha+3}}\sqrt{Z(g/cm^2s^2)}\sqrt{I_0(GW/cm^2)} \tag{4.1}$$

Where P is pressure inside the material, α is the constant, Z is the relative acoustic impedance of the confining layer and target material, defined as $\frac{2}{Z} = \frac{1}{Z_1} + \frac{1}{Z_2}$ and I_0 is the input laser beam intensity at the interface. In contrast to the conventional dynamic loading tools such as gas gun, z-pinch, explosives etc. [34], this technique serves as the most convenient and sophisticated tool for the study of materials behaviour that undergo shock compressions, generation of EOS [35, 36, 37, 38, 39, 40, 41]. The confined LIBO is a volume absorption process, in which a homogeneous target, with laser absorption depth $\frac{1}{\alpha}$, where α is the absorption coefficient much larger than the thermal penetration depth $x_T = (\kappa\rho c\tau)^{1/2}$ [29, 42], where κ is the thermal conductivity, ρ is the density, 'c' is the specific heat of the target, absorbs most of the incident laser energy below the surface of the target. The minimum laser intensity required to create the blow-off in the confined geometry is given by [29, 42]:

$$I_{min} = \frac{240}{\tau^{0.55}}(MW/m^2). \tag{4.2}$$

Where τ is the laser pulse width (FWHM). Although much research have been done so far in order to understand the role of different parameters, there exist few concerns during the laser launched flyer plate. Holding the planarity of the flyer during its evolution plays a critical role in the determination of shock jump states accurately for EOS generation, acceleration of the flyer to higher velocities and effective coupling of the input laser energy to the film [26, 30, 31, 37, 38, 39, 40, 41] are some of the critical challenges. Other area where this technique can be majorly used is space application, where the study of interaction of micron sized flyers moving with very high velocities of few 10 km/s provide micro-thrust to the space vehicle [42, 43]. Laser impact welding (LIW) is another area of application where this technique is relevant, here two dissimilar materials can be assembled which is useful for the air-craft industry, electronics and medical device fabrication [44]. It is well known fact that, with increasing the input laser intensity the plasma pressure can be scaled up [37, 38, 39, 40, 41] and the flyers can be accelerated to higher velocities. However, at a certain threshold intensity the breakdown of the substrate takes place which alters the coupling of input laser energy effectively to the plasma and results in lowering of the hydrodynamic efficiency. The optical breakdown of the substrate with increasing intensity is one of those concerns occur frequently in the laser driven flyer experiments where not much have been focused. Previous studies performed so far have emphasized (focused) mainly on the issues related to the planarity of the flyer ejection, enhancement of the flyer and shock loading pressures and velocities.

In this chapter, we mainly focused on the issue related to the efficient coupling of the input laser energy to the target foils by simply varying/shifting the laser beam focal plane without changing any optics and laser parameters. The technique relies on the fundamentals of the laser focusing conditions. It is well established from the laser wave propagation physics that the Rayleigh length (Z_R) is the spatial extent of the laser intensity where its intensity becomes 1/e times that of the peak intensity focused at the focusing plane. We performed a systematic study on 20 μm thick aluminum and copper foils stuck on glass substrate for varying input laser energies (25 – 200 mJ) and different focusing conditions (F0, F1 and F2) so as to know the conditions where the blow-off of the plasma and flyer ejection takes place effectively. Upon optimizing laser energy and focusing conditions, these studies were further extended to 1.1 μm Cu, 200 nm Titanium, PVA (60 μm) and Au nano rods doped PVA (35 μm) thin films. The blow-off shock waves evolving in ambient air obtained from shadowgraphy images are compared for different focusing conditions to check the efficacy of LIBO plasma.

4.2 Experimental Details

The detailed experimental schematic for the Laser induced blow-off shock waves in air is given in chapter 2. The experiments were performed using second harmonic laser pulses from a Q-switched *Nd: YAG* laser (TITAN-5, M/s. Amplitude Technologies) operating at a wavelength of 532 nm, pulse duration of $\sim$ 10 ns (FWHM) and repetition rate of 5 Hz. Laser pulses ranging from 25–200 mJ energy distributed inside beam diameter of 22 mm were focused using an anti-reflection coated plano-convex lens of 150 mm focal length in f/7 geometry to initiate the breakdown of the thin foils and the subsequent physical processes. The corresponding peak intensities are in the range of 2.5 to 10 GW/cm^2. The M^2 value of Gaussian beam (spatially flat top) is measured to be $\sim$ 1.9 using Grasshopper M^2 camera (from $PointGreyResearch^{®}Inc.$) and the focal spot diameter (ω_0) is around $\sim 500 \pm 50\mu$ in the case of exact focusing at the interface between target film and glass substrate (F0 condition). The corresponding Rayleigh range (Z_R) is estimated theoretically to be $\sim$ 90 μm and experimentally it is taken as the distance (Z) at which the spot diameter ($\omega(Z)$) becomes $\sqrt{2} \times \omega_0$ i.e., $\sim$ 5 to 6 mm. The spatio-temporal evolution of blow-off plasma and subsequent shock front (SF) evolution into the surrounding ambient air from thin foil targets was captured using focused shadowgraphy technique with a probe beam of 47 mm and a fast ICCD camera with 1.5 ns temporal resolution and gate delays from 50 ns to 10 μs in steps of 200 ns gate delay [45, 46]. The experiments were carried for 20 μm thick Al and Cu films stuck on glass substrate of $\sim$1.8 mm thick and further extended to Cu thin film (1.1 μm), Titanium (200 nm) metal films and in house developed dielectric films PVA (10%wt) (60 μm), Au nano rods doped PVA (Au nano rods + 10%wt PVA) (35 μm) thin films ensuring that the laser beam is focused at the desired location.

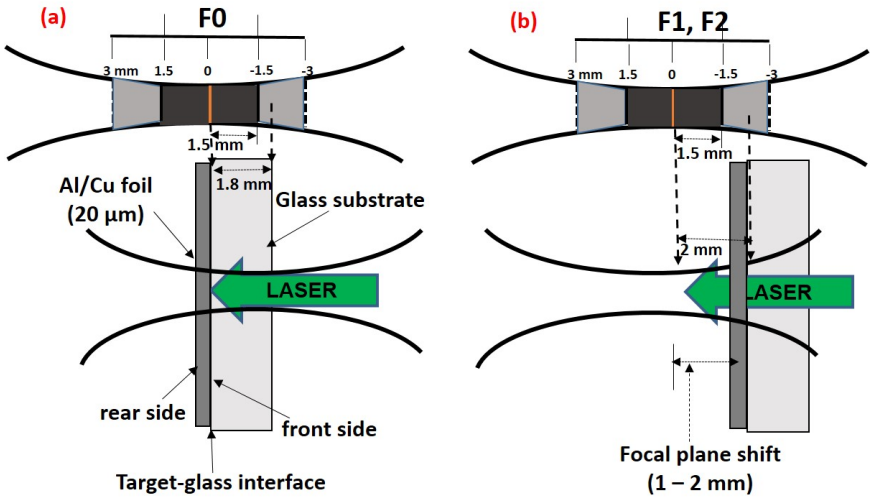

Figure. 4.2 Schematic of laser blow-off from thin foil confined with glass substrate for focusing conditions at (a) exactly on the glass-foil interface (F0) and (b) 1 and 2 mm deep (F1 and F2) from the glass-foil interface.

Figure 4.2(a-b) illustrates the schematic of laser interaction of thin foils or films confined with glass substrate for three different focusing conditions. The caustic curves shown in the Figure 4.2(on the top) represent the laser focusing plane. In the first case i.e., Figure 4.2(a), the laser beam is focused at the interface of the glass substrate and thin foil (Al, Cu, Ti and PVA); and is called herein after as F0 condition. Whereas, in the second and third case i.e., Figure 4.2(b), the laser beam is focused (or the laser focal plane is shifted) at a depth of 1 mm and 2 mm (called as F1 and F2) respectively from F0 focal position ensuring that the laser focal plane is far ahead of 20 μm thin film. Since the focal plane of the laser beam in the F2 condition is shifted, the intensity at the glass-film interface will be lower than that of F0 condition as the Rayleigh range is out of the glass thickness (1.8 mm)used.

4.3 Shadowgraphy imaging of the Laser Blow-off plasma from metal foils

When the laser is focused on to the target material, material temperature increases because of the conversion of optical energy to the thermal energy of translational motion of the molecules inside the target. Since the mechanical relaxations in the material are slower than the temperature rise, nearly a constant volume is heated thus the pressure is increased at that point. When the pressure gradient exceeds the mechanical strength of the material along normal to the target surface, it causes spallation of the material and a flyer (small pieces of the target material with area equal to the laser spot size) will be ejected along the laser direction [25, 26, 27, 28]. In the confined blow-off method, in addition to the pressure build up due to inertial confinement, rapid increase in the

thermal energy of the target material leads to the overheating of the system. If the target heated close to the critical temperature, a phase explosion (explosive boiling) occurs where the ablated solid target will be in gaseous state of individual molecules and clusters of molecules. This phase explosion increases the overall pressure and also provides the fast cooling of the ejected plasma which leads to the higher flyer velocities [16, 17]. Initially,

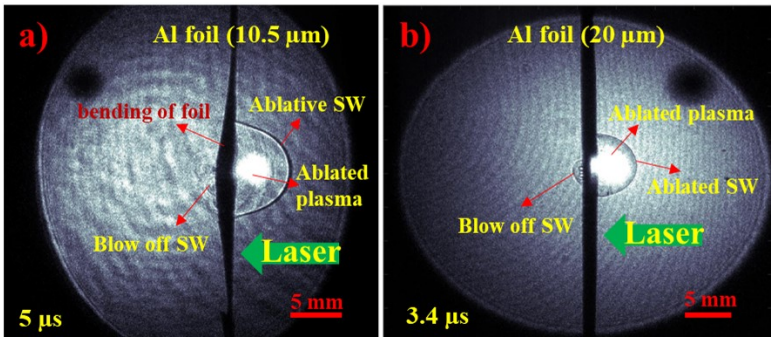

Figure. 4.3 Shadowgrams of the laser induced blow-off plasma from the rear side of (a) ≈ 10-11 μm Al foil (b) 20 μm Al foil targets at 500 mJ laser energy for F0 focusing condition.

the laser ablated blow off plasma and shock waves from ≈ 10-11 μm Al foil in direct LIBO geometry were captured using focused shadowgraphy technique with F0 condition for 500 mJ laser energy as shown in Figure 4.3 (a). When laser beam interacting with ≈ 10-11 μm Al foil alone in direct (unconfined) LIBO geometry, although the laser ablative plasma and shock waves are observed, we have not observed efficient blow off plasma from the foil due to the bending of the Al foil for input laser energies. This is due to the smaller thickness of the foil i.e., 10-11 μm and it is really difficult to hold the Al foil flat along the horizontal and vertical directions without bending using the target holder. For the input laser energy variation from 25 to 1 J also, we have not observed the prominent blow off plasma and shock waves. The same experiment was repeated with the much thicker Al foil of 20 μm in direct LIBO geometry with F0 focusing condition as shown in Figure 4.3 (b). Though we have not observed any wobbling of the 20 μm Al foil due to the laser beam interaction, we have not observed the blow off plasma efficiently for input laser energies 25 to 1 J energy but we have randomly observed the shock waves from the rear side of the foil. In order to observe the efficient plasma and shock waves from 20 μm Al and Cu foils, we have chosen the confined LIBO geometry. In this geometry, the 20 μm Al and Cu metal foils were adhered to the glass substrate of 1.8 mm thickness. The temporal evolution of the confined LIBO plasma and shock waves from 20 μm Al and Cu foils were captured using the focused shadowgraphy technique with different focusing conditions (F0, F1 and F2) as shown in Figure 4.4 (a-d). Figure 4.4 (a-d) shows a series of shadowgraphy images of 20 μm Al and Cu foils confined with glass substrate for F0 and F2 focusing conditions at different instants of time over 0.05 – 6.85 μs at 25 mJ input

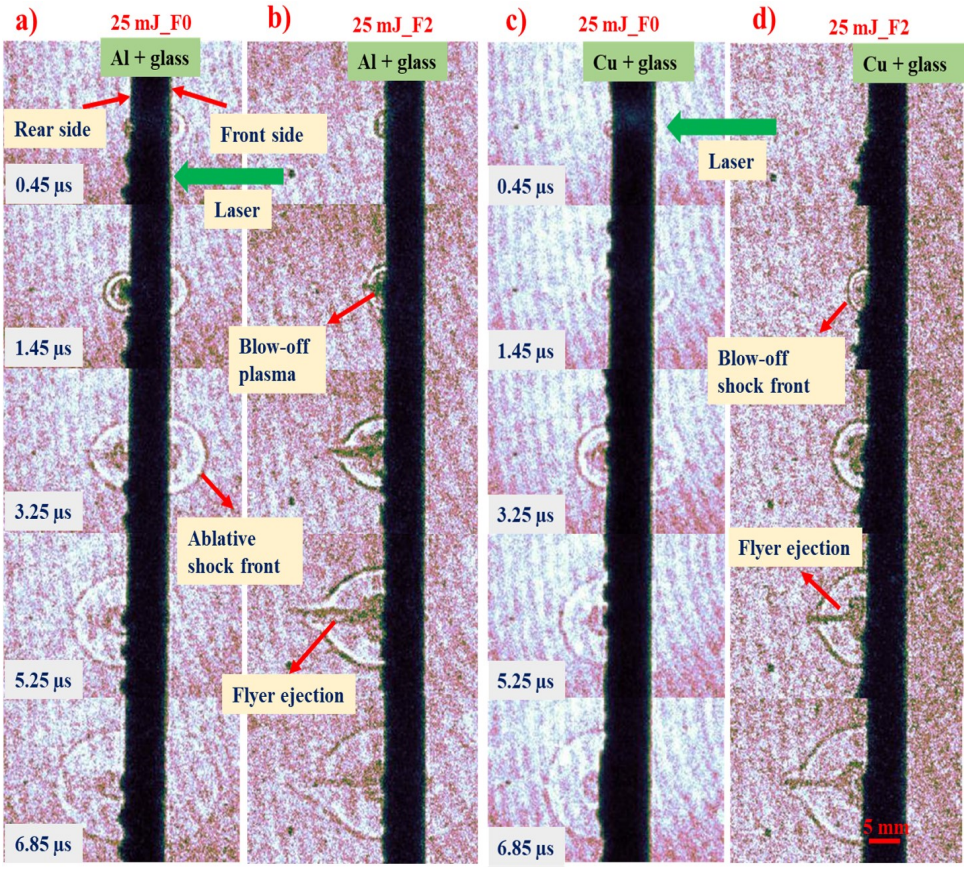

Figure. 4.4 Shadowgrams of the laser induced blow-off plasma from the rear side of 20 μm (a-b) Al and (c-d) Cu foil targets at 25 mJ laser energy for F0 and F2 focusing conditions

laser energy respectively. The front side in the images represent the glass substrate facing the incoming laser pulse, also mentioned as ablative side. The other side represents the Al and Cu foil, mentioned as blow-off side.

4.3.1 Effect of F0 focusing condition

As observed from Figure 4.4 (a) with F0 focusing condition, the plasma blow-off from the rear surface of 20 μm Al foil begins at early times of 0.05 μs. Consequently, an ablative plasma and the corresponding shock wave (SW) expands into the glass target as well as into the ambient air from the front surface. Since our aim is to study the confined LIBO plasma and shock wave properties, we have not provided the corresponding laser ablative plasma and shock waves from the front surface (i.e., from glass) in this chapter. At the rear side of the foil, as the time progresses a small dent and wobbling of the foil occur at 0.45 μs through which the driving plasma blows-off rapidly. Later on at 1.45 μs, due to very high pressure plasma expanding rapidly in to the ambient air the blow off shock wave is launched into the ambient air ahead of the plasma front at the rear side of the Al foil. The blow off shock wave propagates with a higher velocity than the blow off

plasma front F0 focusing condition. At 3.25 μs the expansion of the shock wave at both sides (blow-off and ablative) of the target surface becomes similar (i.e., semi spherical), however the plasma at the front surface is unable to expand further, whereas the plasma at the rear surface spills out and expands freely in to the ambient air.

In the case of 20 μm Cu foil interaction with laser energy of 25 mJ in F0 focusing condition (Figure 4.4 (c)), we observed the similar expansion features as that observed from 20 μm Al foil. However the expansion of the blow-off plasma and the subsequent shock wave was higher compared to that of Al foil as shown in Figure 4.5 (a) at the initial time scales i.e., from 0.45 to 1.05 μs. This may be due to the higher relative acoustic impedance of glass and Cu foil, as the shock velocity is mainly depends on the relative acoustic impedance Z and laser intensity I_0 in confined geometry [16, 17, 20]. At later time scales (> 1.25 μs) the blow off shock wave velocity of Cu foil is less than that from the 20 μm Al foil blow off shock velocity through out the observed time. This suggests that the Cu blow off shock velocity decreases faster than the 20 μm Al foil blow off velocity as shown in Figure 4.5 (a).

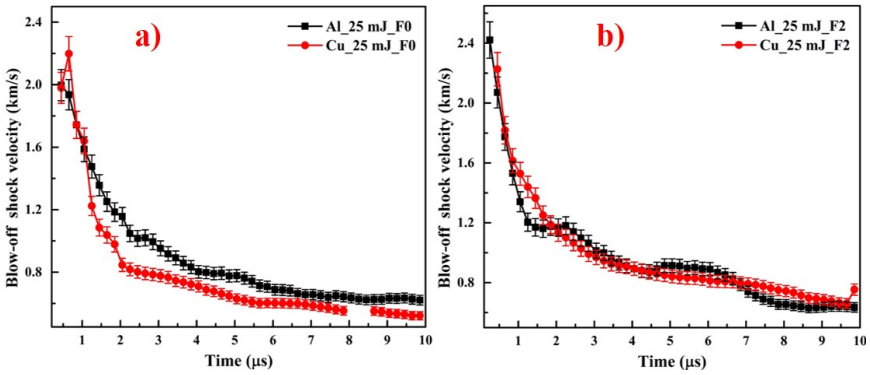

Figure. 4.5 Temporal evolution of laser blow-off shock wave from rear side of 20 μm Al and Cu foils (a) in F0 (b) in F2 focusing conditions at 25 mJ laser energy.

4.3.2 Effect of F2 focusing condition

When the laser focus plane is shifted to F2 focusing condition (2 mm deep into the glass-foil interface) in the case of the 20 μm Al foil, the blow-off of the plasma as well as the ablation at the front surface was not observed at early times of 0.05 μs due to the low laser intensity at the interface. Unlike the F0 condition we didn't observed any wobbling formed at the rear surface, the blow-off plasma and shock wave expansion begins at 0.45 μs as shown in Figure 4.4 (b). Since the area of cross-section of the laser affected zone on the target surface is higher for F2 condition, the diameter of the blow-off region is higher hence, the lateral heat transport happens across this region. As a result, the confined plasma generated at the interface finds ample area to escape out from the rear surface. Hence, we observe larger blow-off area for F2 condition as shown in Figure 4.9. During this time, a small fragment of the target foil in the form of mini-flyers may also have

been ejected. With the shadowgraph diagnostic technique we could not able to clearly determine the presence of the flyer. The rising of sharp tip along the laser axis indicates the rapid expansion of the flyer that is accelerated to a much higher velocities than the shock front. The flyer and plasma debris ejection is observed from 20 μm Al foil at ~1.45 μs in the form of a very sharp cone along the laser axis, which was not seen in the F0 condition. This cone shape indicates that the ejected flyer and plasma debris accelerates with higher velocity than the blow off shock wave. The ablative plasma and shock wave from glass surface (or front surface) is observed to be negligible in F2 configuration for 25 mJ of laser pulse energy used. In the case of Cu thin foil in F2 focusing condition (Figure 4.4 (d)), the flyer ejection was faintly visible at ~ 1.45 μs and the acceleration of the ejected flyer begins after 3.25 μs. Figure 4.5 (b) shows the temporal evolution of blow-off shock wave velocities from Al and Cu thin films in F2 focus condition at 25 mJ laser input energy. From Figure 4.5 (b), we can observe that the blow off shock velocities for 20 μm Al and Cu foils are almost similar (within error bars) in F2 focusing condition and both the shock waves has same decreasing trend throughout the observed time.

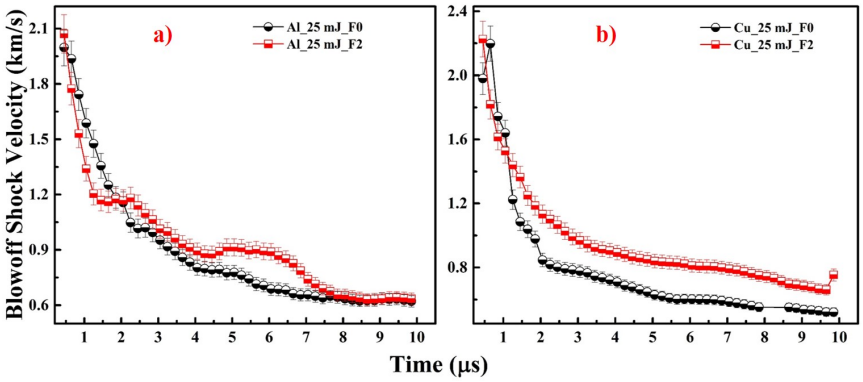

Figure. 4.6 Temporal evolution of laser blow-off shock waves from rear side of 20 μm (a) Al and (b) Cu foils in F0 and F2 focusing conditions at 25 mJ laser energy.

Figure 4.6 (a-b) shows temporal evolution of blow-off shock wave velocities from (a) 20 μm Al and (b) 20 μm Cu foils in F0 and F2 focus conditions for 25 mJ input laser energy. From Figure 4.6 (a), the blow off shock velocity from 20 μm Al foil is almost equal at 0.45 μs in F0 and F2 focusing conditions but for time scales > 0.45 μs the shock velocity is sharply decreased up to 2 μs and later it is slightly increased over the observed time with maximum increment happened around 4 to 7 μs in F2 focusing condition compared to F0 focusing condition. Due to the focal plane shifting, the peak intensity at the interface is less thus creating less density plasma with higher blow off diameter (i.e., $\approx$ equal to the laser beam spot size in F2 condition) lead to the initial decrease in shock velocity in F2 focusing condition. Since, the flyer initiation is happened around 1.45 μs, after 2 μs only we have observed the smaller shock velocity increment at 25 mJ energy. From Figure

4.6 (b), the blow off shock velocity from 20 μm Cu foil is increased at 0.45 μs but it is decreased upto 1.2 μs and for time scales > 1.45 μs, the blow off shock velocity is higher for 25 mJ energy in F2 focusing condition compared to F0 focusing condition. This is due to the fact that, although the increased laser absorption area (i.e., equal to spot size in F2 condition) lead to the decrease in the shock velocity in F2 focusing condition, the flyer ejection from blow off plasma and debris greatly increased the blow off shock velocity for 25 mJ energy.

4.3.3 Effect of the input laser energy on blow off shock waves in F0 and F2 focusing conditions

In the F0 condition, the expansion of the shock wave increases with the input laser energy for 25 and 50 mJ, but when the energy is increased to 200 mJ ($\sim$ 10 GW/cm^2) the optical breakdown of the glass substrate occurs due to laser beam intensity exceeding the breakdown threshold intensity of the glass ($\sim$ 3-9 GW/cm^2) [14, 15]. This phenomenon

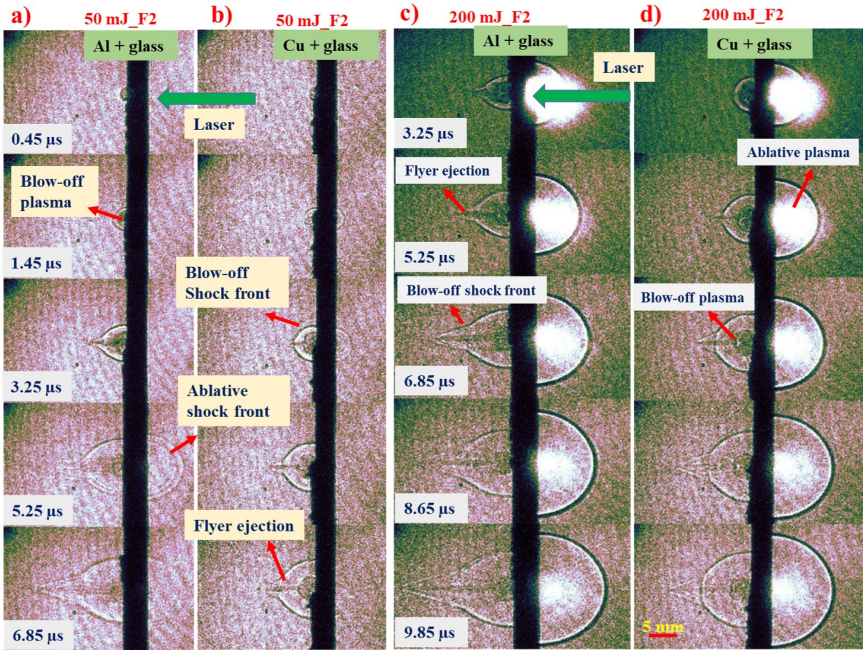

Figure. 4.7 Shadowgrams of laser blow-off plasma and shock waves from rear side of (a,c) Al and (b,d) Cu foils for F2 focusing condition at 50 mJ and 200 mJ respectively

alters the coupling of input laser energy to the thin foil, which results in lower blow off shock wave expansion at 200 mJ than that of 25 and 50 mJ input laser energies. Figure 4.7 (a-d) compares the shadowgrams of 20 μ Al and Cu foil at higher input laser energy of 50 mJ and 200 mJ in F2 focusing condition. For 200 mJ energy, due to the intensified radiation emissions from the plasma region, the evolution of plasma, shock wave and flyer from the foil surface was not clearly visible during the initial times of < 1.45 μs as the ICCD was saturated; only after > 1.45 μs the evolution is clearly observable. For 200 mJ energy, the ablation of the glass plate also causing the high ablative shock velocity

opposite to laser propagation direction. Figure 4.8(a-b) shows the temporal evolution of blow-off shock velocities from Al and Cu thin foils for 25, 50 and 200 mJ energies in F0 and F2 focusing conditions at 0.85, 1.05 and 1.45 μs time scales. Table 4.1 illustrates the blow-off shock velocity comparison from Al and Cu thin foils at 1.45 μs for 25, 50 and 200 mJ at F0 and F2 focusing conditions, respectively. As observed from Figure 4.8 (a),

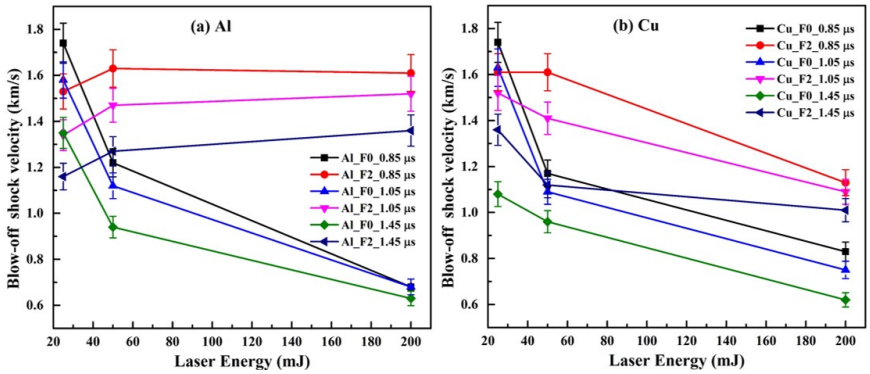

Figure. 4.8 Temporal evolution of the laser blow-off shock waves from 20 μm (a) Al and (b) Cu thin foils in F0 and F2 focusing conditions at 25, 50 and 200 mJ energies respectively.

in the case of F0 condition, the blow off shock velocity from 20 μm Al foil decreases with increasing the input laser energy from 25 to 200 mJ. In the case of F2 focusing condition, the blow off shock velocity from Al foil increases with increasing laser energy from 25 to 200 mJ. The blow off shock velocities from Al foil is observed to be increased by a factor of 1.5 to 2 times for 50 mJ energy and 2 to 3 times for 200 mJ energy in F2 focusing condition compared to F0 focusing condition except for 25 mJ energy. For 25 mJ energy, the blow off shock velocity is higher in F0 focusing condition. The decrease in the blow off shock velocity for 50 and 200 mJ in F0 focusing condition, is due to the decrease in coupling of the input laser energy to the target foil as a part of the energy is utilized in the breakdown of the glass substrate which eventually altering the laser pulse energy reaching the glass-metal interface. The blow off shock velocities from 20 μm Al foil at 1.45 μs, given in the Table 4.1 also shows the same. Figure 4.8 (b) shows the temporal evolution

Table 4.1 Effect of F0 and F2 focusing condition on the blow-off shock velocities from Al and Cu thin foils at 1.45 μs delay time with varying energy

Energy (mJ)	**Al Shock velocity (km/s)**		**Cu Shock velocity (km/s)**	
	F0	F2	F0	F2
25	1.35	1.16	1.08	1.36
50	0.94	1.27	0.96	1.12
200	0.63	1.36	0.62	1.01

of the blow off shock wave velocities from 20 μm Cu foil in F0 and F2 condition for 25 to 200 mJ laser energies at 0.85, 1.05 and 1.45 μs time scales. In Cu thin foil case, we have observed higher blow off shock velocities in the F2 condition than shock velocities in F0 condition for 25, 50 and 200 mJ laser energies as shown in Figure 4.8 (b). As the laser energy increases from 25 to 200 mJ, the blow off shock velocity from Cu foil decreases with increasing the laser input energy in F0 focusing condition. In F2 focusing condition also, the blow off shock velocity decreases with increasing the laser input energy from 50 and 200 mJ but for 25 mJ energy it showed mixed behaviour. For 25 mJ energy, the blow off shock velocity decreases at 0.85, 1.05 μs but increases at 1.45 μs in F2 focusing condition compared to F0 condition. This may be due to the initiation of the flyer at 1.45 μs and also increase in the blow off diameter from the Cu foil. The blow off shock velocities from 20 μm Cu foil at 1.45 μs, given in the Table 4.1 also shows the same.

4.3.4 Morphology of the blow off region from the foils

The shadowgraphy technique we used in the experiment can visualize the evolution of the plasma and shock wave dynamics. It is difficult to capture the motion of the flyer, its nature of expansion and its dimensions (diameter and thickness) during the evolution with the current diagnostic technique. Hence to get the information of how the flyer diameter varies with energy and with the focusing conditions we performed post experiment analysis by estimating the average blow-off diameter using an optical microscope.

Figure 4.9 (a-d) shows the image of the blow-off regions from both Al and Cu foils for 25,

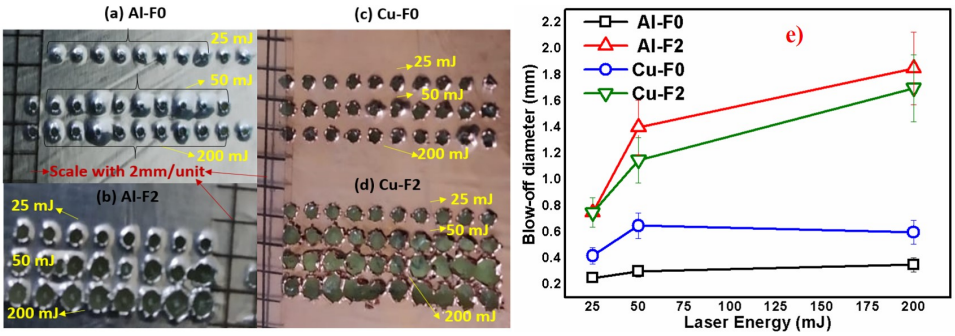

Figure. 4.9 Variation of average blow off diameter of 20 μm Al and Cu foils for different energies at F0 and F2 focusing conditions

50 and 200 mJ laser energies compared with F0 and F2 focusing conditions, respectively. As observed from Figure 4.9 (e), the average blow off diameter of Al thin foil in F0 focusing condition (Figure 4.9 (a)) varied as 0.25, 0.3 and 0.35 mm for 25, 50 and 200 mJ, respectively. In this case, with increasing energy the wobbling of the thin foil around the laser affected perimeter is observed due to which the average blow off diameter does not increase much with energy. When the focusing plane shifted F2 condition (Figure 4.9 (b)), no such wobbling were observed and the average blow off diameter is significantly increased compared to that of the F0 condition. The average blow off diameter in F2 configuration

varies as 0.75, 1.4 and 1.85 mm for 25, 50 and 200 mJ laser energies, respectively (from Figure 4.9 (e)). The average blow off diameter of the Al foil in F2 configuration has increased by a factor of three times for 25 and 50 mJ, respectively and five times for 200 mJ than that of F0 condition.

In the case of Cu thin foil, for the F0 focusing condition, the average blow off diameter increased from 0.42 mm to 0.65 mm, respectively for 25 and 50 mJ, and slightly decreased to 0.6 mm at higher energy of 200 mJ (Figure 4.9 (e)). With F2 focusing condition, it varies as 0.75, 1.15 and 1.7 mm respectively for 25, 50 and 200 mJ laser energies. The average blow-off diameter in F2 focusing condition is observed to be increased by a factor of two for 25 and 50 mJ, respectively and three times for 200 mJ compared to the F0 focusing condition. Overall, when the average blow-off diameter is compared between Al and Cu foils, with F0 condition Cu foil is observed to have the blow off diameters 0.42, 0.65 and 0.6 mm, which is almost two times higher than that of Al foil i.e., 0.25, 0.3 and 0.35 mm, for the 25, 50 and 200 mJ laser energies. Similarly, with F2 condition, this is observed to be almost similar for both Al (0.75, 1.4 and 1.85 mm) and Cu (0.75, 1.15 and 1.75 mm) foils. So the effective enhancement in the flyer diameter is observed to be more significant in the case of Al foil with F2 condition.
To understand the hydrodynamics of the blow-off plasma and shock evolution and to explore the reasons for an ineffective coupling of laser energy to the foil at higher energies, we have performed the one-dimensional numerical simulations using modified MULTI-fs radiation hydrodynamic (1D-RHD) code [47, 48]. The simulated shock radius shows good agreement with the experimental results [48]. The simulation results predicted that, due to the breakdown of glass (confining substrate) the plasma number density increased in F0 case leading to an ineffective coupling of laser energy to the material. The shift in the laser focus conditions from F0 to F2 condition shows that, one can avoid achieving an over dense regime and optimize the coupling of laser energy to the foil [48]. The simulation results are not given in this thesis.

4.4 Shadowgraphy imaging of Laser Blow-off plasma from metal thin films

Since the effect of focal plane shifting to F2 condition is more efficient in 20 μm Al and Cu foils with 50 mJ energy, the LIBO studies are further extended to the Cu thin film 1.1 μm and Ti thin film of 200 nm thickness coated on glass substrate are studied in F0, F1 and F2 focusing conditions at 25, 50 mJ laser input energies. Figure 4.10 (a-c) shows the shadowgrams of the temporal evolution of the blow off plasma and shock waves from 1.1 μm Cu thin films in F0, F1 and F2 focusing conditions at 25 mJ laser input energy. The thickness of the Cu thin film coated on the glass substrate is measured using profilo meter study as shown in Figure 4.10 (d) and the 1.1 μm Cu thin film before and after the

LIBO experiment is given in the Figure 4.10 (e).

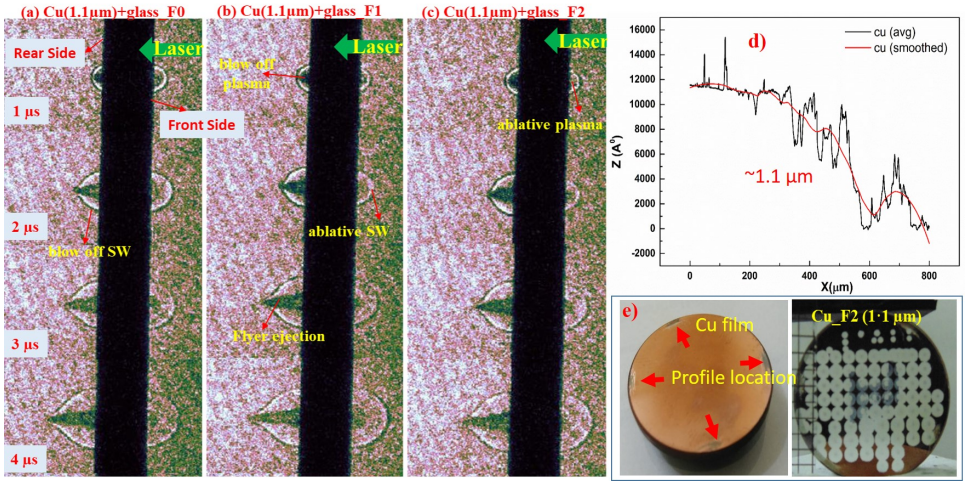

Figure. 4.10 Shadowgrams of the laser blow-off plasma and shock waves from rear side of 1.1μm Cu thin film in F0, F1 and F2 focusing condition at 25 mJ laser energy.

From Figure 4.10 (a-c), the blow off plasma and shock waves from 1.1 μm Cu thin film were visible only from 1.05 μs in F0, F1 and F2 focusing conditions, because of the shadow of the target holder as well as glass substrate thickness. At 1.05 μs the blow off plasma and blow off shock wave at the rear side of the target as well as ablative plasma and ablative shock wave at the front surface of the target are observed for all the three focusing conditions. After 2.05 μs time scales, we have observed the ejection of flyer/plasma debris in the form of cone shape which has higher velocity than the blow off shock wave in F0 condition and in F1 and F2 conditions also. Due to the smaller thickness of the Cu foil (1.1 μm), it is hard to focus the laser beam at the exact interface. In F2 focusing condition, the ablative plasma and shock wave from the target front surface is less than F0 and F1 focusing conditions. Figure 4.11 (a) shows the temporal evolution of the blow off shock waves from 1.1 μm Cu thin film in F0, F1 and F2 focusing conditions at 25 mJ and 50 mJ laser energy. Figure 4.11 (b) shows the blow off shock velocities from 1.1 μm Cu compared to the 20 μm Cu shock velocity in F0 and F2 focusing conditions at 25 mJ energy. From the Figure 4.11 (a), it is evident that the blow off shock velocity from 1.1 μm Cu foil is higher for F1 focusing condition compared to the F0 and F2 focusing condition at 25 mJ laser energy. As the energy increased from 25 mJ to 50 mJ, the increment in the blow off velocity from 1.1 μm Cu film is is clearly visible in F1 focusing than F2 condition, suggesting that F1 focusing condition is optimal for LIBO of the thin films. The smaller thickness of the film leads to the formation of air plasma along with material plasma in F2 focusing condition. Hence the blow off shock velocities are lower in F2 focusing condition than F1 condition. When the blow off shock velocities from 1.1 μm foil compared to the 20 μm Cu foil, initially the blow off shock velocities are $\sim$ 1.5

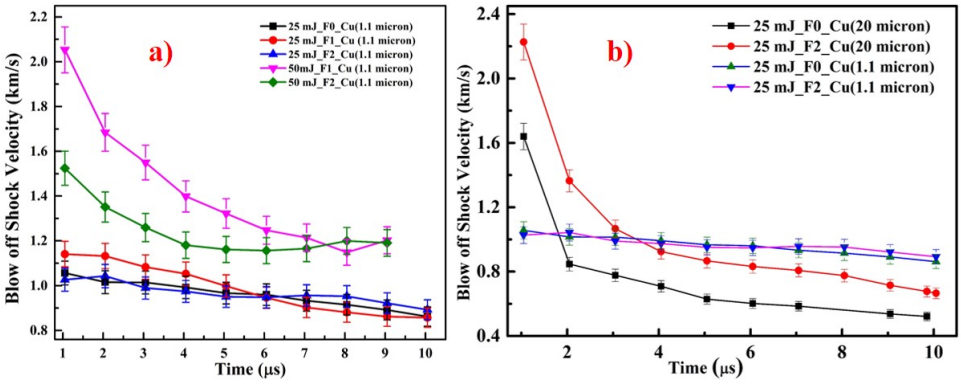

Figure. 4.11 Temporal evolution of the laser blow-off shock waves from 1.1μm Cu thin film (a) in F0, F1 and F2 focusing condition at 25 mJ and 50 mJ laser energy (b) compared to the 20 μm Cu foil blow off shock velocity at 25 mJ.

times higher for 20 μm Cu foil up to $\leq$ 2 μs due to the ejection of flyer. At later time scales $>$ 2 μs, the blow off shock velocities are $\sim$ 1.5 to 2 times higher for 1.1 μm Cu thin film compared to 20 μm Cu foil as shown in Figure 4.11(b). The evolution trend of the 1.1 μm Cu thin film is linear but it follows 1/r for 20 μm Cu foil.

The studies are further extended to get an insight into the effect of systematic shifting of focal plane from F0 to F1 and F2 condition in LIBO of nano meter (nm) thin films. A Ti film with 200 nm thickness is used for LIBO studies with 25, 50 mJ laser energy. Figure 4.12 (a-c) shows the shadowgrams of the temporal evolution of the blow off plasma and shock waves from 200 nm Ti thin films in F0, F1 and F2 focusing conditions at 25 mJ laser input energy. The thickness of the Ti thin film coated on the glass substrate is measured using profilo meter as shown in Figure 4.12 (d). The 200 nm Ti thin film before and after the LIBO experiment is given in the Figure 4.12 (e). From Figure 4.12

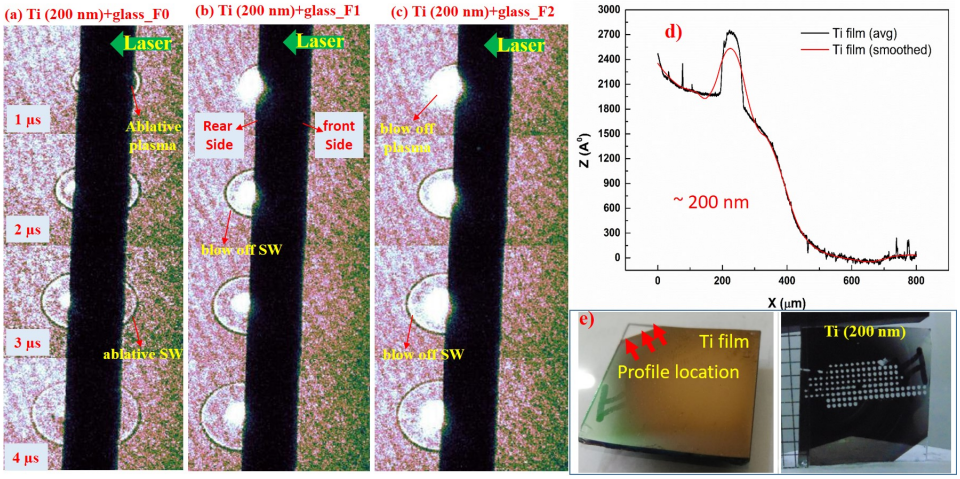

Figure. 4.12 Shadowgrams of the laser blow-off plasma and shock waves from rear side of 200 nm thin film in F0, F1 and F2 focusing condition at 25 mJ laser energy.

(a-c), the blow off plasma and shock waves from 200 nm Ti thin film were visible only from 1.05 μs in F0, F1 and F2 focusing conditions, because of the shadow of the target holder. At 1.05 μs the blow off plasma and blow off shock wave at the rear side of the Ti film as well as ablative plasma and ablative shock wave at the front surface of the Ti film are observed in F0 focusing condition. Since the thickness of the Ti film is in nm, we have not observed any flyer/plasma debris at later time scales. In F1 focusing condition, the blow off plasma is higher compared to F0 condition at 1.05 μs and the blow off shock wave expansion is observed at later time scales ($>$ 1.05 μs) with hemi-spherical shock structure. We have observed the ablative shock wave only after 6 μs in F1 condition. In F2 focusing condition, the blow off plasma is higher than F0 and F1 condition at 1.05 μs time scales and we have not observed any ablative shock wave at the front side of the target at all. Figure 4.13 (a-b) shows the temporal evolution of the blow off shock waves from 200 nm Ti thin film in F0, F1 and F2 focusing conditions compared to the 1.1 μm Cu foil at 25 mJ laser energy and Figure 4.13 (b) shows that the blow off shock velocities from 200 nm Ti film in F0, F1 and F2 focusing conditions at 50 mJ energy.

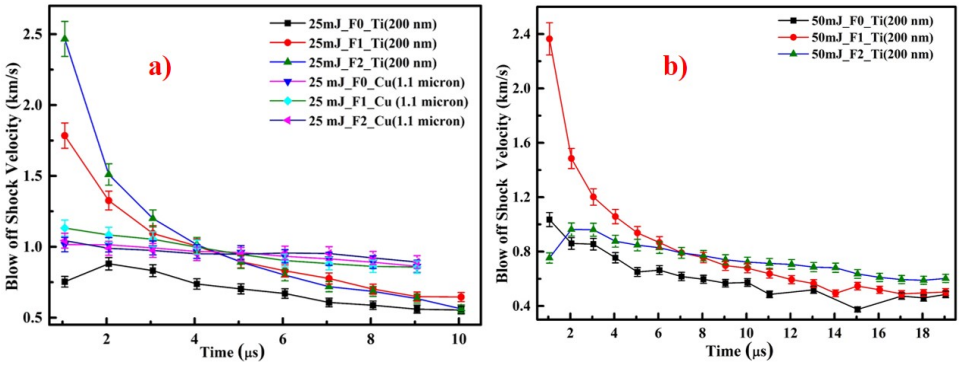

Figure. 4.13 Temporal evolution of the laser blow-off shock waves from 200 nm Ti film (a) compared to 1.1 μ Cu film at 25 mJ energy (b) at 50 mJ in F0, F1 and F2 focusing conditions.

From the Figure 4.13 (a) it is evident that, at initial time scales ($<$ 4 μs) the blow off shock velocities are $\sim$ 2 times higher in F2 focusing condition than F0 condition for 25 mJ energy. The blow off shock velocity is higher in F2 focusing condition than F1 condition until 3 μs time scales after that they are similar. When the blow off shock velocities from 200 nm Ti thin film are compared to the 1.1 μm Cu foil, the blow off shock velocities from 200 nm Ti film are $\sim$ 2 to 3 times higher in F2 focusing condition than 1.1 μm Cu foil at 25 mJ energy. The blow off shock velocities from 200 nm Ti foil follows 1/r relation but the blow off shock waves from the 1.1 μm Cu foil follows linear relation. While for 50 mJ energy, the blow off shock velocities from 200 nm Ti foil in F1 focusing condition is higher than F0 and F2 condition as shown in Figure 4.13 (b). Since the film thickness is too small (i.e., nm), the shifting of focal plane from F0 to F2 condition at higher energy

(50 mJ) lead to the formation of air plasma along with material plasma at the rear side of the film. Hence, at initial time scales (< 8 μs) lower blow off shock velocities are observed in the F2 condition with 50 mJ energy.
The LIBO shock wave velocities from all the metal foil/films studied are summarized in Table 4.2 in F0, F1 and F2 focusing condition for 25 and 50 mJ laser energy at 1.05 μs time scale respectively. From the Table 4.2, it is evident that the blow off shock velocities

Table 4.2 The LIBO shock wave velocity of Ti (200 nm) and Cu (1.1 μm) thin films were compared to the Al, Cu foils (20 μm) at 1.05 μs

Energy	**Ti (km/s)**			**Cu (1.1μm) (km/s)**			**Al (km/s)**		**Cu (km/s)**	
(mJ)	*F0*	*F1*	*F2*	*F0*	*F1*	*F2*	*F0*	*F2*	*F0*	*F2*
25	0.7	1.78	2.46	1.05	1.14	1.02	1.58	1.34	1.63	1.52
50	1.03	2.36	0.75	-	2.05	1.52	1.12	1.47	1.09	1.41

are higher for 200 nm Ti thin film compared to Al and Cu foils/films. It is also evident that, for higher blow off shock velocity at lower energy (25 mJ), F2 focusing condition is suitable and for higher energy (50 mJ) and F1 focusing condition is better in the case of 200 nm Ti thin film.

4.5 Shadowgraphy imaging of laser Blow-off plasma from polymer films

Upon optimizing the laser focusing conditions w.r.t. laser energy for higher blow off velocities from metal foils/films, the studies are further extended to the polymer samples as the LIBO shock waves has specific application towards laser propulsion [29, 42, 43]. The main goal of this chapter is to increase/enhance the blow-off shock velocities with similar or less laser energy by obtaining higher flyer ejection. By varying the laser focusing conditions the enhancement in the blow-off shock velocities were achieved as discussed above. In addition to the focusing conditions, the blow-off shock wave efficiency is further enhanced using different target materials. Only materials with low thermal conductivity i.e., polymers, were suitable targets because they have low ablation threshold and better thermal diffusion than metals [42]. The laser blow-off study of polymers are very useful in organic photo chemistry, lithography, laser ablative micro propulsion and micro thruster experiments etc [49, 50, 51, 52, 53, 54].
Commercially available poly vinyl alcohol (PVA) powder (From *Sigma Aldrich*®) is mixed with deionized water to get PVA solution with 10 %wt PVA. The PVA nano fibres are extracted from PVA solution (10%wt) by Electro spinning method (Instrument model: ESPIN-NANO, India). The 10%wt is maintained through out the process to get in house

developed 10%wt PVA polymer film consisting PVA nano fibres of few mm to cm length. Figure 4.14 (a) show the FESEM (Instrument model: Ultra 55 from Carl Zeiss at 30 kV) image of the electro spun PVA nano fibres having 274 ± 32 nm diameter and few mm to cm length [55]. Figure 4.14 (b) shows the thickness of the 10%wt PVA nano fibre film measured using profilo meter and it is about ~ 60 μm. To understand the blow-off shock

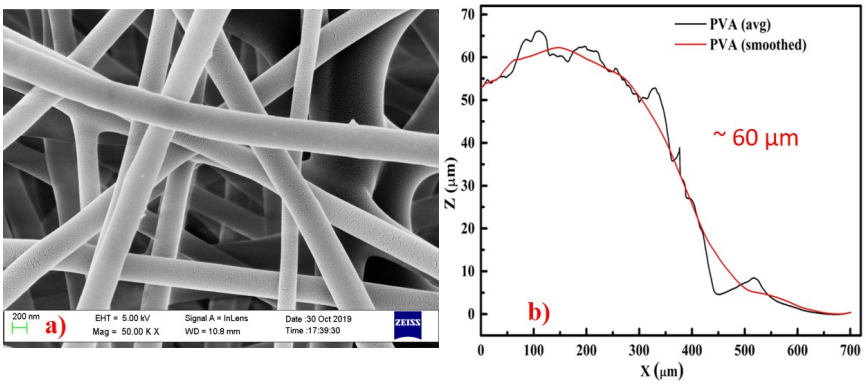

Figure. 4.14 (a) FESEM image of the electro spun PVA nano fibres (b) thickness of the PVA nano fibre film measured using profilometer; the image (a) is used with permission [55]

wave properties from composite polymers, we have doped the gold (Au) nano particles (rods) into the 10%wt PVA nano fibre film. The gold (Au) nano particles (15-20 nm size) are synthesized (in house) using ps laser (EKSPLA, 30 ps, 532 nm, 50 mJ, 10 Hz) ablation of gold plate in distilled water using Ultra fast Laser Ablation in Liquids (ULAL) technique [55, 56]. The PVA powder is mixed with Au nano particle solution instead of the deionized water to get 10%wt Au nano particles doped PVA solution. Later, the solution is processed using Electro spinning to get gold (Au) nano particle doped 10%wt PVA nano fibre film. Figure 4.15 (b-c) show the TEM image (Instrument model: Technai G2 S-Twin at 200 kV) of the colloidal gold (Au) nano particles and FESEM image of the Au nano particles doped 10%wt PVA nano fibres. The main reason to use the Au nano particles in composite polymer film is that, the gold nano particles have light absorption peak around 519 nm as shown in Figure 4.15 (a), which is close the laser wavelength (532 nm) used in the study. This will help to increase the coupling of the laser energy to the polymer film. Figure 4.15 (d) shows the thickness of the 10%wt Au nano particle doped PVA nano fibre film (AuPVA) measured using profilo meter and it is about ~ 35 μm. The 60 μm PVA (10%wt) nano fibre film and 35 μm Au doped PVA (10%wt AuPVA) nano fibre film were adhered to the glass substrate (1.3 mm thick) to study the confined LIBO plasma and shock waves in F0 and F2 focusing condition at 25 mJ and 50 mJ respectively. Figure 4.16 (a-d) shows the shadowgrams of the temporal evolution of blow-off plasma and shock wave from 60 μm PVA and 35 μm AuPVA nano fibre films for 25 and 50 mJ laser energies in F2 focusing condition.

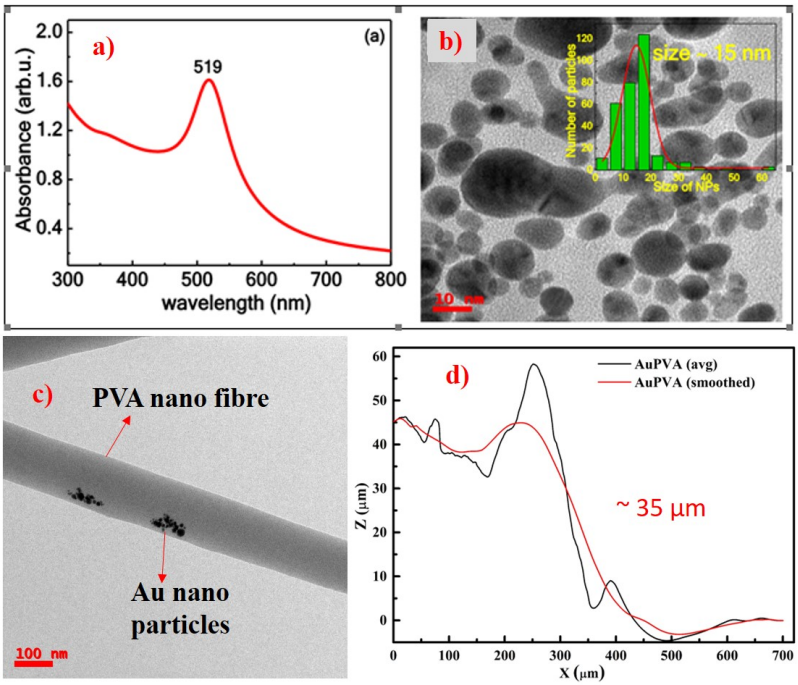

Figure. 4.15 (a) UV-Visible absorption spectra of gold (Au) nano particles (b) TEM image of the colloidal gold (Au) nano particles (c) FESEM image of the Au nano particle doped PVA nano fibres (d) thickness of the Au doped PVA nano fibre film; the images (a-c) are used with permission [55, 56]

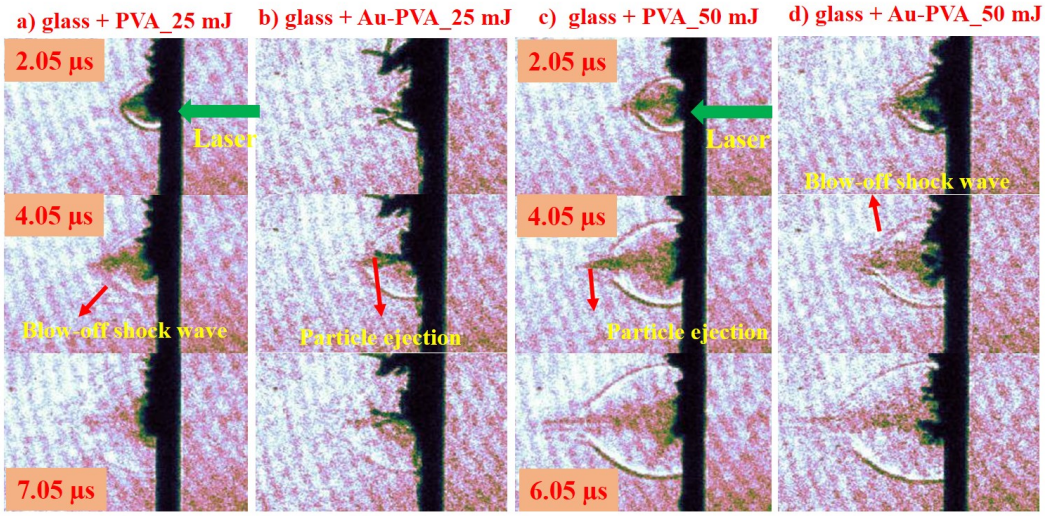

Figure. 4.16 Shadowgrams of the temporal evolution of the laser blow-off shock wave from (a,c) 60 μm PVA and (b,d) 35 μm AuPVA films at 25 mJ and 50 mJ laser energy in F2 focusing condition

From the Figure 4.16 (a-d) we have observed that the appearance of blow-off plasma and shock waves is earlier in the case of polymer films than the metal foils, due to the low

ablation threshold of polymers. The ejection of the flyer/plasma debris is observed around $\sim$ 2 μs time scale in F2 focusing condition for both energies, which is not observed in F0 focusing condition. The flyer acceleration is more than the blow-off shock velocity in F2 condition and it increased with the increase in the laser energy from 25 mJ to 50 mJ. The ablative plasma and shock wave is observed only in F0 focusing condition, it is not visible in F2 condition for both energies. The rupturing of the blow off region from AuPVA polymer film is more than the PVA polymer films. This may be due to the inhomogeneous deposition of gold nano particles in the PVA film as well as due to the weak tensile bonds created between the PVA nano fibre layers as the multiple nano fibre layer are electro spun to achieve the micron thickness of the film. Figure 4.17 (a-b) compares the blow-off shock wave evolution from 20 μm Al and Cu foils with the 60 μm PVA and 35 μm AuPVA polymer films in F0 and F2 focusing conditions at 25 mJ laser energy. In F0 focusing condition, the blow off shock velocity from 20 μm Al and Cu foils is higher than PVA and Au doped PVA for 25 mJ energy at $\leq$ 1 μs time scale. After $\geq$ 2 μs time scale, the Cu foil has lower blow off shock velocity than others and Al foil, PVA and AuPVA polymer films has similar blow off velocity following the trend: $V_{Al,PVA,AuPVA} > V_{Cu}$ as shown in Figure 4.17 (a). The AuPVA blow off shock velocity decay slower than Al, Cu and PVA films and among all the Cu foil has sharp decay nature. In F2 focusing condition, the Cu foil has higher blow off velocity than Al, PVA and AuPVA at $<$ 1.5 μs time scales at 25 mJ energy as shown in Figure 4.17 (b). After 1.5 μs, Cu foil has lowest blow off velocity than

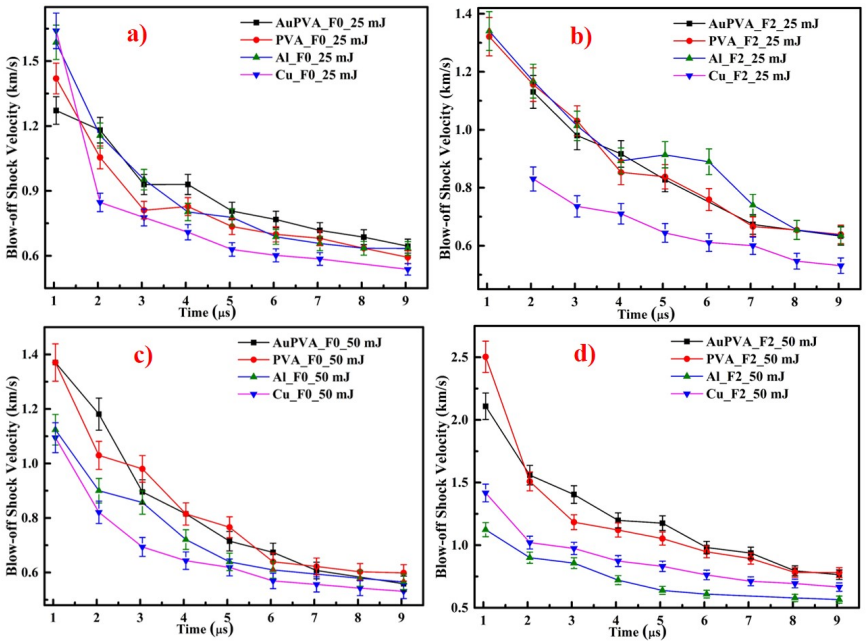

Figure. 4.17 Temporal evolution of the laser blow-off shock wave velocities from 20 μ Al, Cu foils, 60 μm PVA and 35 μm AuPVA polymer films at (a-b) 25 mJ and (c-d) 50 mJ laser energy in F0 and F2 focusing conditions respectively.

other over observed time i.e., $V_{Al,PVA,AuPVA} > V_{Cu}$. While Al, PVA and AuPVA films has similar blow off shock velocities in F2 focusing condition at 25 mJ laser energy except Al has higher blow off shock velocity between 5 to 7 μs than polymer films (PVA and AuPVA) and Cu foil. From Figure 4.17 (c-d), for 50 mJ laser energy the blow-off shock velocity of PVA and AuPVA are higher than Al and Cu foils following the trend: $V_{PVA,AuPVA}$ (1.39 km/s) > $V_{Al,Cu}$ (1.1 km/s) at 1 μs in F0 focusing condition upto 3 μs time scales and almost similar at later time scales. In F2 focusing condition, the blow off shock velocity is higher for PVA film than AuPVA film and it is almost 1.5 to 2 times higher than blow off shock velocities from Al and Cu foils following the trend: $V_{PVA} > V_{AuPVA} > V_{Cu} > V_{Al}$ at < 2 μs time scales. After 2 μs, the blow off shock velocities of PVA and AuPVA films is almost similar; and they are higher than Cu and Al foil shock velocities. The 20 μm Al foil has lowest blow off shock velocity than blow off velocities from Cu, PVA and AuPVA films following the trend: $V_{PVA,AuPVA} > V_{Cu} > V_{Al}$. It was more evident in F2 focusing condition that the blow-off shock velocities from polymer films at 50 mJ laser energy are enhanced atleast $\sim$ 1.5 times than F0 focusing condition and a clear difference between metal and polymer blow-off is observed. This is due to, efficient laser energy coupling to polymer films and lower ablation threshold of the polymer films than metal foils. The LIBO shock wave velocities for metal and polymer films are summarized in Table 4.3. From the results, by changing the focusing condition from F0 to F2 condition, the blow off shock wave velocity is enhanced in both PVA and AuPVA polymer films with optimum laser energy of 50 mJ. But there is no significant enhancement in the blow off shock velocity from composite polymer films (AuPVA) compared to the normal polymer films (PVA), which needs a further systematic study.

Table 4.3 Effect of focusing conditions on LIBO shock wave velocity from 60 μm PVA and 35 μm AuPVA films compared to the 20 μm Al and Cu foils at 1.05 μs.

Energy	**PVA (km/s)**		**AuPVA (km/s)**		**Al (km/s)**		**Cu (km/s)**	
(mJ)	*F0*	*F2*	*F0*	*F2*	*F0*	*F2*	*F0*	*F2*
25	1.41	1.32	1.27	1.2	1.58	1.34	1.6	1.52
50	1.37	2.5	1.37	2.1	1.12	1.47	1.09	1.41

4.6 Conclusions

To summarize, the shifting of the focal plane from F0 to F2 focusing condition resulted in higher blow off shock waves from 20 μm Al and Cu foils at optimal laser energy of 50 mJ because of the ejected shock flyer/plasma debris. The effective enhancement in the flyer diameter is observed to be more significant in the case of Al foil with F2 focusing condition. From the LIBO study of the 1.1 μm Cu and 200 nm Ti thin films it is evident

that the flyer generation is observed only for micron thickness films while for nano meter films only blow off shock waves are observed because of the smaller film thickness. For higher blow off shock velocity at lower energy (25 mJ), F2 focusing condition is suitable. At higher energy (50 mJ) F1 focusing condition is better for the thin films (1.1 μm Cu and 200 nm Ti). The attenuation of the blow off shock waves follows linear relation in the case of thin films (1.1 μm Cu and 200 nm Ti) while it follows 1/r relation for 20 μm Al, Cu foils. The blow-off studies are further extended to the polymer (PVA) and composite polymer (Au doped PVA) films as these studies are helpful to understand the laser ablation propulsion. The enhancement of blow off shock waves are observed with F2 focusing condition with 50 mJ energy for both PVA and AuPVA polymer films than 20 μm Al and Cu foils. But, we have not observed any enhancement in the blow off shock velocities from the composite polymer films (AuPVA) than normal polymer film (PVA).

References

[1] S. I. Anisimov, B. S. Luk'yanchuk and A. Luches, *An analytical model for three-dimensional laser plume expansion into vacuum in hydrodynamic regime*, Appl. Surf. Sci. 96, 24 (1996).

[2] R. K. Singh and J. Narayan, *Pulsed-laser evaporation technique for deposition of thin films: Physics and theoretical model*, Phys. Rev. B 41, 8843 (1990).

[3] B. Toftmann, J. Schou, and J. G. Lunney, *Dynamics of the plume produced by nanosecond ultraviolet laser ablation of metals*, Phys. Rev. B 67, 104101 (2003).

[4] B. Doggett and J. G. Lunney, *Expansion dynamics of laser produced plasma*, J. Appl. Phys. 109, 093304 (2011).

[5] C. Phipps, *Laser Ablation and its Applications*, Springer Series in Optical Sciences, Vol. 129 (2007).

[6] J. G. Lunney and R. Jordan, *Pulsed laser ablation of metals*, Appl. Surf. Sci., 127-129, 941-946 (1998).

[7] S. S. Harilal, C. V. Bindhu, M. S. Tillack, F. Najmabadi and A. C. Gaeris, *Internal structure and expansion dynamics of laser ablation plumes into ambient gases*, J. Appl. Phys. 93, 2380 (2003).

[8] M. Cirisan, J. M. Jouvard, L. Lavisse, L. Hallo and R. Oltra, *Laser plasma plume structure and dynamics in the ambient air: The early stage of expansion*, J. Appl. Phys. 109, 103301 (2011).

[9] G. K. Varier, R. C. Issac, S. S. Harilal, C. V. Bindhu, V. P. N. Nampoori, C. P. G. Vallabhan., *Investigations on nanosecond laser produced plasma in air from the multicomponent material YBa2Cu307*, Spectrochimica Acta B 52, 657 (1997).

[10] J. D. Lindl, *Inertial Confinement Fusion*, Springer, New York, (1998).

[11] K. Nishikawa and M. Wakatani., *Plasma Physics: Basic Theory with Fusion Applications*, 2nd. ed. Berlin, Springer-Verlag (1994).

[12] P. R. Willmott and J. R. Huber., *Pulsed laser vaporization and deposition*, Rev. Mod. Phys. 72, 315 (2000).

[13] R. P. Drake, J. J. Carroll, T. B. Smith and P. Keiter, *Laser experiments to simulate supernova remnants*, Phys. Plasmas 7, 2142 (2000).

[14] S. Eliezer, I. Gilath and T. Bar-Noy, *Laser-induced spall in metals: Experiment and simulation*, Journal of Applied Physics 67, 715 (1990).

[15] Z. Y. Zheng, J. Zhang, X. Lu, Z. Q. Hao, X. H. Yuan, Z. H. Wang and Z. Y. Wei, *Characteristic investigation of ablative laser propulsion driven by nanosecond laser pulses*, Appl. Phys. A 83, 329–332 (2006).

[16] R. Fabbro, J. Fournier, P. Ballard, D. Devaux and J. Virmont, *Physical study of laser-produced plasma in confined geometry*, Journal of Applied Physics 68,775(1990).

[17] D. Devaux, R. Fabbro, L. Tollier and E. Bartnicki, *Generation of shock waves by laser-induced plasma in confined geometry*, Journal of Applied Physics 74, 2268(1993).

[18] F. Cottet and M. Boustie, *Spallation studies in aluminum targets using shock waves induced by laser irradiation at various pulse durations* , Journal of Applied Physics 66, 4067 (1989).

[19] H. Tamura, T. Kohama, K. Kondo and M. Yoshida, *Femtosecond-laser-induced spallation in aluminum*, Journal of Applied Physics 89, 3520 (2001)

[20] K. Ding and L. Ye, *Laser Shock Peening Performance and simulation*, Woodhead publishing Limited (2006).

[21] A. Kumar, R. K. Singh, V. Prahlad and H. C. Joshi, *Comparative study of laser produced Li plasma plumes from thin film and solid target*, J. Appl. Phys. 104, 093302 (2008).

[22] J. Thomas, H. C. Joshi, A. Kumar and R. Philip, *Pulse width dependent dynamics of laser-induced plasma from a Ni thin film*, J. Phys. D: Appl. Phys. 52, 135201 (2019).

[23] Z. Kantor, Z. Toth and T. Szorenyi, *Laser induced forward transfer: The effect of support-film interface and film-to-substrate distance on transfer*, Appl. Phys. A Solids and Surfaces 54, 170 (1992).

[24] A. Kumar, S. George, R. K. Singh and V. P. N. Nampoori, *Influence of laser beam intensity profile on propagation dynamics of laser-blow- off plasma plume*, Laser and Part. Beams, 28, 387 (2010).

[25] A. D. Curtis, A. A. Banishev, W. L. Shaw and D. Dlott, *Laser-driven flyer plates for shock compression science: Launch and target impact probed by photon Doppler velocimetry*, Review of Scientific Instruments 85, 043908 (2014).

[26] X. Zhang, B. Shen, L. Ji, F. Wang, M. Wen, W. Wang, J. Xu and Y. Yu, *Effects of pulse duration and areal density on ultrathin foil acceleration*, Physics of Plasmas 17, 063107 (2010).

[27] C. W. Miller, *set-up and evolution of laser driven mini flyer system*, M.Sc. Thesis, Georgia Institute of Technology (2009).

[28] W. L. Shaw, R. A. Williams, E. L. Dreizin and D. D. Dlott, *Using laser-driven flyer plates to study the shock initiation of nano energetic materials*, Journal of Physics: Conference Series

500, 182010 (2014).

[29] C. R. Phipps, *Laser Ablation and Its Applications*, Springer (2007).

[30] J. S. Bakos, P. N. Ignacz, J. Szigeti and J. Kovacs, *Laser blow off plasma propagating in low pressure gas*, Applied Physics Letters 51, 734 (1987).

[31] D. L. Paisley, S. N. Luo, S. R. Greenfield and A. C. Koskelo, *Laser-launched flyer plate and confined laser ablation for shock wave loading: Validation and applications*, Review of Scientific Instruments 79, 023902 (2008).

[32] S. George, A. Kumar, R. K. Singh, V. P. N. Nampoori., *Effect of ambient gas on the expansion dynamics of plasma plume formed by laser blow off of thin film*, Appl. Phys. A., 98, 901 (2009).

[33] X. Zhao, G. Shan and Y. Gao, *Fiber-coupled laser-driven flyer plates system*, Review of Scientific Instruments 82, 043904 (2011).

[34] M. G. Haines, S. V. Lebedev, J. P. Chittenden, F. N. Beg, S. N. Bland and A. E. Dangor, *The past, present, and future of Z pinches*, Physics of Plasmas 7, 1672 (2000).

[35] S. Tripathi, S. Chaurasia, P. Leshma and L. J. Dhareshwar, *Dynamic imaging and hydrodynamics study of high velocity, laser-accelerated thin foil targets using multiframe optical shadowgraphy*, Pramana 79, 1471 (2012).

[36] L. J. Dhareshwar, N. Gopi, C. G. Murali, N. K. Gupta and B. K. Godwal, *Measurement of laser driven shock wave transit time through thin aluminium targets by optical shadowgraphy*, Shock Waves 14, 231 (2005).

[37] D. Batani, A. Balducci, D. Beretta, A. Bernardinello, T. Lower, M. Koeing, A. Benuzzi, B. Faral and T. Hall, *Equation of state data for gold in the pressure range < 10 TPa*, Phys.Rev. B 61, 14, 9287-9294 (2000).

[38] W. J. Nellis, A. C. Mitchell and D. A. Young, *Equation-of-state measurements for aluminum, copper, and tantalum in the pressure range 80-440 GPa (0.8-4.4 Mbar)*, J. Appl. Phys., Vol. 93, No.1 (2003).

[39] D. Batani, H. Stabile and J. Ullschmied, et al., *Ablation Pressure Scaling at Short Laser Wavelength*, Physical Review E, 68, 067403 (2003).

[40] D. Batani, R. Dezulian, R. Redaelli, R. Benocci and H. Stabile et. al.,*Recent experiments on the hydrodynamics of laser-produced plasmas conducted at the PALS laboratory*, Laser and Particle Beams,25, pp 127-141 (2007).

[41] J. J. Santos, M. Manclossi, V. Malka, D. Batani et al., *Direct Diagnostic of Multi-Temperate Fast Electrons Beams on UHI Laser-Solid Interactions by Optical Transition Radiation Diagnostic*, 32^{nd} EPS Conference on Plasma Physics: 8th International Workshop on Fast Ignition of Fusion Targets, spain (2005).

[42] C. Phipps, J. Luke, T.Lippert, M. Hauer and A. Wokaun, *Micropropulsion Using a Laser Ablation Jet*, Journal of propulsion and power, Vol. 20, No. 6 (2004)..

[43] M. Keidar, I. D. Boyd, J. Luke and C. Phipps, *Plasma Generation and Plume Expansion for a Transmission-mode Micro-laser Ablation Thruster*, 39^{th} AIAA/ASME/SAE/ASEE Joint Propulsion Conference and Exhibit, American Institute of Aeronautics and Astronautics (2003).

[44] H. Wang and Y. Wang, *Characteristics of Flyer Velocity in Laser Impact Welding*, Metals 9, 281 (2019).

[45] Ch. Leela, Suman Bagchi, V. Rakesh Kumar, Surya P. Tiwari and P. Prem Kiran, *Dynamics of laser induced micro-shock waves and hot core plasma in quiescent air*, Laser and Particle Beams 31, 263–272 (2013).

[46] Ch. Leela, P. Venkateshwarlu, R.V. Singh, P. Verma and P. Prem Kiran, *Spatio-temporal dynamics behind the shock front from compacted metal nanopowders*, Opt. Exp. 22, S2, A268 - A275 (2014).

[47] S. Sai Shiva, Ch. Leela, S. Chaturvedi, C. D. Sijoy and P. Prem Kiran, *Development of Numerical Model to Investigate the Laser Driven Shock Waves from Aluminum Target into Ambient Air at Atmospheric Pressure and its comparison with Experiment*, APS - Conference Proceedings of Shock Compression and Condensed Matter (SCCM), W1.42-15-1330 (2015).

[48] N. Guthikonda, S. Sai Shiva, D. P. S. L. Kameswari, P. Prem Kiran, C. D. Sijoy and V. R. Ikkurthi, *Effect of Focusing Plane on Laser Blow-off Shock Waves from Confined Aluminum and Copper Foils*, (Manuscript under preparation) (2020).

[49] R. Srinivasan and V. Mayne-Banton, *Self-developing photo-etching of poly (ethylene terephthalate) films by far ultraviolet excimer laser radiation*, Appl. Phys. Lett. 41, 576 (1982).

[50] Y. Kawamura, K. Toyoda and S. Namba, *Effective deep ultraviolet photoetching of polymethyl methacrylate by an excimer laser*, Appl. Phys. Lett., 40, 374 (1982).

[51] P. E. Dyer, *Photochemical Processing of Materials*, Academic, London (1992).

[52] S. Ravi Kumar, B. Lies, X. Zhang, H. Lyu and H. Qin, *Laser ablation of polymers: a review*, Polym. Int.68, 1391–1401 (2019).

[53] T. Lippert, C. David, M. Hauer, C. Phipps and A. Wokaun, *Tailor-Made Polymers for Laser Applications*, Review of Laser Engineering 29, 734-738 (2001).

[54] T. Lippert, L. Urech, R. Fardel, M. Nagel, C. R. Phipps and A. Wokaun, *Materials for Laser Propulsion: liquid polymers*, Proc. of SPIE Vol. 7005, 700512 (2008).

[55] M. S. S. Bharati, B. Chandu, D. Banerjee, B. Barkakaty and S. Venugopal Rao, *Nanofibers with Au NPs as SERS Substrate for Detection of Methyl Salicylate*, Bulletin of Materials Science (under review) (2021).

[56] C. Byram et. al., *SERS based detection of multiple analytes from dye/explosive mixtures using picosecond laser fabricated gold nanoparticles and nanostructures*, Analyst, 144, 2327-2336 (2019).

Chapter 5

Dynamics of spatially confined ns laser induced air plasma and shock waves

Spatial confinement of laser induced plasma in ambient air depends on the laser energy used to create plasma, cavity geometry, cavity dimensions (i.e., aspect ratio) and the material used to make the cavity. Many research groups confirmed the enhancement of plasma emission properties based on the geometry of the cavity and the laser energy used. However, a clear visualization of the processes leading to enhanced plasma emission are sparse. In this chapter, we present the spatio temporal evolution of the ns laser induced air plasma confinement using two different cavity geometries with the help of shadowgraphy imaging. The first geometry consists of a hollow rectangular cavity made of a glass. While the second one is a cylindrical geometry made of different materials such as glass, Cu, plastic and SS. The effect of input laser energy, cavity aspect ratio (L/D) on the exit times of shock waves is studied. The laser energies used are in the range of 50-400 mJ, corresponding to the peak intensities in the range of 2.5 - 20 $\times 10^9$ *W/cm*^{2}. The aspect ratio is varied over 1 to 2.5 for tube geometries studied.

5.1 Introduction

In recent years, the study of the shock wave propagation inside the mm or micro sized tubes have attracted the research community. Due to the availability of high power short (ns) and ultrashort (ps, fs) lasers and with advancing of micro and nano technology, the characterization of shock waves in mm sized, micron or nano range has emerged as an interdisciplinary research topic [1, 2, 3, 4]. Unlike the conventional shock tubes, the laser induced shock waves requires minimum operation and produces the pressures greater than

GPa on the material surface [5, 6, 7]. Since the laser induced shock waves behaves similar to the shock waves generated by conventional shock tube [8, 9], the shock tubes can be miniaturized to lab scale using lasers. Here, the laser produced plasma acts as the driver and generates shock waves into the tube [1, 3, 10]. The development of lab scale laser based mm sized shock tube require proper understanding of the plasma and shock waves propagation in confined geometry [7, 11, 12, 13, 14]. The downscaling of shock wave effects the properties such as decrease in shock pressure, shock velocity attenuation during the propagation, laminar and turbulent flow [1, 15, 16]. So to balance the interplay between the down scaling of the shock waves to mm size and maintaining the shock wave properties, we need to study the enhancement of the plasma and shock wave properties in the confined geometry [11, 12, 13, 17, 18]. The study of the temporal evolution of the laser induced plasma and shock waves in confined geometry is found applications such as, understanding of the explosions in gas/oil pipes [19, 20, 21], chemical explosions in ducts or tubes [21], flow of the fluids in capillaries i.e., microfluidics [22, 23, 24] and shock wave propagation in solids [7, 21]. In laser based shock tube, the laser induced plasma and its properties plays a key role. But the plasma and its mechanical (shock wave) emissions are highly dependent on fluctuations in laser properties (energy, pulse shape, pre pulse), target material properties (composition, mechanical properties, conductivity, melting point and homogeneity of sample surface) [25, 26, 27, 28, 29]. In the laser based shock tube, the confinement on plasma and shock waves expansion is applied perpendicular to the laser propagation direction. This confinement is known as the lateral confinement or spatial confinement geometry [11, 12, 17]. The process of the spatial confinement and its effect on the laser induced plasma and shock waves inside mm sized tubes is discussed in this chapter.

5.2 Spatial confinement of the laser induced plasma and shock waves

Spatial confinement of plasma is a flexible and cost-effective method for enhancement of optical and mechanical emissions from the plasma. Wherein the plasma is confined to a smaller size by cavities of different geometries (cylindrical, hemi-spherical and rectangular) and structured surfaces (laser craters) [30, 31, 32, 33, 34, 35]. Combination of spatial confinement along with magnetic confinement, spark discharge and dual pulse LIB were also used for studying enhancement of plasma properties [36, 37]. In spatial confinement process, at initial time scales the plasma expansion is similar to that of no-cavity (unconfined) geometry but after the detachment of shock wave from the plasma, shock wave reflects from the cavity walls and compresses the plasma at longer time scales, this is known as **plasma reheating** [12, 17, 38]. Lot of recent reports on enhancement of LIBS signal sensitivity using spatial confinement of plasma in cavity like structures with different geometries [31, 33, 34, 38], attributed the enhancement of plasma properties to the

reflection and compression of the shock waves. However, the visualization of this process is sparse and shock wave reheating is not captured clearly. Additionally, Popov et al. [17] suggested the enhancement could be the more effective collection of plasma radiation due to the reflection from cavity walls. These warrants a complete investigation of the evolution of the plasma and shock waves in confined geometry. In spatial confinement, the plasma properties like plasma temperature and electron densities greatly depends on the aspect ratio of cavity along with cavity geometry [33, 34, 39]. The aspect ratio (L/D) is defined as the ratio between length (L) of the cavity to the inner diameter (D) of the cavity.

5.2.1 Effect of spatial confinement of plasma

In the spatial confinement of laser induced plasma, the properties of plasma is similar to unconfined/free expansion of plasma until the reflected shock wave from the cavity walls compresses the plasma. Due to the spatial confinement and compression of shock wave, the main plasma properties will be effected.

- **Plasma temperature :** In spatial confinement, when the shock wave compresses the plasma, the mean free path (mfp) between the plasma species will decrease thus collision frequency will increase. This leads to the increase in the internal energy of the plasma species or plasma temperature similar to a compression of piston or driver section of shock tube [8, 9, 10]. Several authors suggested that, the electron temperature increases monotonically in plasma confinement [12, 40]. Shen et al. [12], reported the increase in the plasma temperature by about 1000 K during 9 to 17 μs when laser ablated Al plasma is confined in cylindrical confinement with 10.8 mm diameter. It is also found that, as the aspect ratio decreases, the plasma density will be less than or equal to the unconfined geometry [41], this reveals that, the effect of aspect ratio on plasma confinement is dominant.

- **Plasma volume :** Due to the confinement and compression by shock wave, the plasma volume decreases when compared to the free or unconfined geometry. Yin et al. [42] observed that, due to the cylindrical confinement the plasma morphologies were much more stable and LIBS signal fluctuations are reduced.

- **Electron density :** Due to the spatial confinement and compression of the reflected shock wave, the plasma plume confines to a smaller volume. This results in drastic increase of the electron number density. Gao et al. [41] reported that, the enhancement of electron density is better with a cavity of 10 mm diameter and at a delay time of 9μs in case of laser induced Cu plasma.

- **Plasma lifetime:** Due to the reheating of the plasma, the plasma lifetime also increases monotonically compared with free expansion [43, 44]. Choi et. al. [44]

observed that, the signal intensity of Al III (452.8945 nm) emission was enhanced 5.5 times compared to the free expansion case by confining the plasma with acrylic plate at 1 mm confining height from the sample at 1 Torr pressure.

- **Emission intensity :** Due to the plasma re-heating, the plasma lifetime increases, so the plasma species will be excited more that leads to the increase in plasma temperature as well as enhancement of the optical emissions from plasma. Based on recent experimental studies, the emission intensity is greatly increased in spatial confinement by a factor of 2-10 [11, 17, 39], when compared to freely expanding plasma from ablation of solids.

Although many research groups [11, 12, 17, 32, 33, 34, 36, 37, 38, 38, 40, 41, 42, 43, 44] reported the enhancement of plasma emission through semi or partial confinement of laser ablative plasma from solids, clear visualization of the processes [31, 39, 45] (radial shock wave reflections, plasma compression and squeezing) resulted in the plasma emission enhancement are sparse. This chapter presents the results from imaging of plasma and shock waves due to complete spatial confinement of ns laser induced plasma in air. The spatio temporal evolution dynamics of the plasma and shock waves inside symmetric and asymmetric cavities clearly showed the process of plasma reheating by reflected shock waves from cavity walls. This is confirmed by the longer lifetime of the plasma imaged by plasma self emission study. The effect of input laser pulse energy, cavity geometry and aspect ratio of the cavities on plasma and shock wave evolution are presented. The spatio-temporal evolution of the shock waves from ns LIB of air in spatially confined hollow cavities/tubes were compared with that of free evolution of plasma in air to explicitly bring out the physical processes occurring during the confinement.

5.3 Experimental Details

The detailed experimental schematic for imaging the spatially confined laser induced plasma and shock waves in air is described in chapter 2. The experiments were performed using second harmonic laser pulses from a Q-switched Nd: YAG laser (TITAN-5, M/s Amplitude Technologies) beam (10 ns, 532 nm) of 22 mm diameter was focused inside the hollow glass tube (at the centre of tube) using 150 mm focal length in f/7 geometry to initiate the breakdown of air. To clearly understand and visualize the processes involved in the spatial confinement of laser induced air plasma, we have used different cavity geometries with different aspect ratios. A He-Ne probe beam of 47 mm diameter was used to capture the shadowgraphic images using an ICCD camera and the plasma lifetime is visualized from self emission study of plasma confinement. The experimental data (shadowgraphy and self emission studies) was collected from an initial delay time 500 ns to 30 μs with a delay step size of 500 ns. We have used two kinds of spatial confinement geometries: rectangular geometry and cylindrical geometry. The details of geometries

used to describe the dimension of confinement hollow tube were shown in Figure 7.1.

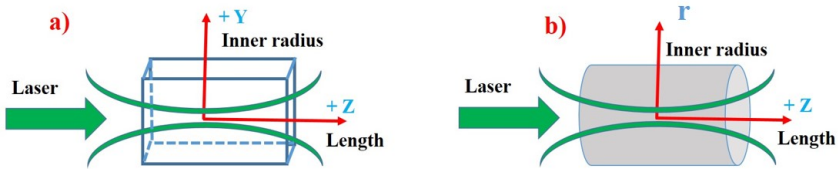

Figure. 5.1 (a) rectangular and (b) cylindrical geometry hollow tubes used for spatial confinement of air plasma

The processes involved in spatial confinement of air plasma viz, radial shock wave reflection, compression of plasma (or plasma reheating), multiple reflection of radial shock waves and plasma lifetime is studied using a rectangular hollow glass tube (made of 4 glass plates) with different aspect ratios. In cylindrical geometry, we have studied the effect of confinement material along with aspect ratio by investigating the shock exit times along laser propagation axis. The spatial confinement of plasma is studied for input laser energies of 50, 200, 400 mJ with corresponding intensities in the range of 1.2 - 20 $\times 10^9$ W/cm^2. We have taken precautions such that the laser pulse is always focused at the centre of the hollow tube. In rectangular spatial confinement geometry, in addition to reflected shock waves from cavity walls at ±Y direction, the reflected shock waves from ±X direction also contribute to the compression and reheating of the plasma. The effects due to the reflected shock waves from ± X direction are integrated along the probe propagation direction and can not be distinguished in our present experimental setup. However, they follow the similar behaviour as reflected shock waves from ± Y direction. As the dimension of the cavity along ±X is 11 mm, the reflected shock waves from ±X direction come later than ±Y direction, leading to the asymmetric compression of the plasma.

5.4 Dynamics of spatially confined air plasma in rectangular geometry

In this geometry, four glass plates of 1.3 mm thickness and of different lengths were glued to create a hollow rectangular tube with different aspect ratios. The details of hollow tube dimensions were listed in table 5.1. The inner separation of the walls along Y-direction is taken as 'D'. As the plasma and shock wave dynamics along Y-direction are captured by the probe beam. A nano second laser is focused at the centre of hollow tube (along Z direction) as shown in Figure 7.1(a). The spatial confinement of air plasma in rectangular geometry is an asymmetric compression process since the two inner diameters of glass tubes are different. This geometry is very useful to visualize the different processes of spatial confinement of air plasma and used to validate the 2-D FLASH simulations [46].

Table 5.1 Dimensions of the hollow tubes used for spatial confinement of air plasma in rectangular geometry

Material	**Rectangular geometry**		
	L (mm)	**D**(mm)	**L/D**
Glass	8±0.5	8±0.2	1
	12±0.5	8±0.2	1.5
	16±0.5	8±0.2	2

5.4.1 Visualization of Spatial confinement of air plasma inside rectangular hollow glass tube of L/D=1.5

A laser pulse of 50 mJ energy is focused (using f/#7 geometry) at the centre of a rectangular glass tube of 12 mm length and 8 mm diameter (L/D =1.5), to create an air plasma. Figure 5.2 shows the shadowgrams of the spatial confinement of air plasma by a hollow glass tube in rectangular geometry with L/D =1.5.

From the images it is observed that, after plasma expansion and detachment of shock waves, the freely propagating shock wave from plasma is reflected by both the confining boundaries (glass) along Y direction around 5.5 μs. The reflected shock wave propagating towards plasma centre (or glass centre) interacted with the plasma boundaries around $\sim$ 7.5 to 8.5 μs and compresses the plasma from both ends ($\pm Y$). This process is known as **plasma re-heating or shock wave focusing** [38, 39]. In the process of shock wave compression of plasma, we observed a secondary shock wave (SSW) detachment from plasma that propagated in the already shocked region (Figure 5.2 (a)). Experimentally, the formation of secondary shock wave is clearly observed for low energy i.e., 50 mJ case only (Figure 5.2 (a)) and for high energies we have not observed clearly. But the coalescence of primary and secondary shock waves along +Y direction is observed for all the laser energies used (see Figure 5.6). The role and effect of the secondary shock wave on the enhancement of plasma properties in rectangular spatial confinement plasma is explicitly observed by imaging the plasma. The observations were corroborated by the numerical simulations performed using 2-D FLASH Radiation Hydrodynamic codes [46]. Details of the simulations are out of scope of the present thesis. However, the highlights of the simulated results were given briefly.

Due to the compression of shock wave, the plasma number density as well as plasma temperature increases and size of the plasma is decreased along transverse (Y) direction. Due to the confinement of plasma along Y direction, it tries to expand along laser propagation direction (± Z) as the tube has no confinement along Z direction. This increases the plasma length (it is defined as the sum of the contact front positions along +Z and

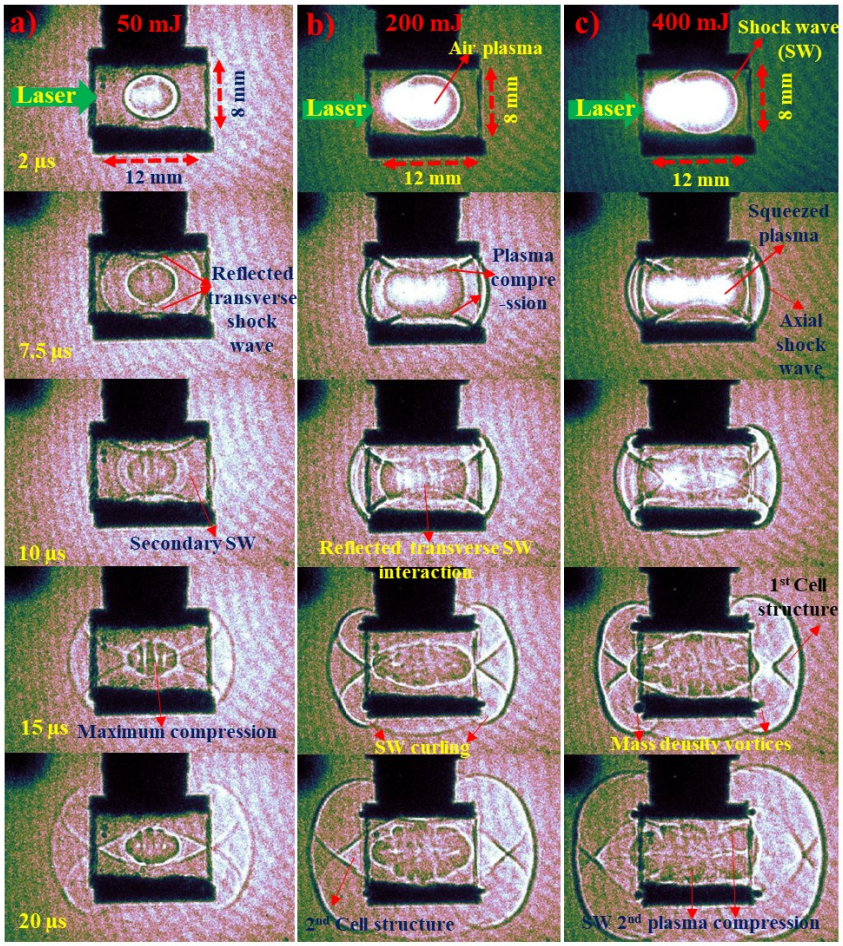

Figure. 5.2 Shadowgrams of temporal evolution of air plasma and shock waves in spatial confinement inside a rectangular glass cavity with L/D=1.5 with different laser input energies (a) 50 mJ (b) 200 mJ (c) 400 mJ

-Z) along laser propagation direction (as shown in Figure 5.2). Due to the squeezing of plasma, the density of the plasma is redistributed, which allows the two reflected shock waves from both cavity walls along Y direction, pass through the plasma. These two reflected shock waves interact with the plasma and with each other along Z axis at $\sim$ 10 μs and $\sim$15 μs respectively (Figure 5.2 (a-c)). After 15 μs, the reflected shock waves from cavity walls $\pm$ Y pass through each other. Due to this, a cell like structure is formed along $\pm$ Z axis. This cell like structure moves in the same direction ($\pm$Z direction) as the primary shock wave, drags the plasma along with it, which resulted in increase in the plasma length along $\pm$ Z direction. The maximum increase in the plasma length is observed when the cell like structure exits from the glass tube ($\sim$ 21-22 μs). This is observed to increase the plasma volume (plasma relaxation) due to the drag of reflected shock waves along Y direction and cell like structure along Z direction. These reflected shock waves from +Y and -Y directions are observed to get reflected again by the cavity

walls of -Y and +Y direction respectively and interacts with the relaxing plasma again. The propagation of reflected shock waves through the plasma continues till the decay of the strength of the shock waves, which in turns depend on the input laser energy. Due to multiple interaction of the shock waves with the plasma, the plasma along ±Z direction is observed to live longer. This is confirmed by the increased plasma length along ±Z directions (Figure 5.3). The same is confirmed by the self emission imaging studies (Figure 5.8).

5.4.2 Energy dependence on the spatial confinement of air plasma and shock waves inside rectangular cavity

As the laser input energy is the main source to create the plasma, the plasma and shock wave properties greatly depends on the input laser energy. The detailed description on the effect of input laser energy on the air plasma and shock wave properties were given below.

5.4.3 Energy dependence on the temporal evolution of plasma length

Figure 5.3(a,b) shows the effect of energy variation on the temporal evolution of spatially confined air plasma length (indicated by contact front position) along ±Z direction inside a rectangular hollow glass tube. Since the confinement is along ± Y direction and we were able to clearly quantify the plasma size along ±Z direction. For 50 mJ energy, in free expansion of air plasma, the contact front position along ±Z direction increases upto 5 μs and it decreases linearly at later time scales (Figure 5.3 (a,b)). In the case of spatial

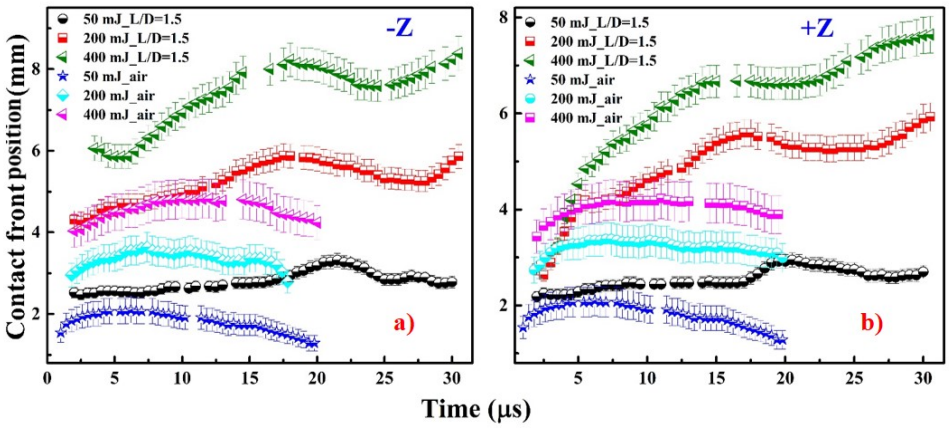

Figure. 5.3 Energy dependence on temporal evolution of plasma contact front position along ±Z in spatial confinement of air plasma inside a rectangular hollow glass tube of L/D=1.5

confinement of air plasma, the plasma contact front position is similar to that of the unconfined expansion upto 5 μs. However beyond 5 μs, the plasma contact front position

does not decrease and showed an interesting evolution depending on the input laser energy. For 50 mJ input laser energy, the plasma contact front position remained at $\sim$ 2.5 mm along -Z and $\sim$ 2.2 mm along +Z direction till 8 to 9 μs. From 9 to 10.5 μs (after reflection of transverse shock wave) onwards the plasma contact front (CF) position increases due to the compression of the reflected shock waves from the cavity walls along the transverse ($\pm$ Y and $\pm$ X) direction. After $\sim$17 μs, a sharp rise in CF position is observed due to the drag of cell like structure and CF position reaches to maximum value i.e., 3.31 mm at $\sim$21.5 μs along -Z and 2.94 mm at $\sim$ 20.5 μs along +Z direction. The cell like structure leaves the cavity and contact front position decreases to $\sim$ 2.5 mm along -Z and $\sim$ 2.2 mm along +Z direction gradually as shown in Figure 5.3. During the 15 to 22 μs, the reflected shock waves from $\pm$ Y cavity walls were observed to pass through the plasma leading to compression and reheating of the plasma. This confirms that the spatial confinement is increasing the both the plasma length and its lifetime.

A similar enhancement of the plasma length is observed with increase of the laser input energy to 200 mJ and 400 mJ. For 200 mJ energy, the confinement has increased the plasma contact front position from $\sim$ 4.3 mm along -Z and 2.6 mm along +Z at 3 μs to $\sim$ 4.6 mm along -Z and 4.1 mm along +Z at 5-6 μs. After 6-7 μs (shock reflection time), the plasma contact front position increases due to the compression of the reflected shock waves from cavity walls along $\pm$Y direction. In this case, the propagation of reflected shock waves through the plasma is observed to increase the plasma length from 7 μs and reaches to maximum i.e., $\sim$5.8 mm along -Z and 5.5 mm along +Z at 17.5 μs (due to the exit of cell like structure) as shown in Figure 5.3. After 17.5 μs, the contact front position decreases until 21.5 μs along -Z and 27.5 μs along +Z direction. After that, the contact front position again increases due to the secondary reflection of reflected shock wave from +Y direction by the cavity wall of -Y direction and vice-versa as shown in Figure 5.6.

For 400 mJ energy, the reflected shock waves from $\pm$ Y cavity wall is observed at 4 to 5 μs and its propagation through the plasma has continued till 20 (along +Z) to 25 μs (along -Z). During this period, the plasma contact front position has reached a maximum of $\sim$8.2 mm along -Z, 6.6 mm along +Z at 17 to 18 μs. After 18 μs, the contact front position decreases to $\sim$7.5 mm along -Z, 6.6 mm along +Z by 21 to 24.5 μs respectively. After that, CF position again increases due to the secondary reflection and interaction of reflected shock waves with the plasma until 30 μs.
For laser input energies 50 mJ, 200 mJ and 400 mJ, the enhancement or increment in the air plasma length (defined as sum of CF position along +Z and -Z) is around 1.5 to 2 times along -Z direction, when compared to the free expansion. The contact front position along +Z direction shown similar evolution to that along -Z direction with a small difference due to the asymmetry of laser deposition at the focal plane [35, 47].

5.4.4 Energy dependence on the temporal evolution of axial shock waves

Figure 5.4 (a,b) shows the effect of energy on the temporal evolution of the shock front position along ± Z direction in spatial confinement of air plasma inside hollow glass cavity. For 50 mJ energy, the temporal evolution of shock waves along ± Z direction in spatial confinement is equal to that of the unconfined shock waves (within the experimental limits) from air plasma along ± Z direction of respective energy. This clearly shows that there is no effect of spatial confinement along laser axis (± Z) as the longitudinal ends of the hollow glass tube were open allowing the shock waves to exit freely. Since the hollow glass tube provides complete confinement along ± Y and ± X direction, the transverse shock waves reflects from the glass walls and compresses or reheats the plasma, is not observed to affect the shock front propagation along the laser axis at these energies. The

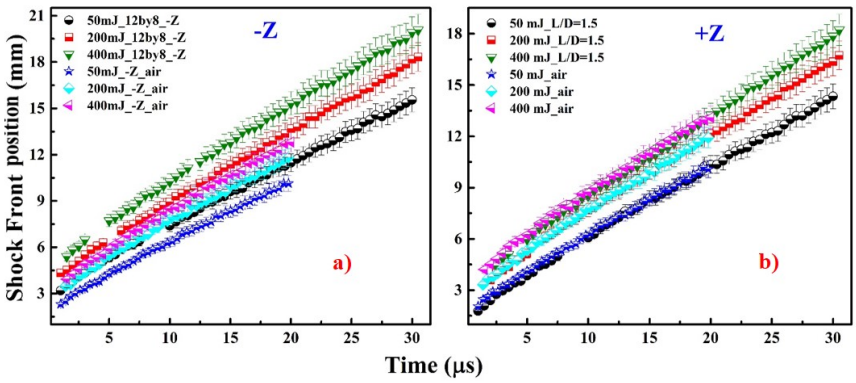

Figure. 5.4 Energy dependence on the temporal evolution of shock waves along ±Z (axial) direction in spatial confinement of air plasma inside a rectangular hollow glass tube with L/D=1.5

shock wave will exit from the hollow glass tube around ∼10 μs along +Z direction and ∼ 10.5 μs along -Z direction in the case of 50 mJ laser input energy. Due to abrupt change in the pressure/density gradient inside hollow glass tube and surrounding air medium, **shock and mass density vortices** are formed at all the eight edges of the glass tube as shown in shadowgrams (see Figure 5.2, 5.5). These shock and mass density vortices with very high density will curl around the glass tube edges depending on the boundary. Figure 5.5 shows the shadowgram of spatial confinement of air plasma at 400 mJ laser input energy at 15 μs time scale, clearly showing the shock vortices at the cavity edges. At the +Z and +Y direction (quadrant I) edges, the shock and mass density flow curls along anti clockwise direction as shown in Figure 5.5. Same behaviour is also observed at the -Z and -Y direction boundary (quadrant III). While the edges falling in quadrant III and IV, the shock and mass density flow is observed to curl along clockwise direction. The shock wave exit times and shock vortices greatly depends on the laser input energy. As

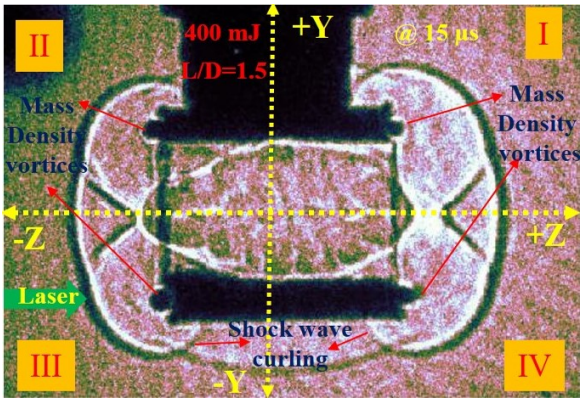

Figure. 5.5 Formation of the shock and mass density vortices along cavity edges in spatial confinement of air plasma inside a rectangular cavity with L/D=1.5

the laser input energy increases from 50 mJ to 400 mJ, the shock exit times will decrease and the shock vortices curling around the glass tube edges are very clearly visible. The energy dependence on shock wave exit times is summarized in Table 5.2. We have not considered the friction factor between propagating shock waves and the walls of cavity i.e., dependence of hollow tube material and its surface roughness, it becomes a dominant factor in case of micro-tubes (i.e., having few μm of diameter) which will effect the shock wave exit times and density of the shock vortices.

Table 5.2 Exit time scales of shock waves along ±Z direction w.r.to the variation of input laser energy in spatial confinement of air plasma inside a rectangular cavity with L/D=1.5

Energy	**L/D=1.5**	
	-Z	**+Z**
50 mJ	5 μs	5.5 μs
200 mJ	3 μs	3.5 μs
400 mJ	2 μs	2.5 μs

5.4.5 Energy dependence on the temporal evolution of radial shock waves

Figure 5.6 shows the energy dependence on the temporal evolution of shock waves from spatially confined air plasma along ± Y (transverse) direction. The temporal evolution of shock waves along +Y direction is compared to the free expansion of shock waves from air plasma along same direction at different input energies of 50, 200 and 400 mJ as shown in Figure 5.6. In the free expansion of shock waves from air plasma, the shock front radius increases linearly following the self-similar solution/Sedov-Taylor theory [8, 35, 47]. In the case of the spatially confined air plasma, the shock evolution along +Y direction followed

the evolution of a freely expanding air plasma till the shock wave front reached the glass tube or cavity walls along ±Y direction. As the separation (diameter) between the glass walls along Y direction is 8 mm, the shock wave front along ±Y direction propagates following Sedov-Taylor expansion till 4 mm in either direction. At ∼ 5 to 6 μs (Figure 5.6) the shock wave front will encounter the glass wall and reflected. After interaction of the transverse shock wave front with the glass plate, the shock wave reflects back into the tube due to the huge acoustic impedance mismatch between air and glass.

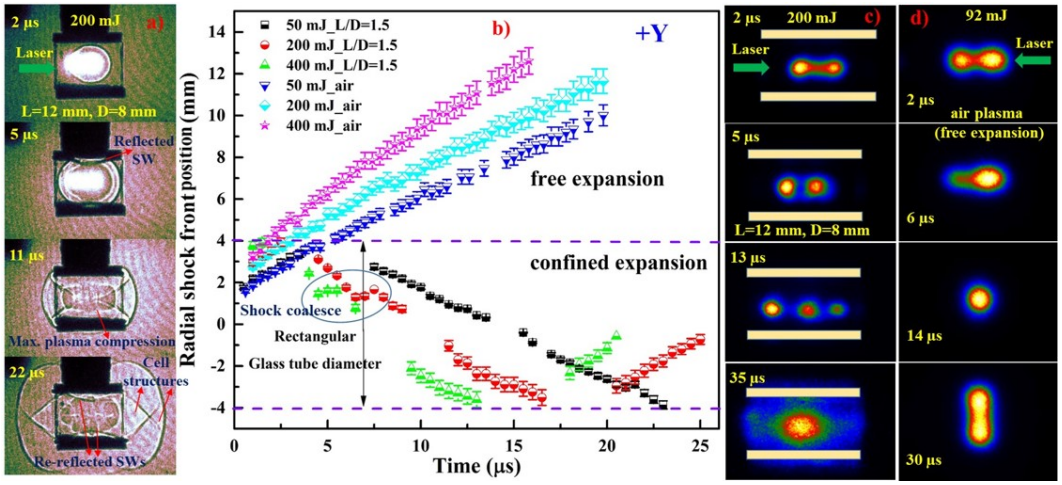

Figure. 5.6 Temporal evolution of (a) shadowgrams of plasma and shock waves (b) transverse shock waves along +Y direction; the plasma self emission images of (c) spatial confinement of air plasma of 200 mJ energy inside a rectangular hollow glass tube with L/D=1.5 (d) freely expanding air plasma with 92 mJ energy; the -ve sign along Y axis (shock front position) is used represent the reflected transverse shock wave propagation from one end of the tube to other end through plasma centre

In the case of 50 mJ air plasma confinement inside glass tube of L/D=1.5 (i.e., L=12 mm, D=8 mm), the reflected transverse shock wave interacts with the plasma outer region (or contact front) around ∼ 7.5 to 8.5 μs and compress the plasma core which increases the plasma CF position around ∼ 2-2.5 mm (max.) compared to free expansion case along both ±Z directions (overall increase in plasma length is around 4-5 mm). Since the plasma has low density/density gradient (i.e., from 7 to 9 μs) the reflected transverse shock waves will propagate through the plasma core and interact with each other at the centre of plasma core around ∼14 to 16 μs. Due to the interaction of shock waves, maximum compression of the plasma core is observed. The simulations also revealed that, the maximum enhancement of the number density and plasma temperature is observed at the same time scales [46]. After the interaction, the two shock waves move forward to other side of glass tube inner surface. Due to this, the plasma size is elongated along ± Y direction (see Figure 5.2). In this case, we have not observed the secondary shock

wave coalescence with the primary shock waves. However, this effect is clearly visible along transverse direction with higher energies as shown in Figure 5.6. The simulations revealed that, due to the shock wave coalescence the plasma properties are greatly enhanced. For higher energies (200 mJ, 400 mJ), the reflected transverse shock waves are again reflected by the other end of the tube leading to another compression of plasma core (Figure 5.6) and mass density vortices also observed at the tube edges.

With the increasing laser energy the plasma dimension increases. Hence for a given cavity with a fixed 'D' (diameter), the reflections of the transverse shock waves from the walls will be occurring earlier. As the input laser energy increased from 50 mJ to 200 mJ and 400 mJ the reflection of the shock waves from +Y direction has reduced as shown in Table 5.3. These reflected shock waves after passing through the plasma, reach the cavity wall at -Y direction at $\sim$ 17 to 18 μs for 200 mJ and $\sim$ 14 μs for 400 mJ of laser energy. At 50 mJ, the second reflection of shock wave from -Y direction is not observed. For higher energies (200 mJ, 400 mJ) the shock wave along $\pm$ Y direction are observed to bounce back and forth between the cavity walls. This is analogous to that of a cavity round trip of a laser, but in transverse/radial direction and is termed as transverse shock wave round trip time (t_{srt}). This t_{srt} dependent primarily on the input laser energy and the cavity dimension. For rectangular glass cavity of D= 8 mm, the t_{srt} is observed to be $\sim$ 17.5 μs, 14.5 μs and 10 μs for input energies of 50, 200 and 400 mJ respectively. This t_{srt} is observed to match with the oscillations of plasma contact front as shown in Figure 5.3. This process i.e., transverse shock wave reflection and compression of the plasma is cyclic until the strength of transverse shock waves reach the ambient air pressure. This is the reason behind the observation of multiple enhanced plasma emissions between certain time delays/scales only [11, 41, 48].

Table 5.3 Reflection time scales of transverse shock wave along $\pm$Y direction w.r.to the variation of input laser energy and aspect ratio (L/D) in spatial confinement of air plasma inside a rectangular glass cavity

Energy	**L/D=1, 1.5, 2 $\pm$Y**
50 mJ	5-6 μs
200 mJ	3.5-4 μs
400 mJ	2.5-3 μs

5.4.6 Energy dependence on the temporal evolution of secondary shock wave

The novelty of the work is the generation of secondary shock wave. When the transverse shock wave is confined and reflected from the glass tube inner surface, the transverse shock wave interacts and compresses the plasma outer region (contact front). Due to the

high pressure gradient between plasma and ambient air inside the rectangular glass cavity, the high pressure/ density plasma decays again by generating another shock wave, which termed as **secondary shock wave (SSW)**. The experimental observation and evolution of secondary shock wave is shown in Figure 5.2(b) clearly for 50 mJ energy inside a rectangular cavity with L/D=1.5. Due to the experimental challenges, the evolution of secondary shock wave front position is measured along ±Z direction only. Figure 5.7 shows the temporal evolution of secondary shock wave along ±Z direction for 50 mJ laser input energy focused inside a rectangular cavity with L/D=1.5. The secondary shock wave detached from the plasma around ∼7 μs, which is the interaction time of transverse shock wave with plasma outer region. Due to the compression of the plasma core by the transverse shock wave, the pressure gradient between plasma and surrounding medium inside glass tube increases, leading to the generation of secondary shock wave.

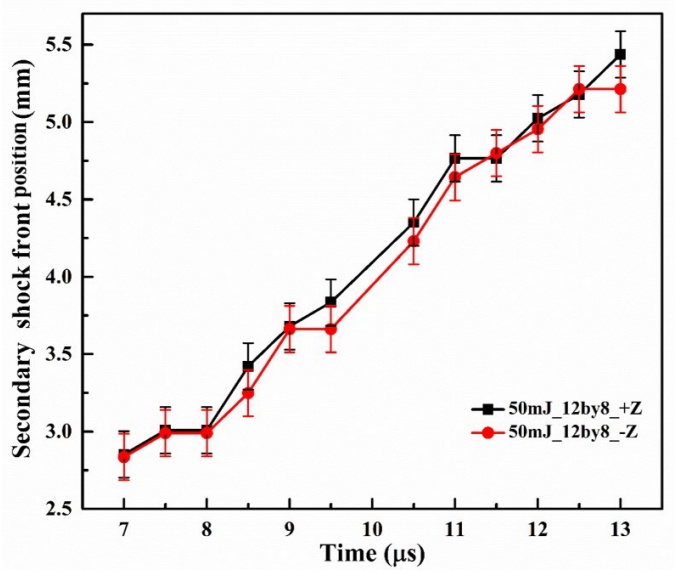

Figure. 5.7 Energy dependence on temporal evolution of secondary shock wave along ±Z direction in spatial confinement of air plasma inside a rectangular glass cavity with L/D=1.5

The secondary shock wave propagates into the shocked medium created by primary shock wave and coalesces with the primary shock wave. The evolution of secondary shock wave is clearly observed in the case of lower laser input energy i.e., 50 mJ (see Figure 5.2 (b), 5.7). As the energy increased from 50 mJ to 400 mJ, the velocity of secondary shock wave also increases and it will coalescence with primary shock wave early. For higher energies, the plasma plume is very bright ($<$ 5 μs) and saturates the ICCD camera. Hence we are not able to capture the secondary shock wave measurement experimentally. However, this is observed in FLASH-2D simulations [46]. The effect of input laser energy on secondary shock wave can be observed in terms of the shock coalescence of primary

and secondary shock waves along radial (± Y) direction. This is manifested by sudden change (decrease and then increase) of the reflected transverse shock front position along +Y direction for 200 mJ, 400 mJ energy around 5 to 7.5 μs, 2 to 4.5 μs respectively. From the captured shadowgrams, we have observed that in the case of 200 mJ energy, the reflected transverse shock wave starts to interact with the plasma outer region around ∼4.5 to 5.5 μs. The transverse shock wave is reflected back and at the same time we have observed the sliding of transverse shock wave from the cavity wall on ± Y direction, causing the shock front position to decrease up to around ∼1 μs (see Figure 5.6). During this time, the secondary shock wave catches the primary shock wave and coalesces with it. This will increase the shock wave strength and the transverse shock waves transmit through the low density plasma core. As the laser input energy further increased to 400 mJ, the reflected shock wave front position has similar behaviour as 200 mJ case and the coalescence/sudden change of shock front position is observed earlier. The generation of secondary shock wave and coalescence of primary and secondary transverse shock waves is also observed at almost same time intervals for the respective input laser energies in FLASH-2D Hydrodynamics simulations [46]. It also observed, due to the coalescence, around these time scales we have observed more enhancement of spatially confined plasma properties like number density and temperature [46].

5.4.7 Self emission study of air plasma inside a rectangular glass cavity with L/D=1.5

Figure 5.8 shows the temporal evolution of self emission from air plasma inside a rectangular glass cavity at 200 mJ laser input energy. The self emission images from air plasma in confinement is captured using fast ICCD with different gate widths ranging from 2 ns to 50 μs and the gate delay from 400 ns to 100 μs with a delay step size of 500 ns. The gate width and gate delay were varied to get a clear image. From the Figure 5.8, at initial time scales the plasma expansion is asymmetric similar to the case of free expansion until the transverse shock wave reflects from the glass tube and compresses the plasma. In spatial confinement of air plasma with 200 mJ energy, the transverse shock waves along ± Y direction is reflected from glass tube inner surfaces around ∼ 3 to 4 μs and compresses the plasma. Since the plasma shape is asymmetric having a dumbel like structure with high temperature region towards laser direction (-Z) (opposite to the laser propagation direction), the compression of the plasma along laser axis (± Z) resulted in two individual plasma hot spots around ∼ 5 to 6 μs with high temperature region towards laser direction as shown in Figure 5.8 (b) [35, 47, 49]. As the transverse shock wave propagates through the plasma core, another hot spot is created around ∼ 9 to 10 μs along laser propagation axis (+Z) which has low emission intensity than the two indicating a lower temperature region. The appearance of three plasma hot emission spots is due to the maximum compression of plasma core as both reflected transverse shock waves meets/interacts at the

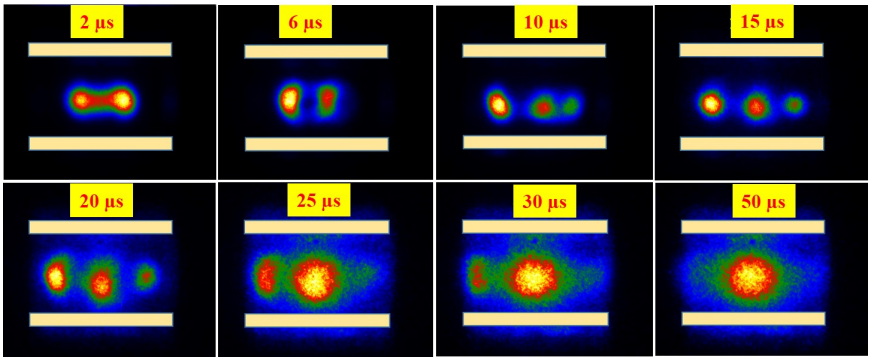

Figure. 5.8 Temporal evolution of self emission study from spatial confinement of air plasma created with 200 mJ input laser energy inside a rectangular glass cavity with L/D=1.5

centre around ∼ 9 to 10 μs time scales. As the two reflected transverse shock waves meet and move forward, the plasma species are dragged along with the shock waves which causes increase in the plasma size (along ±Y) and fluctuations in the contact front position (along ± Z) as explained earlier in Figure 5.3. Due to this, the plasma emission hot spots intensity also gradually decreases at longer time scales (> 15 μs). At time scales > 25 μs the three plasma emission hot spots merged as one big ellipsoidal blob at the tube centre. The increase in emission intensity (i.e, temperature) and emission hot spot size of spatially confined plasma is observed until the time of experimental observation (100 μs). This may be because of secondary compression of plasma core, due to the reflected transverse shock wave from other sides of glass tube inner surfaces as shown in Figures 5.2, 5.6. This shows the increase in plasma emission life time due to the spatial confinement of air plasma inside a rectangular glass cavity.

Figure 5.9 (a) shows the contour plot of line profile of temporal evolution of spatially confined air plasma self emission at 200 mJ energy. Figure 5.9 (b,c) shows the contour plot of line profile analysis of air plasma in free expansion for ∼ 92 mJ energy. Due to the spatial confinement and squeezing of the air plasma, the plasma emission length (emission intensity spread) along laser axis is more compared to the free expansion (see Figure 5.9 (a,b)). In free expansion of air plasma, initially the plasma expands asymmetrically along laser axis (± Z) up to 10 μs (in case 92 mJ energy) then it collapses and begin to expand along transverse direction (± Y) [35, 48, 49], as shown in Figure 5.9 (b,c). In free expansion, the emission intensity (i.e., temperature) is more (single hot spot) at the plasma centre. But in spatial confinement of air plasma of 200 mJ energy, initially the emission intensity is more at plasma centre, once the reflected transverse shock wave compresses the plasma source (around 3 to 4 μs) the emission intensity is spread along laser axis with shifting of maximum emission intensity (i.e, high temperature hot spot) towards laser direction as shown in Figure 5.6, 5.8, 5.9 (a), showing the asymmetric compression

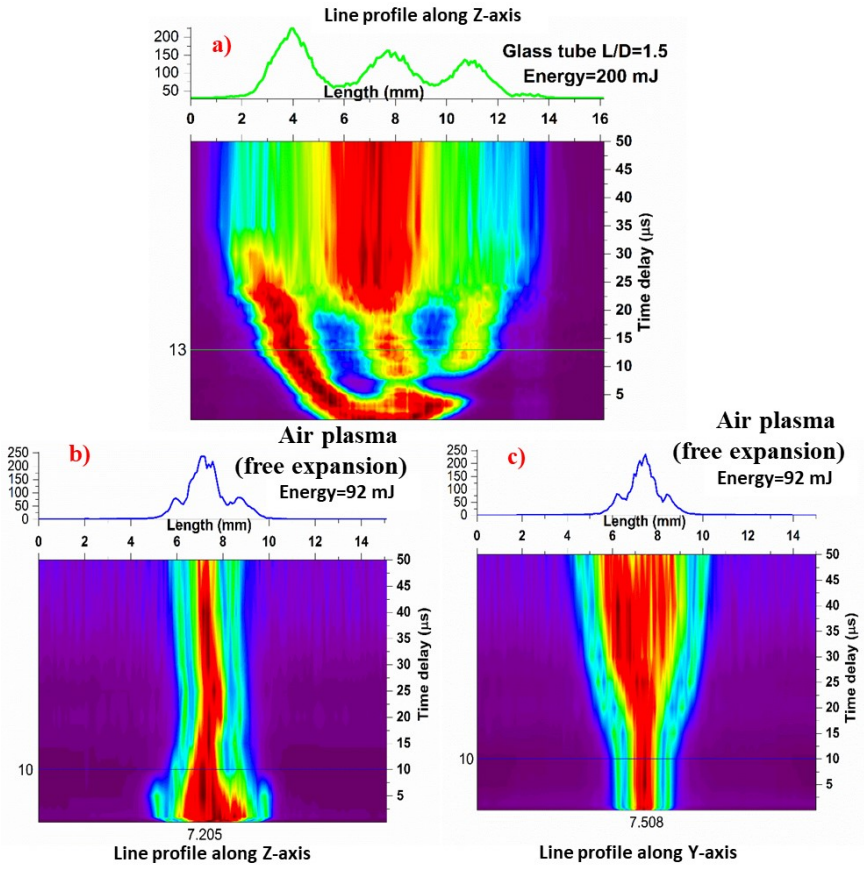

Figure. 5.9 Contour plots of Line profile of (a) air plasma of 200 mJ energy along ± Z direction in spatial confinement inside a rectangular glass cavity with L/D=1.5; free expansion of air plasma at 92 mJ energy (b) along ± Z direction (c) along ± Y direction.

of plasma. At 9 to 10μs, due to the maximum compression the plasma splits into three temperature regions with high intensity towards laser direction, medium intensity at the tube centre (plasma centre) and low intensity along laser propagation direction (Figure 5.8 (a)). At longer time scales (> 20 μs) the plasma emission hot spot on either side of the centre hot spot gradually decays. At the same time the centre hot spot emission intensity as well as size (spatial spread) increases having maximum intensity at the plasma centre. The emission intensity spread/size is almost constant through out the observation time (Figure 5.9 (a)) and it is equal to the size at maximum plasma squeezing time having maximum intensity at the centre of plasma (horizontally). By comparing Figure 5.9 (a), (b) & (c), in spatial confinement of the air plasma the emission intensity region is broad due to compression and the decay of emission intensity is slow i.e, more life time of emission source compared to the case of free expansion. So the spatial confinement of plasma increases the plasma properties such as plasma volume, number density and plasma temperature which in turn increases plasma optical emission intensity and life time of plasma emissions.

5.4.8 Aspect ratio (L/D) dependence on the plasma and shock waves inside the rectangular glass cavity

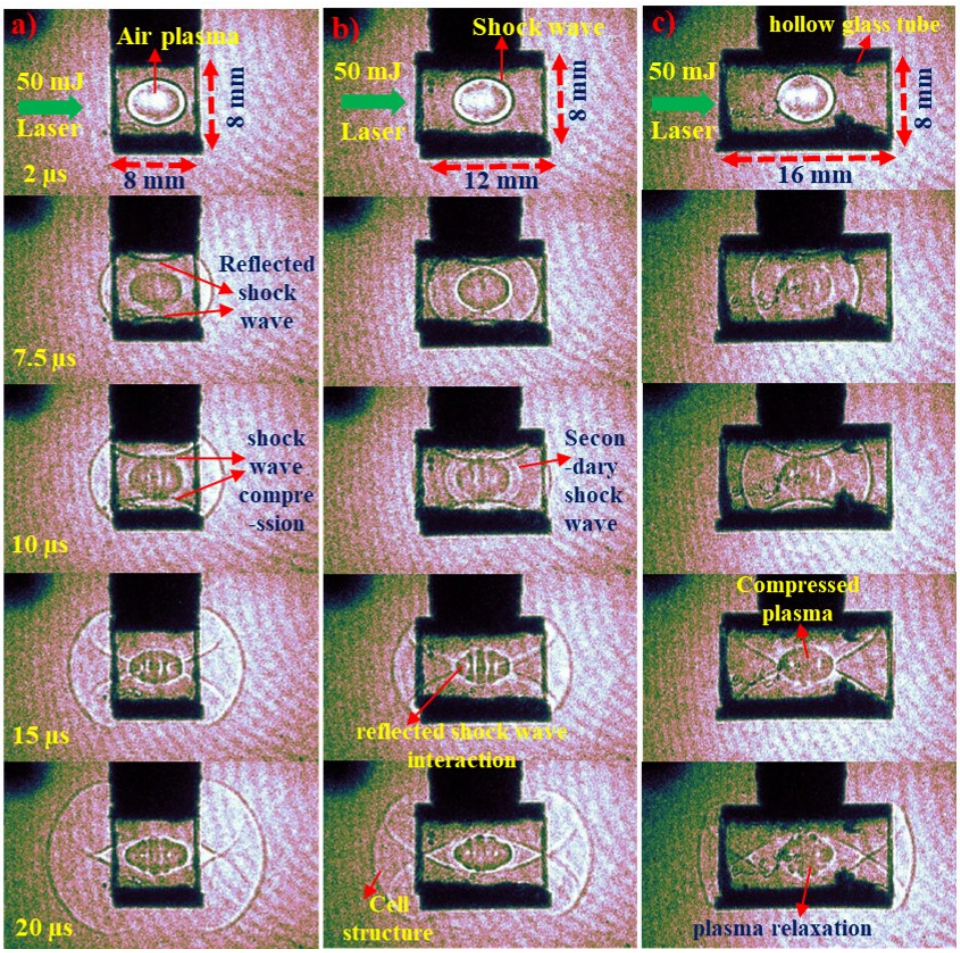

Figure. 5.10 Shadowgrams of temporal evolution of 50 mJ air plasma and shock waves in spatial confinement inside a rectangular glass cavity with different L/D ratios

In spatial confinement of plasma, along with input laser energy the dimensions of cavity plays a crucial role. The cavity dimensions can be described with a single quantity such as *Aspect ratio (L/D)*, which is a ratio between length of cavity to the inner diameter of cavity [17, 39, 50]. To understand the effect of cavity dimensions on the spatial confinement of plasma, we have to change either the length of cavity or inner diameter of the cavity. In this section, we have studied/visualized the effect of aspect ratio (L/D) on the spatial confinement air plasma inside a rectangular glass cavity by changing of cavity length (L) at a constant diameter of the cavity (D). By keeping the diameter 'D' constant, the round trip time (t_{srt}) of the shock front along ± Y direction remains fixed at a given laser energy. The details of rectangular cavity dimensions are mentioned in Table 5.1. Figure 5.10 shows the effect of aspect ratio (L/D) (i.e., length (L)) on the temporal evolution of air plasma and shock waves inside the rectangular glass cavity. A detailed description of the effect of spatial confinement on the air plasma when compared to the free expansion

is explained in previous section.

5.4.9 Aspect ratio (L/D) dependence on the temporal evolution of plasma length

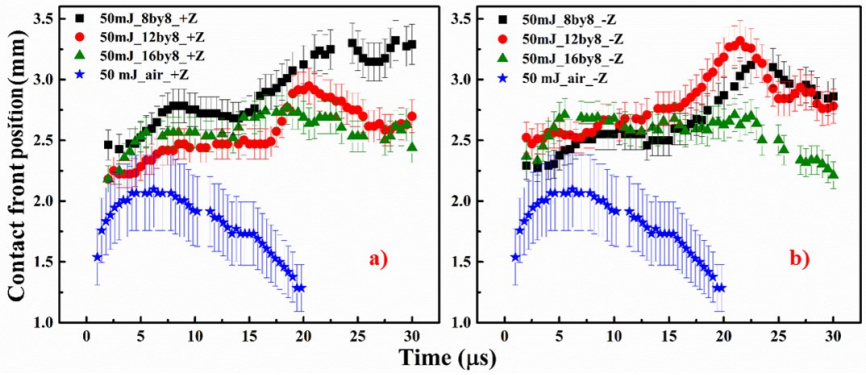

Figure. 5.11 Aspect ratio (L/D) dependence on temporal evolution of plasma length along ±Z in spatial confinement of air plasma inside a rectangular glass cavity

Figure 5.11 (a,b) shows the effect of length of cavity i.e., aspect ratio (L/D) on spatially confined air plasma at 50 mJ energy inside rectangular cavity. By varying the cavity length the contact front position is not varied much upto 15 μs, but it has increased considerably than free expansion, indicating a longer lived plasma. This is due to the fact that, since the diameter (D) of glass cavity kept constant, there is no change in the round trip time of the shock front (t_{srt}) along ± Y direction. But after 15 μs, the occurrence of the maximum contact front position changes in time due to the variation of cavity length.

As the cavity length increases, the morphology/shape of the plasma also changes from ellipsoid to spherical shape. This is due to the change in the exit time of the cell like structure formed by the interaction of reflected transverse shock waves. The maximum contact front position is observed when the cell like structure exits from the cavity and the cell like structure drags the plasma along ± Z direction leads to the change in plasma morphology/shape. As the cavity length increases, the exit time of cell like structure increases thus decreases its strength/drag (i.e., which in turn depends on strength of transverse shock waves) leading to decrease in the contact front position. The FLASH-2D simulations have shown that, due to the variation of length of the cavity there is a slight increment in the plasma properties like average number density, average pressure and peak temperature [46]. This is due to the fact that a longer cavity confines the plasma little longer, for a given laser input energy. For example, at 50 mJ laser input energy and L/D=2, the entire plasma plume will interact with the reflected transverse shock wave, while for L/D=1, the plasma plume will lose its energy along ± Z directions. Hence the density and temperature of the plasma, getting affected by the shock waves reflected from ± Y cavity wall will vary.

5.4.10 Aspect ratio (L/D) dependence on the temporal evolution of shock waves

Figure 5.12 (a,b) shows the effect of aspect ratio (L/D) (i.e., length (L)) on the temporal evolution of shock waves from spatially confined air plasma along ±Z direction inside the rectangular glass cavity. Since the diameter of the tube (D) is kept constant, there is no effect of the aspect ratio i.e., cavity length on (a) reflected transverse shock wave velocity/strength as well as reflection time scales (b) on the generation and evolution secondary shock wave.

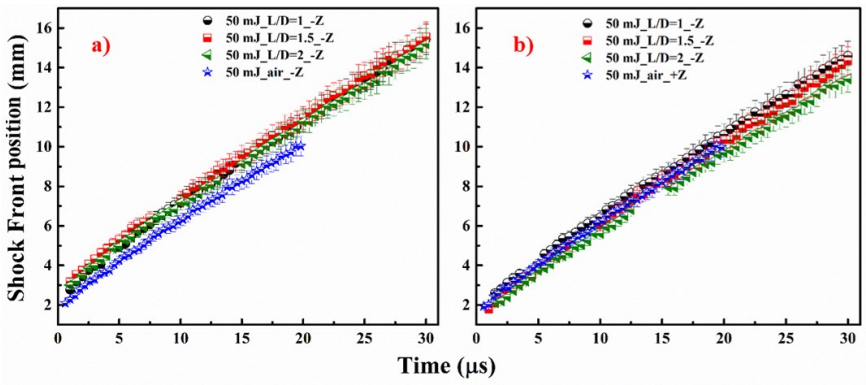

Figure. 5.12 Aspect ratio (L/D) dependence on temporal evolution of the shock waves along ±Z in spatially confined air plasma inside a rectangular glass cavity

Figure 5.12 (a,b) shows the effect of cavity length on spatially confined shock front position of the plasma at 50 mJ energy inside rectangular glass cavity. From the Figure 5.12, it is evident that the evolution of axial shock waves along ± Z direction are not effected due to the variation of cavity length (L/D). However, the axial shock wave exit times varied

Table 5.4 Exit time scales of shock waves along ±Z direction w.r.to the variation of input laser energy and aspect ratio (L/D)in spatial confinement of air plasma inside a rectangular glass cavity

Energy	L/D=1		L/D=1.5		L/D=2	
	-Z	+Z	-Z	+Z	-Z	+Z
50 mJ	5 μs	5.5 μs	10 μs	10.5 μs	15 μs	15.5 μs
200 mJ	3 μs	3.5 μs	6 μs	6.5 μs	11 μs	11.5 μs
400 mJ	2 μs	2.5 μs	4.5 μs	5 μs	8.5 μs	9 μs

slightly. As the cavity length increases from L/D=1 to L/D=2, the axial shock wave exit times also increases from 5 μs to 15 μs but as the energy increases from 50 mJ to 400 mJ, the axial shock wave exit time scales decreases. The aspect ratio dependence (L/D) on the axial shock wave exit times for different energies were summarized in Table 5.4.

5.4.11 Summary of the spatially confined air plasma inside rectangular cavity

To clearly understand and visualize the processes involved in the spatially confined air plasma evolution, we have used rectangular hollow glass tube with 8 mm constant inner dimension (diameter). Since the rectangular cavity inner dimension is more than the plasma size (or width), this enabled us to clearly understand the transverse shock wave propagation, its reflection from the glass cavity inner surfaces of walls and compression (asymmetric due to tube geometry) of plasma source by the reflected transverse shock waves. This study also gave interesting facts about the generation of secondary shock wave, shock wave coalescence effect on the plasma properties and energy dependence of the spatially confined plasma with different aspect ratios (L/D). The axial shock wave exit times and transverse shock waves reflection times from cavity walls w.r.to variation of laser input energy as well as tube length (L/D) were summarized in Table 5.4, 5.3. The compression and squeezing of the spatially confined air plasma inside rectangular glass cavity leading to the variation of the plasma length and shock exit times mainly depends on the laser input energy, cavity aspect ratio (L/D) and surface roughness of the cavity material.

5.5 Dynamics of spatially confined air plasma inside cylindrical cavity

After the clear visualization and understanding of the spatially confined air plasma and shock waves inside a rectangular glass cavity, the studies were extended to the cylindrical geometry. In this geometry, the spatial confinement of air plasma is studied inside hollow cylindrical cavities. The spatial confinement in this geometry produces a radially symmetric compression of air plasma by the reflected radial shock waves. Previous works [11, 50] also confirmed that, the plasma emission enhancement is more in case of cylindrical cavities than all other cavity geometries. Since the cylindrical tube is opaque to the probe beam, the evolution of the axial shock waves exit and the ejection of the plasma mass density along the ± Z direction is visualized using shadowgraphy. Hence, we have studied the effect of laser input energy and aspect ratio (L/D) (i.e., length (L)) on the cylindrical confinement of air plasma inside different metal and non metal hollow tubes in terms of shock wave exit times and evolution of the shock waves and plasma mass density in the surrounding medium.

In this section, we have studied the spatial confinement of air plasma inside a cylindrical hollow copper tube with an inner diameter of 4.7 mm and of different lengths 4.7, 7.05 and 9.14 mm leading to aspect ratios of 1, 1.5 and 2 respectively are used. Since the diameter of the tube is constant, this geometry produces the symmetric compression of air plasma due to the reflected radial shock waves. The dimensions of the cylindrical Cu

Table 5.5 Dimensions of the different cylindrical hollow tubes used in spatial confinement of air plasma in cylindrical geometry

Material	Cylindrical geometry		
	L (mm)	**D**(mm)	**L/D**
Copper	4.65±0.3	4.69±0.12	∼1
	7.05±0.3	4.69±0.12	∼1.5
	9.41±0.3	4.69±0.12	∼2

tube used to study the confinement of air plasma is summarized in Table 5.5.

5.5.1 Visualization of spatial confinement of air plasma inside cylindrical hollow copper tube

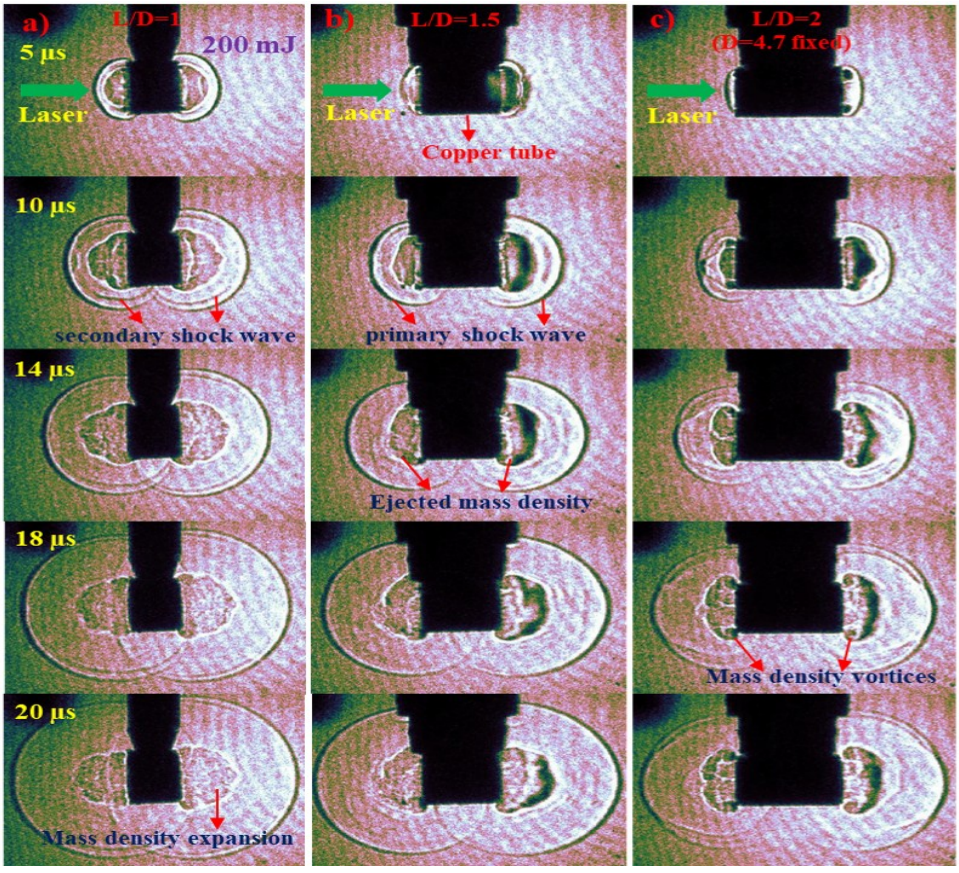

Figure. 5.13 Shadowgrams of the temporal evolution of 200 mJ air plasma and shock waves inside a cylindrical hollow copper tube with different L/D ratios

Nano second laser pulses of 10 ns pulse width are focused at the centre of the copper tube. As the plasma expands, the detached shock wave propagates in all directions. The reflected radial shock compresses the plasma along radial direction, which increases the plasma length as discussed in rectangular geometry (Figure 5.3). Figure 5.13 (a),

(b) & (c) shows the shadowgrams of temporal evolution of shock waves from spatially confined air plasma at 200 mJ laser input energy inside a cylindrical copper tube along ± Z direction with different L/D ratios (i.e., length variation, fixed diameter). Since the diameter (∼ 4.7 mm) of the tube is almost equal to plasma size at higher energies(200 mJ, 400 mJ), the increase in the plasma length due to the symmetric compression of radial shock waves is predominant. We have observed the ejected plasma mass density/ hot gases after the exit of the primary axial shock waves from copper tube along ±Z direction similar to the conventional shock tubes [1, 2, 3, 4, 9]. The high density gradient between the ejected plasma mass density and surrounding ambient air lead to the formation of secondary shock wave in surrounding ambient air after the exit of the primary axial shock wave from copper tube along ± Z direction (observed in all the cases). The exited axial shock waves also have more density/strength because of less propagation of transverse shock waves inside copper tube compared to that of the rectangular cavity. The ejected mass density also expands with time into the surrounding ambient air. We have not observed any shock wave vortices during the shock wave exit for L/D=1, 1.5, may be due to higher energy (200 mJ), lesser tube diameter and also due to the ejection of mass density. But we have observed the mass density vortices clearly with L/D=2 case. As the energy of plasma increases, more plasma mass density/hot air gas is ejected into the surroundings. The cell like structure behind the primary axial shock waves is observed in all the cases, but it is more evident with lower energy (50 mJ) and higher L/D ratio of copper tube.

5.5.2 Energy dependence on the temporal evolution of the shock waves from spatially confined air plasma inside a cylindrical copper tube with L/D=1.5

Figure 5.14 (a,b) shows the energy dependence on the temporal evolution of axial shock waves along ± Z direction exited from the spatially confined air plasma inside a cylindrical copper tube with aspect ratio L/D=1.5. Although we are not able to quantify the shock front position inside the copper tube (because tube is opaque to probe beam), we can compare the shock front position after the exit of the shock wave from copper tube with free expansion shock front position. From rectangular geometry, we can understand that, the effect of confinement is negligible on the axial shock waves propagating along ±Z direction. But the confinement with different L/D ratios or energy dependence with constant L/D, effects on the shock wave exit times from cavity/tube.

From the Figure 5.14 (a,b), it is clear that the shock front position in the case of the cylindrical confinement is more than the case of free expansion. This is due to the fact that, the diameter of copper tube is small and comparable to the plasma size. The symmetric compression of the air plasma due to the reflected radial shock waves will be higher and the plasma mass density ejection from tube will push the shock waves

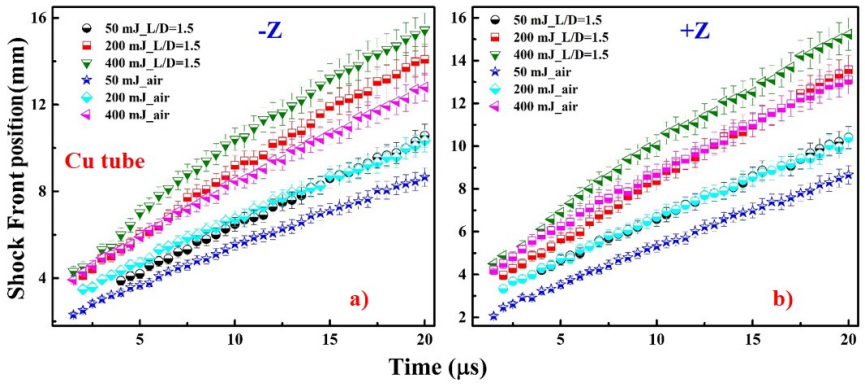

Figure. 5.14 Energy dependence on the temporal evolution of axial shock waves along ± Z direction in spatially confined air plasma inside a cylindrical copper tube with L/D=1.5

position along ±Z direction leading to the higher shock front position than that of the free expansion case over the observed time as shown in Figure 5.14 (a,b). For 50 mJ energy, the shock front position increases by ∼ 0.3 mm to 0.5 mm along -Z direction and ∼ 0.3 mm to 0.5 mm along +Z direction compared to the free expansion case. For 200 mJ energy, the increment in the shock front positions is around ∼ 0.2 mm to 2.4 mm along -Z, ∼ 0.3 mm to 1.8 mm along +Z direction, while for 400 mJ energy, the increment is around ∼ 0.5 mm to 2.8 mm along -Z, ∼ 0.4 mm to 2.3 mm along +Z direction compared to the free expansion of air plasma at respective energies as shown in Figure 5.14 (a,b). As the energy increases, the shock front position increases in the case of confinement due to the more ejection (push) of the plasma mass density w.r.t. the free expansion shock front position. The increment in the mass density ejection due to higher energies, decreases the axial shock wave exit times from the Cu tube. The shock wave exit time scales from copper tube w.r.t. laser energy is summarized in Table 5.6.

Table 5.6 Exit time scales of the axial shock waves along ±Z direction w.r.t. the variation of input laser energy and aspect ratio (L/D) in spatially confined air plasma inside a cylindrical copper tube

Energy	**L/D=1**		**L/D=1.5**		**L/D=2**	
	-Z	**+Z**	**-Z**	**+Z**	**-Z**	**+Z**
50 mJ	1.5 μs	2 μs	4 μs	4.5 μs	6 μs	6.5 μs
200 mJ	0.5 μs	1 μs	2 μs	2.5 μs	3.5 μs	4 μs
400 mJ	-	-	1.5 μs	2 μs	2.5 μs	3 μs

5.5.3 Aspect ratio (L/D) dependence on the temporal evolution of shock wave from spatially confined air plasma inside cylindrical copper tube

Figure 5.15 (a,b) shows the aspect ratio (L/D) dependence on the temporal evolution of axial shock waves along ± Z direction exit from the spatially confined air plasma at 50 mJ laser input energy.

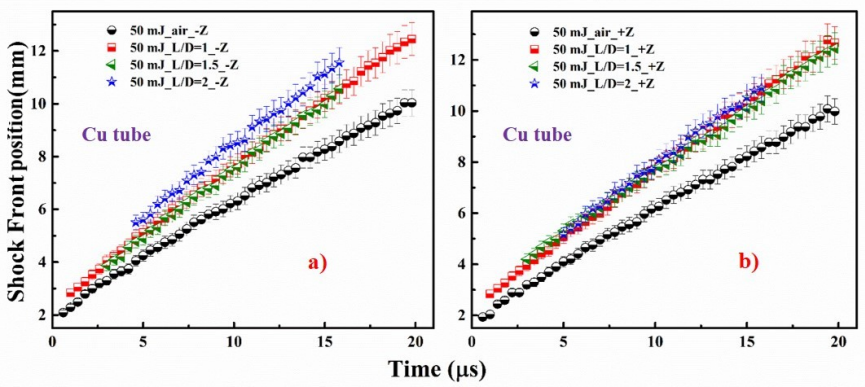

Figure. 5.15 Aspect ratio(L/D) dependence on the temporal evolution of axial shock waves along ± Z direction in spatially confined air plasma inside a cylindrical copper tube

From the Figure 5.15 (a,b), it evident that there is an enhancement of ∼ 10-20 % in the shock front position with the spatial confinement. However, the increase in the aspect ratio from L/D=1 to L/D=2, has not shown any observable enhancement except that it increases the axial shock exit times from the copper tube along ± Z direction. The shock wave exit time from copper tube w.r.t. the aspect ratio(L/D) i.e., tube length is summarized in Table 5.6. For 50 mJ energy, as the aspect ration increases from L/D=1 to L/D=2 the axial shock front exit times are increased from 1.5-2 μs to 6- 6.5 μs along ± Z direction. For 200 mJ, the axial shock front exit times are ∼ 0.5 to 1 μs for L/D=1 and ∼ 3.5 to 4 μs for L/D=2 along ± Z direction. For 400 mJ, the shock exit times are ∼ 1.5 to 2 μs for L/D=1.5 and ∼ 2.5 to 3 μs for L/D=2 along ± Z direction. The visibility of the mass density vortices are better for higher energies with the higher aspect ratio of the copper tube (L/D=2).

5.5.4 Role of the cavity/tube diameter in terms of aspect ratio (L/D) on air plasma confinement in cylindrical geometry

From above work we observed that the diameter of the tube/cavity plays a key role than the tube/cavity length. To understand the effect of tube diameter alone in aspect ratio (L/D) on the spatial confinement of air plasma in cylindrical geometry, we have studied the confinement process inside different cylindrical tubes made with different materials.

This is performed by keeping the length of the tube almost constant and varying the diameter (D) at the constant laser energy of the 200 mJ per pulse. The details of the different type of cylindrical tubes used in this study are summarized in Table 5.7.

Table 5.7 Dimensions of the different cylindrical tubes used to study the effect of tube diameter on the spatially confined air plasma in cylindrical geometry

Material	**Cylindrical geometry**		
	L (mm)	**D**(mm)	**L/D**
Glass	15±0.5	12.5±0.2	∼1.2
	15.5±0.5	10.5±0.2	∼1.47
Plastic	17.8±0.22	16±0.15	∼1.1
	17.8±0.22	13±0.15	∼1.36
Stainless steel	12.72±0.2	6.47±0.1	∼1.96
	12.81±0.2	5.4±0.1	∼2.37

5.5.5 Glass cylindrical tube

To study the role of tube diameter (D) on the aspect ratio L/D in air plasma confinement, we used glass tube of different diameters (12.5 ± 0.2 and 10.5 ± 0.2 mm) with almost constant lengths (see Table 5.7). A nano second laser pulse of 200 mJ energy is focused to create air plasma at the centre of the glass tube. Figure 5.16 (a-f) shows the shadowgrams

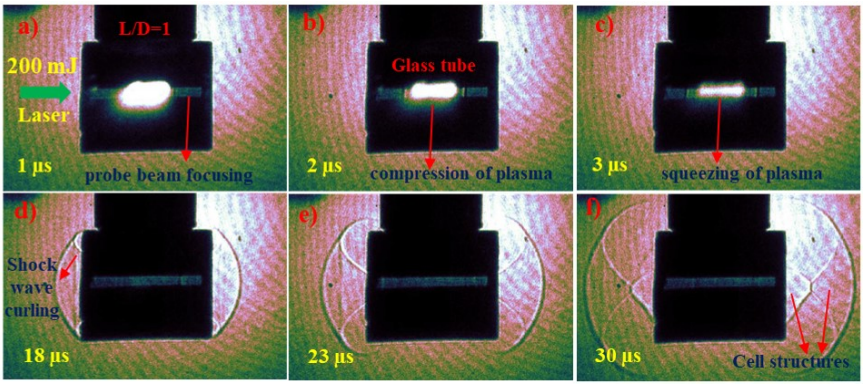

Figure. 5.16 Shadowgrams of the temporal evolution of spatially confined air plasma inside a cylindrical glass tube

of temporal evolution of air plasma with 200 mJ energy inside a glass tube with aspect ratio L/D =1. As already explained, due to the cylindrical curvature, the evolution of air plasma and shock waves inside the tube is not clearly visible. But due to plasma continuum, we can observe the symmetric compression and squeezing of the plasma at

initial time scales <5 μs (Figure 5.16 (b)). We have not observed the ejection of mass density as in the case of copper cylindrical tube. This may be attributed to the large diameter of glass tube compared to the copper tube or compared to the size of the plasma (typically 4-6 mm for 200 mJ energy [35, 47, 51]). From the shdowgrams, the axial shock waves are exited from the cylindrical glass tube around $\sim$ 10.5 μs along -Z and around $\sim$ 11 μs along +Z directions. While exiting from the glass tube, the shock waves curled around the edges of glass tube forming shock vortices as shown in Figure 5.16. At longer time scales > 20 μs, we have observed a cell like structures behind the axial shock wave as shown in Figure 5.16(f). The first cell structure is due to the expansion of the curled shock waves along $\pm$ Z directions. This confirms that the mass density curling forms the shock wave vortices leading to the cell like structure due to the squeezing of the plasma by the reflected radial shock waves. The second cell structure clearly confirms the propagation of the reflected radial shock waves through plasma core towards other ends of the tube. Based on the number of cell structures appeared in the surrounding air, one can estimate the number of radial shock wave reflections. Figure 5.17 (a,b)

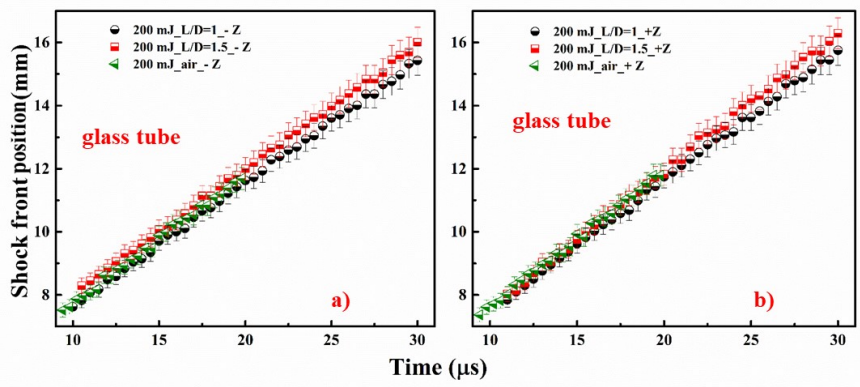

Figure. 5.17 Temporal evolution of the shock waves along $\pm$Z direction exited from the spatial confinement of air plasma inside a cylindrical glass tube

shows the temporal evolution of axial shock waves emitted from the spatially confined air plasma inside a cylindrical glass tubes with two L/D ratios. The shock front position from the spatial confinement is also compared with the free expanding shock waves at the corresponding plasma energy. The results show that there is no effect of a large tube diameter on the exited shock wave evolution in ambient air. This is due to the fact that the glass tube diameter is large compared to the plasma size (diameter), so the effect of the spatial confinement on the air plasma is minimal. Although we have observed the plasma compression but the squeezing of plasma is less in the case of higher tube diameter compared to that observed with the rectangular glass cavity and cylindrical Cu cavity.

5.5.6 Plastic (PVA) cylindrical tube

Figure 5.18 (a-f) shows the shadowgrams of the temporal evolution of spatially confined air plasma at 200 mJ laser input energy inside a plastic tube of aspect ratio L/D =1.5 as

mentioned in Table 5.7. Since the plastic tube is not completely transparent to the probe beam, the evolution of the air plasma and shock waves inside the tube is not clearly visible. However, the plasma continuum confirms the squeezing of plasma size due to compression of reflected radial shock waves at initial time scales < 3 μs (Figure 5.18 (b)). In this case also, we have not observed the ejection of the plasma mass density as in the case of copper cylindrical tube. This may be attributed to the large diameter of plastic tube compared to copper tube or size of the plasma. The shock waves exited from the

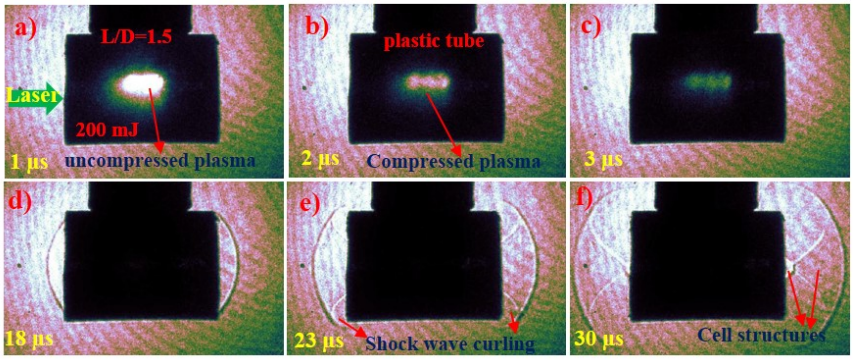

Figure. 5.18 Shadowgrams of the temporal evolution of spatially confined air plasma and shock waves along ±Z direction inside a cylindrical plastic tube

cylindrical plastic tube around $\sim$ 13.5 μs along -Z direction and around $\sim$ 14 μs along +Z direction. While exiting from the glass tube, the shock waves curled around the edges of the plastic tube (i.e., shock vortices). At longer time scales > 18 μs, we have observed the cell like structures behind the shock wave as shown in Figure 5.18(f) similar to the case of cylindrical glass tube. However, as the diameter of the plastic tube is more than

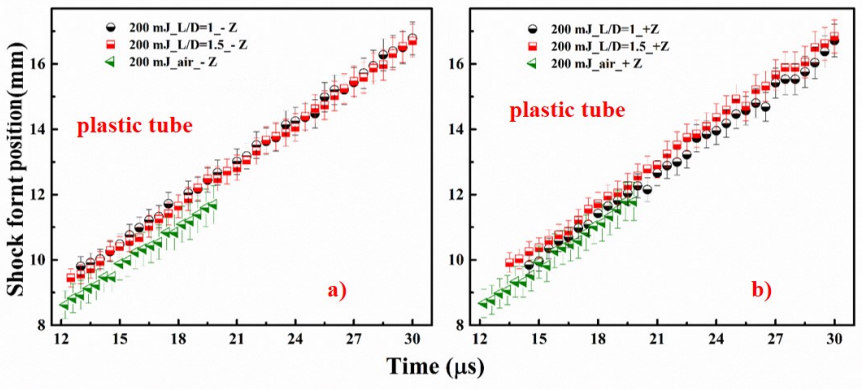

Figure. 5.19 Temporal evolution of the shock waves along ± Z direction exited from the spatial confinement of air plasma inside a cylindrical plastic tube

that of cylindrical glass tube by 2 mm, only the first cell like structure is clearly visible, the second cell structure is delayed slightly at 30 μs as shown in Figure 5.18 (f). Figure

5.19 (a,b) shows the temporal evolution of shock waves exited from spatially confined air plasma inside a cylindrical plastic tubes width two L/D ratios, (i.e., different diameter tubes) along ± Z direction. The results confirmed that a larger tube diameter is not effective in enhancing axial shock waves.

5.5.7 Stainless steel (SS) cylindrical tube

Based on previous results, we have repeated the spatial confinement of air plasma inside a stainless steel (SS) cylindrical tube with diameters almost similar to the air plasma size in ambient conditions at 200 mJ laser input energy (i.e., typically 4-6 mm for 200 mJ energy [35]). Figure 5.20 (a,b) shows the shadowgrams of the temporal evolution of spatially confined air plasma at 200 mJ laser input energy inside a SS tube with aspect ratios L/D ∼ 2, 2.4 as mentioned in Table 5.7. Since the SS tube is opaque to the probe beam, we will observe only the evolution of exited shock waves from the tube and the ejected plasma mass density. From the shdowgrams, the shock waves are exited from the cylindrical SS

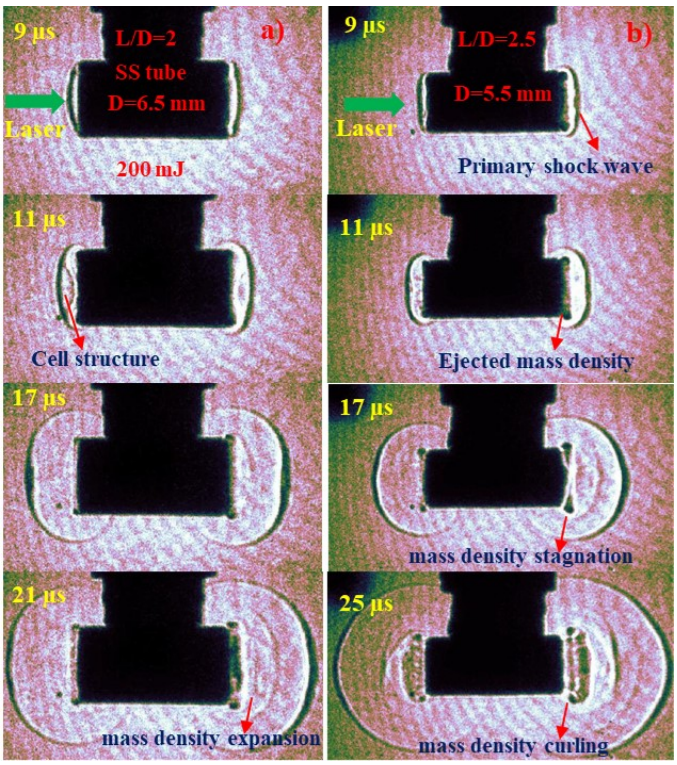

Figure. 5.20 Shadowgrams of the temporal evolution of spatially confined air plasma inside a cylindrical SS tube

tube around ∼ 7.5 μs along -Z direction and around ∼ 8 μs along +Z directions. Since the both the SS tube diameters are almost equal to the plasma size of respective energy, we have observed the shock waves with high density exiting along ± Z directions. In the case of SS cylindrical tube with small diameter (i.e., high L/D ratio), we have observed the ejection of the plasma mass density as well as mass density vortices similar to the copper tube case around ∼ 10 μs . While for SS tube with large diameter, the ejection

of the plasma mass density is observed at longer times i.e., > 17 μs). While comparing the shadowgrams of SS tube with that of the images from Cu tube, the structures appear to be similar to that of plasma mass density than that of cell like structures. So the cell like structures are observed in the case of large diameter tubes only. Figure 5.21

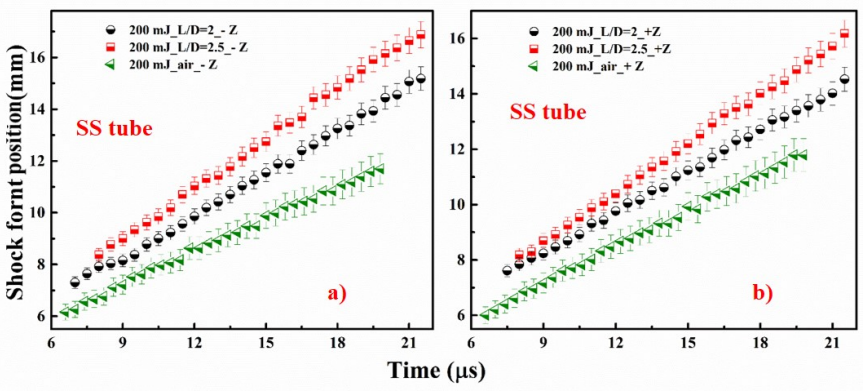

Figure. 5.21 Temporal evolution of the shock waves along ± Z direction exited from the spatial confinement of air plasma inside a cylindrical SS tube

(a,b) shows the temporal evolution of shock waves exited from the spatially confined air plasma inside a cylindrical SS tubes with two L/D ratios, (i.e., different diameter tubes) along ± Z direction. The shock front position in confinement geometry (with both tube diameters) is more than that of the free expanding case. The ejection of the plasma mass density is similar to the case of copper tube. This confirms that, as long as confinement tube diameters are in the range of plasma size, we can observe the enhanced axial shock wave evolution along ± Z direction irrespective of length due to the plasma mass density ejection. Since the diameter of the tube is almost equal to plasma size, the reflection of the radial shock wave occurs earlier (i.e., less t_{srt}) and the compression force on the plasma greatly increases leading to more squeezing of the plasma along ± Z direction. So the increment in the plasma length due to reflected radial shock wave compression forces the shock waves along ± Z direction until they reach an open end of the tube. Due to the high pressure/density conditions inside the tube compared to the ambient air, the plasma mass density as well as shock wave will be forced out along ± Z direction like a stream flow. The force with which they are ejected is equal to the pressure/density difference between the ambient air pressure/density and the pressure/density inside tube. This confirms that, the increment in the shock front position (except shock exit times) in the confinement geometry mainly depends on the tube diameter and laser input energy but not on the tube length. As the tube diameter decreases, the more plasma mass density as well as shock waves along ±Z direction forced out, that leads to the more increment in the shock front position between confinement case and free expansion case as shown in Figure 5.21 (a,b).

5.5.8 Summary of the spatially confined air plasma in cylindrical geometry

In the spatial confinement of air plasma inside a cylindrical tube, the reflected radial shock waves compresses the air plasma symmetrically from all directions. Since the cylindrical tubes are opaque to the probe beam, we could not able to visualize clearly, the radial shock wave reflection and compression of the air plasma inside the tube but the squeezing of the plasma is visible in semi-transparent non metal tubes due to the plasma continuum at initial time scales < 5 μs. In spatial confinement of the air plasma, the diameter of the tube (D) plays a key role than the tube length(L), because the compression and squeezing of the air plasma highly depends on the strength of the reflected radial shock waves. This is confirmed by the increment in axial shock wave position due to the ejection of plasma mass density in smaller diameter tubes (copper and SS) while the larger diameter tubes (plastic and glass) have no effect on axial shock waves. It is also noted that, the plasma mass density observed only in tubes with diameter almost equal to the plasma size (or diameter) at the respective laser input energy and the cell like structure is clearly observed in tube with higher diameter ($>$ plasma size).

5.6 Conclusions

To conclude, the temporal evolution of spatially confined air plasma and shock waves inside rectangular glass cavity gave clear visualization of compression and squeezing of the air plasma by reflected transverse/radial shock waves from cavity walls. The compression and axial shock waves exit times mainly depends on the laser input energy and cavity aspect ratio (L/D). The self emission study of the spatially confined air plasma confirmed the enhancement of plasma life time. Since the tube diameter is more than plasma size, the shock wave vortices formed due to sharp density gradient at the cavity edges and cell like structures are observed due to the reflected radial shock wave interaction. From cylindrical geometry, it is confirmed that the tube/cavity length alone is not effective on the axial shock waves in the spatial confinement of air plasma. If the tube diameter is almost equal to the plasma size (or diameter), we observe the ejection of plasma mass density due to the symmetric compression and squeezing of the plasma, leads to the increment of the axial shock front position. The ejection of the plasma mass density mainly depends on the laser energy and tube diameter and it is constant for a particular laser input energy and tube diameter irrespective of the tube length. The study of the spatial confinement of the air plasma revealed the inter-dependency of the plasma and shock waves. The reflected radial shock wave compression increases the plasma properties such as plasma length, plasma life time and the squeezing of the plasma forces out plasma mass density which increases the axial shock wave position. For a better understanding and quantification of the enhancement factors of air plasma and shock wave properties, we have utilized these experimental data to validate FLASH-2D simulations.

References

[1] U. Teubner, Y. Kai, T. Schlegel, D. E. Zeitoun and W. Garen, *Laser-plasma induced shock waves in micro shock tubes*, New J. Phys. 19, 103016 (2017).

[2] M. Brouillette, *Shock waves at micro scales*, Shock Waves 13, 3–12 (2003).

[3] Y. Kai, W. Garen and U. Teubner, *Generation and propagation of shock waves in sub-milli meter capillaries*, Proceedings of International symposium on shock waves (ISSW-30), Tel Aviv (2015).

[4] G. Mirshekari, *Micro scale shock tube*, Ph.D. Thesis, University of Sherbrooke, Canada (2008).

[5] B. P. Fairand and A. H. Clauer, *Laser generation of high-amplitude stress waves in materials*, Journal of Applied Physics 50, 1497–502 (1978).

[6] D. Batani, A. Balducci, D. Beretta, A. Bernardinello, T. Lower, M. Koeing, A. Benuzzi, B. Faral and T. Hall, *Equation of state data for gold in the pressure range < 10 TPa*, Phys.Rev. B 61, 14, 9287-9294 (2000).

[7] K. Ding and L. Ye, *Laser Shock Peening Performance and Simulation*, Woodhead publishing Limited (2006).

[8] Y. B. Zel'dovich and Y. P. Raizer, *Physics of Shock Waves and High-Temperature Hydrodynamic Phenomena*, Dover Publications/Academic Press Inc., New York (2012).

[9] H. J. Davies and H. D. Curchack, *Shock Tube techniques and Instrumentation*, Technical report-1429, US army command, Harry Diamond Laboratory (1969).

[10] Y. Kai, W. Garen and U. Teubner, *A novel shock tube with a laser-plasma driver*, Laser Particle Beams (2017).

[11] Y. Li, D. Tian, Y. Ding, G. Yang, K. Liu, C. Wang and X. Han, *A review of laser-induced breakdown spectroscopy signal enhancement*, Applied Spectroscopy Reviews, Vol. 53, No.1, 1-35 (2018).

[12] X. K. Shen, J. Sun, H. Ling and Y.F. Lu,*Spatial confinement effects in laser-induced breakdown spectroscopy*, Appl. Phys. Lett. 91 (8)(2007).

[13] J. E. Balmer, R. Weber, P. F. Cunningham and P. Ladrach, *Plasma evolution in laser-irradiated hollow micro cylinders*, Laser and Particle Beams, Vol. 8, no. 1-2, pp. 327-337 (1990).

[14] R. Fabbro, J. Fournier, P. Ballard, D. Devaux and J. Virmont, *Physical study of laser-produced plasma in confined geometry*, Journal of Applied Physics 68,775(1990).

[15] D. E. Zeitoun, *Correlations of shock mach number attenuation in small size diameter tubes*, Phys. Fluids 27, 011701 (2015).

[16] D. E. Zeitoun and Y. Burtschell, *Navier-stokes computations in micro shock tubes*, Shock Waves 15, 241–6 (2006).

[17] A. M. Popov, F. Colao and R. Fantoni, *Enhancement of LIBS signal by spatially confining the laser-induced plasma*, J. Anal. At. Spectrom. 24 (5), 602–604 (2009).

[18] C. Phipps, M. Birkan, W. Bohn, H. A. Eckel, H. Horisawa, T. Lippert, M. Michaelis, Y. Rezunkov, A. Sasoh, W. Schall, S. Scharring and J. Sinko, *Review-Laser Ablation Propulsion*, Journal of Propulsion and Power 26 (4), 609-637 (2010).

[19] A. D. Craven and T. R. Greig, *The development of detonation over-pressures in pipelines*, I.Chem.E. SYMPOSIUM SERIES No. 25 (Instn. chem. Engrs, London, 1968).

[20] H. P. Schildberg, *Gas-Phase Detonations in Pipes: the 8 Possible Different Pressure Scenarios and their Static Equivalent Pressures Determined by the Pipe Wall Deformation Method (part 1)*, Chemical Engineering Transactions, 48, 241-246 (2016).

[21] G. Ben-Dor, O. Igra and T. Elperin, *Handbook of Shock Waves: Volume 2, Shock wave Interactions and Propagation*, Academic Press (2001).

[22] T. M. Squires and S. R. Quake, *Microfluidics: fluid physics at the nano-liter scale*, Rev. Mod. Phys. 77, 977 (2005).

[23] W. Sparreboom, A. Van Den Berg and J. C. T. Eijkel, *Transport in nano-fluidic systems: a review of theory and applications*, New J. Phys. 12, 015004 (2010).

[24] R. Nickel, K. Bobzin, E. Lugscheider, D. Parkot, W. Varava, H. Olivier and X. Luo, *Numerical studies of the application of shock tube technology for cold gas dynamic spray process*, J. Therm. Spray Technol. 16, 729–35 (2007).

[25] C. Phipps, *Laser Ablation and its Applications*, Springer Series in Optical Sciences, Vol. 129 (2007).

[26] K. Chaudhary, S .Rizvi and J. Ali, *Laser-Induced Plasma and its Applications*, Intech-open publishers (2016).

[27] F. F. Chen, A. Rubenchik, S. Witkowski, *Physics of Laser Plasmas*, Edition 3, North Holland, Amsterdam (1991).

[28] A. Dwivedi, *Recent advances in pulsed laser ablated plasma plumes: A review*, Surface Review And Letters 14(1):57-69 (2007).

[29] X. Hong, S. Wang, D. Guo, H. Wu, J. Wang, Y. Dai, X. Xia and Y. Xie, *Confining Medium*

and Absorptive Overlay: Their Effects on a Laser-induced Shock Wave, Optics and Lasers in Engineering 29, 447-455 (1998).

[30] H. Sobral and A. Robledo-Martinez, *Signal enhancement in laser-induced breakdown spectroscopy using fast square-pulse discharges*, Spectrochim. Acta Part B At. Spectrosc. 124, 67–73 (2016).

[31] X. Li, Z. Wang, X. Mao and R.E. Russo, *Spatially and temporally resolved spectral emission of laser-induced plasmas confined by cylindrical cavities*, J. Anal. At. Spectrom. 29 (11), 2127–2135 (2014).

[32] D. S. Meng, N. J. Zhao, M. J. Ma, Y. Wang, L. Hu, Y. Yu, L. Fang and W. Q. Liu, *Heavy metal detection in soils by laser induced breakdown spectroscopy using hemispherical spatial confinement*, Plasma Sci. Technol. 17 (8), 632–637 (2015).

[33] S. S. Mao, X. Zeng, X. Mao and R. E. Russo, *Laser-induced breakdown spectroscopy: Flat surface vs. cavity structures*, J. Anal. At. Spectrom. 19 (4), 495–498 (2003).

[34] X. Zeng, X. Mao, S. S. Mao, S. B. Wen, R. Greif and R.E. Russo, *Laser-induced shock wave propagation from ablation in a cavity*, Appl. Phys. Lett. 88 (6)(2006).

[35] Ch. Leela, Ph. D. thesis, University of Hyderabad, India (2014).

[36] L. B. Guo, W. Hu, B. Y. Zhang, X. N. He, C. M. Li, Y. S. Zhou, Z. X. Cai, X. Y. Zeng and Y. F. Lu, *Enhancement of optical emission from laser-induced plasmas by combined spatial and magnetic confinement*, Opt. Express 19 (15), 14067–14075 (2011).

[37] Z. Hou, Z. Wang, J. Liu, W. Ni and Z. Li, *Combination of cylindrical confinement and spark discharge for signal improvement using laser induced breakdown spectroscopy*, Opt.Express 22 (11), 12909–12914 (2014).

[38] J. Shao et.al., *Effect of cylindrical cavity height on laser induced breakdown spectroscopy with spatial confinement*, Plasma Sci. and Tech.19(2), p.025506 (2017).

[39] P. Yeates and E. T. Kennedy, *Spectroscopic, imaging, and probe diagnostics of laser plasma plumes expanding between confining surfaces*, J. Appl. Phys. 108 (9)(2010).

[40] C. Li, J. Wang and X. Wang, *Shock wave confinement-induced plume temperature increase in laser-induced breakdown spectroscopy*, Phys. Lett. A 378 (45), 3319–3325 (2014).

[41] X. Gao, L. Liu, C. Song and J. Lin, *The role of spatial confinement on nanosecond YAG laser-induced Cu plasma*, J. Phys. D: Appl. Phys. 48 (17), 175205 (2015).

[42] H. Yin, Z. Hou, T. Yuan, Z. Wang, W. Ni and Z. Li, *Application of spatial confinement for gas analysis using laser-induced breakdown spectroscopy to improve signal stability*, J. Anal.At. Spectrom. 30 (4), 922–928 (2015).

[43] V. Pinon and D. Anglos, *Optical emission studies of plasma induced by single and double femto second laser pulses*, Spectrochim. Acta Part B At. Spectrosc. 64 (10), 950–960 (2009).

[44] S. J. Choi, K. J. Lee and J. J. Yoh, *The laser-induced plasma persistence time extension in low*

pressures using the ablated mass confinement method, Spectrochim. Acta B At. Spectrosc. 97 (7), 113–117 (2014).

[45] Y. Fu, Z. Hou and Z. Wang, *Physical insights of cavity confinement enhancing effect in laser-induced breakdown spectroscopy*, Opt. Express 24 (3), 3055–3066 (2016).

[46] N. Guthikonda, D. P. S. L. Kameswari, E. Manikanta, S. Sai Shiva, S. Sree Harsha and P. Prem Kiran, *Dynamics of confined laser induced air plasma inside a hollow tube*, (Manuscript under preparation)(2020).

[47] S. Sai shiva, Ph. D. thesis, University of Hyderabad, India (2016).

[48] Y. Wang et al., *Two sequential enhancements of laser-induced Cu plasma with cylindrical cavity confinement*, Journal of Analytical Atomic Spectrometry 31(10), p. 1974-1977 (2016).

[49] Ch. Leela, S. Bagchi, V. Rakesh Kumar, S. P. Tiwari and P. Prem Kiran, *Dynamics of laser induced micro-shock waves and hot core plasma in quiescent air*, Laser and Particle Beams 31, 263–272 (2013).

[50] Q. Wang, A. Chen, D. Zhang, Y. Wang, L. Sui, S. Li, Y. Jiang and M. Jin, *The role of cavity shape on spatially confined laser-induced breakdown spectroscopy*, Physics Of Plasmas 25,073301 (2018).

[51] N. Guthikonda, E. Manikanta, Ch. Leela, S. Sai Shiva, S. Sree Harsha, V. R. Ikkurthi and P. Prem Kiran, *Interaction of two counter-propagating laser induced plasmas and shock waves in air*, Physics of Plasmas 27, 023107 (2020).

Chapter 6

Dynamics of laser ablative shock waves inside transparent dielectric media

When a nano second (ns) laser ablates the target material in ambient conditions, the shock waves are generated in surrounding medium as well as inside the target material. The shock wave propagation inside target material is increased (or ablative shock waves propagation in surrounding medium is minimized), using a thin layer (tamping layers/coating/black paint) adhered onto the target material as a confining medium. The enhanced shock wave properties like velocity, pressure are very useful in laser shock wave processing of materials, especially for laser shock peening. Though most of the work is done on enhancement of shock properties due to confinement, the clear visualization of the process of enhancement and the effect of different laser and material parameters on the enhancement factor is inadequate due to the opaqueness of solid materials to visible radiation. Here, in this chapter, we present the visualization of shock wave propagation inside a transparent solid, BK-7 glass due to the direct (unconfined) ablation and confined ablation of BK-7 glass using metal thin films (Al, Cu) as confining medium. The relative acoustic impedances of confining material and target material plays a crucial role in the shock wave propagation inside the BK-7 glass. As the relative impedance increases, the shock velocities are increased. In addition to the confinement material impedance, the focusing conditions also effects the enhancement of the transmitted shock waves inside BK-7 glass. This chapter provides a clear insight into how the shock wave properties enhance in the confined ablation and effect of the relative impedance of the confining thin film and target material. The results of confined ablation are compared to the unconfined/direct ablation case in the intensity ranging from 20 – 100 GW/cm^2 (i.e., for energies 0.5 - 2 J).

6.1 Introduction

Laser solid interaction is different for short ($\sim$ ns) and ultra-short ($\sim$ ps and fs) laser pulses due to different laser energy coupling mechanism to the material. In the case of ns laser ablation, it can be characterized by thermal, non-thermal and combination of both mechanisms [1]. Laser solid interaction can be divided into three phases [2, 3]: (i) bond-breaking and plasma formation, (ii) plasma expansion and cooling and (iii) particle ejection and condensation of the solid material. The laser ablation process will start with electronic energy absorption (in $\sim$ fs time scales) and ends with particle re-condensation ($\sim$ms time scales). When ns laser pulses with irradiation $\leq 10^9$ W/cm^2 interacts with the solid material, the absorption of the laser energy due the thermal vaporization causes the breakdown of the medium within a small volume that leads to the bond breaking and formation of the plasma until the termination of the laser pulse. Plasma formation process includes bond breaking and plasma shielding during the laser pulse interaction with the solid material surface. During the continuous ablation and heating of the plasma (in case of ns pulses) high thermal pressures builds up inside the core of plasma. After the pulse termination, the expansion of the plasma depends on the initial mass and energy of the plume, which governed by initial plasma properties such as electron density, temperature and velocity. The plasma plume expansion is adiabatic during the first microsecond after the laser pulse, afterwards, the plasma is cooled rapidly due to the loss the energy by radiation and sudden release of the deposited energy into the surrounding gas in the form of the Shock wave. The wave thus formed has a high pressure, density and energy across it and propagates through the surrounding gas(or unperturbed gas medium) with the supersonic speed. During the propagation, the undisturbed gas present ahead of the shock wave is rapidly compressed and changes the density of the medium after passing through it. Simultaneously, it also imparts momentum into the solid material in the form of a compression wave due to the recoiling momentum of the plasma expansion. For our work, the intensities are in the range $10^9 - 10^{10}$ W/cm^2, which are slightly more than breakdown threshold intensity (I_{th}) of a solid dielectric material. The plasma thus formed at the ambient conditions, can be typically in laser supported detonation (LSD) regime [3, 4, 5]. The Laser produced plasmas (LPP) were more interested in different fields because of its substantial applications to areas like inertial confinement fusion (ICF), X-ray lasers, material processing, plasma diagnostics, lithography, pulsed laser deposition and the study of elemental and chemical analysis of materials using LIBS, strengthening of solid materials using laser shock peening, to generate the Equation-of-State (EOS), micro-propulsion and also in medicine [6, 7, 8, 9, 10, 11, 12, 13, 14, 15, 16, 17, 18, 19, 20, 21, 22]. In contrast to the conventional impact experiments, with laser induced shock waves (LISW) the investigation of laser induced dynamic loading of materials can be done within

shorter (ns to μs) time scales and high pressures (> 1 GPa) [22, 23, 24]. The main challenge of the laser induced dynamic loading is to understand the behaviour of the shock wave propagating inside the solid material. There are different techniques available to understand the shock loading behaviour: Pressure gauges and Optical probe imaging with fast camera (VISAR with streak camera/ICCD camera) [25, 26]. Pressure gauges will gives only the information of shock pressure acted on the material after the shock waves reached at the material surface only. The studies on the visualization of shock wave propagation inside solid material are sparsely available due to the opaqueness of solids to visible radiation. It needs sophisticated instruments such as X-ray sources, detectors and VISAR with streak camera to monitor the shock wave inside solid materials [23, 26]. If the solid material is transparent to the visible radiation, one can visualize the evolution of the shock wave propagation inside the material and characterize the shock waves in terms of radius/pressure. Hence, we used BK-7 glass slab which is transparent to visible probe beam (633 nm) to study the shock propagation inside the solid material. The laser induced breakdown of optical glass material found potential applications in various fields such as laser micro-machining, 3-D wave guide structures, non-contact cutting of brittle materials, making confining geometry targets, understanding damage morphology at interaction zone, fabrication of micro-photonic devices and to clean the radioactive particles from glass surface etc. to name a few [27, 28, 30, 31, 32, 33, 34, 35].
This chapter provides the combined effects of axial confinement (as discussed in Chapter 4) and spatial confinement (as discussed in Chapter 5) on evolution of shock wave propagation inside BK-7 dielectric glass. The axial confinement of shock waves is achieved using an overlay of Al/Cu foils, while the dimensions of the BK-7 glass has provided the spatial confinement (due to glass-air impedance mismatch) of the shock waves propagated inside BK-7 glass.

6.2 Experimental Details

Laser grade BK-7 (transparent dielectric) glass slab of 50 mm × 50 mm × 15 mm (L × B × H) purchased from *Holmarc*® (India) is used as target. BK-7 glass is a borosilicate crown glass extensively used for lenses, mirrors, windows, wave guides and laser components. The BK-7 glass has a refractive index of 1.51 (n_0), band gap of 4.7 eV, non linear refractive index (n_2) of 3.45 $\times 10^{-16}$ cm^2/W, sound velocity (C_0) of 5.1 km/s and a shock impedance of 1.27 g/$cm^2 - s$ [36].

The experiments were performed using laser beam from a Q-switched *Nd: YAG* laser (TITAN-5, 10 ns, 532 nm, 5 Hz) with 22 mm beam diameter, which was focused using an anti-reflection coated plano-convex lens of 150 mm focal length in f/7 geometry to initiate the breakdown of the BK-7 glass. The input laser peak energies were ranging from 0.5 – 2 J were focused inside the BK-7 glass to a focal spot diameter of $\sim 500 \pm 50$ μm with corresponding laser intensities 2-100 GW/cm^2. In this chapter, the dynamics

of the laser induced shock waves inside BK-7 glass under the following conditions are presented: (i) direct ablation of BK-7 glass and effect of laser input energy (ii) effect of acoustic impedance of confining overlays by using Al, Cu foils of same thickness (20 μm): Z_{Cu} (3.93) > Z_{Al} (1.45) > Z_{BK-7}(1.27) (in 10^6 g/$cm^2 - s$) (see Table 6.2) (iii) effect of laser focal plane position shifting w.r.t. air-glass (direct ablation) and the foil-glass (confined ablation) interface along with the effect of laser pulse energy. The spatio temporal evolution of the laser ablative plasma and subsequent shock front (SF) evolution inside the BK-7 glass as well as into the surrounding air medium from BK-7/Al+BK-7/Cu+BK-7 targets was captured using focused shadowgraphy technique [25, 37, 38]. An expanded and collimated He-Ne probe beam of (a) 33 mm diameter is used for initial studies on the effect of laser input energy in direct ablation of BK-7 glass (b) 47 mm diameter is used to study the effect of laser input energy as well as the effect of focal plane shifting in direct and confined ablation of BK-7 glass. The detailed experimental schematic and settings of the diagnostic tools are described in chapter 2. Figure 6.1(a-d) illustrates the schematic of laser irradiation of BK-7 glass in direct ablation mode and ablation of Al/Cu foils confined to BK-7 glass as confining layers for different focusing conditions. The caustic curves shown in the Figure 6.1(on the top) represent the laser focusing plane. In the first case i.e., Figure 6.1(a,c), the laser beam is focused at the interface of the air-BK-7 glass (direct ablation) or at the interface of Al/Cu foil-BK-7 glass (confined ablation). This case is called herein after as F0 focusing condition. In the second case i.e., Figure 6.1(b,d), the laser beam is focused at a depth of 6 mm from the air-BK-7 glass interface (direct ablation) or a depth of 6 mm from the Al/Cu foil-BK-7

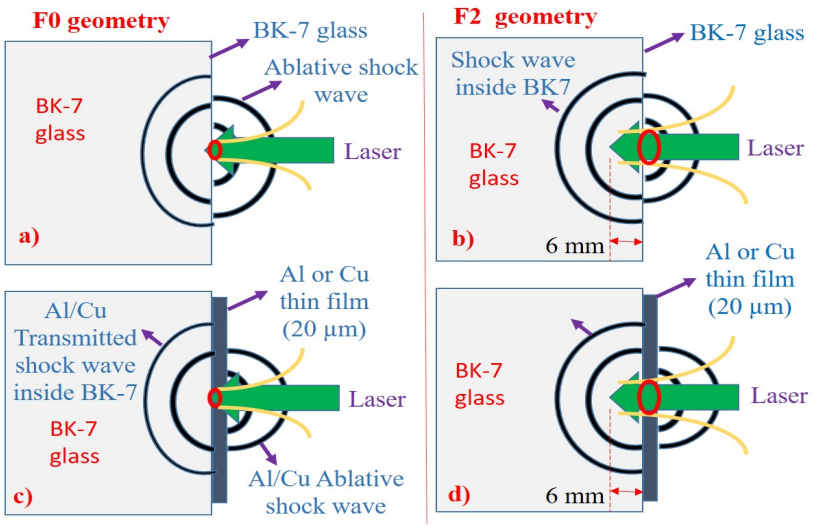

Figure. 6.1 Schematic of laser induced breakdown of BK-7 glass in (a-b) direct ablation mode and (c-d) Confined (Al/Cu + BK-7) ablation mode for different focusing conditions

interface (confined ablation). This case is called herein after as F2 focusing condition. Since the focusing plane position in the F2 condition is shifted, the intensity at the air-glass or foil-glass interface is lower than that of F0 condition.

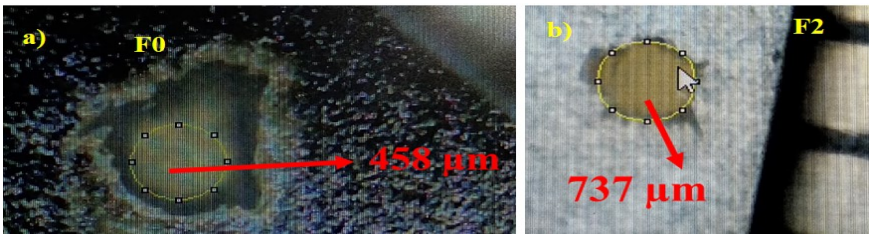

Figure. 6.2 The focal spot diameter at the target surface measured using burn patterns (a) at F0 focusing condition (b) at F2 focusing condition

Figure 6.2(a,b) shows the burn patterns of experimentally measured approximate focal spot diameters for 150 mm lens in f/#7 geometry at F0 and F2 conditions in the direct ablation of BK-7 glass. From the analysis of burn patterns, the focal spot diameter at F0 focusing is $\sim 458 \pm 50$ μm while it is $\sim 737 \pm 50$ μm at F2 focusing condition.

6.3 Shadowgraphy imaging of Laser induced breakdown of BK-7 glass: initial study

The laser induced breakdown of opaque solids are different to that of transparent solids such as BK-7 glass. To understand the laser induced breakdown of the BK-7 glass, the laser pulses of 10 ns pulse width having energies 0.5-2 J per pulse were focused inside the BK-7 glass around 6 mm deep from the surface to avoid air breakdown before the laser beam interacts with the BK-7 glass using a plane convex lens of 150 mm focal length and $2\omega_0 \sim 0.5$ mm in f/#7 geometry. The spatio temporal evolution of the laser ablated shock waves in ambient air as well as inside the BK-7 glass was captured using an fast gated (ns) ICCD camera and an expanded and collimated He-Ne probe beam of 33 mm beam diameter with the help of shadowgraphy imaging. The ICCD gate delays are varied from 50 ns to 20 μs in steps of 250 ns with 2 ns gate width. Figure 6.3 (a-d) shows the shadowgrams of the laser induced breakdown of BK-7 glass. Due to the laser induced breakdown of BK-7 glass, we have observed permanent damage tracks inside the BK-7 glass [39] that showed an interesting energy dependence as shown in Figure 6.3(d).

Since our ICCD can capture $\sim$ 1 frame per second, the experiment was repeated with multiple shots on the BK-7 glass, with each laser shot interacting with a fresh BK-7 glass surface, thus multiple permanent damages are visible inside BK-7 glass slab. Since the material is transparent to laser wavelength and the laser intensity (20-100 GW/cm^2) is much greater than BK-7 breakdown threshold ($I_{th} \sim 0.1 GW/cm^2$), a permanent damage is observed inside BK-7 is in the form of a channel. The length and width of the permanent

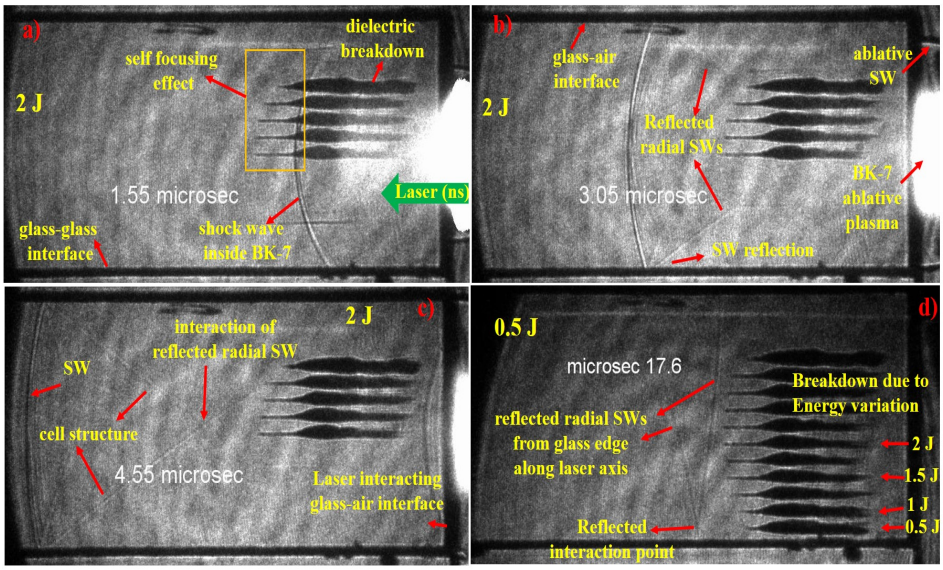

Figure. 6.3 Shadowgrams of laser induced breakdown of BK-7 glass in direct ablation mode at (a-c) 2 J (d) 0.5 J laser input energies

damage inside BK-7 glass with varying energy is analysed using line profile and the average values are given in Table 6.1. Since, the high energy ns laser pulses are interacting with the BK-7 glass there could be a chance for self-focusing effect inside the material due to the non linear optical processes [40, 41, 42, 43]. The self-focusing effect is a non linear process in which due to the change in refractive index of the material, the diverging laser beam gets focused again to create breakdown of material. In the Figure 6.3 (a), the sharp tips at the end of the permanent damage tracks along laser propagation direction is due to the self-focusing effect. This is verified by calculating the critical power required for self-focusing of a 10 ns pulse inside BK-7 glass. The critical power for self-focusing in BK-7 glass is given by [41]:

$$P_{cr} = \frac{\alpha\lambda^2}{4\pi n_0 n_2} \tag{6.1}$$

Where λ is laser wavelength, n_0 is refractive index of BK-7 glass (n_0=1.51), n_2 is the non linear refractive index of BK-7 (n_2=3.45 $\times 10^{-16}$ cm^2/W) and α is a constant, which depends on the initial spatial distribution of the laser beam (for Gaussian beams α=1.8962) [44]. The calculated critical power for BK-7 glass is $0.8MW$. The power required for self-focusing is: $P = 3.7 \times P_{cr}$. So, for a 10 ns laser beam, the energy required for self focusing is about $\sim 30mJ$. The self-focusing also affects the laser pulse to be shorter due to the optical Kerr effect, until the laser power is less than the critical power (P_{cr}). The input laser peak powers used in the study are of the order 50-200 MW, which is much higher than the critical power of the self-focusing (P_{cr}) of the BK-7 glass i.e., 0.8 MW [41]. Hence, due to the self focusing of the laser beam a sharp tip at the end of the permanent damage track is observed along laser propagation direction inside the BK-7

glass. As the input laser energy increased from 0.5 to 2 J, the permanent damage track length is increased due to the increased self focusing of laser beam while the width of the damage track is saturated as shown in Table 6.1 and Figure 6.4 (b).

Table 6.1 Averaged Dimensions of the permanent damage tracks inside the BK-7 glass with varying laser input energy

Energy (J)	**Laser fluence** (J/cm^2)	**Breakdown Length in BK-7** (mm)	**Breakdown Width in BK-7** (mm)
0.5	0.25×10^3	4.76±0.2	0.39±0.12
1.0	0.5×10^3	6.35±0.5	0.47±0.17
1.5	0.76×10^3	6.63±0.2	0.43±0.12
2.0	1.01×10^3	7.03±0.2	0.43±0.18

During the plasma cooling, a shock wave is launched into the BK-7 glass slab along 50 mm length as well as an ablative shock wave travelled into the ambient air simultaneously [45, 46]. Since the probe beam diameter in the initial study of BK-7 direct ablation is around 33 mm, which is less than the length of the BK-7 glass (50 mm) used, we are not able to visualize the laser ablative shock waves in the surrounding air and inside the BK-7 glass simultaneously. The evolution of the laser ablative shock waves from transparent solids (BK-7 glass) in surrounding air is similar to the laser ablation of opaque solids as discussed by our group earlier [25, 47]. The temporal evolution of laser ablative shock waves inside BK-7 glass is shown in Figure 6.3 (a-d). Although the permanent damage is occurred 6 mm deep inside BK-7 glass, the shock wave evolution is observed from the air-glass interface (or BK-7 glass surface) as shown in Figure 6.3 (a). So, the shock wave velocity inside the BK-7 glass is measured from the glass surface only. The BK-7 glass slab is stacked on top of another BK-7 glass slab to observe the shock reflections and transmissions due to the glass-glass/glass-air interfaces at different input laser pulse energies in direct ablation and confined ablation. The evolution of the shock wave inside the BK-7 glass is similar to that of the shock wave propagation in spatial confinement i.e., inside tubes (chapter 5) [48], because the BK-7 glass boundaries acts as confinement boundaries in all directions due to the impedance mismatch at the glass-air interface. When the shock wave expands inside BK-7 glass, it reflects from the surfaces of the BK-7 glass perpendicular to the laser propagation direction due to the impedance mismatch at the glass-air/glass-air-glass interface [49] (as explained in chapter 5). When the shock wave interacts with the glass-air interface perpendicular to laser propagation, a part of it is reflected from the interface and a part is transmitted to the air. The strength of the reflected shock wave depends on the impedance condition of the both mediums (air and glass) i.e., $Z_{glass} > Z_{air}$ (see Table 6.2). We have not observed any transmitted

shock wave from BK-7 glass to surrounding air or another BK-7 glass due to impedance mismatch (glass-air/glass-air-glass interface). These reflected radial shock waves from both the surfaces will interact and moves forward through each other forming a cell like structure (as explained in Chapter 5) as shown in Figure 6.3 (c). Since the probe beam diameter (33 mm) is less than the BK-7 glass slab length (50 mm), the reflection of shock wave from the glass-air interface along laser propagation direction is not visible. But the reflected shock wave front is almost planar, and it is propagated inside BK-7 glass opposite to the laser propagation direction (Figure 6.3 (d)) followed by the cell like structure. The interaction of reflected radial shock waves and cell like structure is more visible with higher energies.

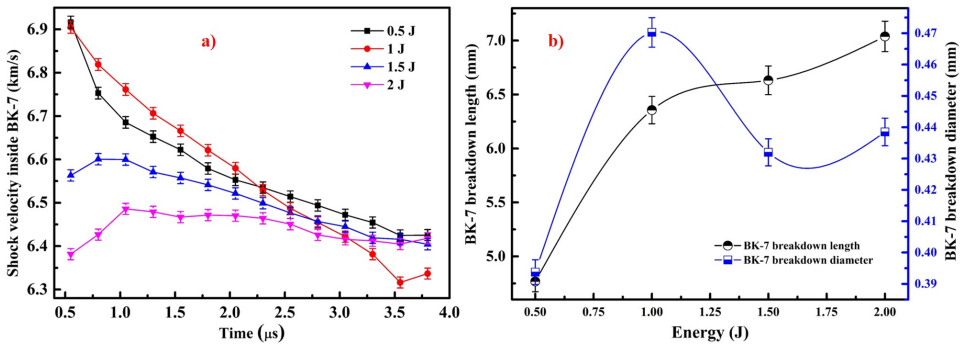

Figure. 6.4 Energy dependence on (a) temporal evolution of shock waves propagation (b) optical breakdown length and width inside BK-7 glass

Figure 6.4 (a) shows that, as the input laser energy increases the shock wave velocity is decreased [50] for all energies except for 1 J energy until time scales $\leq 2.3\ \mu s$ by following the trend: 1 J > 0.5 J > 1.5 J > 2 J. As the energy increases, most of the energy is utilized to increase the permanent damage inside BK-7 glass by self focusing effect. After 2.3 μs, the shock velocity follows the trend: 0.5 J > 1 J $\geq$ 1.5 J > 2 J. At later time scales $\geq 3\ \mu s$ the shock wave velocity is constant for all the energies. The Figure 6.4 (b) shows the energy dependent behaviour of optical breakdown length and width. It is observed that, optical breakdown length is increasing and optical breakdown width is saturated with laser input energy.

6.4 Effect of the laser focusing conditions on direct and confined ablation of the BK-7 glass

To understand the coupling of the input laser energy to the material (here BK-7 glass), we have studied the effect of the laser focal plane position w.r.t. BK-7 surface (F0 and F2) in the laser ablation of (a) only BK-7 glass (direct ablation) and (b) 20 μm Al/Cu thin foil confined to BK-7 glass (confined ablation). The temporal evolution of the laser ablative shock waves inside the BK-7 glass at two focusing conditions (F0 and F2) were

captured using an ICCD camera, with the help of a He-Ne probe beam of 47 mm beam diameter. The efficient coupling of the laser energy results in the enhancement of the shock wave velocity inside BK-7 glass. So, the shock wave velocity inside BK-7 glass in focusing conditions F0 and F2 were compared in both direct ablation mode and confined mode individually.

6.4.1 Direct ablation of the BK-7 glass

Figure 6.5 (a,b) shows the shadowgrams of the temporal evolution of the laser ablative plasma and shock waves in ambient air as well as shock wave propagation inside the BK-7 glass simultaneously, due to the direct ablation of BK-7 glass using 0.5 J laser input energy at two focusing conditions (F0 and F2).

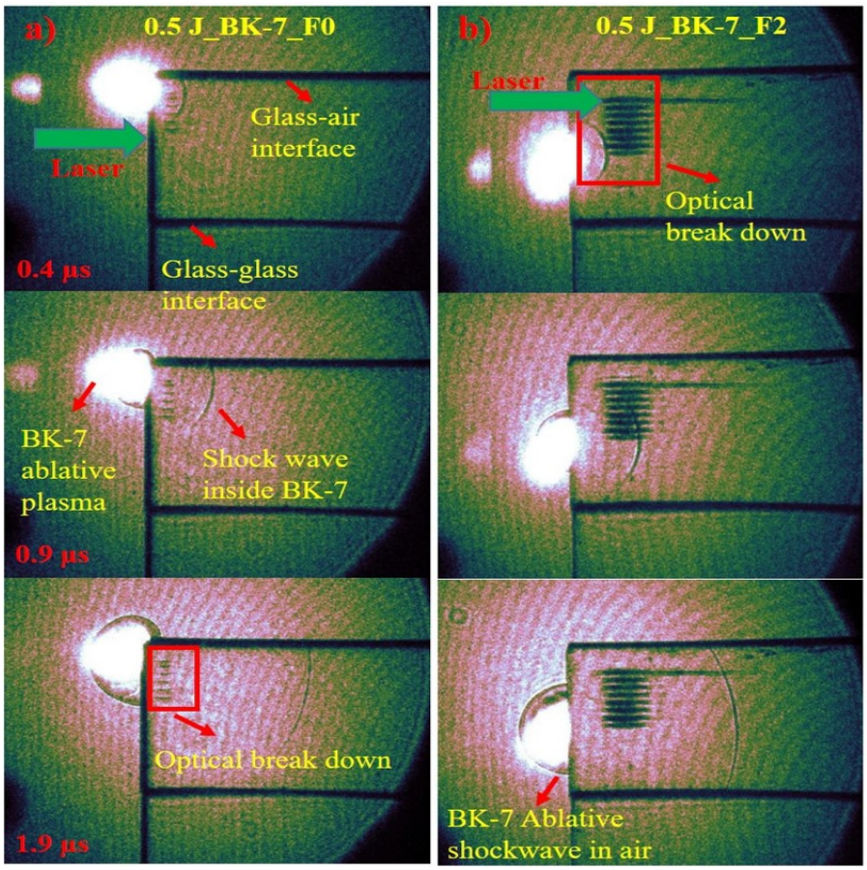

Figure. 6.5 Shadowgrams of the laser ablative shock waves in ambient air as well as inside BK-7 glass from direct ablation of BK-7 glass at 0.5 J in (a) F0 (b) F2 focusing geometries

In F0 focusing condition, the laser beam focused on the surface of BK-7 glass (or at the air-glass interface). Due to the laser ablation, the permanent damage tracks as well as shock waves were observed from the target surface (Figure 6.5 (a)) as explained in the previous section 6.4. In F2 focusing condition, the laser beam is focused 6 mm deep inside BK-7 glass from the surface. Due to the ablation, although the permanent damage tracks

are observed at 6 mm deep inside BK-7 glass, the shock wave evolution is observed from the glass surface (Figure 6.5 (b)). As the laser input energy varied from 0.5 to 2 J, the shock wave reflection from the edges of the glass due to glass-air impedance mismatch is clearly visible and the propagation of cell like structure behind the shock wave is also observed as explained in the previous section 6.4.

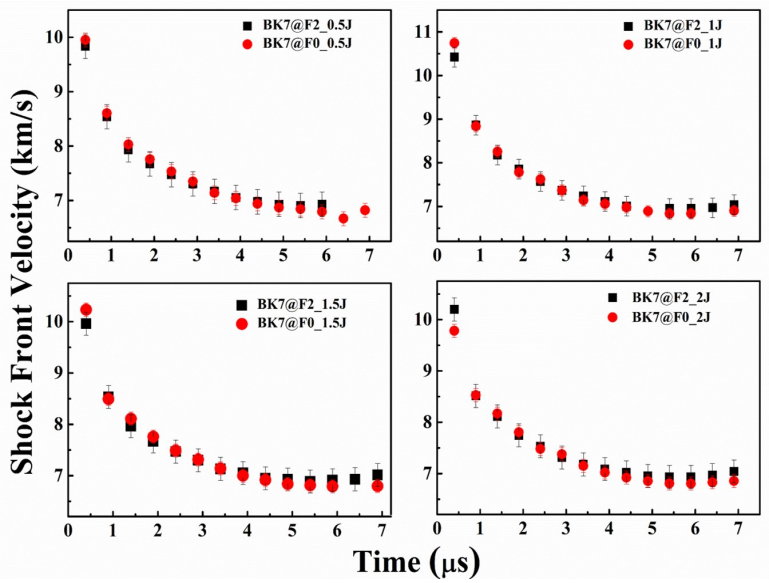

Figure. 6.6 Temporal evolution of laser induced shock waves inside BK-7 glass from direct ablation of BK-7 glass at 0.5 -2 J laser energy for F0 and F2 focusing geometries

Figure 6.6 shows the energy dependence on the temporal evolution of the shock wave inside BK-7 glass at F0 and F2 focusing conditions. From the Figure 6.6, as the laser energy increased from 0.5 to 2 J, the shock velocity inside the BK-7 glass is not effected by the laser input energy except for 1 J energy, it is slightly increased (as discussed in section 6.4). The shift in focal plane position of laser beam from F0 to F2 condition has also not effected the shock wave propagation inside BK-7 glass except for 2 J energy it is slightly increased at 0.4 μs in the direct ablation of BK-7 glass as shown in Figure 6.6.

6.4.2 Confined ablation of the BK-7 glass

To understand the effect of axial confinement on the laser induced breakdown of BK-7 glass (similar to the role of sacrificial layer in the case of laser shock peening [51]), we performed the laser ablation of BK-7 glass confined with Al and Cu thin foils of 20 μm thickness. Due to the ablation of Al/Cu thin foils, the shock waves propagating inside the Al/Cu foil transmitted into the BK-7 glass similar to the propagation of shock waves from one medium (Z1) to another medium (Z2) [49]. This study gave a chance to understand the effect of acoustic impedance (Z) of confining layer on the shock wave propagation inside BK-7 glass. Figure **??** (a-d) shows the shadowgrams of the temporal evolution of the transmitted laser ablative shock waves inside the BK-7 glass from the Al/Cu foils of

20 μm thickness for 0.5 J laser energy at two focusing conditions F0 and F2.

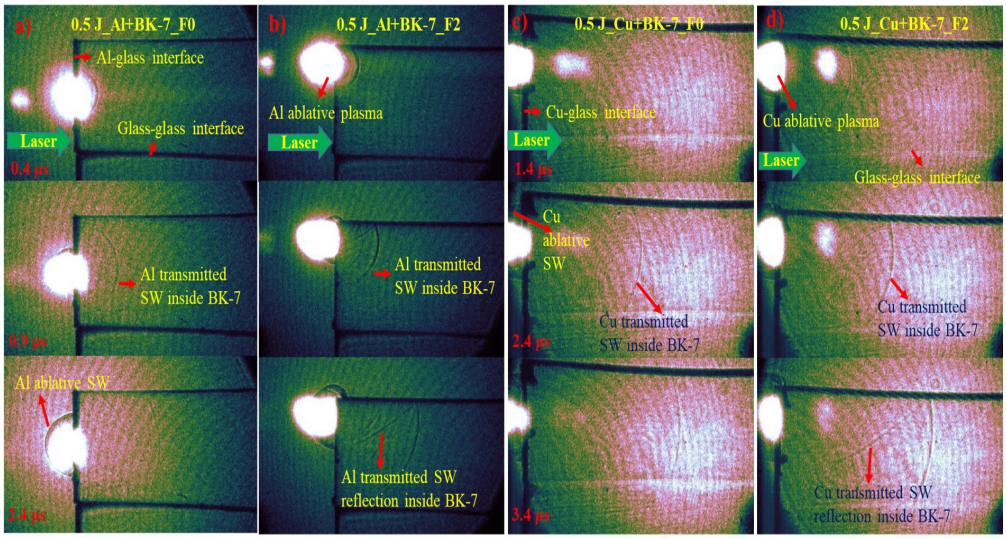

Figure. 6.7 Shadowgrams of the laser induced shock waves from (a-b) Al confined to BK-7 glass (Al+BK-7) (c-d) Cu confined to BK-7 glass (Cu+BK-7) at 0.5 J laser energy for F0 and F2 focusing conditions

In the confined ablation, due to the ablation of the Al/Cu thin foils of 20 μm thickness, the shock wave propagates into the surrounding air as well as into the Al/Cu thin foil [45, 46, 47] as shown in Figure 6.7 (a-d). In confined ablation, we have not observed any permanent damage inside BK-7 glass. Due to the higher thickness of Al/Cu foils ($\sim$ 20 μm), the laser ablation will not remove the confining layer completely for 532 nm laser beam [4]. The Al, Cu foils acts as sacrificial layers protecting direct damage to BK-7 glass. So, the laser ablative shock waves inside Al/Cu foils will transmit into the BK-7 glass as shown in Figure 6.7(a-d). During the shock wave transmission, the shock wave faces the acoustic impedance (Z) variation due to the Al/Cu foil and BK-7 glass interface. Thus the transmitted shock wave velocity greatly depends on the relative acoustic impedances ($Z = \rho U$) of both mediums i.e., the confining layer and the target material [34, 35, 49]. The mechanical properties such as acoustic impedances and shock velocities of Al, Cu and BK-7 glass along with their shock transit times is listed in Table 6.2. The shock transit time is defined as the time required for propagation of the shock wave inside a medium with specific length. For example, the shock velocity (C_0) inside BK-7 glass is around $\sim$ 5.1 km/s and the length of the BK-7 glass is 50 mm, so the shock transit time inside BK-7 glass is around $\sim$ 10 μs.

When the laser beam is focused on to the interface of Al/Cu foil confined to BK-7 glass (Al +BK-7/Cu+BK-7) i.e., F0 focusing condition, the shock wave generated from the ablation of Al/Cu thin foil propagates inside the Al/Cu thin film of 20 μm and it will

Table 6.2 Mechanical properties of Al, Cu and BK-7 glass

Material	**Density** (ρ)(gr/cc)	**Shock velocity** (C_0) (km/s)	**Shock impedance** (Z) (10^6 gr/cm^2-s)	**Shock transit time** (ns)
Al foil (t=20 μm)	2.7	5.38	1.45	3.7
Cu foil (t=20 μm)	8.93	3.93	3.49	5
BK-7 glass (L=50 mm)	2.5	5.1	1.27	10000

interact with the metal-dielectric interface of Al/Cu foil and BK-7 glass around 3 to 5 ns (as per calculated shock transit time in Table 6.2). At the interface, the shock wave will be reflected partially into the Al/Cu thin foil and partially transmitted into the BK-7 glass simultaneously. The strength or velocity of the transmitted shock wave inside BK-7 glass depends on the relative acoustic impedance of both mediums, Al/Cu foil and BK-7 glass [34, 35, 49, 51] as well as laser input energy. Figure 6.8 (a,d) shows the energy dependent temporal evolution of the transmitted shock wave velocity inside BK-7 glass due to the confined ablation of 20 μm thick Al, Cu foils compared with the direct ablation of BK-7 glass in F0 focusing condition.

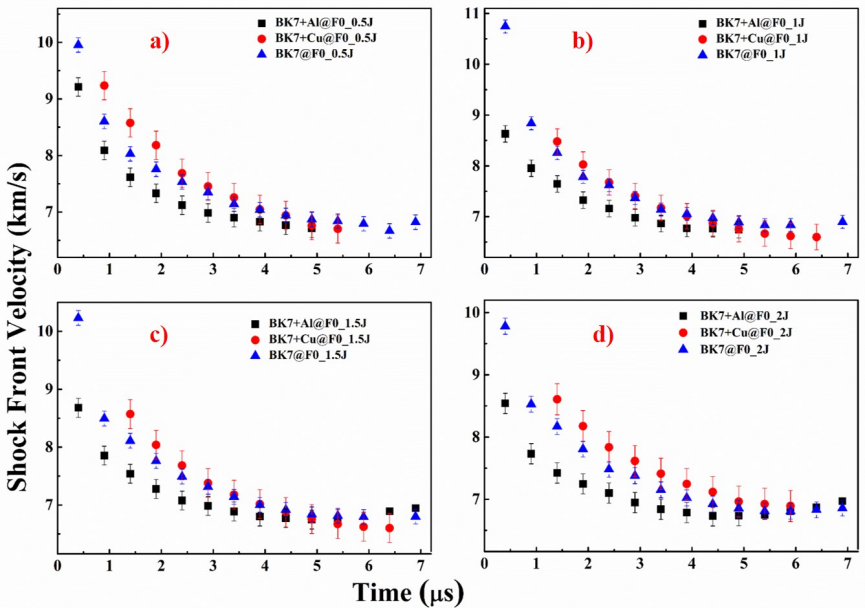

Figure. 6.8 Energy dependence on the temporal evolution of transmitted shock waves inside BK-7 glass due to the ablation of BK-7 glass (direct ablation) and Al, Cu thin foils confined to BK-7 glass (confined ablation) in F0 focusing condition

In F0 focusing condition, the shock waves propagated inside BK-7 glass due to the ablation

of the Cu thin foil (Cu+BK-7) has higher shock velocities than the shock waves generated by the Al thin foil ablation (Al+BK-7) and the direct ablation of BK-7 glass upto 3 μs time scales and at later time scales the shock velocity propagation is almost constant as shown in Figure 6.8(a-d). From Figure 6.8 (a-d) it is evident that, the shock velocity inside the BK-7 glass follows the trend: Al+BK-7 < BK-7 ≤ Cu+BK-7 for all the input laser energies upto 3 μs time scales. This is due to the fact that, the acoustic impedance of Al, Cu foils and BK-7 glass are such that, $Z_{Cu}(3.93) > Z_{Al}(1.45) > Z_{BK-7}(1.27)$ (in $10^6 gr/cm^2 - s$) (Table 6.2). So, the shock wave velocity inside BK-7 glass is higher in the confined ablation compared to the direct ablation of BK-7 glass in F0 focusing condition as shown in Table 6.3. However, the relative acoustic impedance (ΔZ) of the confining layer with the target material plays a crucial role in the enhancement of shock wave propagation inside target material [34, 35, 51] (as discussed in Chapter 4).

Table 6.3 The velocity of shock waves inside the BK-7 glass in direct and confined ablation geometry at 1.4 μs

Energy(J)	**BK-7 (km/s)**		**Al+BK-7 (km/s)**		**Cu+BK-7 (km/s)**	
	F0	*F2*	*F0*	*F2*	*F0*	*F2*
0.5	8.02	7.92	7.61	8.42	8.57	8.62
1.0	8.25	8.17	7.64	-	8.48	8.63
1.5	8.10	7.96	7.54	8.40	8.57	8.82
2.0	8.16	8.11	7.42	8.53	8.60	8.72

In F2 focusing condition, the focal plane of the laser beam is shifted 6 mm deep inside the target material in confined ablation. Figure 6.9(a,d) shows the energy dependence on the shock wave evolution inside BK-7 due to the direct ablation of the BK-7 glass and in confined geometry.

From the Figure 6.9(a-d), it is evident that in F2 focusing condition the transmitted shock velocity inside the BK-7 glass is almost constant (within error bars) for both confined and direct ablation geometries. The same is observed for all the input laser energies from 0.5 J to 2 J. This is due to the fact that, higher focal volume or spot size gives lower intensity distribution at the laser metal interface. The shock velocity is not increased in F2 focusing condition compared to the F0 condition except for the Al confined BK-7 glass case. The focal plane shifting from F0 to F2 condition has increased the transmitted shock wave velocity inside BK-7 glass due to the ablation of Al foil confined to the BK-7 glass. Since the relative impedance of the Al foil and BK-7 glass (Z_{Al}= 1.45 > Z_{BK-7}= 1.27) is less, the increment in the shock velocity is observed. The shock velocity inside BK-7 glass due to the confined ablation of Al foil confined to the BK-7 glass and Cu foil confined to the

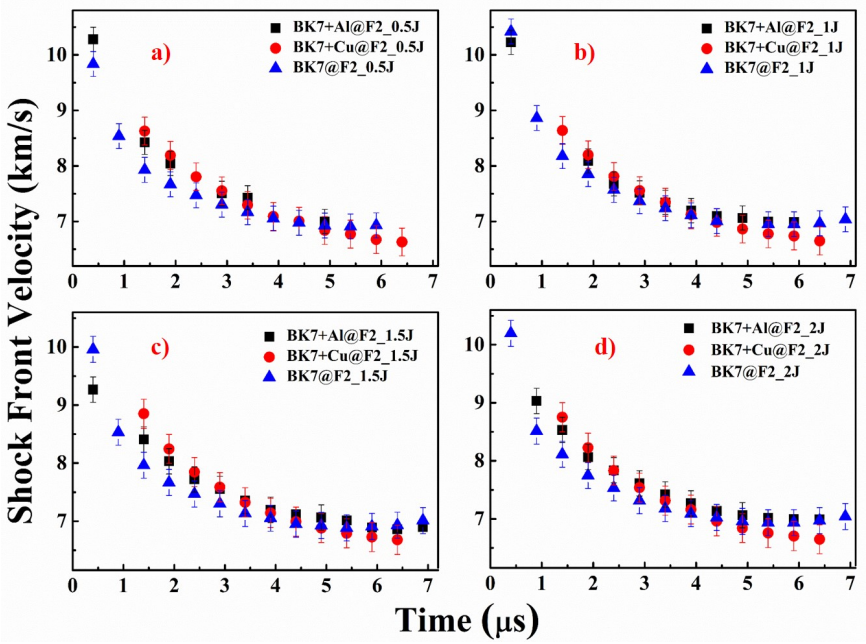

Figure. 6.9 Energy dependence on the temporal evolution of the transmitted shock waves inside BK-7 glass from the ablation of BK-7 glass (direct ablation) and the Al, Cu thin foils confined to BK-7 glass (confined ablation) in F2 focusing condition

BK-7 glass in F2 focusing condition were compared to the F0 condition as well as direct ablation of BK-7 glass as shown in Table 6.3.

6.4.3 Effect of Acoustic impedance of materials

In confined ablation, the relative impedance plays a key role in the enhancement of the shock wave propagation inside BK-7 glass along with laser input energy [34, 35, 51]. According to Fabbro et. al. [34, 35], in confined ablation the shock pressure inside the material can be given by:

$$P(GPa) = 0.01\sqrt{\frac{\alpha}{2\alpha+3}}\sqrt{Z(g/cm^2s^2)}\sqrt{I_0(GW/cm^2)} \tag{6.2}$$

But from Rankie-Hugoniot equations [49, 52],

$$P(GPa) = \rho_0(g/cm^3){V_{sw}}^2(km/s) \tag{6.3}$$

So, the shock velocity inside the material depends on:

$$V_{sw} \propto \frac{1}{\sqrt{\rho_0}} Z^{1/4} {I_0}^{1/4} \tag{6.4}$$

Where P is pressure inside the material, V_{sw} is the shock velocity inside the material, Z is the relative acoustic impedance of the confining layer and target material i.e., $\frac{2}{Z} = \frac{1}{Z_1} + \frac{1}{Z_2}$ [34, 35, 51], I_0 is the input laser beam intensity at the interface and α is the constant. Since the shock velocity inside the material mainly depends on the relative impedance (

$\propto Z^{1/4}$) and on the laser beam intensity ($\propto {I_0}^{1/4}$). For higher relative acoustic impedance between confining layer and target material, the shock velocity inside the target material is increased. This can be confirmed with the help of visualization of transmitted shock wave velocity inside BK-7 glass in the confined ablation of the BK-7 glass with 20 μm Al and Cu foils as confining layers . Figure 6.10 (a-h) shows the effect of relative impedance

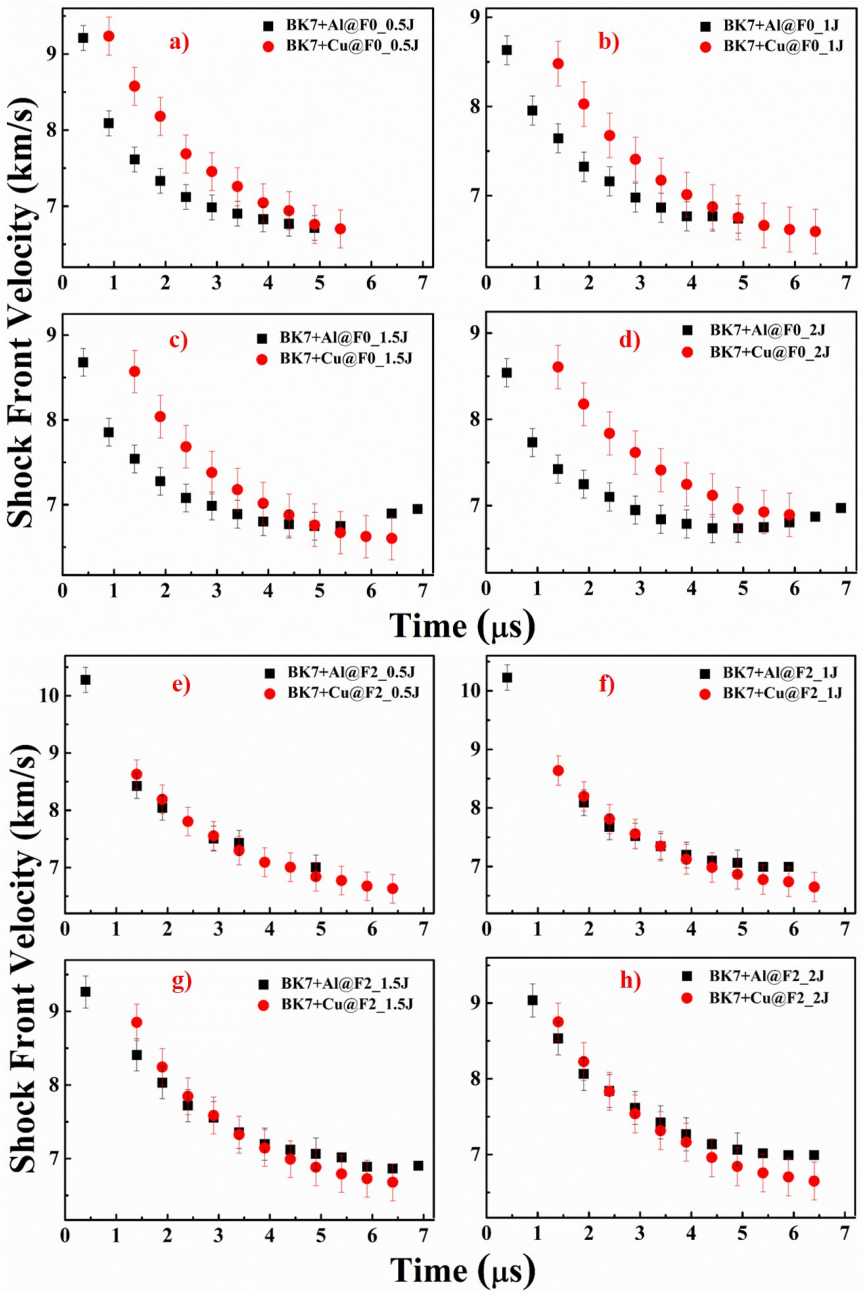

Figure. 6.10 Energy dependent temporal evolution of laser induced shock waves inside BK-7 glass from the confined ablation of the 20 μm Al and Cu thin foils confined to the BK-7 glass at F0 and F2 focusing conditions

of 20 μm Al/Cu foils with BK-7 glass on shock wave velocity inside the BK-7 glass in F0

and F2 focusing condition. In F0 focusing condition, transmitted shock velocity inside BK-7 glass is more for the confined ablation of 20 μm Cu foil confined to the BK-7 glass than 20 μm Al foil confined to the BK-7 glass. This is due to the higher relative impedance ($Z = 2.5 \times 10^6 g/cm^2 - s$) of Cu foil and BK-7 glass than in the case of the Al foil confined to the BK-7 glass ($Z = 1.2 \times 10^6 g/cm^2 - s$). As the laser input energy increases from 0.5 J to 2 J, the difference in the shock velocity inside BK-7 glass due to the confined ablation of the 20 μm Al foil and Cu foils confined to the BK-7 glass is observed upto 5 μs and it is almost constant at later time scales. The maximum difference is observed for 2 J input laser energy as shown in Figure 6.10 (a-d).

In F2 focusing condition, although the relative acoustic impedance of the Cu foil and BK-7 glass is more, the transmitted velocity inside the BK-7 glass due to the confined ablation of the 20 μm Al foil and Cu foils confined to BK-7 glass is almost constant (Figure 6.10 (e-h)). This shows that, due to the effect of focal plane shifting from F0 to F2, the shock velocity inside the BK-7 glass is increased in the confined ablation of the Al foil confined to BK-7 glass and matched with the shock velocity induced by the ablation of the Cu foil confined to BK-7 glass as shown in Figure 6.10 (e-h). But the focal plane shifting from F0 to F2 has no effect on the confined ablation of the Cu foil confined to the BK-7 glass. This can also confirmed by comparing the shock velocities inside BK-7 glass due to the confined ablation of the 20 μm Al/Cu foils confined to BK-7 glass in F0 and F2 focusing conditions as shown in Figure 6.11 (a-h).

Figure 6.11 (a-h) shows the energy dependent temporal evolution of the shock velocities inside BK-7 glass due to the confined ablation of Al and Cu foils confined to the BK-7 glass compared individually in the F0 and F2 focusing conditions. Due to shifting of the laser beam focal plane from F0 to F2, the transmitted shock velocity inside BK-7 glass is increased in the case of confined ablation of Al thin foil confined to BK-7 glass. The maximum enhancement is observed for 2 J energy in F2 focusing condition. This may be due to the fact that, for lower laser energy density in the focal volume i.e., higher focal spot diameter that leads to lower intensity (F2 condition), the shock waves propagation inside the material (BK-7 glass) follows $\frac{1}{r}$ relation, while for higher energy density i.e., lower focal spot diameter (F0 condition) the shock propagation follows $\frac{1}{r^2}$ relation as explained by Fabbro et. al. [34, 35, 51]. The shifting of focusing plane from F0 to F2 condition has no effect on the confined ablation of the Cu thin foil confined to the BK-7 glass. This can be attributed to the saturation of transmitted shock velocities inside the BK-7 glass in confined ablation of the 20 μm Cu foil confined to the BK-7 glass for input laser intensities $\geq$ 10 GW/cm^2 (In F2 condition, $I = 10.02\ GW/cm^2$ and in F0 condition $I = 25\ GW/cm^2$).

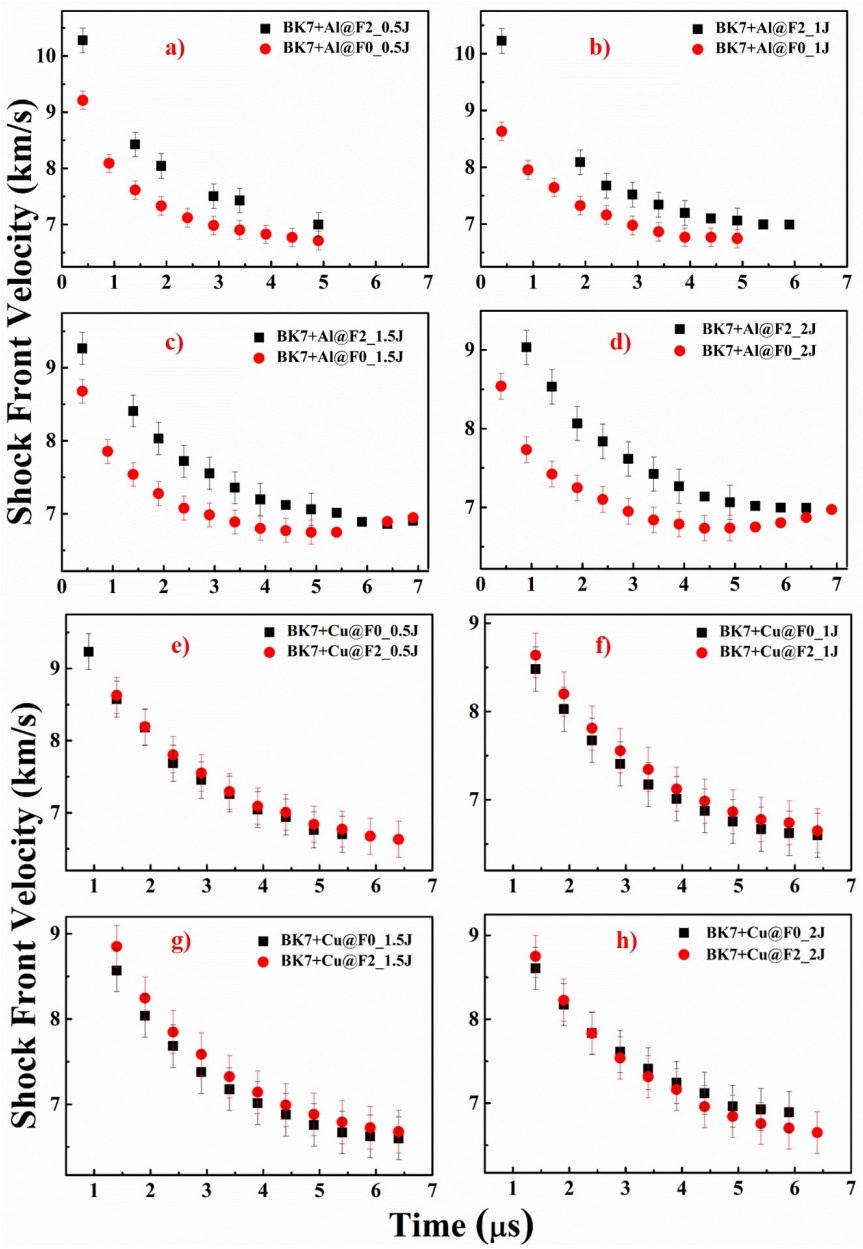

Figure. 6.11 Energy dependent temporal evolution of laser induced shock waves inside BK-7 glass from the confined ablation of the 20 μm Al and Cu thin foils confined to the BK-7 glass at F0 and F2 focusing conditions

6.5 Conclusions

From the laser ablation of the BK-7 glass in direct and confined geometry with 20 μm Al and Cu foils, we can conclude that the shock velocities inside the BK-7 glass are enhanced in the confined geometry compared to the direct ablation in F0 focusing conditions. It is also confirmed that, due to the ablation of the confining layer the target material surface is not damaged. Due the shifting of the laser beam focal plane from F0 to F2 focusing condition, the shock wave velocities inside the BK-7 glass were enhanced (around

0.6 - 2.2 km/s) in the case of the confined ablation with Al foil but has not affected the confined ablation with Cu foil and direct ablation of the BK-7 glass. The same behaviour is observed for all the laser input energies used in the study. The energy dependence study on the transmitted shock wave propagation inside BK-7 glass revealed that, the enhancement of the shock wave inside material (BK-7 glass) greatly depends on (a) relative acoustic impedance of the confining layer (20 μm Al and Cu thin foils) and target material (BK-7 glass) and (b) laser energy density in the focal volume at the interface.

References

[1] K. Chaudhary, S. Z. H. Rizvi and J. Ali, *Laser-Induced Plasma and its Applications*, Intechopen publishers (2016).

[2] S. S. Harilal, C. V. Bindhu, M. S. Tillack, F. Najmabadi, A. C. Gaeris, *Internal structure and expansion dynamics of laser ablation plumes into ambient gases*, J Appl Phys.93(5), 2380–8 (2003).

[3] J. P. Singh and S. N. Thakur, *Laser-Induced Breakdown Spectroscopy*, Elsevier Science (2007).

[4] D. A. Cremers, L. J. Radziemski, *Handbook of Laser-Induced Breakdown Spectroscopy*, Second Edition, John Wiley & Sons (2013).

[5] Z. Rui, L. Zhong-Cheng, H. Bing, Z. Hong-Chao, X. Rong-Qing and L. Jian et. al., *Mechanism of laser-induced plasma shock wave evolution in air*, Chinese Phys B.18(5), 1877–83 (2009).

[6] C. Phipps, *Laser Ablation and its Applications*, Springer Series in Optical Sciences, Vol. 129 (2007).

[7] J. G. Lunney and R. Jordan, *Pulsed laser ablation of metals*, Appl. Surf. Sci., 127-129: 941-946 (1998).

[8] M. Cirisan, J. M. Jouvard, L. Lavisse, L. Hallo and R. Oltra., *Laser plasma plume structure and dynamics in the ambient air: The early stage of expansion*, J. Appl. Phys. 109, 103301 (2011).

[9] G. K. Varier, R. C. Issac, S. S. Harilal, C. V. Bindhu, V. P. N. Nampoori, C. P. G. Vallabhan., *Investigations on nanosecond laser produced plasma in air from the multi-component material YBa2Cu3O7*, Spectrochimica Act B 52, 657 (1997).

[10] J. D. Lindl, *Inertial Confinement Fusion*, Springer, New York, (1998).

[11] K. Nishikawa and M. Wakatani., *Plasma Physics: Basic Theory with Fusion Applications*, 2nd. ed. Berlin, Springer-Verlag (1994).

[12] P. R. Willmott and J. R. Huber., *Pulsed laser vaporization and deposition*, Rev. Mod. Phys. 72, 315 (2000).

[13] S. Atzeni and J. Meyer-ter-Vehn, *The Physics of Inertial Fusion: Beam Plasma Interaction,*

Hydrodynamics, Hot Dense Matter, OUP Oxford (2004).

[14] D. Batani, H. Stabile, A. Ravasio, G. Lucchini, F. Strati, T. Desai, J. Ullschmied, E. Krousky, J. Skala, L. Juha, B. Kralikova, M. Pfeifer, C. Kadlec, T. Mocek, A. Präg, H. Nishimura and Y. Ochi, *Ablation pressure scaling at short laser wavelength*, Physical Review E 68 (6), 067403 (2003).

[15] D. W. Bäuerle, *Laser Processing and Chemistry*, Springer Berlin Heidelberg (2013).

[16] A. Vogel and V. Venugopalan, *Mechanisms of Pulsed Laser Ablation of Biological Tissues*, Chemical Reviews 103 (2), 577-644 (2003).

[17] D. B. Chrisey and G. K. Hubler, *Pulsed Laser Deposition of Thin Films*, Wiley (1994).

[18] S. C. Singh and R. Gopal, *Laser Irradiance and Wavelength-Dependent Compositional Evolution of Inorganic ZnO and ZnOOH/Organic SDS Nanocomposite Material*, The Journal of Physical Chemistry C 112 (8), 2812-2819 (2008).

[19] L. J. Radziemski, *From LASER to LIBS, the path of technology development*, Spectrochimica Acta Part B: Atomic Spectroscopy 57 (7), 1109-1113 (2002).

[20] H. Chen, *Microscale Laser Shock Peening: Experiment, Modelling and Spatially Resolved Material Characterization*, Ph. D. Thesis, Columbia University (2004).

[21] C. Phipps, M. Birkan, W. Bohn, H. A. Eckel, H. Horisawa, T. Lippert, M. Michaelis, Y. Rezunkov, A. Sasoh, W. Schall, S. Scharring and J. Sinko, *Review: Laser-Ablation Propulsion*, Journal of Propulsion and Power 26 (4), 609-637 (2010).

[22] M. Shukla, H. C. Pant, V. K. Senecha, V. N. Rai, P. Khare, A. K. Verma, R. S. Rao, N. K. Gupta and B. K. Godwal, *Equation-of-state study of copper using laser-induced shocks near 10 Mbar pressure and revalidation of theoretical modelling*, CURRENT SCIENCE 85 (6), 802-808 (2003).

[23] A. Moorti, *Kiran: A bulletin of the Indian Laser Association, India*, Vol. 26, pp. 19-27 (2015),.

[24] K. Ding and L. Ye, *Laser Shock Peening Performance and simulation*, Woodhead publishing Limited (2006).

[25] Ch. Leela, Ph. D. Thesis, University of Hyderabad, India (2014).

[26] P. A. Naik, V. Arora, S. Bagchi, Y. B. S. R. Prasad, S. Barnwal and P. D. Gupta, *Laser induced shock studies at RRCAT, Indore* , 23rd International Conference on High Pressure Science and Technology (AIRAPT-23), Journal of Physics: Conference Series 377-012052 (2012).

[27] A. M. Streltsov, N. F. Borrelli, *Fabrication and analysis of a directional coupler written in glass by nanojoule femtosecond laser pulses*, Opt. Lett. 26, 42 (2001).

[28] H. B. Zhang, S. M. Eaton, J. Z. Li, A. H. Nejadmalayeri, P. R. Herman, *Type II high-strength Bragg grating wave guides photo written with ultrashort laser pulses*, Opt. Express 15, 4182 (2007).

[29] R. M. Wood, *Laser induced damage thresholds and laser safety levels: Do the units of measure-*

ment matter?, Opt. Laser Technol. 29(8), 51722 (1997).

[30] K. Miura, H. Inouye, J. Qiu, T. Mitsuyu, K. Hirao, *Deformation and improvement of the IR transmission of single-crystal silicon by direct current heating*, Nucl. Instrum. Methods Phys Res B 141, 72632 (1998).

[31] K. Hirao and K. Miura, *Writing wave guides and gratings in silica and related materials by a femtosecond laser*, J. Non-Cryst. Solids 239, 91-95 (1998).

[32] T. Salleo and S. E. Genin, *Machining of transparent materials using and IR and UV nanosecond pulsed laser*, Appl. Phys. A. 71, 601-608 (2000).

[33] A. Kumar, M. Prasad, R. B. Bhatt, P. G. Behere, Mohd. Afzal, A. Kumar, J. P. Nilaya, D. J. Biswas, *Laser shock cleaning of radioactive particulates from glass surface*, Optics and Lasers in Engineering 57, 114-120 (2014).

[34] R. Fabbro, J. Fournier, P. Ballard, D. Devaux and J. Virmont, *Physical study of laser-produced plasma in confined geometry*, Journal of Applied Physics 68, 775(1990).

[35] D. Devaux, R. Fabbro, L. Tollier and E. Bartnicki, *Generation of shock waves by laser-induced plasma in confined geometry*, Journal of Applied Physics 74, 2268(1993).

[36] C. W. Miller, M.Sc. degree thesis, Georgia Institute of Technology (2009).

[37] Ch. Leela, P. Venkateshwarlu, R. V. Singh, P. Verma and P. Prem Kiran, *Spatio-temporal dynamics behind the shock front from compacted metal nano powders*, Opt. Exp. 22, S2, A268 - A275 (2014).

[38] Ch. Leela, S. Bagchi, V. Rakesh Kumar, S. P. Tiwari and P. Prem Kiran, *Dynamics of laser induced micro-shock waves and hot core plasma in quiescent air*, Laser Particle Beams 31(02), 263–272 (2013).

[39] N. Bloembergen, *Laser Induced Electrical Breakdown in solids*, IEEE Journal of Quantum Electronics, pp. 375-385 (1974).

[40] R. W. Boyd, *Nonlinear Optics*, 3rd edition, Academic press (2008).

[41] A. Couairon and A. Mysyrowicz, *Femtosecond filamentation in transparent media*, Physics Reports 441, 47 – 189 (2007).

[42] S. L. Chin, *Femtosecond Laser Filamentation*, springer series on atomic, optical and plasma physics 55 (2009).

[43] P. Prem Kiran, S. Bagchi, C. L. Arnold, S. Rama Krishnan, G. Ravindra Kumar and A. Couairon, *Filamentation without intensity clamping*, Optics Express Vol. 18, No. 20 (2010).

[44] A. Horn, E. W. Kreutz, R. Poprawe, *Ultrafast time-resolved photography of femtosecond laser induced modifications in BK7 glass and fused silica*, Appl. Phys. A 79, 923–925 (2004).

[45] S. Sai Shiva, Ch. Leela, P. Prem Kiran, C. D. Sijoy and S. Chaturvedi, *The effects of electron thermal radiation on laser ablative shock waves from aluminum plasma into ambient air*, Phys.Plasmas 23, 053107 (2016).

[46] S. Sai Shiva, Ch. Leela, S. Chaturvedi, C. D. Sijoy and P. Prem Kiran, *Development of Numerical Model to Investigate the Laser Driven Shock Waves from Aluminum Target into Ambient Air at Atmospheric Pressure and its comparison with Experiment*, APS - Conference Proceedings of Shock Compression and Condensed Matter (SCCM), W1, 42-15-1330 (2015).

[47] S. Saisiva, Ph. D. Thesis, University of Hyderabad, India (2016).

[48] U. Teubner, Y. Kai, T. Schlegel, D. E. Zeitoun and W. Garen, *Laser-plasma induced shock waves in micro shock tubes*, New J. Phys.19, 103016 (2017).

[49] P. W. Cooper, *Explosives engineering*, Wiley-VCH (1996).

[50] D. E. Grady and L. C. Chhabildas, *Shock wave properties of soda-lime glass*, Sandia National Laboratories Report, United States (1996).

[51] K. Ding and L. Ye, *Laser Shock Peening Performance and simulation*, Woodhead publishing Limited (2006).

[52] Y. B. Zel'dovich and Y. P. Raizer, *Physics of Shock Waves and High-Temperature Hydrodynamic Phenomena*, Dover Publications/Academic Press Inc., New York (2012).

Chapter 7

Conclusions

7.1 Summary and Conclusions

In view of understanding and designing of the miniaturized ns laser based shock tube with few mm diameter and few cm length, a study on the dynamics of confined laser induced/ablative plasma sources and shock waves was undertaken as an initial study. The miniaturization of the ns laser shock tube requires the ns laser induced/ablative plasma as a driver at the entrance of the mm sized tube and the high pressure plasma (from metal or non metal) launches shock waves into the hollow tube. The propagation of the shock waves inside hollow tubes with few mm diameter lead to the down scaling of the shock wave properties such as velocity, pressure, laminar and turbulence compared to the freely expanding shock waves. So, there is a need for balancing the down scaling of the shock waves to mm size and maintaining the shock wave properties. This requires a study to understand the enhancement of the plasma and shock wave properties in the confined geometry. The laser induced plasma and shock wave properties in the confined geometry greatly depends on the laser properties, tube properties and the confinement geometry. Although a lot of studies available on enhancement of plasma and shock wave properties with different confined geometries, the visualization of the dynamic processes in the confinement geometry and the role of the shock waves itself as a self reheating system in the enhancement of the plasma and shock wave properties is inadequate. So, we have visualized the temporal evolution of laser induced plasma and shock waves in different confining geometries using focused/defocused shadowgraphy technique. In this thesis, we gave simple solutions to overcome the problems related to (a) the efficient coupling of laser energy to the target material based on optimal laser energy and better focusing conditions; (b) choosing of the confining layer based on the relative acoustic impedance between confining layer and target material and (c) optimized tube diameter for better enhancement of the plasma and shock wave properties in the confinement geometry. Based

on the confinement applied on the plasma source w.r.t. the laser propagation direction, we have divided the confinement geometries into: Axial confinement and Later/spatial confinement. The chapters 3 and 4 discussed about the axial confinement of the laser induced plasma with a temporally expanding fluid as confining medium and laser induced blow off plasma with glass as confining medium, respectively. The chapter 5 discussed about the lateral/spatial confinement of the air plasma inside hollow tubes with different tube geometries. The chapter 6 explained both the axial and lateral confinement as an application towards understanding the shock wave behaviour inside the solid target. The same is given below in the Figure 7.1.

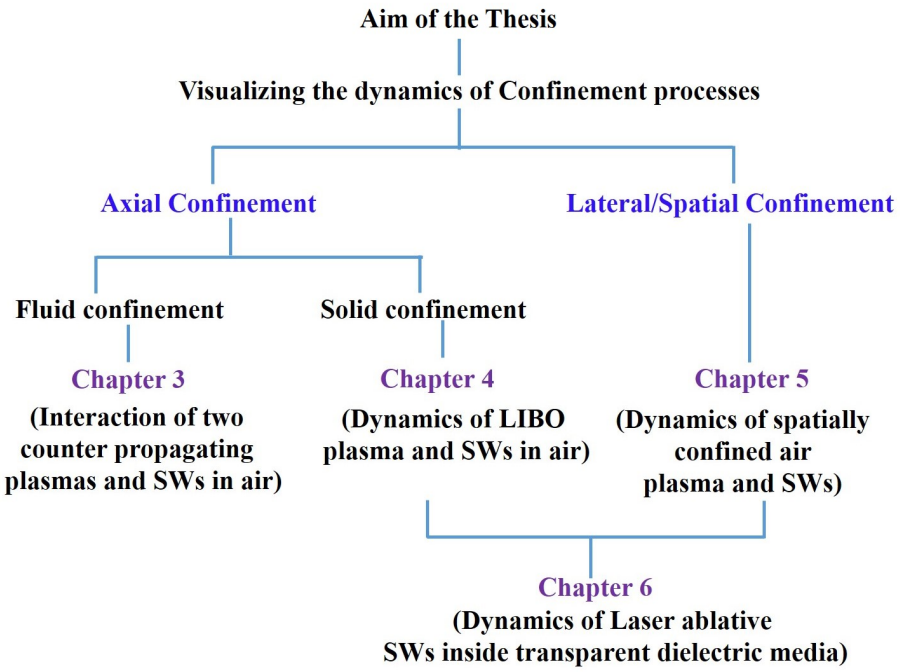

Figure. 7.1 Flow chart of the different confinement geometries used in the thesis study

The collision dynamics of the two counter propagating laser induced plasmas and shock waves revealed the effect of the separation distance (d) between the confining plasma and confining medium (another plasma as fluid confinement). Here, the plasma source S2 is used as the temporally expanding fluid confining medium, which confines the plasma source S1 generated by 25 mJ laser energy. This study also helped us to understand the effect of the relative impedance of the confining plasma and the fluid medium with different impedances ($Z = \rho U_{sw}$). The impedance of the confining fluid medium (S2) is varied by changing the laser energies (from 25 mJ to 92 mJ), which in turn changes the density of the plasma source S2. In this study, the separation distance (d) between confining plasma source S1 and fluid confining medium (S2) is varied from 0 to 6 mm systematically. The shadowgraphy imaging is used to capture the spatio temporal evolution of the collision of two counter propagating plasma sources and shock waves in

ambient air. The fast imaging study is used to capture the self emission or 2D emissions from the colliding plasma plumes. From the results, it is observed that when the two laser pulses are focused at the same position i.e., d=0 mm or with separation of 1 mm (d=1 mm) between the two plasma sources, the both plasma sources were merged into a single colliding plasma source. In this case, we have not observed the stagnation layer because of complete overlap/merger of two plasma sources into one. But, the plasma and shock wave properties (i.e., radius and velocity) of colliding plasma source is higher than individual plasma sources i.e., S1 or S2 properties. An increment in plasma contact front (CF) radius and shock wave front (SF) velocity is observed for both d=0, 1 mm in the case of equal energy ratio and in the case of unequal energy with energy ratio 1:1.7. But the increment is observed with d=0 mm only in the case of unequal energy ratio 1:3.7, when compared to individual source (S1/S2) properties. For the interaction of two plasma sources with separation distance (d) $\geq$ 2 mm, two kinds of stagnation layers are observed at the interaction zone (d=0 mm). For the case of equal laser energy plasma sources, a hard stagnation layer is observed. This is due to the equal momentum exerted by each plasma source on the other. While for unequal energy plasma sources (S2 > S1), a soft stagnation layer allowing the energy flow from higher source (S2) to that of the lower source (S1) is observed. Although the plasma outer regions (PORs)/contact fronts (CFs) of the two plasma sources stagnate at the interaction zone, the corresponding shock wave fronts (SFs) initially penetrate through each other, then through the other plasma sources. Due to the propagation of shock front of the first source (SF1) through the second plasma source and vice-versa, the line of force represented by bright spots on each side of the interaction zone was observed. These bright spots are termed as "*Plasma Jet*" in our study (Figure 3.6). This plasma jet is visible inside POR of the two plasma sources in case of equal energy while it was strongly visible inside the POR of the lower energy plasma source (S1) in the case of unequal energy plasma sources due to their respective plasma densities and momentum conservation. The propagation of shock front of the higher energy source (SF2), through lower energy plasma source (S1) results in a discontinuity of the plasma source S1. This discontinuity, called as *plasma Jetlet*, is observed to be dominant in case of unequal plasma sources of high energy ratio of 1:3.7 (Figure 3.10). In the case of equal energy ratio, the plasma jetlet is observed in both the sources at longer time scales (> 50 μs). The plasma jetlet evolution is sensitive to both the separation distance (d) as well as the energy ratio (S1:S2) which is confirmed by the plasma emission or 2D emission studies for all the cases, using fast (ICCD) imaging. The jetlet diameter is increases with increasing the energy ratio while it is decreases with increasing of the separation distance (d) between the two plasma sources (Figure 3.17). This study reveals that the separation distance (d) between confining target medium and confining layer mostly depends on the relative acoustic impedance (Z) for better confinement. This study helped us to understand the thickness of the plasma (L(t)) at the interface between

target and confining layer.

The evolution dynamics of the LIBO SWs in ambient air from metal films (Al, Cu, Ti) and polymer films (PVA, Au doped PVA) confined with glass (BK-7) substrate, revealed that the efficient blow off shock waves can be achieved by using optimal laser input energy with efficient focusing conditions which resulted in the effective coupling of the laser energy to the target material. This study also useful in understanding the effect of the relative impedance between target and confining metal layer on the blow off shock wave properties. Initially, the blow off shock velocity was observed to increase as a function of the input laser energy for energies upto 50 mJ. At higher input laser energy 200 mJ, the blow off shock velocity was observed to be decreasing due to inefficient coupling of laser energy to the target foil. By moving the glass-metal interface around the focal plane systematically, the efficient coupling of the laser energy to the target is demonstrated. The shifting of the focal plane from F0 (exact focal plane position) to F2 (shifting of the focal plane by 2 mm towards the glass-metal interface) focusing condition resulted in higher blow off shock waves from 20 μm Al and Cu foils at optimal laser energy of 50 mJ because of the ejected shock flyer/plasma debris. The analysis showed that with a 2 mm shift (F2), the blow-off has high reproducibility. The shock velocity as well as the diameter of the blow-off region increases as a function of laser energy. The ruptured region was observed to be smoother and circular in shape, than that observed in F0, F1 cases. The effective enhancement in the flyer diameter is observed to be more significant in the case of Al foil with F2 focusing condition. The 1D-RHD MULTI-ns numerical simulations also revealed that, by shifting the laser focus conditions from F0 to F2, one can avoid achieving an over dense regime and optimize the coupling of laser energy to the target foil. The simulation results are in good agreement with experimental results. The simulations are not presented in the thesis. Since the effect of shifting focal plane (F2) is more efficient in 20 μm Al, Cu foils with 50 mJ energy, the LIBO studies are extended to 1.1 μm Cu and 200 nm Ti thin foils. From the results, it is evident that the flyer generation is observed only for micron thickness films while for nano meter films only blow off shock waves are observed because of the smaller film thickness. For higher blow off shock velocity at lower energy (25 mJ), F2 focusing condition is suitable. At higher energy (50 mJ) F1 focusing condition is better for the thin films (1.1 μm Cu and 200 nm Ti). The attenuation of the blow off shock waves follows linear relation in the case of thin films (1.1 μm Cu and 200 nm Ti) while it follows 1/r relation for 20 μm Al, Cu foils. The blow-off studies are further extended to the polymer (PVA) and composite polymer (Au doped PVA) films as these studies are helpful to understand the laser ablation based micro propulsion. The results showed that the PVA and AuPVA polymers give higher LIBO SWs than Al (20 μm), Cu (20 μm) foils in F2 focusing condition with 50 mJ energy. But, we have not

observed any enhancement in the blow off shock velocities from the composite polymer films (AuPVA) than normal polymer film (PVA). This study gave the simple solution to improve the efficient laser energy coupling to the target material in the form of focal plane shifting around the interface. This study gave insight into the choosing of the optimal laser energy, better focusing focusing conditions and relative acoustic impedance between confining layer and target material for the generation of the efficient blow off shock waves.

The dynamics of the spatially confined laser induced air plasma and shock waves inside rectangular hollow tube/cavity with 8 mm constant inner dimension (diameter) and different tube lengths (8, 12, 16 mm) revealed that the temporal evolution of air plasma and shock waves is similar to that of the free expansion case (no confinement) until the reflection of radial shock waves from the inner walls. The reflected radial SWs interact with plasma core and asymmetrically compress it. Due to which, the generation and evolution of the secondary shock wave (SSW) from air plasma is observed. The reflected shock waves from both X and Y directions compress (asymmetrically) the plasma resulting in longer lived and elongated plasma along the laser propagation direction ($\pm$ Z). Due to the compression of the air plasma, the secondary shock wave is generated and its coalescence with the primary shock wave lead to the transmission of the reflected transverse shock waves through the plasma core. The maximum compression of the air plasma is achieved, when the two transverse reflected shock waves meet at the air plasma core centre. This is confirmed by the 2D emission imaging, which showed the splitting of plasma plume into three regions at the same time scales. During axial shock wave exit from the tube, we observed the shock wave vortices formed due to sharp density gradient at the cavity edges and cell like structures due to the reflected radial shock wave interaction. When the cell like structure exits from the tube/cavity the maximum increase in the plasma length as well as the change in plasma morphology/shape is observed. As the cavity length increases, the exit time of cell like structure increases thus decreases its strength/drag (i.e., which in turn depends on strength of transverse shock waves) leading to decrease in the plasma length. The compression of the plasma and axial shock waves exit times from the cavity mainly depends on the laser input energy and cavity aspect ratio (L/D) and surface roughness of the cavity material. From this study, we also understood that the variation of cavity length alone will not be sufficient to study the effect of aspect ratio (L/D) on the axial shock waves and air plasma properties. To get an insight into the enhancement of plasma properties such as number density, plasma temperature due to reflected transverse shock wave compression of air plasma inside a rectangular glass tube, we have performed the 2-D numerical simulations using modified FLASH-2D hydrodynamic codes. The simulated plasma and shock wave properties show good agreement with the experimental results. The generation of SSW is also confirmed by simulations. The

simulation results are not given in this thesis, as they are part of my colleagues thesis.

Upon visualizing and understanding the dynamic processes in the rectangular confinement, the studies are further extended to the cylindrical geometry to bring out the role aspect ratio (L/D) (especially the tube diameter (d)) in the enhancement of the axial shock wave properties. Since the cylindrical tubes (Cu, plastic, glass and SS tube) were either semi transparent or opaque to the probe beam, we can only observe the axial shock waves exiting from the tubes. Plasma compression and squeezing is only visible in semi transparent tubes during the plasma continuum radiation (i.e., at initial time scales). From the cylindrical geometry, it is confirmed that the tube/cavity length alone is not effective on the axial shock waves evolution in the spatial confinement of air plasma. this study also revealed that, if the tube diameter is almost equal to the plasma size (or diameter), we can observe the ejection of plasma mass density due to the symmetric compression and squeezing of the plasma. This ejected plasma mass density leads to the increment/enhancement of the axial shock wave properties. The ejection of the plasma mass density mainly depends on the input laser energy and tube diameter. It is almost constant for a particular laser input energy and tube diameter irrespective of the tube length. The study of the spatial confinement of the air plasma inside mm size tubes revealed the interaction of the plasma and shock waves. This is because, the reflected radial shock wave compression increases the plasma properties such as plasma length, plasma life time, plasma number density and plasma temperature. The squeezing of the air plasma forces out plasma mass density which increases the axial shock wave position i.e., its velocity. This study helped us to understand the air plasma generated shock wave propagation inside mm sized tubes and also the dependence of the laser energy, tube aspect ratio (L/D) on the axial shock wave propagation.

The dynamics of the temporal evolution of the laser induced/ablative shock waves inside a transparent dielectric material, BK-7 glass slab is used to understand the effect of the axial confinement and spatial confinement on the shock wave propagating inside a solid material. The axial confinement of shock waves is achieved using an overlay of 20 μm Al/Cu foils, while the dimensions of BK-7 glass have provided the spatial confinement to shock waves launched and propagated inside BK-7 glass slab. The studies on the visualization of shock wave propagation inside the solid material are sparsely available due to the opaqueness of solids to visible radiation in view of the need of sophisticated instruments. If the material is transparent to the visible radiation, one can visualize the evolution shock waves inside the material and quantify the shock wave characteristics in terms of radius/velocity. Hence, we have used BK-7 glass slab of 50 mm$\times$ 50 mm$\times$15 mm (l$\times$b$\times$ h) which is transparent to visible probe beam (633 nm) to study the temporal evolution of laser ablative shock waves inside BK-7 due to confining and direct geometries.

In direct ablation geometry, due to the laser ablation of the BK-7 glass slab, shock waves are launched into ambient air as well as into the BK-7 glass simultaneously. Due to the laser induced breakdown of BK-7, we have observed permanent damage tracks inside the BK-7 glass that showed an interesting behaviour with the input laser energy. Since, the input laser peak powers used in the study are of order of 50-200 MW, which is much higher than the critical power of self focusing (P_{cr}) of BK-7 glass i.e., 0.8 MW, we observed the self focusing of laser beam that leads to a sharp tip at the end of the damage track inside BK-7 glass along laser propagation direction. As the laser energy increases, the breakdown length is increased due to the increased self focusing of laser beam while breakdown width has saturated. When the shock wave propagates inside BK-7 glass, the radially expanding shock front is reflected from the surfaces of the BK-7 glass due to the impedance mismatch at the glass-air/glass-air-glass interface (i.e., spatial confinement). These reflected radial shock waves from both the surfaces will interact and moves forward through each other forming a cell like structure which moves behind the primary shock wave. As the input laser energy increases the shock wave velocity inside the BK-7 glass slab is decreased except for 1 J energy until time scales ≤ 2.3 μ s by following the trend: 1 J $>$ 0.5 J $>$ 1.5 J $>$ 2 J. As the energy increases, most of the energy is utilized to increase the permanent damage inside BK-7 glass by increasing self focusing effect. The shifting of focal plane (F0- laser focuses on the BK-7 surface and F2- laser focuses 6 mm deep inside BK-7) lead to the shift of permanent damage tracks inside the BK-7 glass. However it does not affect the shock wave evolution inside BK-7 glass slab in direct ablation geometry.

In the confined ablation, due to the ablation of the 20 μm Al/Cu thin foils, the shock wave propagates into the surrounding air as well as into the Al/Cu thin foil. Due to the confining layer, we have not observed any permanent damage inside BK-7 glass. This is due to the higher thickness of Al/Cu foils ($\sim$ 20 μm), and the laser ablation will not remove the confining layer completely (as the skin depth inside material for 532 nm is few nm only). So, the laser ablative shock waves inside the 20 μm Al/Cu foils will transmit into the BK-7 glass. The transmitted shock wave velocity greatly depends on the relative acoustic impedances ($Z = \rho U_{sw}$) of both mediums i.e., the confining layer and the target (Al/Cu foil and BK-7 glass interface) as well as on the input laser energy. Due to the confinement, the shock velocities inside the BK-7 glass are greatly enhanced compared to the direct ablation geometry.

Due the shifting of the laser beam focal plane from F0 to F2 focusing condition, the shock wave velocities inside the BK-7 glass were enhanced (around 0.6 - 2.2 km/s) in the case of the confined ablation of the 20 μm Al foil adhered to the BK-7 glass. However, it has not affected the confined ablation of the 20 μm Cu foil adhered to the BK-7 glass and direct ablation of the BK-7 glass. The same behaviour is observed for all the laser input energies used in the study. The energy dependence study on the transmitted shock wave

propagation inside BK-7 glass revealed that, the enhancement of the shock wave inside material (BK-7 glass) greatly depends on relative acoustic impedance of the confining layer (20 μm Al and Cu thin foils) and target material (BK-7 glass) and laser energy density in the focal volume at the interface. Since, the relative acoustic impedance (Z) of the confining layer with the target material plays a crucial role in the enhancement of shock wave propagation inside target material, we have observed higher shock velocities inside the BK-7 glass due the Cu thin foil (Cu+BK-7) confinement than the Al thin foil confinement (Al+BK-7) as $Z_{Cu}(3.93) > Z_{Al}(1.45) > Z_{BK-7}(1.27)$ (in $10^6 gr/cm^2 - s$).

The study of laser induced breakdown of the BK-7 glass in the direct and confined ablation geometry is useful to understand the shock wave nature inside the solids w.r.t. the input laser energy and relative acoustic impedance between confining medium and solid target.

7.2 Future Work

∗ **Confined laser ablative shock waves inside the solids**

The studies on the laser ablative shock waves inside BK-7 glass due to the Al/Cu confinement of BK-7 glass (Chapter 6), can be extended by adding the glass substrate confinement to the Al/Cu confining layer to understand the further enhancement of the shock wave propagating inside the BK-7 glass. The schematic used for the laser ablative shock waves inside BK-7 glass due to the glass confinement is shown in Figure 7.2.

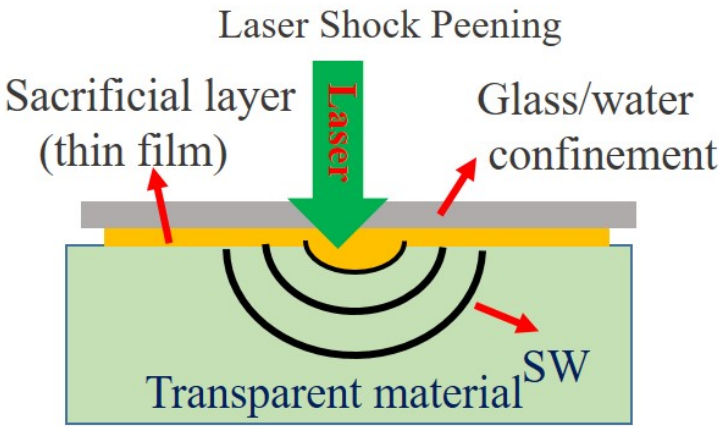

Figure. 7.2 Schematic used for the confined laser ablative shock waves inside the BK-7 glass.

As we know the relative acoustic impedance, laser energy and focusing conditions plays crucial role on the shock waves inside the BK-7 glass, by proper selection of the confining overlays and laser energy we can enhance the shock wave pressure inside the BK-7 glass. This study will helps to understand the Laser Shock Peening (LSP) of the solids in the confined geometry.

∗ **LIBO studies from the composite polymers**

As the LIBO SWs from the polymers with optimal energy and focusing conditions gave higher shock velocities compared to the metals in the confined geometry, the studies were further extended to the LIBO from composite polymer films as they have specific application towards the laser ablation propulsion. With proper coating of the composite polymers on the glass substrate and using the optimal laser energy, focusing conditions we can achieve the higher blow off shock velocities.

∗ **Designing of the ns laser based shock tube**

The thesis studies can be extended to the designing of the ns laser based shock tube. By combining the results obtained from the LIBO studies (Chapter 4) and the spatial confinement (Chapter 5) inside hollow tubes, the temporal evolution of the LIBO shock waves (SW) propagating inside the mm sized tube can be studied using the shadowgraphy imaging. Figure 7.3 (a) shows the schematic used for the shadowgraphy imaging of LIBO SWs inside the mm sized tubes with different geometries and Figure 7.3 (b) shows the experimental visualization of the initial study of ns laser based shock tube using rectangular tube geometry with L=15 mm and d=8 mm. The same study can be further extended to the propagation of LIBO SWs inside the mm size tube filled with transparent liquids to understand the behaviour shock wave based micro fluid jets which are used in the field of the nano coatings and biomedicine. With the help of the different tube geometries (cone, spherical, hemi-spherical and square shape) and different tube material, this study can be utilized for the shock wave focusing also. As the ns laser based mm sized shock tube

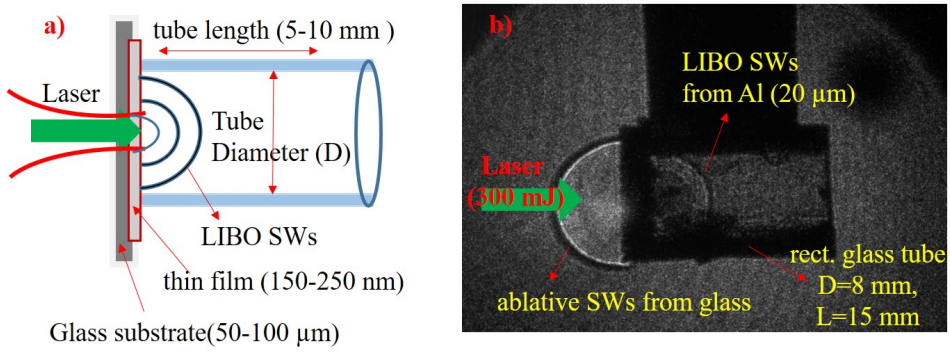

Figure. 7.3 (a) Schematic used for the LIBO SWs propagation inside the mm sized tubes (b) experimental visualization of ns laser shock tube using rectangular tube geometry .

needs metal plasma as the driver at the entrance of the tube, the metal plasma can be replaced with composite polymer plasma as it has low breakdown threshold values. The shock waves from ns laser based shock tubes can be utilized for the processing of the different materials placed at the exit of the shock tube.

List of Publications

Journal Papers:

1. **Nagaraju Guthikonda**, E. Manikanta, Ch. Leela, S. Sai Shiva, S. Sree Harsha, V. R. Ikkurthi and P. Prem Kiran, *Interaction of two counter-propagating laser induced plasmas and shock waves in air*, Physics of Plasmas 27, 023107 (2020).

Invited publications:

1. **Nagaraju Guthikonda**, Ch. Leela and P. Prem Kiran, *Interaction of Two Counter-Propagating Laser Induced Shock Waves in air*, Bulletin of Indian Laser Association: Kiran, vol. 26, No.1 (2017).

Manuscripts under preparation:

- **Nagaraju Guthikonda**, S. Sai Shiva, D. P. S. L. Kameswari, P. Prem Kiran, C. D. Sijoy and V. R. Ikkurthi, *Effect of Focusing Plane on Laser Blow-off Shock Waves from Confined Aluminum and Copper Foils*, (2021).

- **Nagaraju Guthikonda**, D. P. S. L Kameswari, E. Manikanta, S. Sai Shiva, S. Sree Harsha and P. Prem Kiran, *Dynamics of confined laser induced air plasma inside a hollow tube*, (2021).

- E. Manikanta, **Nagaraju Guthikonda**, S. Sai Shiva and P. Prem Kiran, *Acoustic probing of the interaction of two counter-propagating shock waves*, (2021).

- E. Manikanta, **Nagaraju Guthikonda**, S. Sai Shiva and P. Prem Kiran, *Enhancement of Laser produced Acoustic features in the presence of Argon gas environment*, (2021).

- **Nagaraju Guthikonda**, E. Manikanta, G. Muthukumaran and P. Prem Kiran, *Shadowgraphy Imaging of Laser Induced Shock waves in Transparent Media* (2021).

Achievements/Recognitions:

∗ ***Best poster presentation award***

- **Nagaraju Guthikonda**, Ch. Leela and P. Prem Kiran, *Interaction of Two Counter-Propagating Laser Induced Shock Waves in air*, 25^{th} DAE-BRNS National Laser symposium (NLS-25), KIIT University, Bhubaneswar, India (2016).

∗ ***Best oral presentation award***

- **Nagaraju Guthikonda**, B. Ganesh Muthukumaran and P. Prem Kiran, *Shadowgraphy Imaging of Laser Blow-off of metal and polymer films*, 5^{th} National Symposium on Shock Waves, TBRL, Chandigarh, India (2018).

Schools/Workshops:

- **DST-SERB School** on, *Modern Optics & Its Applications*, Department of Physics, IIT-Patna, Patna, India, 30^{th} November- 18^{th} December (2015).

- **DST-SERB School** on, *Ultrahigh Intensity Laser Produced Plasmas: Physics and Applications*, RRCAT, Indore, India, January 7^{th}- 25^{th} (2019).

Conference Proceedings:

- **Nagaraju Guthikonda**, B. Ganesh Muthukumaran and P. Prem Kiran, *Shadowgraphy Imaging of Laser Induced Shockwaves in Transparent Media*, HEMCE Proceedings, 11^{th} International High Energy Materials Conference & Exhibits (HEMCE-2017), HEMRL, Pune, India (2017).

- **Nagaraju Guthikonda**, D. P. S. L. Kameswari, S. Sai Shiva, S. Sree Harsha, B. Barkakaty and P. Prem Kiran, *Laser induced Blow off shock waves from Metals and dielectrics: Effect of depth of focus*, HEMCE Proceedings, 12^{th} International High Energy Materials Conference & Exhibits (HEMCE-2019), IIT-Madras, Madras, India (2019).

- S. Sai Shiva, **Nagaraju Guthikonda**, P. Prem Kiran, C. D. Sijoy, V. R. Ikkurthi and S. Chaturvedi , *A parametric study of Laser Generated Plasma Driven Flyer and Shock Wave Characteristics from Rear Side of Aluminum, Copper and Titanium Targets Confined with Glass Substrate*, HEMCE Proceedings, 12^{th} International High Energy Materials Conference & Exhibits (HEMCE-2019), IIT-Madras, Madras, India (2019).

- J. Yellaiah, E. Manikanta, **Nagaraju Guthikonda** and P. Prem Kiran, *Effect of laser energy on Underwater acoustic shock wave emissions from optical breakdown*, Proceedings of the International Conference on Optics and Electro-Optics (ICOL-2019): Springer Proceedings in Physics, Dehradun, India (2020).

Conference Presentations (National/International):

- **Nagaraju Guthikonda**, Ch. Leela and P. Prem Kiran, *Interaction dynamics of two counter-propagating laser induced shock waves in air* , Recent Advances in Optical Science II (RAOS-II), University of Hyderabad, Hyderabad, India (2016). (POSTER)

- E. Manikanta, **Nagaraju Guthikonda**, L. Vinoth Kumar and P. Prem Kiran, *Acoustic diagnostics of interacting shock waves in air*, Recent Advances in Optical Science II (RAOS-II), University of Hyderabad, Hyderabad, India (2016). (POSTER)

- **Nagaraju Guthikonda**, B. Ganesh Muthukumaran, P. Naveen Kumar and P. Prem Kiran, *Shadowgraphy Imaging of Laser Induced Shock waves in Transparent Media*, National Laser Symposium (NLS-26), BARC Mumbai, India (2017). (POSTER)

- P. Naveen Kumar, **Nagaraju Guthikonda**, B. Ganesh Muthukumaran, P. Prem Kiran and V. S. Ashok, *Shock wave and Cavitation bubble dynamics by ns, ps laser pulse induced breakdown in water*, 5^{th} National Symposium on Shock Waves, TBRL, Chandigarh, India (2018). (POSTER)

- **Nagaraju Guthikonda**, B. Ganesh Muthukumaran and P. Prem Kiran, *Shadowgraphy imaging of Laser Induced Shock Waves in Transparent Media: Effect of plasma confinement due to a thin film*, National Laser Symposium (NLS-27), RRCAT, Indore, India (2018). (POSTER)

- D. P. S. L. Kameswari, **Nagaraju Guthikonda**, S. Sai Shiva and P. Prem Kiran, *2D Numerical Simulation of Spatio-Temporal Evolution of Laser Induced Shock Waves In Air*, National Laser Symposium (NLS-27), RRCAT, Indore, India (2018). (POSTER)

- **Nagaraju Guthikonda** and P. Prem Kiran, *Shadowgraphy Imaging of Laser Blow-off of Metal Thin Films*, National Laser Symposium (NLS-27), RRCAT, Indore, India (2018). (POSTER)

- **Nagaraju Guthikonda**, D. P. S. L. Kameswari, S. Sree Harsha and P. Prem Kiran, *Dynamics of laser induced plasma confinement: effect on shock waves*, 33^{rd} National Symposium on Plasma Science & Technology (PLASMA 2018), University of Delhi, Delhi, India (2018). (POSTER)

Dynamics of Confined Laser Induced/Ablative Plasmas and Shock Waves

by Nagaraju Guthikonda

Dynamics of Confined Laser Induced/Ablative Plasmas and Shock Waves

ORIGINALITY REPORT

17%	12%	16%	1%
SIMILARITY INDEX	INTERNET SOURCES	PUBLICATIONS	STUDENT PAPERS

PRIMARY SOURCES

# 1	aip.scitation.org Internet Source	10%
# 2	Nagaraju Guthikonda, Elle Manikanta, Leela Chelikani, S. Sai Shiva, S. Sree Harsha, V. R. Ikkurthi, P. Prem Kiran. "Interaction of two counterpropagating laser induced plasmas and shock waves in air", Physics of Plasmas, 2020 Publication	1%
# 3	orcid.org Internet Source	1%
4	S. Wu, X. Lu. "Two counter-propagating He plasma plumes and ignition of a third plasma plume without external applied voltage", Physics of Plasmas, 2014 Publication	<1%
5	doras.dcu.ie Internet Source	<1%
6	dyuthi.cusat.ac.in Internet Source	<1%

The first three sources are from student's publications

P. Prem Kiran

Dr. P. Prem Kiran
Associate Professor
School of Physics
University of Hyderabad
Hyderabad-500 046. (TS) INDIA

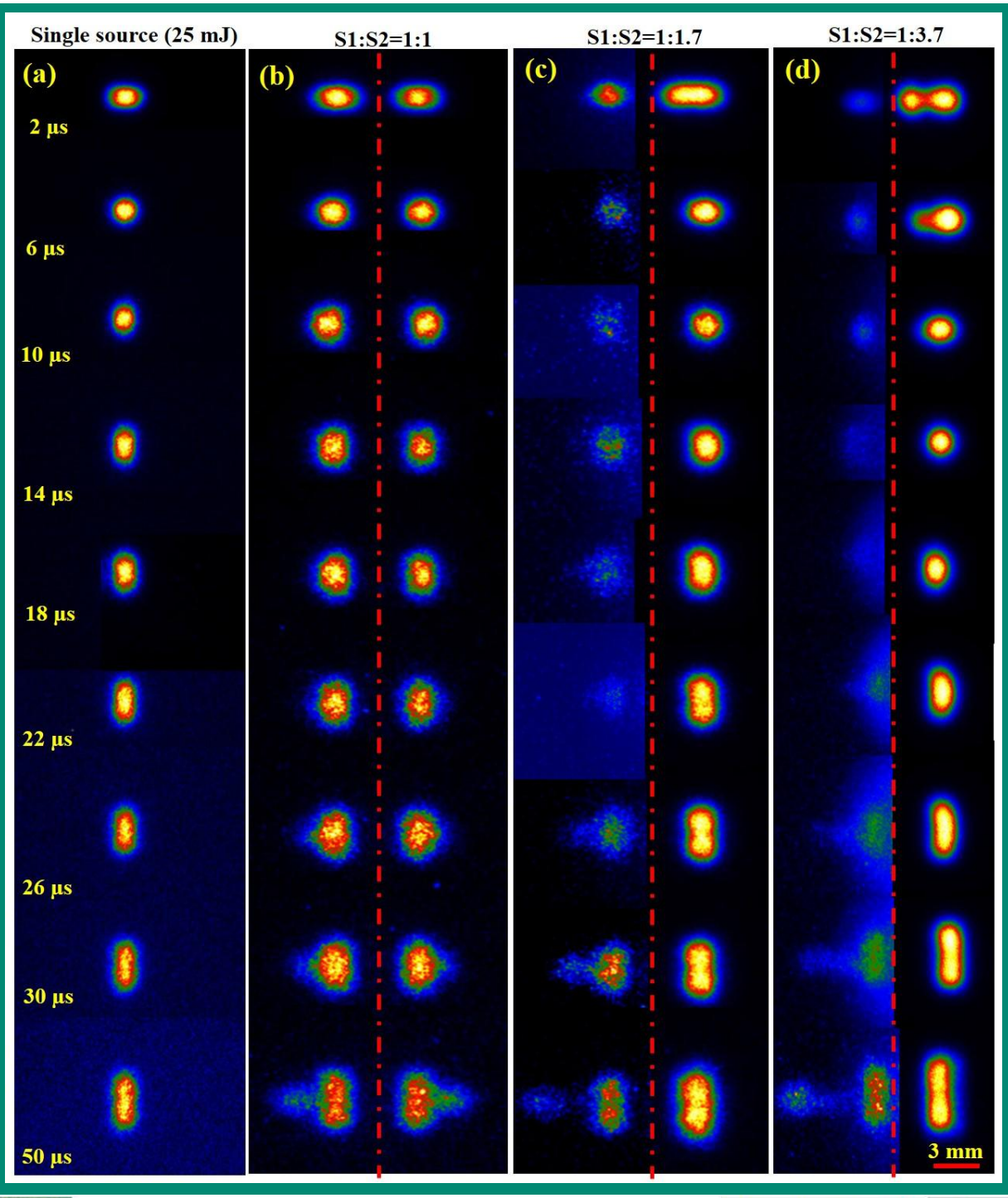
Single source (25 mJ)
S1:S2=1:1
S1:S2=1:1.7
S1:S2=1:3.7
(a)
(b)
(c)
(d)
2 μs
6 μs
10 μs
14 μs
18 μs
22 μs
26 μs
30 μs
50 μs
3 mm

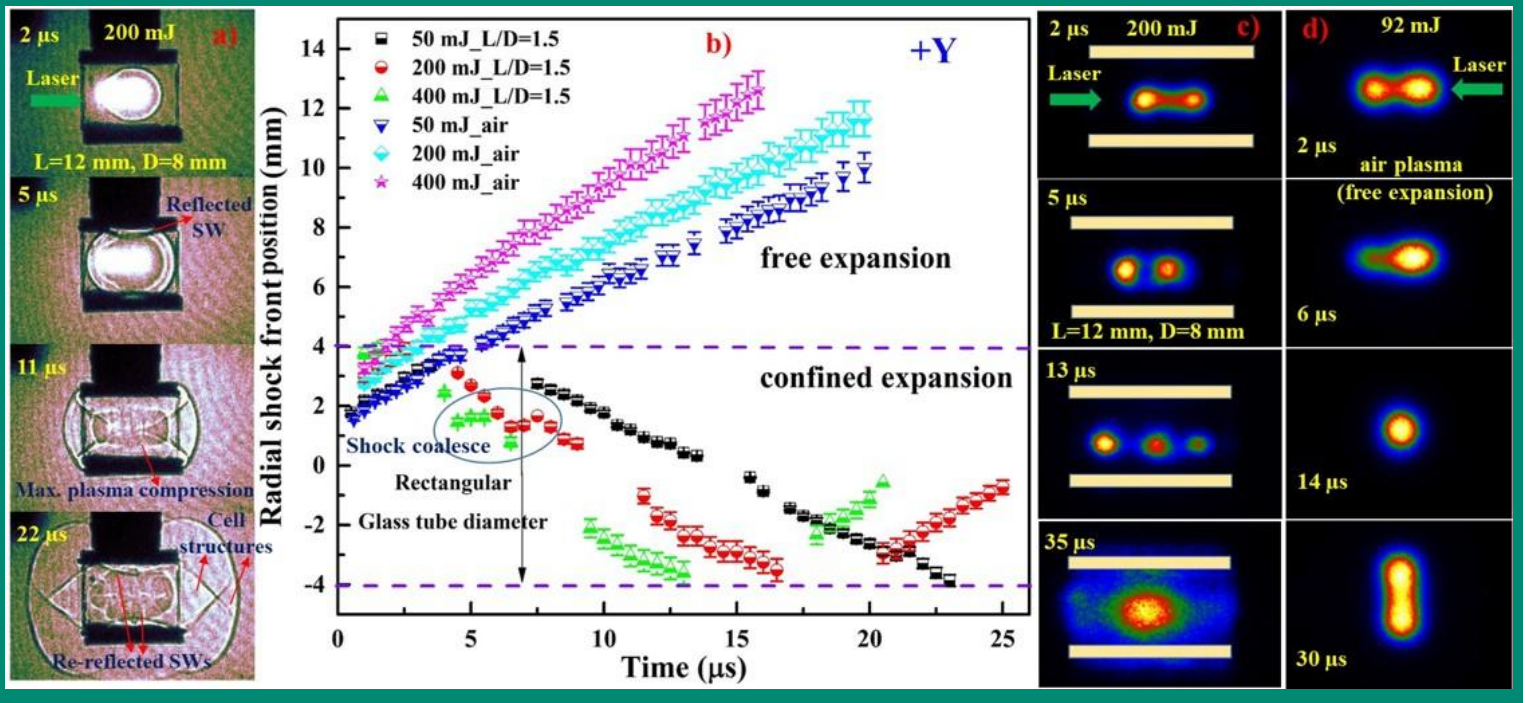
2 μs
200 mJ
a)
Laser
L=12 mm, D=8 mm
5 μs
Reflected SW
11 μs
Max. plasma compression
22 μs
Cell structures
Re-reflected SWs
b)
+Y
50 mJ_L/D=1.5
200 mJ_L/D=1.5
400 mJ_L/D=1.5
50 mJ_air
200 mJ_air
400 mJ_air
free expansion
confined expansion
Shock coalesce
Rectangular
Glass tube diameter
Radial shock front position (mm)
Time (μs)
c)
2 μs
200 mJ
Laser
5 μs
L=12 mm, D=8 mm
13 μs
35 μs
d)
92 mJ
Laser
2 μs
air plasma
(free expansion)
6 μs
14 μs
30 μs